

# Chemical Fractionation at Environmental Interfaces

Thesis by

Jie Cheng

In Partial Fulfillment of the Requirements

for the Degree of

Doctor of Philosophy



CALIFORNIA INSTITUTE OF TECHNOLOGY

Pasadena, California

2010

(Defended October 14, 2009)

© 2010

Jie Cheng

All Rights Reserved

## Acknowledgements

Looking back at my years at Caltech, I have every reason to be grateful. Caltech has not only offered abundant resources and a creative environment for scientific research, but has also provided enriching opportunities for self-discovery. Above all, I would like to extend my gratitude to all those who have made my years at Caltech rewarding and enjoyable.

First, I would like to thank Professor Michael Hoffmann for being a great advisor. In my junior year of college, I read a few of his articles on  $\text{TiO}_2$  photocatalysis and got very interested in the work. So I sent him an email, expressing interest in doing graduate work with him, and he replied with six words: “I strongly recommend you to apply.” Thus, here I am. Although I did not end up working on  $\text{TiO}_2$  photocatalysis, Professor Hoffmann has allowed me the freedom to explore my interest and to work on a variety of topics in environmental chemistry. Professor Hoffmann was always ready to listen to me and to provide guidance on many issues that matter to me.

I wish to thank my other committee members, Professors John Seinfeld, Richard Flagan, and Paul Wennberg, for their valuable time and comments. Working with Professor Richard Flagan on the pollen project was a great learning experience and a lot of fun. The wonderful courses taught by Professor John Seinfeld and Professor Paul Wennberg further developed my interest in atmospheric chemistry.

I owe many thanks to Dr. A. J. Colussi, with whom I have worked closely on several projects. Dr. Colussi impressed me with his unflinching passion for science, and his ability to connect the dots and come up with new ideas.

I benefited a great deal from collaboration with Dr. Chad Vecitis and Dr. Hyunwoong Park on the ion fractionation project and the perfluorochemical remediation project. Dr. Chad Vecitis was able to use analytical instrument in very creative ways and was always willing to help other group members. Dr. Hyunwoong Park had excellent multitasking skills and worked very efficiently in the lab. I enjoyed working with Cherrie Soetjipto, a SURF student, on the ice-pH project. Waiting endlessly for our samples to freeze on the microscope stage could have been boring without those interesting stories she told me about Indonesia. Dr. Shinichi Enami and I collaborated on the ozone-electrospray project. He did not talk much but consistently produced quality work. I would also like to thank collaborators Professor Deming Zhao and Professor Eleferia Psillakis.

My thesis could not have been completed without the help of a number of people. Dr. Nathan Dalleska at the Environmental Analysis Center graciously shared his expertise in analytical chemistry with me. Dr. Sonjong Hwang and Dr. Chris Waters provided training and support for the solid-state NMR and the confocal microscope, respectively. Mike Vondrus at the machine shop, Tom Dunn at the electronics shop, and Richard Gerhart at the glass shop made it possible for me to conduct experiments with tailor-made equipment. I want to thank Cecilia Gamboa, Fran Matzen, Linda Scott, and Dian Buchness for keeping the department running smoothly.

I cannot forget other members of the Hoffmann group who have helped me along the way, including Dr. Christopher Boxe, Dr. Marcello Guzman, Dr. Suyoung Ryu, Dr. Angela Rincon, Jina Choi, Tammy Campbell, Will Ford, and Rifkha Kameel. I enjoyed the time we spent together in group meetings, and group activities such as barbecue on the beach, celebrations at the Hoffmann house, and Friday nights at the Athenaeum.

There are many people at Caltech who have been great friends over the years. Dinners out with Yue Zou, Dr. Xin Guo, Dr. Dongping Zhuang, Dr. Bo Li, Yingying Wang, Le Kuai, Xiaobai Li, Ying Wang, Dr. Hua Wang, Hongjing Tan, Tong Chen, and Jinghao Huang were always relaxing and full of fun. I had a great time working with Yizhou Liu, Yao Sha, Lijun Liu, Dr. Ruihua Fang, Molei Tao, and Brian Yu at the Caltech Chinese Association. Dr. Mingshr Lin, Dr. Wanwan Yang, Dr. Hilary Glidden, Dr. Shankar Kalyanaraman, Dr. Shripad Thite, Dr. Jonas Oxgaard, Dr. Guangxi Wang, Kai Shen, Ming Gu, and Jay Chen shared interest in management consulting. Will Yardley helped me better understand the American culture and the Chinese culture! Susanna Tran taught me Italian of which I can still speak a few words. Jim Endrizzi and Athena Trentin at ISP worked hard to ensure that international students like me quickly adjust to life in the United States. Yvonne Banzali at the Career Development Center offered useful job-hunting tips. I am also thankful to Dr. Ling Zheng, Dr. Yi Liu, Dr. Mo Li, Dr. Yajuan Wang, Dr. Chengzhong Zhang, Dr. Xiao Lu, Dr. Changlin Pang, and many other friends for their help.

My friends from Tsinghua University have been a good source of encouragement as well as entertainment. Dr. Xin Dong kept me updated with all the exciting news of old friends from college. Yeqing Zheng kindly provided professional literature search services at no charge. Shuo Wang and I agreed on both the danger of procrastination and the awesomeness of certain video games.

My final thanks go to my family for their unconditional support and love. My parents, Yongfang Cheng and Jing Zhang, always gave me the freedom to chart my own course and respected my decisions. My fiancée Li Liu has been my best friend. We have learned and will continue to grow together and to nurture, support, and encourage each other.

## Abstract

Chemical processes at the interfaces often differ kinetically and mechanistically from the bulk counterparts, partly due to the concentration inhomogeneity of different chemicals at the interfaces. The fractionation of chemicals at the interfaces not only determines their interfacial concentrations, but also affects the physicochemical properties of the interfaces. In this thesis, three sets of chemicals/interfaces with important environmental implications are studied: (1) anion fractionation at the gas–liquid microdroplet interfaces, (2) fractionation of perfluoroalkyl surfactants and matrix components at the bubble–water interface in ultrasonically irradiated solutions, and (3) ion fractionation across the ice–water interface during the freeze–thaw cycle of electrolyte solutions.

The relative anion affinity for the air–water interface, as measured by Electrospray Mass Spectrometry (ES–MS), is exponentially correlated with ionic radius. The affinities respond differently to different additives, suggesting that specific anion effects are due to different energy levels of physical interactions. Relative anion affinities at the air–methanol interfaces are almost identical to those at the air–water interface, suggesting that surface structure is not the primary driving force for interfacial anion fractionation.

Perfluoroalkyl carboxylates and sulfonates can be transferred from the ocean to marine aerosols due to their high affinity for the air–water interface, but transfer to gas phase is unlikely as they remain deprotonated in aqueous phase because of their low pKa. Organic matrix components may reduce the sonochemical kinetics of Perfluorooctanesulfonate (PFOS) and Perfluorooctanoate (PFOA) by competitive adsorption onto the bubble–water interface or by lowering the interfacial temperatures. Inorganic anions, but not cations, may significantly enhance or reduce the sonochemical kinetics of PFOS and PFOA. The

specific anion effects following the Hofmeister series are likely related to anions' partitioning to and interaction with the bubble–water interface.

Time–resolved confocal fluorescence microscopy of freezing electrolyte solutions reveals that the thickness of interstitial liquid films depends non–monotonically on electrolyte concentration. It also confirms that selective incorporation of cations (anions) into the ice lattice decreases (increases) the pH of the interstitial liquid films. Since the magnitude of pH change during freezing is smaller than during the subsequent thawing process, it is likely to be limited by the seepage of  $H^+$  ( $OH^-$ ) slowly produced via water dissociation.

## Table of Contents

List of Figures .....	xiii
List of Tables .....	xii
List of Schemes.....	xiv
Chapter 1: Introduction .....	1
1.1 Overview of Chemical Fractionation at Environmental Interfaces.....	2
1.2 Ions at Air–Water Interface.....	3
1.3 Sonochemical Degradation of Perfluorochemicals at Water–Bubble Interface.....	7
1.4 Chemical Fractionation during Freezing of Electrolyte Solutions.....	10
1.5 Outline of the Thesis .....	13
1.6 References .....	18
Chapter 2: Experimental Anion Affinities for the Air–Water Interface .....	26
2.1 Abstract.....	27
2.2 Introduction .....	28
2.3 Experimental Section.....	29
2.4 Results and Discussion .....	30
2.5 Acknowledgments.....	35
2.6 References.....	36
Chapter 3: Anion Fractionation and Reactivity at Air–Water and Air–Methanol Interfaces: Implications for the Origin of Hofmeister Effects.....	50
3.1 Abstract .....	51
3.2 Introduction.....	52
3.3 Experimental Section.....	53
3.4 Results and Discussion .....	55
3.5 Acknowledgement.....	59
3.6 References.....	59
Chapter 4: Enrichment Factors of Perfluoroalkyl Oxoanions at the Air–Water Interface ...	72
4.1 Abstract.....	73
4.2 Introduction.....	74

4.3 Experimental Section .....	75
4.4 Results and Discussion .....	77
4.5 Acknowledgments .....	81
4.6 References.....	81
Chapter 5: Acid Dissociation versus Molecular Association of Perfluoroalkyl Oxoacids: Environmental Implications .....	93
5.1 Abstract.....	94
5.2 Introduction.....	95
5.3 Experimental Section .....	96
5.4 Results and Discussion.....	97
5.5 Acknowledgments .....	100
5.6 References.....	100
Chapter 6: Sonochemical Degradation of Perfluorooctane Sulfonate (PFOS) and Perfluorooctanoate (PFOA) in Landfill Groundwater: Environmental Matrix Effect .....	113
6.1 Abstract.....	114
6.2 Introduction.....	115
6.3 Experimental Methods .....	117
6.4 Experimental Results.....	119
6.5 Discussion.....	122
6.6 Acknowledgements .....	127
6.7 References.....	127
Chapter 7: Sonochemical Degradation of Perfluorooctane Sulfonate (PFOS) and Perfluorooctanoate (PFOA) in Groundwater: Kinetic Effects of Matrix Inorganics .....	144
7.1 Abstract.....	145
7.2 Introduction.....	146
7.3 Experimental Methods .....	147
7.4 Results.....	149
7.5 Discussion.....	153
7.6 Acknowledgements .....	159

7.7 References.....	159
Chapter 8: Confocal Fluorescence Microscopy of Interstitial Fluids in Freezing Electrolyte Solutions.....	172
8.1 Abstract.....	173
8.2 Introduction .....	174
8.3 Experimental Section .....	175
8.4 Results and Discussion.....	177
8.5 Acknowledgements .....	180
8.6 References .....	180

## List of Figures

Figure	Page
Figure 2.1 ES–MS spectrum of equimolar aqueous $\text{SCN}^-$ , $\text{NO}_3^-$ , $\text{Br}^-$ , $\text{BF}_4^-$ , $\text{ClO}_4^-$ , and $\text{I}^-$	42
Figure 2.2 Anion affinities versus anionic radius .....	43
Figure 2.3 Normalized anion affinity versus free energy of anion dehydration.....	44
Figure 2.4. Normalized anion affinity versus anion polarizability.....	45
Figure 2.5 Ratios of normalized anion affinity versus urea concentration .....	46
Figure 2.6 Ratios of normalized anion affinity versus (CTAC) concentration.....	47
Figure 2.7 Ratios of normalized anion affinity versus Triton X–114 concentration.....	48
Figure 2.8 Normalized anion affinity versus SDS concentration.....	49
Figure 3.1 ES–MS spectrum of equimolar aqueous $\text{NO}_3^-$ , $\text{BF}_4^-$ , $\text{ClO}_4^-$ , $\text{PF}_6^-$ , and $\text{IO}_3^-$ .....	65
Figure 3.2 Normalized anion affinity versus ionic radius .....	66
Figure 3.3 (a) Relative anion affinities of $\text{NO}_3^-$ , $\text{BF}_4^-$ , $\text{ClO}_4^-$ , $\text{PF}_6^-$ , and $\text{IO}_3^-$ (b) The surface coverage of $-\text{CH}_3$ groups (c) The dielectric permittivity versus methanol molar fraction....	67
Figure 3.3 (c) The dielectric permittivity versus methanol molar fraction .....	67
Figure 3.4 Interfacial iodide concentration versus $[\text{O}_3(\text{g})]$ in $\text{H}_2\text{O}$ and $\text{MeOH}$ .....	68
Figure 3.5 The product branching ratio $[\text{IO}_3^-]/[\text{I}_3^-]$ versus $[\text{O}_3(\text{g})]/[\text{I}^-]$ .....	69
Figure 4.1 ES–MS calibration curves of perfluoroalkyl sulfonate .....	88
Figure 4.2 ES–MS spectrum of a 1 $\mu\text{M}$ equimolar multianion aqueous solution .....	89
Figure 4.3 Enrichment factor versus n–alkyl chain length.....	90
Figure 4.4 The effect of $\text{NaCl}$ and 1–octanol on the enrichment factor .....	91
Figure 5.1 ES–MS titration curves of n–hexanoic and n–octanoic acids .....	107
Figure 5.2 ES–MS spectra of PFOS under different pH and electrolyte conditions .....	108
Figure 5.3 ES–MS spectra of PFO under different pH and electrolyte conditions .....	109
Figure 5.4 ES–MS titration curves for PFOSA and PFOA.....	110
Figure 5.5 Signal intensity ratio of $(\text{PFOA})_2\text{H}^-$ to the sum of PFOA species versus pH.....	111
Figure 6.1 PFOX sonolysis in MilliQ water and landfill groundwater at 354 kHz.....	134
Figure 6.2 The effect of five VOCs on PFOX sonolysis kinetics.....	135
Figure 6.3 The effect of alkyl benzenes and MIBK on PFOX sonolysis kinetics.....	136

Figure 6.4 The effect of humic and fulvic acids .....	137
Figure 6.5 Sonolysis and sonozone of PFOX in MilliQ and landfill groundwater .....	138
Figure 6.6 Surface tension curves for the VOCs in figure 6.2 .....	139
Figure 6.7 PFOX sonolysis in MilliQ water and landfill groundwater at 612 kHz.....	140
Figure 6.8 PFOX sonolysis under Ar, O <sub>2</sub> , and O <sub>3</sub> .....	141
Figure 6.9 Temperature dependence of C <sub>p,g</sub> and k <sub>iaw</sub> for the VOCs in figure 6.2.....	142
Figure 6.10 LC/MS calibration curves for PFOX .....	143
Figure 7.1 PFOX sonolysis in MilliQ water and groundwater at 612 kHz.....	165
Figure 7.2 The effect of anions on PFOX sonolysis kinetics .....	166
Figure 7.3 The effect of cations on PFOX sonolysis kinetics .....	167
Figure 7.4 Rate constant for sonolysis of PFOX versus solution pH .....	168
Figure 7.5 Effect of pH adjustment on PFOX sonolysis kinetics in groundwater .....	169
Figure 7.6 PFOX sonolysis in MilliQ water and groundwater at 354 kHz.....	170
Figure 7.7 The acid–base titration curve of the groundwater sample .....	171
Figure 8.1 Temperature profile during the freeze–thaw cycle of sample .....	185
Figure 8.2 Fluorescence emission ratio versus pH by fluorometer and CLSM.....	186
Figure 8.3 C-SNARF-1 in MilliQ, NaCl and (NH <sub>4</sub> ) <sub>2</sub> SO <sub>4</sub> solution during freezing.....	187
Figure 8.4 Fluorescence image of C-SNARF-1 in NaCl during freeze–thaw cycle .....	189
Figure 8.5 Fluorescence image of C-SNARF-1 in (NH <sub>4</sub> ) <sub>2</sub> SO <sub>4</sub> during freeze–thaw cycle .	191
Figure 8.6 Fluorescence emission ratio versus pH curves at different temperatures .....	193
Figure 8.7 Fluorescence emission ratio versus laser intensity and probe concentration ....	194

**List of Tables**

Table	Page
Table 2.1 Interfacial affinities and molecular properties of anions.....	41
Table 3.1 Interfacial affinities and molecular properties of anions.....	64
Table 4.1 Relative anion enrichment factors $f$ at the air–water interface.....	87
Table 5.1 Isotope ratios of PFO species observed by ES–MS. ....	106
Table 6.1 Primary components of the landfill groundwater.....	131
Table 6.2 Physical and thermodynamic properties of the five VOCs in figure 6.2.....	132
Table 6.3 Representative analytical results of quality-control samples.....	133
Table 7.1 Primary components of the groundwater sample.....	164
Table 8.1 Fitting parameters of equation (8.2) .....	184

**List of Schemes**

Scheme	Page
Scheme 1.1 Sonochemical PFOS transformation into its organic constituents .....	25
Scheme 3.1 Iodide oxidation by ozone in water.....	70
Scheme 3.2 Schematic diagram of the iodide–ozone reaction chamber.....	71
Scheme 4.1 <i>Anti</i> - and <i>gauche</i> -perfluorobutanoate at the air–water interface.....	92
Scheme 5.1 Schematic drawing of The MM2 structure of the (PFO) <sub>2</sub> H <sup>-</sup> cluster.....	112
Scheme 8.1 The chemical structure of C-SNARF-1 .....	195

# **Chapter 1**

## **Introduction**

## 1.1 Overview of Chemical Fractionation at Environmental Interfaces

Fractionation, is of, relating to, or involving a process for separating components of a mixture through differences in physical or chemical properties. In this thesis, it is occasionally used more broadly to mean partitioning, which emphasizes the separation of a species between different phases. An interface is a surface that forms the common boundary of two different phases. It can alternatively be defined by the concentration inhomogeneity of the different species, whereas the bulk is defined as the region where the species are homogeneously mixed. More broadly, gradients in not only the chemical composition but also in physicochemical properties such as dielectric constant and density are present across the interface, with the boundary values being those of the two phases the interface connects. The thickness of the interface as defined by the gradient can thus vary depending on the specific property in consideration. For example, the water-vapor interface is considered very broad as the water density gradient effectively covers a distance of roughly 0.5 nm.<sup>1</sup>

Interfaces provide a unique chemical environment: the kinetics and mechanisms of chemical processes occurring at the interfaces are usually neither identical to nor readily extrapolated from those of the bulk processes. There are many examples in which interfacial chemical transformation is the rate-determining step of a heterogeneous chemical reaction series. The fractionation behavior of chemical species at the interface is important in that it affects not only the interfacial concentration of the chemical species of interest, but also the physicochemical properties of the interface through a variety of specific or nonspecific interactions.

Interfaces play important roles in many physical, chemical, and biological processes, many of which have important environmental implications. In this thesis, I present three independent studies on the fractionation of chemicals at environmental interfaces. The first part describes anion fractionation and reactivity at the air-liquid interfaces. The second part focuses on the partitioning of common groundwater matrix components at the bubble-water interface under ultrasonic irradiation and the effect of partitioning on the sonochemical degradation efficiency of two perfluorinated chemicals. The third part provides direct experimental evidence of the compositional change in the interstitial liquid channels during freezing of electrolyte solutions due to fractionation of ionic species at the ice-water interface.

## **1.2 Ions at air-water interface**

The behavior of ions at aqueous interfaces is important in numerous chemical and biological systems.<sup>2-3</sup> For example, the distribution and transport of ions at the air-water interface has important implications for heterogeneous atmospheric chemistry in that they affect not only the reactive uptake of gaseous species on aqueous aerosols but also the surface reactivity of ions toward gas phase reactants such as O<sub>3</sub> or OH radical. Understanding the equilibrium and dynamic properties of ions at the air-water interface is thus essential in modeling and even the chemical reactivity in many environmental systems that involve an air-water interface.

### **1.2.1 Historical view**

A traditional view in physical chemistry has it that small ions are effectively repelled from the air-water interface simply due to Coulomb interactions. According to the Born model, the dehydration energy, i.e., the free energy change upon moving an ion from

water to air (vacuum), is  $\Delta G = (1 - 1/\epsilon)q^2 / 4\pi\epsilon_0 R$ , where  $\epsilon \approx 80$  is the dielectric constant of water,  $\epsilon_0$  is the permittivity of a vacuum,  $q$  and  $R$  are the size of charge and radius of the ion, respectively. The large value of  $\Delta G$ , which is on the order of  $10^2$  kT for small ions such as  $\text{Na}^+$ , forces the ion to stay in bulk liquid. This concept has also been illustrated with a classical image charge model, in which an ion with charge  $q$  at the air-water interface can be conceived as being repelled by an image charge with the same sign  $q' = q(\epsilon - 1)/(\epsilon + 1)$ .

Given a finite ion size and a smooth gradual interface between the two phases, the energy required to bring an ion from bulk water to the water side of the air-water interface is only a few kT,<sup>4</sup> and may thus be compensated by other interactions that are neglected by the classic models, including ion-water interactions, polarization and dispersion effects, and solvation entropy effects.<sup>5</sup> In this more complete picture of ion solvation, it is possible for ions to be present or even enriched at the air-water interface.

### 1.2.2 Simulation results

Molecular simulations such as molecular dynamics (MD) and Monte Carlo (MC) methods can directly probe the molecular details of solutes at the interface. These approaches have been used to examine the equilibrium properties of neat-water surfaces, and the distribution and transport of ions at the air-water interface.<sup>6-7</sup> For molecular dynamics simulations, either the classical force-field approach or the *ab initio* approach is employed.<sup>8</sup> In the former case, the use of polarizable force fields is considered essential for an accurate description of ions at the aqueous interfaces.<sup>6-7</sup>

The traditional view of ion depletion at the air-water interface has recently been challenged by the results of molecular simulation studies, which predict that certain ions

are present or even enriched at the air-water interface. In particular, MD simulations have suggested that ions such as  $\text{Cl}^-$ ,  $\text{Br}^-$ ,  $\text{I}^-$ ,  $\text{SCN}^-$ ,  $\text{NO}_3^-$ ,  $\text{N}_3^-$  and  $\text{H}_3\text{O}^+$  are enriched at the air-water interface to varying degrees, whereas  $\text{F}^-$ ,  $\text{Na}^+$ ,  $\text{SO}_4^{2-}$  prefer to stay in the bulk solution.<sup>9-15</sup> The propensity for ions to reside at the air-water interface is believed to positively correlate with their size and polarizability. In addition, surface curvature also plays an important role in determining the solvation of ions.<sup>16</sup>

### 1.2.3 Experimental results

Results from surface tension and surface potential measurements have been used to infer the microscopic structures at the air-water interface. The surface tension of most aqueous salt solutions has been found to increase with increasing salt concentration.<sup>17-19</sup>

According to the Gibbs adsorption isotherm,  $\left(\frac{\partial \gamma}{\partial \ln c}\right)_T = -RT\Gamma$ , where  $\gamma$  is the surface tension,  $c$  is the bulk concentration, and  $\Gamma$  is the surface excess, i.e., the concentration at the air-water interface in excess of the bulk concentration, a positive correlation between the surface tension and electrolyte concentration is often seen as evidence for the depletion of ions at the air-water interface. However, an alternative explanation is that ions may indeed be enriched at the outermost layers of the interface, but depleted in the sublayers due to strong electrostatic repulsion, thus leading to an overall depletion of ions across the interfacial region to which the surface tension measurements are relevant. Surface potential measurements show little correlation with the surface tension measurements.<sup>20</sup> Anions play a more important role than cations in determining the sign and magnitude of the surface potential, and anions with smaller hydration energies lead to

lower surface potentials. In addition to the electrostatic effect, ions may also affect the surface potential by changing the orientation of polar water molecules at the surface.

The presence of halides at the air-water interface has been inferred from several laboratory measurements of the chemical reaction kinetics of halogen species. For example, the magnitude of the measured uptake of gas phase  $\text{Cl}_2$  and  $\text{Br}_2$  by their respective sodium halide solutions, and its dependence on ion concentration suggest a significant role of the reaction at the air-water interface.<sup>21</sup> The kinetics of chlorine oxidation in sea salt aerosol by hydroxyl radical also suggests that chlorine occupies a significant fraction of the sea salt aerosol surface.<sup>12</sup>

The development of surface specific techniques such as nonlinear optical spectroscopy (vibrational sum-frequency generation, or VSFG, and second harmonic generation, or SHG),<sup>22-24</sup> X-ray photoelectron spectroscopy (XPS),<sup>25</sup> X-ray diffraction and reflection, and neutron reflection,<sup>26</sup> has made it possible to directly probe the molecular details, including the behavior of ions, at the air-water interface. These experimental results are in qualitative agreement with the molecular simulation results, revealing the presence or enhancement of large and polarizable ions at the air-water interface.<sup>10,25,27</sup> The interfacial depth of aqueous solutions is also found to depend on the electrolyte. For example, the interfacial depth of the NaBr and NaI solutions is observed to be greater than that of neat water, NaF, and NaCl solution, implying that there are concentration gradients of the various species that extend the interfacial region several layers into what was the bulk.

#### **1.2.4 Hofmeister effects**

The difference in the preference of ions for the air-water interface versus the bulk liquid phase is an example of specific ion effects, also known as the Hofmeister effects.

The Hofmeister series originally ranked common ions according to their ability to affect protein solubility in aqueous solution, and has since been found relevant to a wide range of interfacial phenomena such as surface tensions to ion exchange resins, zeta potentials, critical micelle concentrations, transport across membranes, and gas bubble-bubble interactions.<sup>28-29</sup> At the air-water interface, for example, the following order is observed regarding ions' propensity to orient interfacial water molecules:  $\text{SCN}^- > \text{NaClO}_4^- > \text{I}^- > \text{NO}_3^- \approx \text{Br}^- > \text{Cl}^- > (\text{pure water}) \approx \text{F}^- \approx \text{SO}_4^{2-}$ .<sup>30</sup> These effects have been attributed to a wide range of “forces” such as hydration forces, specific pi electron-cation interactions, ionic bonding, hydrogen bonding, and hydrophobic forces,<sup>29</sup> but a comprehensive molecular understanding remains elusive.

### **1.3 Sonochemical degradation of perfluorochemicals at water-bubble interface**

#### **1.3.1 Reaction sites and mechanisms in an ultrasonically irradiated liquid**

Sonochemistry, the chemical reactivity induced by ultrasonic irradiation in a liquid medium, has emerged as an alternative method for the removal of recalcitrant organic compounds in the wastewater treatment process. The efficacy of sonochemical degradation has been demonstrated for a wide variety of organic compounds such as phenol and phenolic compounds, methyl tert-butyl ether (MTBE), and perfluorinated surfactants.<sup>31-35</sup>

The sonochemical effects derive principally from acoustic cavitation, i.e., the formation, growth and implosive collapse of bubbles in a liquid medium under ultrasonic irradiation. When a liquid medium is exposed to ultrasonic irradiation, acoustic pressure waves consisting of compression and rarefaction cycles are produced. During the rarefaction cycle, the acoustic pressure waves lead to the formation and growth of vapor bubbles from preexisting gas nuclei. If the intensity of the acoustic pressure waves exceeds that of the

acoustic cavitation threshold, the bubbles would overgrow and eventually collapse.<sup>36</sup> The transient collapse of bubbles leads to almost adiabatic compression of gas and vapor inside the bubbles, thus creating extremely high temperatures and pressures. The average vapor temperatures within the bubble have been shown through chemical methods to reach values as high as 4200–5000 K,<sup>37-38</sup> consistent with the single-bubble collapse model,<sup>39</sup> and bubble-water interface temperatures have been calculated to be in the range of 600 to 1000 K.<sup>40-41</sup> These transient high temperatures lead to *in situ* pyrolytic reactions in the vapor and interfacial regions of each collapsing bubble resulting in the breakdown of gaseous water molecules to produce highly reactive radical species such as hydroxyl radicals ( $\cdot\text{OH}$ ). These radicals react readily with compounds in the bubble gas phase or at the bubble-water interface. Some of the radical species may be dispersed into the bulk solution by nonspherical bubble collapse. The hydroxyl radicals also recombine rapidly at the bubble-water interface or in the solution bulk to produce hydrogen peroxide and water.<sup>32</sup>

Sonochemical decomposition can occur at three potential sites in an ultrasonically irradiated liquid: (1) the cavitation bubble where the temperatures are the highest, (2) the bubble-water interface where temperatures are still high enough to induce thermal effects, and (3) the solution bulk where temperatures are ambient. The target compound can be decomposed at the first two sites via both pyrolytic decomposition and hydroxylation, or in the solution bulk via reaction with hydroxyl radicals and hydrogen peroxide. The sonochemical degradation kinetics and mechanisms of a given compound thus critically depend on its partition coefficient between the solution phase and the liquid phase, and on that between the bulk solution and the bubble-water interface. Sonochemical degradation is effective for the removal of contaminants with high Henry's law constants that readily

partition into the vapor phase of the bubble,<sup>42-43</sup> and those preferentially partition to the bubble-water interface. Nonvolatile surfactants have been found to undergo pyrolytic decomposition at the bubble-water interface where they are oriented radially with their polar head groups pointing to the bulk solution.<sup>44</sup>

### **1.3.2 Sonochemical degradation of perfluorinated chemicals**

Perfluorinated chemicals (PFCs) such as perfluorooctanoate (PFOA) and perfluorooctane sulfonate (PFOS) have been categorized as emerging contaminants. PFOS and PFOA have been consistently detected at  $\text{pg L}^{-1}$  to low  $\text{ng L}^{-1}$  in surface waters worldwide,<sup>45-48</sup> and at  $\text{mg L}^{-1}$  in waters near point sources.<sup>49-53</sup> Given their potential environmental and health effects, efforts are underway to establish regulatory standards of PFOS and PFOA in drinking water. The United States Environmental Protection Agency (EPA) recently set short-term provisional health advisories (PHA) for PFOS and PFOA of  $0.2$  and  $0.4 \mu\text{g L}^{-1}$ , respectively.<sup>54</sup>

Not only are PFCs persistent in the environment, but they are also recalcitrant to most conventional water and wastewater treatment methods.<sup>55-57</sup> Various other treatment techniques have been studied for PFOS and PFOA<sup>58</sup>, among which sonochemical degradation has been shown to be effective. A representative scheme of the sonochemical degradation of PFOS into its inorganic constituents is shown in scheme 1.1. In aqueous solution, perfluorinated surfactants are found to accumulate at the air-water interface with its hydrophobic perfluorinated carbon tail pointing to the gas phase, and its ionic headgroup pointing to the aqueous phase.<sup>59-60</sup> Thus the first step of PFOS sonochemical degradation involves its adsorption onto the bubble-water interface, where it then undergoes pyrolytic decomposition via cleavage of the C-S bond. The sulfur trioxide

hydrolyzes to form sulfate, and the fluoro-intermeidates are transformed into C<sub>1</sub> fluoro-radicals via pyrolysis in the bubble vapor phase. The C<sub>1</sub> fluoro-radicals were eventually transformed to CO, CO<sub>2</sub> and F<sup>-</sup>. The sonochemical degradation kinetics depend on the PFC concentration, and on the ultrasound parameters that determine the total bubble-water interface area and the average temperatures of the cavitation bubble and of the bubble-water interface.<sup>35,61</sup>

To evaluate the application of sonochemical degradation for environmental remediation of aqueous PFCs, it is important to understand the effect of various environmental matrix components, in particular how their fractionation behaviors at the bubble-water interface would affect the PFC degradation kinetics. For example, surface active species may compete with PFCs for the bubble-water interface, and volatile species may affect the composition and thus the temperature of the cavitation bubble.

## **1.4 Chemical fractionation during freezing of electrolyte solutions**

### **1.4.1 Unfrozen liquid in ice**

Ice, in the form of sea ice, ice crystals in clouds, snow, glacier and polar ice, and so on, is an important medium for many chemical and photochemical reactions. The transport and transformation of chemical species in ice actually take place in a small liquid fraction in the form of microscopic films at grain boundaries and ice surfaces.<sup>62-64</sup>

Liquid water exists in ice at temperatures below its thermodynamic melting point due to the presence of impurities, the curvature depression of the freezing point known as the Gibbs-Thomson effect, and the formation of disordered quasi-liquid layers at ice-vapor interfaces and grain boundaries, i.e., interfacial premelting.<sup>65</sup> In polycrystalline ice, liquid water driven by impurity and curvature effects forms a network of microscopic channels

that are approximately 10 to 100  $\mu\text{m}$  in thickness at temperatures near the bulk freezing point.<sup>66</sup> Bulk ice is also covered by a quasi-liquid layer of variable thickness down to about 240 K.<sup>67</sup> Many calibrated techniques such as x-ray scattering, atomic force microscopy (AFM), proton scattering, ellipsometry, optical microscopy, attenuated total reflection in the IR (ATR-IR), and photoelectron spectroscopy have been employed to measure the thickness of the quasi-liquid layer, but there is considerable variance between measurements using different techniques.<sup>68</sup> In addition, the thickness of both the quasi-liquid layer and the grain boundary liquid channels markedly depends on the presence of ice impurities,<sup>69</sup> although the thickness at a given temperature is not necessarily a monotonically increasing function of the impurity concentration.<sup>70</sup>

#### **1.4.2 Solute rejection and fractionation during freezing**

During freezing of most solutions, solutes are mostly rejected from the growing ice lattice and concentrated in the remaining liquid phase.<sup>71-73</sup> Impurities in glacial ice are found to be preferentially located at grain boundaries and bubble surfaces.<sup>74-75</sup> Even within the liquid layer, solute distribution within microcrystalline ice aggregates is not homogenous, but tends to peak at the triple intersection of grain boundaries. For example, it has been found that the liquid  $\text{H}_2\text{SO}_4$  is concentrated at the junctions, but that  $\text{NaCl}$  and its ions could not be detected inside ice crystals. A spectroscopic study revealed that upon fast freezing of an aqueous methylene blue (MB) solution ( $c > 10^{-7}$  M) at 77 K, the local concentration at the grain boundaries increased by approximately 3 orders of magnitude relative to the initial bulk concentration, and the concentration rose by at least 6 orders of magnitude upon "slow" freezing at 243 K.<sup>76</sup>

It is also of note that different anions and cations are selectively incorporated into or rather rejected from the ice due to their different structural relationship with the ice lattice.<sup>72,77-78</sup> For example,  $\text{NH}_4^+$  and  $\text{F}^-$  are preferentially incorporated into ice as substitutional impurities due to structural similarity to  $\text{H}_3\text{O}^+$  and  $\text{OH}^-$ , respectively. As a result of solute fractionation at the ice-water interface, the liquid fractions between ice grains are not simply concentrates of the initial solutions.

### **1.4.3 Electrical and pH changes at the ice-solution interface during freezing**

Solute fractionation at the ice-solution interface during freezing may also induce significant electrical and chemical changes. Specifically, the differential partitioning of anions and cations across the water-ice interface during freezing creates a potential difference between the liquid phase and ice phase, whose sign and magnitude depend on the ionic species in the solution, their concentration, and the freezing rate.<sup>71,79-80</sup> For example, a significant positive potential of liquid with respect to ice was measured during freezing of a dilute NaCl aqueous solution due to the preferential incorporation of  $\text{Cl}^-$  over  $\text{Na}^+$  into the ice lattice.<sup>71</sup> Since the diffusion of ions in ice is very slow,<sup>81-82</sup> the electrical imbalance across the water-ice interface can relax on a short timescale only via migration of  $\text{H}_3\text{O}^+$  and  $\text{OH}^-$ , the highly mobile intrinsic charge carriers of ice.<sup>83</sup> This, according to Bronshteyn and Chernov,<sup>84</sup> will subsequently change the acidity of the remaining liquid in grain boundaries, i.e., preferential incorporation of cations into the ice lattice leads to acidification of the remaining liquid, whereas preferential incorporation of anions has the opposite effect.

The freezing-induced pH change of electrolyte solution due to freeze-concentration and/or freezing hydrolysis has been experimentally confirmed. UV-Vis spectroscopic

measurements of cresol red (CR) in frozen aqueous solution of various acids (HF, HCl, HNO<sub>3</sub>, H<sub>2</sub>SO<sub>4</sub>) showed significant enhancement in CR protonation at the grain boundaries due to increased acid concentration.<sup>85</sup> Solid-state <sup>19</sup>F NMR chemical shift of 3-fluorobenzoic acid was used to probe the acidity of frozen electrolyte solutions. It was observed that upon freezing, aqueous solution of NaCl became more basic, that of (NH<sub>4</sub>)<sub>2</sub>SO<sub>4</sub> became more acidic, and that of 2-(N-morpholino)ethanesulfonic acid zwitterion retained its acidity.<sup>86</sup>

Freezing-induced changes in the composition, in particular the increase in solute concentration and change in acidity, of the microscopic channels affect not only the exchange of chemical species between ice and gas phase,<sup>64,87</sup> but also the kinetics of certain chemical reactions.<sup>88</sup> Most chemical and physical processes are slowed down since the phase transition radically modifies the reaction microenvironment, but certain reactions can be accelerated in partially frozen aqueous solutions. Examples of chemical reactions whose kinetics have been shown to be significantly enhanced during freezing include the oxidation of nitrate by dissolved oxygen to form nitrate,<sup>89</sup> the oxidative decomposition of gallic acid,<sup>90</sup> the photochemical nucleophilic substitution of p-nitroanisole with pyridine,<sup>91</sup> and the reaction between nitrite and iodide to form gas-phase nitric oxide and iodine.<sup>92</sup> The magnitude of the freezing-induced effect on chemical reaction kinetics is usually a function of temperature, freezing rate, and initial solution composition.

## **1.5 Outline of the thesis**

This thesis consists of relatively independent chapters that fit into the unifying theme of chemical fractionation at environmental interfaces. Chapter 1 provides an overview of

this theme and an introduction to the topics covered in later chapters. Chapters 2 to 8, each focusing on a specific research topic, are reproduced from seven articles published in or submitted to journals such as Environmental Science and Technology and Journal of Physical Chemistry.

Chapters 2 to 3 report the studies on the fractionation and reactivity of simple anions at the air-liquid interface of aerosol droplets. In chapter 2, the relative enrichment factor of a set of anions at the air-water interface of microdroplets, as measured by the electrospray mass spectrometry (ES-MS), is found to correlate exponentially with the ionic radius rather than the polarizability. The dissimilar effects of solution pH, cationic surfactant, anionic surfactant, neutral surfactant, glycerol, and urea on relative anion enrichment factor suggest that different levels of physical forces are at play at the air-water interface.

The work in chapter 2 is extended in chapter 3 to include the large  $\text{PF}_6^-$  and the highly polarizable  $\text{IO}_3^-$  species. A strict exponential correlation between relative anion enrichment factor and ionic radius is confirmed. Experiments performed on microdroplets of water/methanol mixtures show that the relative enrichment factor is almost independent of the molar fraction of methanol. The rates of the heterogeneous reaction between the gas-phase ozone and aqueous iodide on water and methanol microdroplets are found to be virtually identical.

In this project, I also collaborated with Dr. Shinichi Enami and Dr. Chad Vecitis on the studies of heterogeneous ozone-anion reactions, which resulted in three coauthor papers that are not included in this thesis: [1] Enami S.; Vecitis C. D.; Cheng J.; Hoffmann M. R.; Colussi A. J. "Global inorganic sources of atmospheric bromine", *J. Phys. Chem. A*, **2007**, 111, 8749, [2] Enami S.; Vecitis C. D.; Cheng J.; Hoffmann M. R.;

Colussi A. J. “Electrospray mass spectrometric detection of products and short-lived Intermediates in Aqueous Aerosol Microdroplets Exposed to a Reactive Gas”, *J. Phys. Chem. A*, **2007**, 111, 13032, and [3] Enami S.; Vecitis C. D.; Cheng J.; Hoffmann M. R.; Colussi A. J. “Interfacial chemistry of aqueous S(IV)/iodide aerosol microdroplets in gaseous ozone”, *Chem. Phys. Lett.*, **2008**, 455, 316.

Chapters 4 to 7 describe a variety of interfacial processes pertaining to the transport and transformation of perfluoroalkyl surfactants such as PFOS and PFOA in the environment. In chapter 4, relative enrichment factor at the air-water interface for the perfluoroalkyl carboxylates and sulfonates of different carbon chain length, as measured by electrospray mass spectrometry, positively correlates with carbon chain length. Perfluoroalkyl sulfonates are found to be more highly enriched at the air-water interface than perfluoroalkyl carboxylates of the same carbon chain length, as the sulfonate head group is less well hydrated than the carboxylate. A hyperbolic rather than linear correlation between the logarithm of enrichment factor and chain length is due to conformational restrictions. The study suggests that marine aerosols produced from contaminated ocean surface waters may be highly enriched in these perfluoroalkyl surfactants. My role in this study was to conduct part of the experiments and to edit the manuscript.

Chapter 5 seeks to determine the acid dissociation constants, i.e., pKa values, of perfluorooctanoate (PFO) and perfluorooctanesulfate (PFOS). An acid-base titration method based on electrospray mass spectrometry is developed to determine the pKa values for chemicals that are sufficiently surface active yet poorly soluble in water, and is validated with two carboxylic acids (C<sub>6</sub> and C<sub>8</sub>). Although PFO is observed to form a

very stable  $(\text{PFO})_2\text{H}^-$  cluster at low pH, the  $\text{pK}_a$  values of PFOS and PFOA are both well below 1.0, suggesting that the species will remain deprotonated and therefore non-volatile under environmentally relevant conditions.

Chapters 6 and 7 describe the effects of matrix components on the sonochemical degradation kinetics of two perfluoroalkyl surfactants, PFOS and PFOA. The study has important implications for the application of sonochemical techniques in the environmental remediation of these chemicals. Since the sonochemical degradation of PFOS and PFOA is actually via pyrolysis at the bubble-water interface, the fractionation of both the target compounds and the various other matrix components at the bubble-water interface can markedly affect the sonochemical reaction kinetics. In chapter 6, it is found that organic compounds in environmental matrices may reduce the sonochemical degradation rates of PFOS and PFOA by competitive adsorption onto the bubble-water interface or by lowering the average interfacial temperatures during transient bubble collapse events. The magnitude of the negative effect positively correlates with the Langmuir adsorption constant, the Henry's law constant, the specific heat capacity, and the total endothermic heat of dissociation of an individual compound.

Chapter 7 focuses on the effect of common groundwater anions and cations on the sonochemical degradation kinetics of PFOS and PFOA. The effect of anions follows the Hofmeister series; the more-surface-active species enhance the reaction rate, whereas the better-hydrated species have the opposite effect. In contrast, cations have much less pronounced effect than anions over the same concentration range. Initial solution pH enhances the degradation rates of PFOA at 3, but has negligible effects over the range of

4 to 11. The observed inorganic effects on sonochemical kinetics are hypothesized to be due to ions' partitioning to and interaction with the bubble-water interface.

In addition to the perfluorochemical remediation work presented in this thesis, I have collaborated with Dr. Chad Vecitis, Dr. Hyunwoong Park, Dr. Yajuan Wang, and Dr. Deming Zhao on the study of perfluorochemical removal in pure water and other matrices such as the aqueous film-forming foam (AFFF), using sonochemical degradation, photocatalytic reduction, and granular activated carbon (GAC) adsorption. Below is a list of related coauthor papers that have been published but are not included in this thesis: [1] Vecitis C. D.; Park H.; Cheng J.; Mader B. T.; Hoffmann M. R. "Kinetics and mechanism of the sonochemical transformation of perfluorooctane derivatives, PFOS and PFOA, into primary inorganic constituents", *J. Phys. Chem. A*, **2008**, 112, 4261, [2] Vecitis C. D.; Park H.; Cheng J.; Mader B. T.; Hoffmann M. R. "Enhancement of perfluorooctanoate and perfluorooctanesulfonate activity at acoustic cavitation bubble interfaces", *J. Phys. Chem. C*, **2008**, 112, 16850, [3] Park H.; Vecitis C. D.; Cheng J.; Mader B. T.; Hoffmann M. R. "Reductive defluorination of aqueous perfluorinated surfactants: effects of ionic headgroup and chain length", *J. Phys. Chem. A*, **2009**, 113, 690, and [4] Vecitis C. D.; Park H.; Cheng J.; Mader B.T.; Hoffmann M. R. "Treatment technologies for aqueous perfluorooctanesulfonate (PFOS) and perfluorooctanoate (PFOA)", *Front. Environ. Sci. Engin. China*, **2009**, 3, 129. Two more related papers are in print.

The final chapter concerns the fractionation of ions at the ice-water interface during freezing of dilute aqueous electrolyte solutions. Time-resolved confocal fluorescence microscopy is used to monitor the composition, in particular the pH, of the interstitial liquid films in freezing electrolyte solutions. The dependence of the liquid film thickness

on electrolyte concentration is observed to be non-monotonic. In addition, moderate pH changes ( $\pm 0.4$  pH) in the microscopic liquid channels are observed during freezing of dilute aqueous NaCl and NH<sub>4</sub>Ac solutions, respectively, whereas more dramatic pH changes ( $> \pm 1.0$  pH unit) are observed during the thawing process, suggesting that the pH change is limited by the relatively slow process of water dissociation. The results corroborate the theory of freezing hydrolysis by Bronshteyn and Chernov.<sup>83</sup>

### 1.5 References

- (1) Marrink, S. J.; Marcelja, S. *Langmuir* **2001**, *17*, 7929.
- (2) Tieleman, D. P.; Biggin, P. C.; Smith, G. R.; Sansom, M. S. P. *Q. Rev. Biophys.* **2001**, *34*, 473.
- (3) Benjamin, I. *Chem. Rev.* **1996**, *96*, 1449.
- (4) Markin, V. S.; Volkov, A. G. *J. Phys. Chem. B* **2002**, *106*, 11810.
- (5) Lynden-Bell, R. M.; Rasaiah, J. C. *J. Chem. Phys.* **1997**, *107*, 1981.
- (6) Jungwirth, P.; Tobias, D. J. *Chem. Rev.* **2005**, *106*, 1259.
- (7) Chang, T. M.; Dang, L. X. *Chem. Rev.* **2006**, *106*, 1305.
- (8) Kuo, I. F. W.; Mundy, C. J. *Science* **2004**, *303*, 658.
- (9) Salvador, P.; Curtis, J. E.; Tobias, D. J.; Jungwirth, P. *Phys. Chem. Chem. Phys.* **2003**, *5*, 3752.
- (10) Petersen, P. B.; Saykally, R. J.; Mucha, M.; Jungwirth, P. *J. Phys. Chem. B* **2005**, *109*, 10915.
- (11) Yang, X.; Kiran, B.; Wang, X.-B.; Wang, L.-S.; Mucha, M.; Jungwirth, P. *J. Phys. Chem. A* **2004**, *108*, 7820.

- (12) Knipping, E. M.; Lakin, M. J.; Foster, K. L.; Jungwirth, P.; Tobias, D. J.; Gerber, R. B.; Dabdub, D.; Finlayson-Pitts, B. J. *Science* **2000**, *288*, 301.
- (13) Buch, V.; Milet, A.; Vacha, R.; Jungwirth, P.; Devlin, J. P. *Proc. Natl. Acad. Sci. U. S.A.* **2007**, *104*, 7342.
- (14) Gopalakrishnan, S.; Jungwirth, P.; Tobias, D. J.; Allen, H. C. *J. Phys. Chem. B* **2005**, *109*, 8861.
- (15) Jungwirth, P.; Tobias, D. J. *J. Phys. Chem. B* **2002**, *106*, 6361.
- (16) Stuart, S. J.; Berne, B. J. *J. Phys. Chem. A* **1999**, *103*, 10300.
- (17) Jones, G.; Ray, W. A. *J. Am. Chem. Soc.* **1937**, *59*, 187.
- (18) Jones, G.; Ray, W. A. *J. Am. Chem. Soc.* **1941**, *63*, 3262.
- (19) Jones, G.; Ray, W. A. *J. Am. Chem. Soc.* **1942**, *64*, 2744.
- (20) Jarvis, N. L.; Scheiman, M. A. *J. Phys. Chem.* **1968**, *72*, 74.
- (21) Hu, J. H.; Shi, Q.; Davidovits, P.; Worsnop, D. R.; Zahniser, M. S.; Kolb, C. E. *J. Phys. Chem.* **1995**, *99*, 8768.
- (22) Zhuang, X.; Miranda, P. B.; Kim, D.; Shen, Y. R. *Phys. Rev. B* **1999**, *59*, 12632.
- (23) Miranda, P. B.; Shen, Y. R. *J. Phys. Chem. B* **1999**, *103*, 3292.
- (24) Richmond, G. L. *Chem. Rev.* **2002**, *102*, 2693.
- (25) Ghosal, S.; Hemminger, J. C.; Bluhm, H.; Mun, B. S.; Hebenstreit, E. L. D.; Ketteler, G.; Ogletree, D. F.; Requejo, F. G.; Salmeron, M. *Science* **2005**, *307*, 563.
- (26) Alsnielsen, J.; Jacquemain, D.; Kjaer, K.; Leveiller, F.; Lahav, M.; Leiserowitz, L. *Phys. Rep.-Rev. Sec. Phys. Lett.* **1994**, *246*, 252.
- (27) Gopalakrishnan, S.; Liu, D. F.; Allen, H. C.; Kuo, M.; Shultz, M. J. *Chem. Rev.* **2006**, *106*, 1155.

- (28) Kunz, W.; Henle, J.; Ninham, B. W. *Curr. Opin. Colloid Interface Sci.* **2004**, *9*, 19.
- (29) Kunz, W.; Lo Nostro, P.; Ninham, B. W. *Curr. Opin. Colloid Interface Sci.* **2004**, *9*, 1.
- (30) Chen, X.; Yang, T.; Kataoka, S.; Cremer, P. S. *J. Am. Chem. Soc.* **2007**, *129*, 12272.
- (31) Kotronarou, A.; Mills, G.; Hoffmann, M. R. *J. Phys. Chem.* **1991**, *95*, 3630.
- (32) Serpone, N.; Terzian, R.; Hidaka, H.; Pelizzetti, E. *J. Phys. Chem.* **1994**, *98*, 2634.
- (33) Kang, J. W.; Hoffmann, M. R. *Environ. Sci. Technol.* **1998**, *32*, 3194.
- (34) Moriwaki, H.; Takagi, Y.; Tanaka, M.; Tsuruho, K.; Okitsu, K.; Maeda, Y. *Environ. Sci. Technol.* **2005**, *39*, 3388.
- (35) Vecitis, C. D.; Park, H.; Cheng, J.; Mader, B. T.; Hoffmann, M. R. *J. Phys. Chem. A* **2008**, *112*, 4261.
- (36) Ince, N. H.; Tezcanli, G.; Belen, R. K.; Apikyan, I. G. *Appl. Catal. B-Environ.* **2001**, *29*, 167.
- (37) Suslick, K. S. *Science* **1990**, *247*, 1439.
- (38) Misik, V.; Miyoshi, N.; Riesz, P. *J. Phys. Chem.* **2002**, *99*, 3605.
- (39) Colussi, A. J.; Weavers, L. K.; Hoffmann, M. R. *J. Phys. Chem. A* **1998**, *102*, 6927.
- (40) Hua, I.; Hoffmann, M. R. *Environ. Sci. Technol.* **1996**, *30*, 864.
- (41) Weavers, L. K.; Ling, F. H.; Hoffmann, M. R. *Environ. Sci. Technol.* **1998**, *32*, 2727.
- (42) Colussi, A. J.; Hung, H.-M.; Hoffmann, M. R. *J. Phys. Chem. A* **1999**, *103*, 2696.

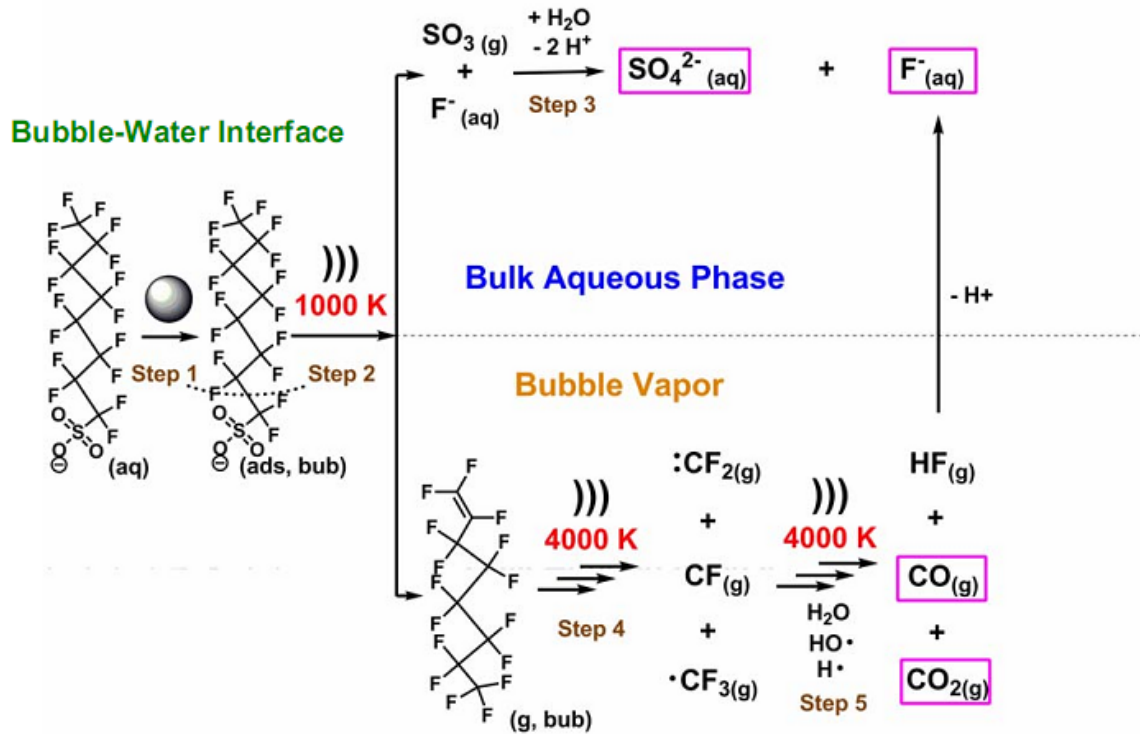
- (43) Krishna, C. M.; Lion, Y.; Kondo, T.; Riesz, P. *J. Phys. Chem.* **2002**, *91*, 5847.
- (44) Alegria, A. E.; Lion, Y.; Kondo, T.; Riesz, P. *J. Phys. Chem.* **2002**, *93*, 4908.
- (45) So, M. K.; Taniyasu, S.; Yamashita, N.; Giesy, J. P.; Zheng, J.; Fang, Z.; Im, S. H.; Lam, P. K. S. *Environ. Sci. Technol.* **2004**, *38*, 4056.
- (46) Murakami, M.; Imamura, E.; Shinohara, H.; Kiri, K.; Muramatsu, Y.; Harada, A.; Takada, H. *Environ. Sci. Technol.* **2008**, *42*, 6566.
- (47) Furdui, V. I.; Helm, P. A.; Crozier, P. W.; Lucaciu, C.; Reiner, E. J.; Marvin, C. H.; Whittle, D. M.; Mabury, S. A.; Tomy, G. T. *Environ. Sci. Technol.* **2008**, *42*, 4739.
- (48) Yamashita, N.; Kannan, K.; Taniyasu, S.; Horii, Y.; Petrick, G.; Gamo, T. "A global survey of perfluorinated acids in oceans", 2005.
- (49) Konwick, B. J.; Tomy, G. T.; Ismail, N.; Peterson, J. T.; Fauver, R. J.; Higginbotham, D.; Fisk, A. T. *Env. Toxicol. Chem.* **2008**, *27*, 2011.
- (50) Clara, M.; Scheffknecht, C.; Scharf, S.; Weiss, S.; Gans, O. *Wat. Sci. Technol.* **2008**, *58*, 59.
- (51) Oliaei, F. O.; Kriens, D.; Kessler, K. "Investigation of perfluorochemical (PFC) contamination in minnesota phase one," Minnesota Pollution Control Agency, 2006.
- (52) Schultz, M. M.; Barofsky, D. F.; Field, J. A. *Environ. Sci. Technol.* **2004**, *38*, 1828.
- (53) Moody, C. A.; Hebert, G. N.; Strauss, S. H.; Field, J. A. *J Environ. Monit.* **2003**, *5*, 341.
- (54) Provisional Health Advisories for Perfluorooctanoic Acid (PFOA) and Perfluorooctane Sulfonate (PFOS); U.S.E.P.A., Ed., 2009.
- (55) Key, B. D.; Howell, R. D.; Criddle, C. S. *Environ. Sci. Technol.* **1998**, *32*, 2283.

- (56) Schultz, M. M.; Higgins, C. P.; Huset, C. A.; Luthy, R. G.; Barofsky, D. F.; Field, J. A. *Environ. Sci. Technol.* **2006**, *40*, 7350.
- (57) Sinclair, E.; Kannan, K. *Environ. Sci. Technol.* **2006**, *40*, 1408.
- (58) Vecitis, C. D.; Park, H.; Cheng, J.; Mader, B. T.; Hoffmann, M. R. *Front. Environ. Sci. Engin. China* **2009**, *3*, 129.
- (59) Lu, J. R.; Ottewill, R. H.; Rennie, A. R. *Colloid Surf. A-Physicochem. Eng. Asp.* **2001**, *183*, 15.
- (60) Lopez-Fontan, J. L.; Sarmiento, F.; Schulz, P. C. *Colloid Polym. Sci.* **2005**, *283*, 862.
- (61) Vecitis, C. D.; Park, H.; Cheng, J.; Mader, B. T.; Hoffmann, M. R. *J. Phys. Chem. C* **2008**, *112*, 16850.
- (62) Grannas, A. M.; Jones, A. E.; Dibb, J.; Ammann, M.; Anastasio, C.; Beine, H. J.; Bergin, M.; Bottenheim, J.; Boxe, C. S.; Carver, G.; Chen, G.; Crawford, J. H.; Domine, F.; Frey, M. M.; Guzman, M. I.; Heard, D. E.; Helmig, D.; Hoffmann, M. R.; Honrath, R. E.; Huey, L. G.; Hutterli, M.; Jacobi, H. W.; Klan, P.; Lefer, B.; McConnell, J.; Plane, J.; Sander, R.; Savarino, J.; Shepson, P. B.; Simpson, W. R.; Sodeau, J. R.; von Glasow, R.; Weller, R.; Wolff, E. W.; Zhu, T. *Atmos. Chem. Phys.* **2007**, *7*, 4329.
- (63) Domine, F.; Albert, M.; Huthwelker, T.; Jacobi, H. W.; Kokhanovsky, A. A.; Lehning, M.; Picard, G.; Simpson, W. R. *Atmos. Chem. Phys.* **2008**, *8*, 171.
- (64) Huthwelker, T.; Ammann, M.; Peter, T. *Chem. Rev.* **2006**, *106*, 1375.
- (65) Wettlaufer, J. S.; Worster, M. G. *Annu. Rev. Fluid Mech.* **2006**, *38*, 427.
- (66) Rempel, A. W.; Waddington, E. D.; Wettlaufer, J. S.; Worster, M. G. *Nature* **2001**, *411*, 568.

- (67) Doppenschmidt, A.; Butt, H. J. *Langmuir* **2000**, *16*, 6709.
- (68) Henson, B. F.; Voss, L. F.; Wilson, K. R.; Robinson, J. M. *J. Chem. Phys.* **2005**, *123*.
- (69) McNeill, V. F.; Loerting, T.; Geiger, F. M.; Trout, B. L.; Molina, M. J. *Proc. Natl. Acad. Sci. U. S. A.* **2006**, *103*, 9422.
- (70) Benatov, L.; Wettlaufer, J. S. *Phys. Rev. E* **2004**, *70*.
- (71) Workman, E. J.; Reynolds, S. E. *Phys. Rev.* **1950**, *78*, 254.
- (72) Lodge, J. P.; Baker, M. L.; Pierrard, J. M. *J. Chem. Phys.* **1956**, *24*, 716.
- (73) Carignano, M. A.; Shepson, P. B.; Szleifer, I. *Chem. Phys. Lett.* **2007**, *436*, 99.
- (74) Barnes, P. R. F.; Wolff, E. W. *J. Glaciol.* **2004**, *50*, 311.
- (75) Mulvaney, R.; Wolff, E. W.; Oates, K. *Nature* **1988**, *331*, 247.
- (76) Heger, D.; Jirkovsky, J.; Klan, P. *J. Phys. Chem. A* **2005**, *109*, 6702.
- (77) Gross, G. W.; Wong, P. M.; Humes, K. *J. Chem. Phys.* **1977**, *67*, 5264.
- (78) Vrbka, L.; Jungwirth, P. *Phys. Rev. Lett.* **2005**, *95*.
- (79) Wilson, P. W.; Haymet, A. D. J. *J. Phys. Chem. B* **2008**, *112*, 11750.
- (80) Cobb, A. W.; Gross, G. W. *J. Electrochem. Soc.* **1969**, *116*, 796.
- (81) Thibert, E.; Domine, F. *The J. Phys. Chem. B* **1998**, *102*, 4432.
- (82) Thibert, E.; Domine, F. *The J. Phys. Chem. B* **1997**, *101*, 3554.
- (83) Petrenko, V. F.; Whitworth, R. W. *Physics of Ice*; New York: Oxford University Press, 2002.
- (84) Bronshteyn, V. L.; Chernov, A. A. *J. Cryst. Growth* **1991**, *112*, 129.
- (85) Heger, D.; Klanova, J.; Klan, P. *J. Phys. Chem. B* **2006**, *110*, 1277.

- (86) Robinson, C.; Boxe, C. S.; Guzman, M. I.; Colussi, A. J.; Hoffmann, M. R. *J. Phys. Chem. B* **2006**, *110*, 7613.
- (87) Sato, K.; Takenaka, N.; Bandow, H.; Maeda, Y. *J. Phys. Chem. A* **2008**, *112*, 7600.
- (88) Takenaka, N.; Bandow, H. *J. Phys. Chem. A* **2007**, *111*, 8780.
- (89) Takenaka, N.; Ueda, A.; Maeda, Y. *Nature* **1992**, *358*, 736.
- (90) Takenaka, N.; Tanaka, M.; Okitsu, K.; Bandow, H. *J. Phys. Chem. A* **2006**, *110*, 10628.
- (91) Grannas, A. M.; Bausch, A. R.; Mahanna, K. M. *J. Phys. Chem. A* **2007**, *111*, 11043.
- (92) O'Driscoll, P.; Minogue, N.; Takenaka, N.; Sodeau, J. *J. Phys. Chem. A* **2008**, *112*, 1677.

Scheme 1.1. A representative scheme of the sonochemical PFOS transformation into its organic constituents. The inorganic products are highlighted in purple boxes.



## Chapter 2

### Experimental Anion Affinities for the Air–Water Interface\*

---

\*This chapter is reproduced with permission from J. Cheng, C. D. Vecitis, M. R. Hoffmann, and A. J. Colussi, *Journal of Physical Chemistry B*, **2006**, *110*, 25598. Copyright © 2006, American Chemical Society

## 2.1 Abstract

Anion affinities,  $\gamma_X$ , for the aerial interface of aqueous ( $\text{Br}^- + \text{NO}_3^- + \text{I}^- + \text{SCN}^- + \text{BF}_4^- + \text{ClO}_4^-$ ) solutions are determined by electrospray ionization-mass spectrometry. The composition of the ions ejected from the surface of fissioning nanodroplets shows that  $\gamma_X$ 's increase (decrease) exponentially with anionic radii,  $a_X$  (dehydration free energies,  ${}^dG_X$ ), and selectively respond to the presence of surfactants.  $\text{BF}_4^-$ , the least hydrated and polarizable anion of the set, has one of the largest  $\gamma_X$ 's. Non-ionic surfactants decrease  $\gamma_I$  and  $\gamma_{\text{SCN}}$ , but increase  $\gamma_{\text{BF}_4}$ . Cetyltrimethyl ammonium markedly enhances the  $\gamma_X$ 's of smaller anions over those of larger ones. A similar, but weaker effect is observed upon lowering the pH of the bulk solutions from 8.2 to 3.0. Dodecyl sulfate has a negligible effect on  $\gamma_X$ 's. Considering that: (1) universal many-body electrodynamic interactions will progressively stabilize the interfacial layer as its dielectric permittivity falls relative to that of the bulk solution, (2) water permittivity is uniformly depressed by increasing concentrations of these anions, we infer that the observed Hofmeister correlation:  $\ln \gamma_X \propto -{}^dG_X$ , is consistent with the *optimal depression of the permittivity of the drier interfacial layer by the least hydrated ions*. Ion-ion interactions can significantly influence  $\gamma_X$ 's in environmental aqueous media.

## 2.2 Introduction

Few phenomena are more ubiquitous, or have been more investigated, than those induced by the dissimilar propensities of anions for aqueous interfaces.<sup>1-4</sup> Fundamental biochemical, technological and environmental processes are driven by the selective affinities of the various anions for the interfaces involved. They are labeled “Hofmeister effects” (HEs) after observations made 118 years ago.<sup>5-6</sup> Explanations abound. They range from those based on continuum,<sup>7-13</sup> or heuristic molecular models,<sup>14</sup> to non-primitive molecular dynamic simulations.<sup>15-18</sup> However, “*HEs remain a mystery after more than 100 years*”,<sup>10</sup> “*perhaps the only thing certain about HEs is that we do not understand the physical basis for the process*”,<sup>19</sup> “*simulations that confirm intuitions should be considered tautological*”.<sup>11</sup>

Hofmeister correctly linked anion propensities for the boundaries between water and less polar media with the ‘water withdrawing power’ of anions, an unquantified property at the time.<sup>20</sup> It has been recently argued, however, that anion polarizability is the most important factor determining HEs at air/electrolyte solution interfaces.<sup>18,21-22</sup> The argument rests on molecular dynamic (MD) calculations in which anions accumulate in the outermost layer after their polarizabilities are turned on in the models, and on similarly interpreted surface-sensitive experiments.<sup>23</sup> Thus, it has been alleged that halide anion propensities are proportional to their polarizabilities.<sup>24</sup> Notice that the negative surface potentials measured over (most) electrolyte solutions ~50 years ago themselves require anions to be closer than cations to the interface.<sup>25-27</sup>

The affinities of the heavier halide anions for aerosol interfaces play important roles in atmospheric chemistry.<sup>2,28-36</sup> The same tendencies underlie the fact that the saline aerosol (up to  $\sim 10^4$  Tg/yr) incessantly released by the oceans is highly (10 to  $10^4$  times) enriched in

bromide and iodide.<sup>32,37</sup> Considering that these huge enrichment factors cannot be accounted for by the modest differential Cl<sup>-</sup>/Br<sup>-</sup>/I<sup>-</sup> concentration gradients predicted for the interfacial region, we decided to reinvestigate the mechanism of anion fractionation during the aerosolization of electrolyte solutions.<sup>33,38-43</sup> In this chapter we report experiments on the simultaneous detection of Br<sup>-</sup>, NO<sub>3</sub><sup>-</sup>, I<sup>-</sup>, SCN<sup>-</sup>, BF<sub>4</sub><sup>-</sup> and ClO<sub>4</sub><sup>-</sup> at the aerial interface of sub-millimolar aqueous binary solutions via electrospray ionization-mass spectrometry<sup>40,44-48</sup> in the presence or absence of surfactants and urea.<sup>31,49-55</sup> The results are analyzed in terms of fundamental concepts and new information.

### 2.3 Experimental Section

An electrospray ionization mass spectrometer (HP-1100 MSD) with an atmospheric pressure ionization interface of orthogonal geometry was used in this study. Electrolyte solutions (50  $\mu\text{L min}^{-1}$ ) were pumped into the spraying chamber through a grounded stainless steel needle injector (100  $\mu\text{m}$  bore). Continuous flow conditions minimize contamination by spurious tensioactive species, which often compromises static experiments. Instrumental parameters (drying gas flow: 10  $\text{L min}^{-1}$ ; drying gas temperature: 250  $^{\circ}\text{C}$ ; nebulizer pressure: 35 psi; collector capillary voltage: 1.5 kV; fragmentor voltage: 80 V) were chosen to optimize mass signals with minimal ion fragmentation. Mass spectra were acquired at preset  $m/z$  values: 58 and 60 (<sup>32,34</sup>SCN<sup>-</sup>), 62 (NO<sub>3</sub><sup>-</sup>), 79 and 81 (Br<sup>-</sup>), 86 and 87 (<sup>10,11</sup>BF<sub>4</sub><sup>-</sup>), 99 and 101 (<sup>35,37</sup>ClO<sub>4</sub><sup>-</sup>) and 127 (I<sup>-</sup>). Reported data are the average of at least duplicate experiments.

Pure (98% purity or higher) NaBr, NaI, NaNO<sub>3</sub>, NaClO<sub>4</sub>, NaBF<sub>4</sub> and NaSCN (EM science or Sigma-Aldrich), Triton X-114 and cetyltrimethyl ammonium chloride (CTAC, Sigma-Aldrich), sodium dodecylsulfate (SDS, Bio-Rad) and urea (Mallinckrodt) were used as received. Equimolar binary solutions were prepared in MilliQ water or D<sub>2</sub>O (Cambridge

Isotopes) with and without surfactants or urea. The use of senary solutions substantially reduces experimental dispersion, and the possible effect of potential impurities on present measurements. The pH of senary solutions, initially at 6.5, was adjusted by addition of 1 mM NaOH or HCl at constant ionic strength, and measured with a calibrated pH meter.

## 2.4 Results and Discussion

Figure 2.1 shows a negative ion mass spectrum of electrosprayed salt solutions. From this information, normalized anion affinities,  $f_{X^-}$ , were calculated from the sum of ion counts,  $I_{m/z}$ , for the isotopic variants of each anionic species (e.g.,  $(I_{58} + I_{60})$  for  $\text{SCN}^-$ , etc.) and the total ion count:

$$f_{X^-} = \frac{\sum I_{m/z}}{\sum I_{m/z}} \quad (2.1)$$

Relative anion affinities,  $\gamma_{X^-}$ , are defined as multiples of  $f_{\text{Br}^-}$ , the value for the least enriched anion at the interface in the absence of surfactants:  $\gamma_{X^-} = f_{X^-}/f_{\text{Br}^-}$  (table 2.1).  $\gamma_{X^-}$ s measured in  $\text{H}_2\text{O}$  or  $\text{D}_2\text{O}$  are identical within experimental error.

Droplets generated during breakup of the liquid jet issuing from the grounded nozzle are spontaneously charged via microscopic fluctuations. The subsequent, uneven shedding of mass and charge by electrosprayed droplets forces the anions present at the air/water interface to preferentially carry most of the excess charge into offspring droplets.<sup>56</sup> Individual anions are ultimately ejected into the gas-phase via field desorption from negatively charged nanodroplets.<sup>40,45-46,57-63</sup> Therefore, the relative anion abundances registered by the mass spectra (figure 2.1) reflect the anion distribution in the ensemble of single-ion water clusters ejected from the surface of disintegrating nanodroplets.<sup>57-58</sup> In the orthogonal geometry

employed in these experiments the instrument samples the nanodroplets ejected laterally from the electrosprayed jet. There is conclusive evidence that tensioactive species tend to accumulate in the periphery of the conical mist created ahead of the inlet orifice.<sup>48</sup> Considering that the relative anion signals obtained by spraying solutions doped with 10  $\mu\text{M}$  SDS (anionic) or CTAC (cationic) surfactants are identical within experimental error, we conclude that the basic mechanism of anion enrichment does not involve ion-ion interactions.

Figures 2.2 to 2.4 show semilogarithmic plots of  $f_X$  as a function of the aqueous anionic radius,  $a_X$ , free energy of dehydration  ${}^dG_X$ , and polarizability  $\alpha_X$ , respectively.<sup>64</sup> It is apparent that anion affinities for the air/water interface are strongly correlated with anionic radii:  $\ln f_X \propto a_X$  ( $R^2 = 0.96$ ), and free energies of dehydration:  $\ln f_X \propto {}^dG_X$  ( $R^2 = 0.91$ ), in full accord with Hofmeister's analysis,<sup>20</sup> and Monte Carlo calculations.<sup>15,65</sup> However, there is no discernible correlation between  $f_X$ 's and anion polarizabilities  $\alpha_X$ 's (Figure 2.4).<sup>3,7,18,21,66-67</sup> Tetrahedral  $\text{BF}_4^-$ , which has the smallest dehydration free energy of this set of anions, but is approximately 2.75 times less polarizable than iodide (table 2.1), provides a fair test of the relative importance of anion polarizability versus anion dehydration energy in the mechanism of interfacial enrichment. Although the reported anion affinities depend to a certain extent on instrumental settings, these correlations are robust:  $f_X$ 's measured at 3 kV capillary voltage still increase exponentially with  $a_X$ .  $f_X$ 's measured in the 10  $\mu\text{M}$  to 10 mM concentration range are identical within experimental error.

Surfactants significantly affect  $f_X$ 's. All surfactants uniformly depress the total anion count at concentrations below their critical micellar concentrations.<sup>68-69</sup> Since nonionic surfactants do not displace anions from the interface at these concentrations (a weak

attraction might be even expected) this finding suggests that surfactants compete with anions in decreasing surface energy. Urea (Figure 2.5), a water structure-breaker,<sup>52</sup> and Triton X-114 (Figures 2.7 and 2.8), a non-ionic polyether amphiphile, comparably, slightly, but selectively influence  $f_X$ 's. The interfacial layer becomes more populated by the least hydrated  $\text{BF}_4^-$  at the expense of the more polarizable  $\text{I}^-$  and  $\text{SCN}^-$  anions upon addition of urea or Triton X-114. The devaluation of the comparative advantage of  $\text{I}^-$  and  $\text{SCN}^-$  over  $\text{BF}_4^-$  ( $\text{BF}_4^-$ , having the smallest  $^dG_X$ , is indeed underrepresented at the interface, cf. Figure 2.3) further suggests that the more polarizable anions are somewhat more efficient in stabilizing the interfacial layer.<sup>70-</sup>

71

While the anionic dodecylsulfate indiscriminately repels all anions from the interface, as expected from electrostatics,  $f_X$ 's are quite sensitive to the cationic amphiphile cetyltrimethylammonium (Figure 2.6).<sup>72-73</sup> The smallest (and least enriched in the absence of additives) anions,  $\text{NO}_3^-$  and  $\text{Br}^-$ , are specifically enhanced several fold. As a result, the  $f_X$ 's measured in the presence of 1 mM CTAC no longer correlate with anion radii or dehydration free energies. Positive headgroups seem to attract the smaller anions into closer contact, and induce significant changes in their orientation and solvation at the interface.<sup>74</sup> It is well known that ion charges *and* radii both affect ion distributions near interfaces.<sup>75</sup> We also found that  $\gamma_{\text{NO}_3^-}$  increases 2.3 times, respectively, while most  $\gamma_X$ 's remain nearly constant as the pH of the bulk solutions is lowered from 8.2 to 3.0. The onset of  $\gamma_{\text{NO}_3^-}$  increases occurs at about pH 4.0, suggesting that the interface becomes positively charged via proton adsorption under acidic conditions.<sup>4</sup> In this context, it is relevant to point out that the marine aerosol, which is generated during bubble bursting at the ocean surface, consists of positively charged

droplets.<sup>39,76</sup>

Much of the current literature focuses on the width of the interfacial region.<sup>77</sup> However, since even surface-sensitive spectroscopies collect signals from interfacial slabs of  $\delta \approx 1.0$  nm thicknesses,<sup>23</sup> the fine-grained interfacial concentration profiles obtained by MD calculations, if they were consequential, represent an authentic challenge.<sup>18</sup> Anions are effectively enriched in the layers probed in our experiments because the combined  $\text{ClO}_4^-$  ( $m/z = 99$  and  $101$ ) signals are only 2.5 times smaller than the  $m/z = 265$  signal of the SDS surfactant in equimolar  $10 \mu\text{M}$  solutions. Assuming that SDS is bound to a  $\delta \approx 0.3$  nm outermost layer, we tentatively infer that  $\text{ClO}_4^-$  ions are sampled from  $\delta \approx 1.0$  nm interfacial sections that are smaller than the estimated  $\approx 2.5$  nm radii of fissioning droplets,<sup>57-58</sup> On the other hand, surface tension measurements involve integral concentration profiles. The possibility that different interactions dominate at various depths, i.e., that the results obtained by different techniques could not be comparable, cannot be dismissed at this time.<sup>23</sup>

A physically meaningful interpretation of interfacial anion affinities should be based on an energy balance between opposing effects, rather than on simply correlating affinities with specific ion properties. Since anions *are* polarizable, the finding that some anions become enriched at the interface after their polarizabilities are included in MD calculations strictly shows that a deficiency has been corrected, not that anion enrichments should correlate with anion polarizabilities. While it is easy to envision that water density decreases smoothly toward the interface, the factors that determine the concentration profiles of cations and anions in the boundary layer are not immediately apparent. The sizable dehydration free energies of most ions, in conjunction with lower water density at the interface, will draw them into the bulk.<sup>9,15,65</sup> Image charge repulsion will enhance this tendency. This drive would

be ultimately balanced by the entropy losses associated with ion confinement into a reduced volume. Hence, large dehydration free energies conspire against significant interfacial ion excesses. The preferential stabilization of the more polarizable anions in the strong electric field at the interface would, in principle, contribute to mitigate the adverse energy balance. Figure 2.4 shows, however, that this contribution is at best minor. Clearly, the major interactions remain to be identified that draw anions toward the interface and offset their aversion for this drier medium. Notice that if these were the only interactions involved, the solution bulk would be separated from air by a more dilute layer.

The thermodynamic stability of a contiguous three-layer macroscopic array cannot be exclusively analyzed in terms of localized ion-water interactions. Macroscopic phases in contact are mutually stabilized via collective dispersive interactions arising from density and orientation fluctuations over the entire system.<sup>78-80</sup> By properly accounting for the global, many-body electrodynamic interactions among three contiguous phases, it is possible to infer that the central layer is stabilized when its overall (i.e., dispersive and orientational) polarizability lies between those of the bulk solution and air.<sup>78-79</sup> This powerful criterion shifts the focus from ion polarizabilities to ion effects on the polarizability of water as a macroscopic medium. The broad temporal scales of many-body interactions in dielectric water are presumably better captured by Monte Carlo than by Molecular Dynamic calculations. The large difference between the dielectric permittivities of water and air, due to the unique properties of water as a hydrogen-bonded solvent, tends to amplify the effects of perturbations to water dynamics. Since electrolytes, as a rule, decrease the dielectric permittivity of water,<sup>81-84</sup> *aqueous layers separating electrolyte solutions from air are expected to be stabilized by excess ion concentrations.* Anions largely achieve this effect in

the bulk by shortening the range and slowing down water dipolar correlations. From this perspective, we propose that the rival factors controlling ion affinities for the air/water interface appear to be: (1) ion dehydration energies and (2) nonlocal stabilization energies resulting from the depression of interfacial water permittivity by local ion excesses.<sup>9</sup>

Since the concentration dependences of the static permittivities and relaxation times of water in NaBr, NaI, NaNO<sub>3</sub>, NaClO<sub>4</sub> and NaSCN solutions are nearly independent of the nature of the anion,<sup>85-86</sup> *anion affinities largely reflect differences in dehydration free energies*. Considering that the dehydration energies of anions are considerably smaller than those of cations, this analysis naturally accounts for the negative (relative to the bulk) surface potentials measured long ago.<sup>26-27</sup> The Jones-Ray effect,<sup>87</sup> i.e., the lower surface tensions of dilute aqueous electrolyte solutions, also follows from this analysis and the Gibbs isotherm. This view readily allows for variations of anion affinities when air is replaced by other media, such as hydrophobic membranes or proteins.<sup>1,11,20</sup> If for no other reason, anions, particularly in the ~1 M model solutions used in MD simulations, *must* be polarizable to relay (rather than shield) electrodynamic interactions over the entire molecular ensemble.

Summing up, the Hofmeister series of anion affinities for the air/water interface is paradoxically realized by the nonspecific effect of anions on the dielectric properties of interfacial water. Under realistic environmental conditions, surfactants may decisively affect anion affinities. The huge anion enrichments found in the finest marine aerosol likely result from the amplification of relative anion affinities in successive droplet fission events.<sup>39,47</sup> Further work is underway.

## **2.5 Acknowledgments**

This work was financed by NSF grant ATM-0534990.

## 2.6 References

- (1) Kunz, W. *Pure Appl. Chem.* **2006**, *78*, 1611.
- (2) Lewis, E. R.; Schwartz, S. E. *Sea Salt Aerosol Production: Mechanisms, Methods, Measurements and Models – A Critical Review*; American Geophysical Union: Washington, DC, 2004; Geophysical Monograph, Vol. 152.
- (3) Ghosal, S.; Hemminger, J. C.; Bluhm, H.; Mun, B. S.; Hebenstreit, E. L. D.; Ketteler, G.; Ogletree, D. F.; Requejo, F. G.; Salmeron, M. *Science* **2005**, *307*, 563.
- (4) Pegram, L. M.; Record, M. T. *Proc. Nat. Acad. Sci. U.S.A.* **2006**, *103*, 14278.
- (5) Hofmeister, F. *Arch. Exp. Pathol. Pharmacol. (Leipzig)* **1888**, *24*, 247.
- (6) Gurau, M. C.; S.M., L.; Castellana, E. T.; Albertorio, F.; Kataoka, S.; Cremer, P. S. *J. Am. Chem Soc.* **2004**, *126*, 10522.
- (7) Bondesson, L.; Frediani, L.; Agren, H.; Mennucci, B. *J. Phys. Chem. B* **2006**, *110*, 11361.
- (8) Edwards, S. A.; Williams, D. R. M. *Europhys. Lett.* **2006**, *74*, 854.
- (9) Bostrom, M.; Kunz, W.; Ninham, B. W. *Langmuir* **2005**, *21*, 2619.
- (10) Bostrom, M.; Ninham, B. W. *Langmuir* **2004**, *20*, 7569.
- (11) Kunz, W.; Lo Nostro, P.; Ninham, B. W. *Curr. Opin. Colloid Interface Sci.* **2004**, *9*, 1.
- (12) Zhou, H. X. *Proteins* **2005**, *61*, 69.
- (13) Frediani, L.; Mennucci, B.; Cammi, R. *J. Phys. Chem. B* **2004**, *108*, 13796.
- (14) Dill, K. A.; Truskett, T. M.; Vlachy, V.; Hribar-Lee, B. *Annu. Rev. Biophys. Biomol. Struct.* **2005**, *34*, 173.
- (15) Hagberg, D.; Brdarski, S.; Karlstrom, G. *J. Phys. Chem. B* **2005**, *109*, 4111.

- (16) Wilson, M. A.; Pohorille, A. *J. Chem. Phys.* **1991**, *95*, 6005.
- (17) Cacace, M. G.; Landau, E. M.; Ramsden, J. J. *Quarterly Rev. Biophys.* **1997**, *30*, 241.
- (18) Jungwirth, P.; Tobias, D. J. *Chem. Rev.* **2006**, *106*, 1259.
- (19) Bowron, D. T.; Finney, J. L. *J. Chem. Phys.* **2003**, *118*, 8357.
- (20) Kunz, W.; Henle, J.; Ninham, B. W. *Curr. Opin. Colloid Interface Sci.* **2004**, *9*, 19.
- (21) Petersen, P. B.; Saykally, R. J. *Annu. Rev. Phys. Chem.* **2006**, *57*, 333.
- (22) Jungwirth, P.; Tobias, D. J. *J. Phys. Chem. B* **2002**, *106*, 6361.
- (23) Petersen, P. B.; Saykally, R. J. *J. Phys. Chem. B* **2006**, *110*, 14060.
- (24) Knipping, E. M.; Lakin, M. J.; Foster, K. L.; Jungwirth, P.; Tobias, D. J.; Gerber, R. B.; Dabdub, D.; Finlayson-Pitts, B. J. *Science* **2000**, *288*, 301.
- (25) Randles, J. E. B. *Discuss. Faraday Soc.* **1957**, *24*, 194.
- (26) Jarvis, N. L. *J. Geophys. Res.* **1972**, *77*, 5177.
- (27) Jarvis, N. L.; Scheiman, M. A. *J. Phys. Chem.* **1968**, *72*, 74.
- (28) McFiggans, G. *Nature* **2005**, *433*, E13.
- (29) O'Dowd, C. D.; Jimenez, J. L.; Bahreini, R.; Flagan, R. C.; Seinfeld, J. H.; Hameri, K.; Pirjola, L.; Kulmala, M.; Jennings, S. G.; Hoffmann, T. *Nature* **2002**, *417*, 632.
- (30) Carpenter, L. J. *Chem. Rev.* **2003**, *103*, 4953.
- (31) Liss, P. S.; Duce, R. A. *The Sea Surface and Global Change*; Cambridge University Press: Cambridge, UK, 1997.
- (32) Duce, R. A.; Hoffman, E. J. *Ann. Rev. Earth Planet. Sci.* **1976**, *4*, 187.
- (33) Macintyre, F. *Tellus* **1970**, *22*, 451.
- (34) Sander, R.; Keene, W. C.; Pszenny, A. A. P.; Arimoto, R.; Ayers, G. P.; Baboukas, E.; Cainey, J. M.; Crutzen, P. J.; Duce, R. A.; Honninger, G.; Huebert, B. J.; Maenhaut, W.;

- Mihalopoulos, N.; Turekian, V. C.; Van Dingenen, R. *Atmos. Chem. Phys.* **2003**, *3*, 1301.
- (35) Finlayson-Pitts, B. J. *Chem. Rev.* **2003**, *103*, 4801.
- (36) Garrett, B. C. *Science* **2004**, *303*, 1146.
- (37) Boyce, S. G. *Science* **1951**, *113*, 620.
- (38) Macintyre, F. J. *Phys. Chem.* **1968**, *72*, 589.
- (39) Blanchard, D. C. *Prog. Oceanogr.* **1963**, *1*, 71.
- (40) Lin, S. P.; Reitz, R. D. *Ann. Rev. Fluid Mech.* **1998**, *30*, 85.
- (41) Leifer, I.; de Leeuw, G.; Cohen, L. H. *Geophys. Res. Lett.* **2000**, *27*, 4077.
- (42) Blanchard, D. C.; Syzdek, L. D. *Limnol. Oceanogr.* **1978**, *23*, 389.
- (43) Duchemin, L.; Popinet, S.; Josserand, C.; Zaleski, S. *Phys. Fluids* **2002**, *14*, 3000.
- (44) Yamashita, M.; Fenn, J. B. *J. Phys. Chem.* **1984**, *88*, 4451.
- (45) Fenn, J. B. *Angew. Chem. Int. Ed.* **2003**, *42*, 3871.
- (46) Fenn, J. B. *J. Am. Soc. Mass Spectrom.* **1993**, *4*, 524.
- (47) Cech, N. B.; Enke, C. G. *Anal. Chem.* **2001**, *73*, 4632.
- (48) Tang, K. Q.; Smith, R. D. *J. Am. Soc. Mass Spectrom.* **2001**, *12*, 343.
- (49) Liu, X.; Duncan, J. H. *Nature* **2003**, *421*, 520.
- (50) Quinn, J. A.; Steinbrook, R. A.; Anderson, J. L. *Chem. Eng. Sci.* **1975**, *30*, 1177.
- (51) Stepanets, O. V.; Soloveva, G. Y.; Mikhailova, A. M.; Kulapin, A. I. *J. Anal. Chem.* **2001**, *56*, 290.
- (52) Franks, F. *Water, a Comprehensive Treatise*; New York: Plenum Press, 1975; Vol. 4.
- (53) Ohmine, I. *J. Phys. Chem.* **1995**, *99*, 6767.
- (54) Siu, D.; Koga, Y. *J. Phys. Chem. B* **2005**, *109*, 16886.
- (55) Frinak, E. K.; Abbatt, J. P. D. *J. Phys. Chem. A* **2006**, *110*, 10456.

- (56) Enke, C. G. *Anal. Chem.* **1997**, *69*, 4885.
- (57) Consta, S. *Theor. Chem. Acc.* **2006**, *116*, 373.
- (58) Ichiki, K.; Consta, S. *J. Phys. Chem. B* **2006**, *110*, 19168.
- (59) Rohner, T. C.; Lion, N.; Girault, H. H. *Phys. Chem. Chem. Phys.* **2004**, *6*, 3056.
- (60) Cech, N. B.; Enke, C. G. *Mass Spectrom. Rev.* **2001**, *20*, 362.
- (61) Iribarne, J. V.; Dziedzic, P. J.; Thomson, B. A. *Int. J. Mass Spectrom. Ion Processes* **1983**, *50*, 331.
- (62) Iribarne, J. V.; Thomson, B. A. *J. Chem. Phys.* **1976**, *64*, 2287.
- (63) Znamenskiy, V.; Marginean, I.; Vertes, A. *J. Phys. Chem. A* **2003**, *107*, 7406.
- (64) Marcus, Y. *Ion Properties*; Marcel Dekker: New York, 1997.
- (65) Karlstrom, G.; Hagberg, D. *J. Phys. Chem. B* **2002**, *106*, 11585.
- (66) Weber, R.; Winter, B.; Schmidt, P. M.; Widdra, W.; Hertel, I. V.; Dittmar, M.; Faubel, M. *J. Phys. Chem. B* **2004**, *108*, 4729.
- (67) Chang, T. M.; Dang, L. X. *Chem. Rev.* **2006**, *106*, 1305.
- (68) Hernainz, F.; Calero, M.; Blazquez, G.; Caro, A. *J. Chem. Eng. Data* **2006**, *51*, 1216.
- (69) Chang, H. C.; Hwang, B. J.; Lin, Y. Y.; Chen, L. J.; S.Y., L. *Rev. Sci. Instr.* **1998**, *69*, 2514.
- (70) Schrodle, S.; Hefter, G.; Kunz, W.; Buchner, R. *Langmuir* **2006**, *22*, 924.
- (71) Fernandez, P.; Schrodle, S.; Buchner, R.; Kunz, W. *ChemPhysChem.* **2003**, *4*, 1065.
- (72) Ryhanen, S. J.; Saily, V. M. J.; Kinnunen, P. K. J. *J. Phys. Condens. Matter* **2006**, *18*, S1139.
- (73) Baar, C.; Buchner, R.; Kunz, W. *J. Phys. Chem. B* **2001**, *105*, 2906.
- (74) Benderskii, A. V.; Henzie, J.; Basu, S.; Shang, X.; Eisenthal, K. B. *J. Phys. Chem. B*

**2004**, *108*, 14017.

(75) Luo, G.; Malkova, S.; Yoon, J.; Schultz, D. J.; Lin, B.; Meron, M.; Benjamin, I.; Vanysek, P.; Schlossman, M. L. *Science* **2006**, *311*, 216

(76) Blanchard, D. C. *J. Meteor.* **1958**, *15*, 383.

(77) Deutsch, M. *Faraday Discuss.* **2005**, *129*, 89.

(78) Israelachvili, J. *Intermolecular & Surface Forces*, 2nd ed.; Academic Press: London, 1992.

(79) Dzyaloshinskii, I.E.; Lifshitz, E. M.; Pitaevskii, L. P. *Adv. Phys.* **1961**, *10*, 165.

(80) Wilen, L. A.; Wettlaufer, J. S.; Elbaum, M.; Schick, M. *Phys. Rev. B* **1995**, *52*, 12426.

(81) Kaatze, U. *J. Solut. Chem.* **1997**, *26*, 1049.

(82) Barthel, J.; Buchner, R. *Pure Appl. Chem.* **1991**, *63*, 1473.

(83) Hildebrandt, A.; Blossey, R.; Rjasanow, S.; Kohlbacher, O.; Lenhof, H. P. *Phys. Rev. Lett.* **2004**, *93*, 108104.

(84) Gavryushov, S.; Linse, P. *J. Phys. Chem. B* **2003**, *107*, 7135.

(85) Wachter, W.; Kunz, W.; Buchner, R.; Hefter, G. *J. Phys. Chem. A* **2005**, *109*, 8675.

(86) Koga, Y.; Westh, P.; Davies, J. V.; Miki, K.; Nishikawa, K.; Katayanagi, H. *J. Phys. Chem. A* **2004**, *108*, 8533.

(87) Petersen, P. B.; Saykally, R. J. *J. Am. Chem Soc.* **2006**, *127*, 15446.

Table 2.1 Interfacial affinities and molecular properties of anions

<b>Anion X<sup>-</sup></b>	<b>Normalized Affinities<sup>a</sup> <math>f_{X^-}</math><sup>b</sup></b>	<b>Relative Affinities<sup>a</sup> <math>\gamma_{X^-}</math><sup>b</sup></b>	<b>Radii<sup>c</sup> <math>a_{X^-} \times 10^{12}</math> /m</b>	<b>Dehydration Free Energies<sup>c</sup> <sup>d</sup>G<sub>X<sup>-</sup></sub>/ kJ mol<sup>-1</sup></b>	<b>Polarizabilities<sup>c</sup> <math>\alpha_{X^-} \times 10^{30}</math> /m<sup>3</sup></b>
<b>Br<sup>-</sup></b>	0.023	1.00	196	321	4.99
<b>NO<sub>3</sub><sup>-</sup></b>	0.033	1.40	206 <sup>d</sup>	306	4.20
<b>I<sup>-</sup></b>	0.090	3.85	220	283	7.65
<b>SCN<sup>-</sup></b>	0.098	4.17	213	287	6.86
<b>BF<sub>4</sub><sup>-</sup></b>	0.301	12.86	230	200	2.78
<b>ClO<sub>4</sub><sup>-</sup></b>	0.455	19.45	240	214	4.92

<sup>a</sup> See text for definition

<sup>b</sup> This work

<sup>c</sup> Reference 60

<sup>d</sup> Equatorial radius

Figure 2.1. ESI-MS of a 100  $\mu\text{M}$  aqueous solution of the sodium salts of each of the following anions:  $\text{SCN}^-$ ,  $\text{NO}_3^-$ ,  $\text{Br}^-$ ,  $\text{BF}_4^-$ ,  $\text{ClO}_4^-$  and  $\text{I}^-$ , at pH 6.5. Ion signal intensities normalized to the total ion intensity:  $\sum I_i = 1$ .  $I_{\text{SCN}^-} = 0.097$ ,  $I_{\text{NO}_3^-} = 0.033$ ,  $I_{\text{Br}^-} = 0.023$ ,  $I_{\text{BF}_4^-} = 0.301$ ,  $I_{\text{ClO}_4^-} = 0.455$ ,  $I_{\text{I}^-} = 0.090$ .

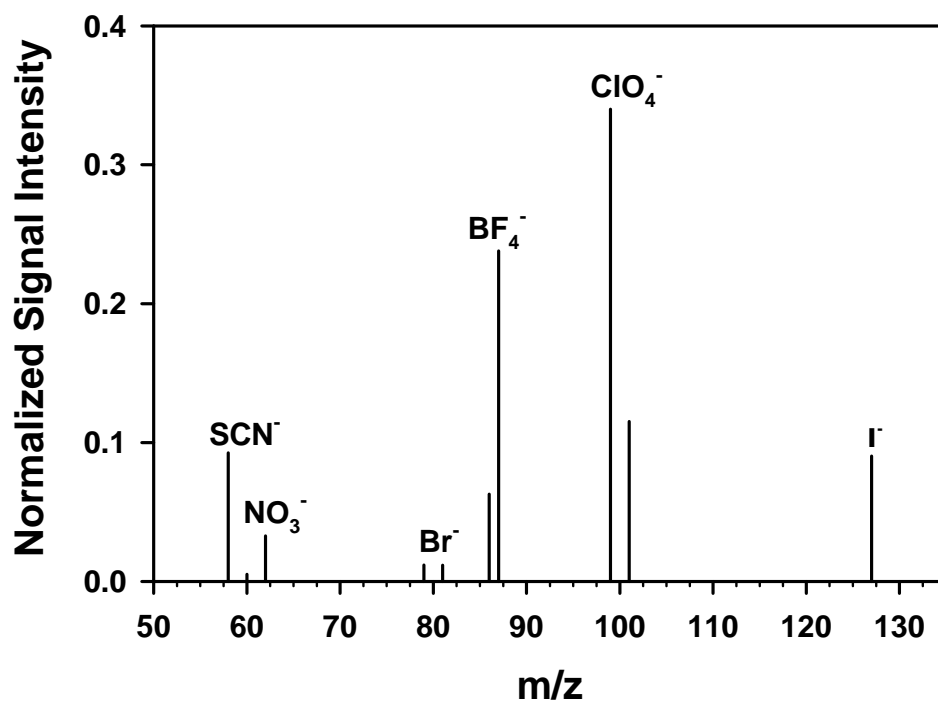


Figure 2.2. Symbols: Normalized anion affinities,  $f_X^-$ , versus anionic radii,  $a_X^-$ , from Reference 60. Solid line: linear regression:  $\ln f_X^- \propto a_X^-$  ( $R^2 = 0.956$ ).

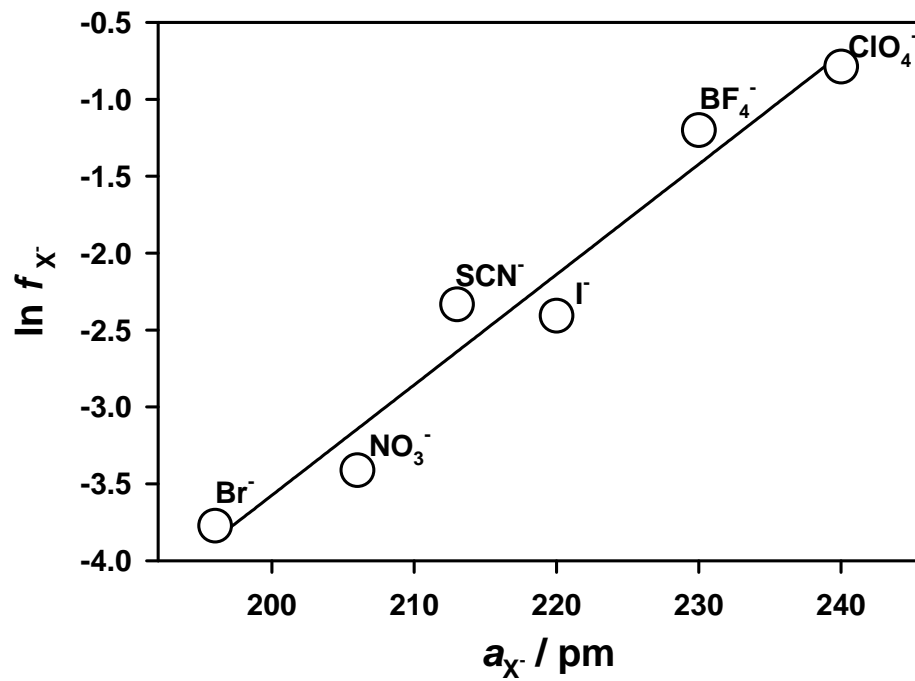


Figure 2.3. Symbols: Normalized anion affinities,  $f_X^-$ , versus free energies of anion dehydration,  ${}^dG_{X^-}$ , from Ref. 60. Solid line: linear regression:  $\ln f_X^- \propto {}^dG_{X^-}$  ( $R^2=0.910$ ).

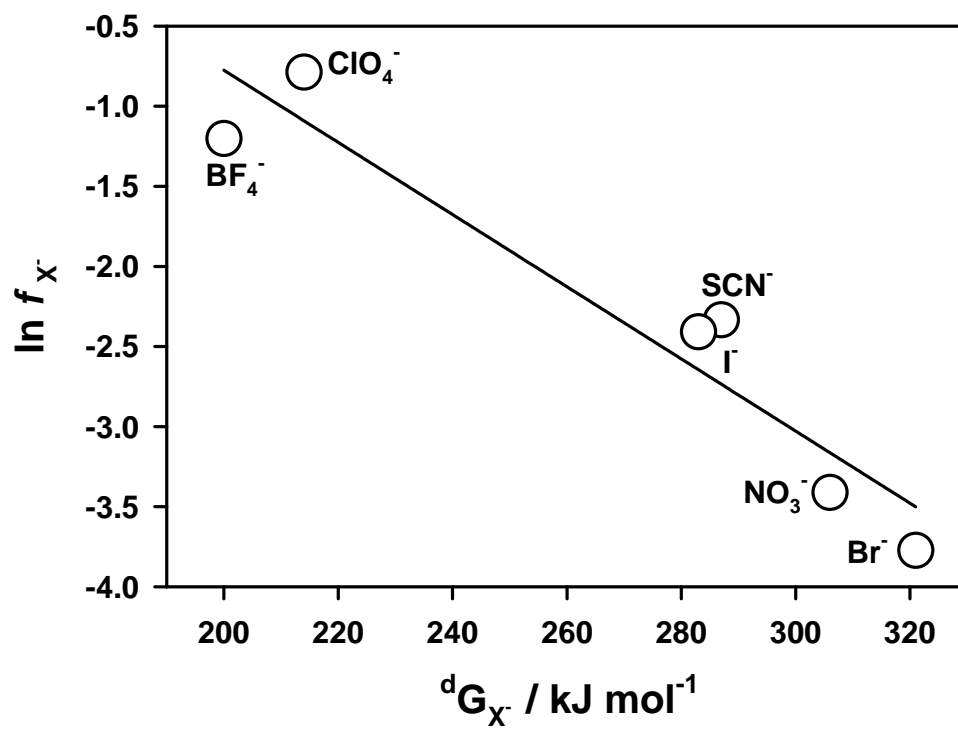


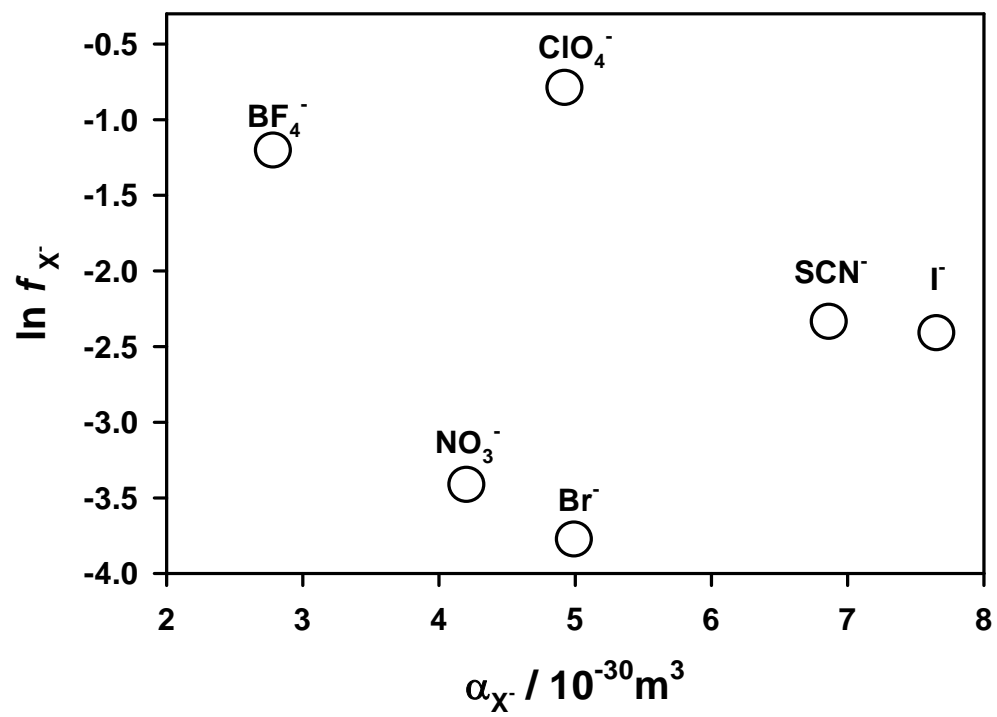
Figure 2.4. Normalized anion affinities,  $f_X^-$ , versus anion polarizabilities,  $\alpha_X^-$ , from Ref. 60.

Figure 2.5. Symbols: Ratios of normalized anion affinities,  $f_X/f_X(0)$ , as function of urea concentration. ■( $\text{BF}_4^-$ ); ◇( $\text{NO}_3^-$ ); ▽( $\text{ClO}_4^-$ ); □( $\text{Br}^-$ ); ○( $\text{I}^-$ ); △( $\text{SCN}^-$ ).  $[\text{X}_i^-] = 0.1 \text{ mM}$ .

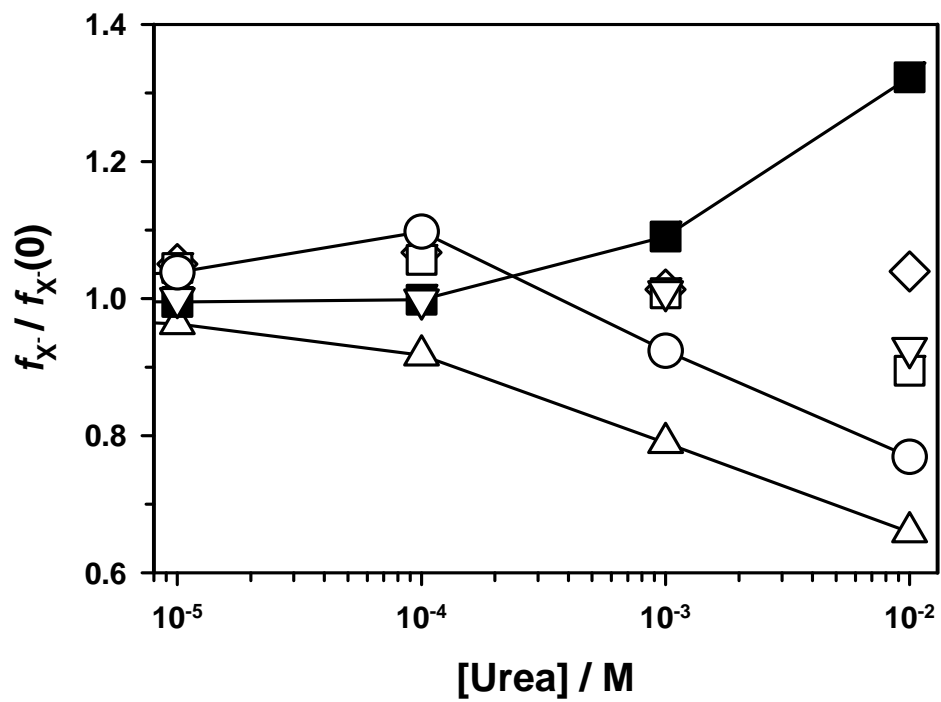


Figure 2.6. Symbols: Ratios of normalized anion affinities,  $f_x/f_x(0)$ , as function of cetyltrimethyl ammonium chloride (CTAC) concentration. ■( $\text{BF}_4^-$ ); ◇( $\text{NO}_3^-$ ); ▽( $\text{ClO}_4^-$ ); □( $\text{Br}^-$ ); ○( $\text{I}^-$ ); △( $\text{SCN}^-$ ).  $[\text{X}_i^-] = 0.1 \text{ mM}$ .

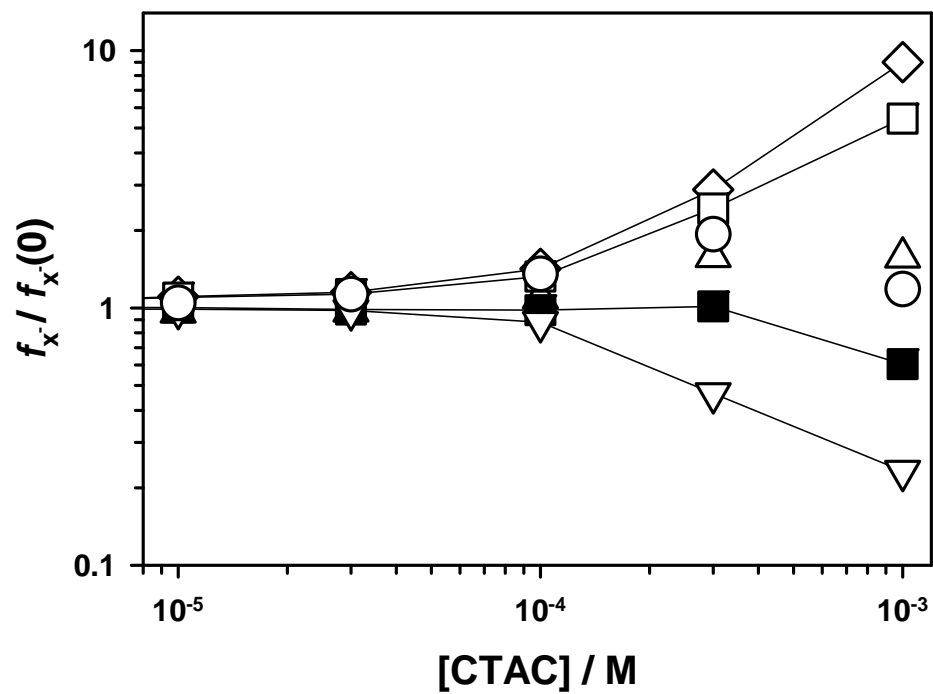


Figure 2.7. Symbols: Ratios of normalized anion affinities,  $f_{X^-}/f_{X^-}(0)$ , as function of Triton X-114. ■( $\text{BF}_4^-$ ); ◇( $\text{NO}_3^-$ ); ▽( $\text{ClO}_4^-$ ); □( $\text{Br}^-$ ); ○( $\text{I}^-$ ); △( $\text{SCN}^-$ ).  $[\text{X}_i^-] = 0.1 \text{ mM}$ .

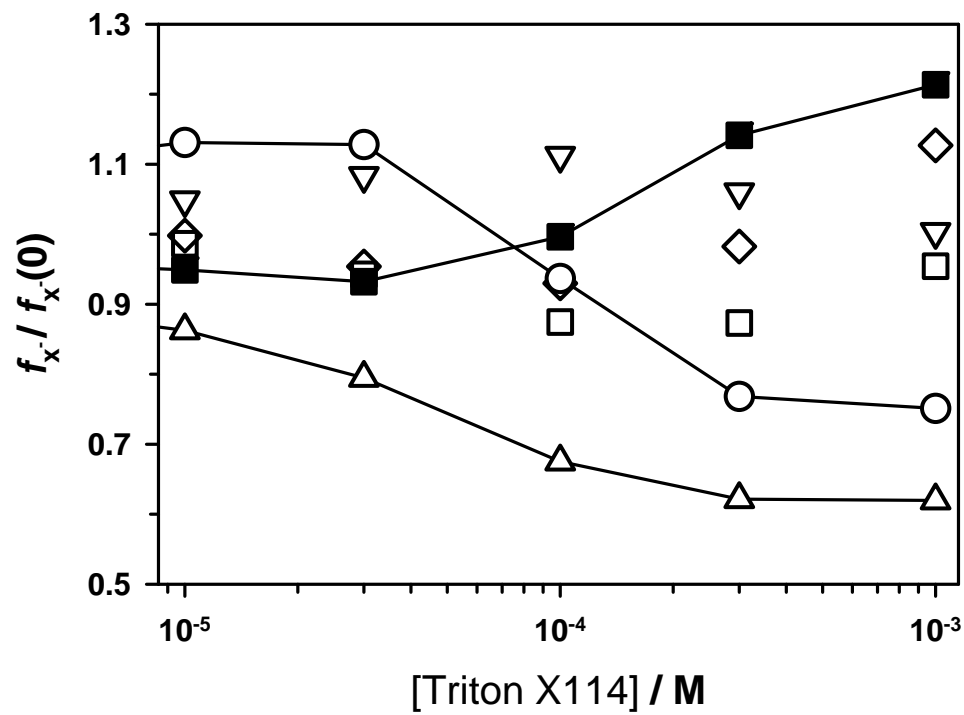
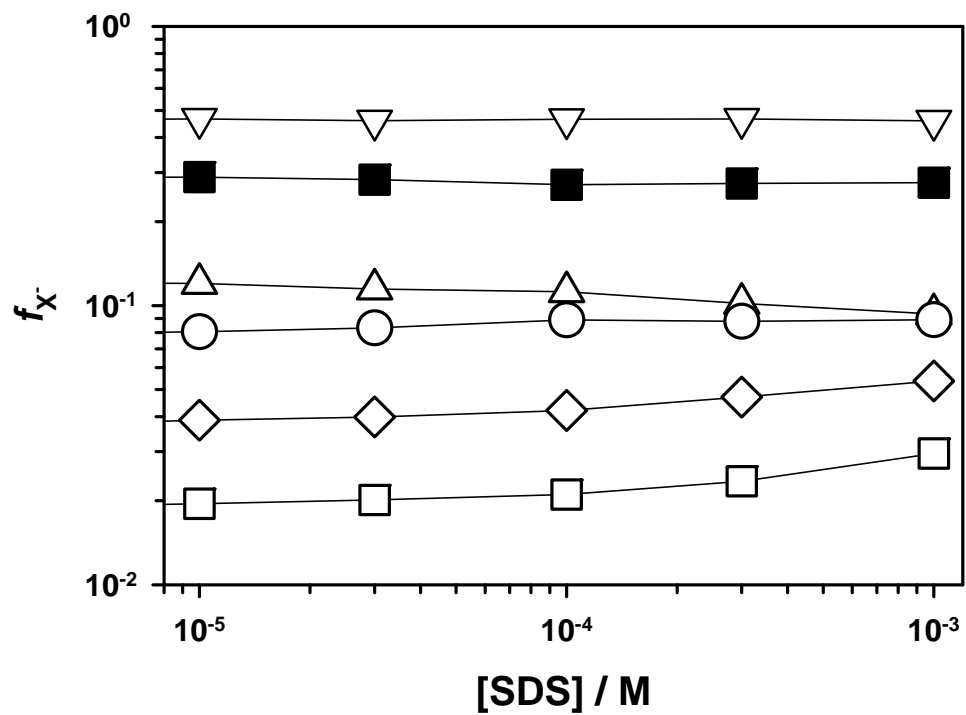


Figure 2.8. Symbols: Normalized anion affinities,  $f_{X^-}$ , as function of sodium dodecylsulfate (SDS) concentration. ■( $\text{BF}_4^-$ ); ◇( $\text{NO}_3^-$ ); ▽( $\text{ClO}_4^-$ ); □( $\text{Br}^-$ ); ○( $\text{I}^-$ ); △( $\text{SCN}^-$ ).  $[\text{X}_i^-] = 0.1 \text{ mM}$ .



## Chapter 3

### **Anion fractionation and reactivity at air–water and air–methanol interfaces: implications for the origin of Hofmeister effects\***

---

\* This chapter is reproduced with permission from J. Cheng, M. R. Hoffmann, and A. J. Colussi, *Journal of Physical Chemistry B*, **2008**, 112, 7157. Copyright © 2008, American Chemical Society

### 3.1 Abstract

Anions are selectively enriched in interfacial layers. This universal phenomenon, first identified in connection with protein precipitation 120 years ago, underlies fundamental processes. Its physical causes, however, remain conjectural. It has been speculated that the more polarizable anions should have larger affinities for air/liquid interfaces, and that their reactivities toward gaseous species would be affected by whether the liquid is capped by hydroxyl groups, as in water itself, or by hydrophobic layers of organic contaminants. These issues are particularly relevant to the composition and fate of atmospheric aerosols. Recently we found that fractionation factors  $f_{X^-}$  of simple anions at the air/water interface increase exponentially with ion radius  $a_{X^-}$ . In this chapter we report new experimental results on a set of anions that include the large  $\text{PF}_6^-$  and the highly polarizable  $\text{IO}_3^-$  species. A strict  $\ln f_{X^-} \propto a_{X^-}$  correlation is confirmed. Experiments performed in  $\{x_w \text{H}_2\text{O} + (1 - x_w) \text{MeOH}\}$  mixtures show that  $f_{X^-}$  is almost independent of  $x_w$ . Furthermore,  $\text{O}_3(\text{g})$  oxidizes  $\text{I}^-$  at virtually identical rates on  $\text{H}_2\text{O}$  and  $\text{MeOH}$ .

### 3.2 Introduction

Bromide and particularly iodide are known to be highly enriched in the finest marine aerosol particles.<sup>1-3</sup> This phenomenon has long been ascribed to the binding of halide ions to surface-active organic material,<sup>2</sup> and/or the release of biogenic halocarbon gases from the ocean.<sup>4,5</sup> Since the aerial interfaces of most electrolyte solutions are negatively charged relative to the bulk,<sup>6-8</sup> i.e., anions are selectively enriched at the interface as a matter of course, anion fractionation will inevitably take place during the aerosolization of the ocean upper layers upon bubble breakup.<sup>9,10</sup> Establishing the physical basis of this universal,<sup>11,12</sup> as opposed to contingent or episodic, mechanism of solute fractionation at the air/water interface is key to our understanding of aerosol chemistry<sup>13-15</sup> and its global impact on atmospheric processes.<sup>16,17</sup>

The origin of interfacial ion partitioning is not well understood.<sup>18-20</sup> Electrostatic, hydration, dispersion and hydrophobic forces, hydrogen bonding, and chaotropic/kosmotropic effects on solvent structure<sup>12,18,20-26</sup> have been invoked to explain specific ion effects. Molecular dynamics and Monte Carlo calculations have revitalized the subject,<sup>15,27,28</sup> using *ab initio* water-water potential energy functions calibrated to account for many-body effects in the bulk.<sup>29</sup> Since the modest enrichment factors (less than an order of magnitude) associated with most interfacial phenomena entail free energy differences  $\Delta G \leq 5 \text{ kJ mol}^{-1} \sim 2 kT$  at 300 K, one may envision multiple explanations for ‘anion enrichment’.<sup>19,30,31</sup> A more stringent test for theory and calculations would be to account for robust, quantitative correlations between reliable interfacial fractionation data with ion and/or solvent properties.

The very concept of ‘interface’, i.e., the depth of what is considered the ‘interface’ as opposed to the ‘interfacial region’, is itself ambiguous because it depends on both the phenomenon studied and the probing technique. Surface-specific techniques collect signals from  $\sim 1$  nm deep layers,<sup>32-37</sup> but again, since the free energy gradients associated with interfacial ion enrichment are commensurate with  $kT$ , chemically activated processes specifically confined to the ‘interface’ proper appear to be a contradiction in terms. Perhaps only the fastest reactions, which occur upon heterogeneous reactant encounters could truly probe interfacial structure and dynamics.<sup>38</sup>

In this article, we extend our previous study on anion fractionation<sup>39</sup> to the large  $\text{PF}_6^-$  and the highly polarizable  $\text{IO}_3^-$ , and report experimental tests of whether anion fractionation depends on local interfacial properties in water:methanol mixtures, which are largely capped with  $-\text{CH}_3$  groups above  $x_{\text{MeOH}} \sim 0.2$ .<sup>40-42</sup> We also investigate whether the rates and course of the diffusion-controlled oxidation of interfacial  $\Gamma$  by  $\text{O}_3(\text{g})$  change from water to methanol.<sup>43-47</sup>

### 3.3 Experimental Section

$\text{NaSCN}$  (98%, Sigma-Aldrich),  $\text{NaNO}_3$  (99 %, EM Science),  $\text{NaBr}$  (99.5%, EM Science),  $\text{NaBF}_4$  (98%, Fluka),  $\text{NaClO}_4$  (99%, EM Science),  $\text{NaI}$  (99%, EM Science),  $\text{NaPF}_6$  (98%, Sigma-Aldrich), and  $\text{NaIO}_3$  (99%, Sigma-Aldrich) were used as received. Equimolar stock solutions were prepared in purified water ( $18.2 \text{ M}\Omega \text{ cm}^{-1}$  resistivity) from a Millipore Milli-Q Gradient water purification system or in methanol (HRGC grade, EMD Chemicals). Anions at the liquid-air interfaces are directly monitored by electrospray mass spectrometry (ES-MS).<sup>48-50</sup> Equimolar solutions of the sodium salts of various anions were pumped (at  $50 \mu\text{L min}^{-1}$ ) into the spraying chamber of the

electrospray mass spectrometer (HP-1100) through a grounded stainless steel needle (100  $\mu\text{m}$  ID, 150  $\mu\text{m}$  OD) surrounded by a coaxial sheath (250  $\mu\text{m}$  ID) that issues  $\text{N}_2(\text{g})$  at 0.5  $\text{L min}^{-1}$ . The large difference between the exit velocities of the liquid jet ( $10.6 \text{ cm s}^{-1}$ ) and the  $\text{N}_2$  gas ( $2.65 \times 10^4 \text{ cm s}^{-1}$ ) forces the liquid to fragment into fine droplets. The spray produced from a grounded nozzle injector consists of a normal distribution of weakly charged microdroplets (centered at zero charge) arising from statistical charge separation during the fragmentation of a neutral liquid. In the electrospray chamber, rapid solvent evaporation leads to the shrinking, and concomitant surface charge crowding of droplets that become mechanically unstable when electric repulsion overtakes liquid cohesion; as a result, they shed their interfacial films to produce finer droplets. This process repeats itself until anions are ultimately field-ejected from the last-generation nanodroplets, and deflected into the mass spectrometer region by applying an appropriate bias to its inlet port. This technique therefore reports the multiplicatively amplified differences in composition of the outermost layers of original droplets. Typical instrumental parameters were: drying gas temperature, 250  $^\circ\text{C}$ ; drying gas flow, 10  $\text{L min}^{-1}$ ; nebulizer pressure, 35 psi; collector capillary voltage, +3.5 kV; fragmentor voltage, 80 V. Mass spectra were acquired at preset  $m/z$  values, 58 and 60 ( $^{32,34}\text{SCN}^-$ ), 62 ( $\text{NO}_3^-$ ), 79 and 81 ( $\text{Br}^-$ ), 86 and 87 ( $^{10,11}\text{BF}_4^-$ ), 99 and 101 ( $^{35, 37}\text{ClO}_4^-$ ), 127 ( $\text{I}^-$ ), 145 ( $\text{PF}_6^-$ ), and 175 ( $\text{IO}_3^-$ ). The composition of the interfacial layers of reacting droplets is directly monitored after sub-millisecond contact times,  $\tau$ , by online electrospray mass spectrometry (ES-MS) of field-ejected anions.<sup>49</sup> Ozone was produced by passing  $\text{O}_2(\text{g})$  (ultrapure, Air Liquid America Co.) through an ozone generator (Ozone Solutions), diluted 10-fold with ultrapure  $\text{N}_2(\text{g})$ , and quantified by a UV-Vis spectrophotometer (Agilent 8452). Ozone concentrations

were calculated from absorbance measurements using recommended values for its absorption cross sections:  $\sigma = 1.1 \times 10^{-17}$  (250 nm) and  $\sigma = 3.9 \times 10^{-19}$  (300 nm)  $\text{cm}^2$  molecule<sup>-1</sup>. The mixed gas was then injected into the chamber, where it was further diluted six-fold by the countercurrent drying gas. Gas flows were regulated by calibrated mass flow controllers (MKS). A schematic diagram of the ozone reaction chamber is shown in Scheme 3.2.

### 3.4 Results and Discussion

Figure 3.1 shows the negative ion mass spectrum of an electrosprayed equimolar solution of sodium  $\text{NO}_3^-$ ,  $\text{BF}_4^-$ ,  $\text{ClO}_4^-$ ,  $\text{PF}_6^-$  and  $\text{IO}_3^-$  salts. Since the technique detects ions already present in solution, Figure 3.1 should display similarly intense signals in the absence of interfacial fractionation. This is clearly not the case. From the mass spectrum of Figure 3.1, normalized anion fractionation factors,  $f_{X^-}$ , are calculated from the sum of ion counts,  $I_{m/z}$ , for the isotopic variants of each anionic species (e.g., ( $I_{99} + I_{101}$ ) for  $\text{ClO}_4^-$ , etc.) and the total ion count:

$$f_{X^-} = \frac{I_{m/z, X^-}}{\sum I_{m/z, X^-}} \quad (3.1)$$

Thus, by definition,  $f_{X^-}$ 's are relative (rather than absolute, i.e., interfacial versus bulk) fractionation factors. They are independent of bulk concentration from 10 to 1000  $\mu\text{M}$ .  $\text{PF}_6^-$ , which has the largest radius ( $a_{X^-} = 295$  pm) of the set, is exceedingly enriched at the droplet surface. This is consistent with previous surface potential measurements in which  $\text{PF}_6^-$  displayed a several-fold stronger affinity for the air-water interface than either  $\text{ClO}_4^-$  or  $\text{SCN}^-$ .<sup>6</sup> In line with this finding, the smallest anion in the group,  $\text{IO}_3^-$ , is the least

enriched,<sup>15,34,51,52</sup> despite possessing the largest polarizability (see Table 3-1). The *strict* linearity of the  $\ln f_{X^-}$  vs.  $a_{X^-}$  plots (correlation coefficients  $r^2 > 0.98$ ) of Figure 3.2 demonstrates that the (*negative*) free energies associated with the segregation of anions from the bulk solution to the air-liquid interface (i.e.,  $f_{X^-} \propto \exp[-^{B \rightarrow IF} \Delta G/kT]$ ) increase with the first power of ion radius  $a_{X^-}$ <sup>39,53</sup> rather than with ion volume or polarizability. Because many ion properties concomitantly depend on ion radius in one way or another, and to avoid confounding cause and effect, we adopted the criterion that the nature of the interactions involved should be sought in the best functional correlation. Thus, since solvation free energies  $^S \Delta G_{X^-} \propto (1/a_{X^-})$  are inversely rather than directly proportional to  $a_{X^-}$ <sup>54,55</sup>,  $\ln f_{X^-}$  vs.  $-^S \Delta G_{X^-}$  plots are also quasi-linear (with a negative slope) within a limited range, but they have smaller correlation coefficients than  $\ln f_{X^-}$  vs.  $a_{X^-}$  plots<sup>39</sup>; we therefore reject  $^S \Delta G_{X^-}$  differences as the origin of anion fractionation.

Perhaps unexpectedly, interfacial anion fractionation factors  $f_{X^-}$  measured in water/methanol mixtures are weakly dependent on solvent composition over the entire range (Figure 3.3a). Methanol preferentially partitions to the liquid-air interface,<sup>56,57</sup> where water hydroxyls are readily replaced by hydrophobic methyl groups that project into the vapor phase (Figure 3.3b).<sup>41</sup> Thus, we find no experimental grounds to support the hypothesis that interfacial anion fractionation is driven by surface structure or dynamics. By excluding local effects, we realize that any explanation of ‘interfacial affinities’ becomes conceptually related to Archimedes’s principle: lower density bodies float not because they have ‘affinity’ for the surface, but because the fluid forces them there.<sup>24,25,58-60</sup> We infer that anions are enriched and/or fractionated at air/liquid interfaces

*not because they have ‘affinity’ for these boundaries, but because they are expelled by the whole liquid.* The collective underlying interaction in this case is many-body electrodynamic rather than gravitational.

It has been hypothesized that the reactivity of solutes at the air/water interface might be different from in the bulk. This issue arises, for example, in connection with gas-liquid reactions occurring in atmospheric aerosol droplets exposed to reactive gaseous species such as OH-radicals, O<sub>3</sub> or NO<sub>2</sub>. Note that, in principle, only the fastest reactions could display ‘kinetic surface effects’ before the gaseous species have the chance to be solvated and diffuse into the bulk medium. Besides solute fractionation, which expresses preexisting equilibrium interfacial gradients, reactivity is expected to be affected by the state of the solute at the interface, particularly its solvation state, and by the intrinsic asymmetry of an interfacial region open to mass transfer with both the gas-phase and the bulk.

Figure 3.4 shows relative iodide concentrations  $[I^-]/[I^-]_0$  at the air-liquid interface as a function of  $[O_3(g)]$ . We have shown that the initial slopes,  $S_0$ , of  $[I^-]/[I^-]_0$  vs.  $[O_3(g)]$  curves are proportional to the ratio of the second-order-reaction rate constant,  $k$ , over the diffusion coefficient  $D_I$  in the condensed phase:  $S_0 \propto k/D_I$ .<sup>61</sup> Despite the dissimilar structures of the aerial interfaces of water and methanol, and an estimated ten-fold larger solubility in methanol than in water,<sup>62</sup> O<sub>3</sub>(g) oxidizes I<sup>-</sup> at identical rates in both solvents:  $S_0 = 0.0152 \pm 0.0010$  ppmv<sup>-1</sup> (H<sub>2</sub>O),  $S_0 = 0.0145 \pm 0.0002$  ppmv<sup>-1</sup> (MeOH), regardless of the diverse interactions it may experience upon approaching each surface. Product branching ratios:  $\Gamma = [IO_3^-]/[I^-]$ , are also similar in water and methanol. By assuming that

$k_3 \gg k_2$ ,  $k_5 \gg k_4$ , the mechanism in Scheme 3.1 implies that  $\Gamma$  should be a linear function of  $[\text{O}_3(\text{g})]/[\text{I}^-]$ .<sup>13</sup>

$$\frac{[\text{IO}_3^-]}{[\text{I}_3^-]} = \frac{k_2}{k_4} \frac{[\text{O}_3]}{[\text{I}^-]} \quad (3.2)$$

This functional dependence is experimentally confirmed in both solvents, with slopes  $(k_2/k_4)_{\text{MeOH}} \sim 1.03 (k_2/k_4)_{\text{water}}$  (Figure 3.5a,b). Thus, secondary reactions, which possibly take place in subsurficial layers (such as the one denoted by  $\sigma$  in Figure 3.3b) are also insensitive to the nature of the solvent surface.

Based on the above results and considerations, we propose that the selective enrichment of larger radius anions in air/liquid interfacial layers likely results from rejection by the medium via collective dispersive interactions.<sup>24-26,59,63</sup> The current view is that “the dominant forces on ions in water are short range forces of a chemical nature”,<sup>21</sup> i.e., ions hardly perturb the solvent beyond the first solvation shell.<sup>64,65</sup> By strongly binding solvent molecules, the dielectric permittivities of the solvated ions  $\epsilon_X$  are necessarily smaller than that of the bulk solvent’s  $\epsilon_S$ , except at the air/liquid interface, where  $\epsilon_S(z)$  monotonically falls off to  $\epsilon_S(z) \rightarrow \epsilon_{\text{air}} = 1$  as  $z \rightarrow 0$ .<sup>66</sup> Electrolyte solutions should be realistically viewed as ‘colloidal’ suspensions of weakly dielectric, inert solvated ions of radius  $a_X$  in a continuous dielectric medium, rather than intermolecularly perturbed fluids.<sup>65,67,68</sup> Far from the interface, ions remain in a state of indifferent equilibrium, but in the interfacial region, where  $\epsilon_S(z) \rightarrow \epsilon_{\text{air}}$ , they experience a net electrodynamic force toward the interface because  $\epsilon_S(z+\delta) > \epsilon_X > \epsilon_S(z-\delta) > 1$ .<sup>26,58-60</sup> Furthermore, ions can be treated as large spheres close to the infinite planes separating

solvents from air, and therefore will be repelled toward the interface by many-body dispersion energies that scale with  $\sim(a_X/z) [(\epsilon_X - \epsilon_S(z)) (\epsilon_X + \epsilon_S(z))^{-1} (1 - \epsilon_S(z)) (1 + \epsilon_S(z))^{-1}]$  as  $z \rightarrow 0$ ,<sup>25</sup> conforming to the  $\ln f_X$  vs.  $a_X$  correlation of Figure 3.2. Notice that if the likely condition  $\epsilon_X \propto \epsilon_S$  applies, these energies, which involve dielectric permittivity ratios, are expected to be weakly dependent on absolute  $\epsilon_S$  values (cf. Figure 3.3c). How far ions approach, or even protrude into the gas-phase will be ultimately limited, of course, by hydration energy losses. Summing up, interfacial anion fractionation is the electrodynamic equivalent of flotation in a gravitational field, and is determined by ionic radii and solvent permittivity profiles across interfacial layers.

### 3.5 Acknowledgement

This project was financially supported by the National Science Foundation (ATM-0534990).

### 3.6 References

- (1) Moyers, J. L.; Duce, R. A. *J. Geophys. Res.* **1972**, *77*, 5229.
- (2) Duce, R. A.; Hoffman, E. J. *Ann. Rev. Earth Planet. Sci.* **1976**, *4*, 187.
- (3) Liss, P. S.; Duce, R. A. *The sea surface and global change*; Cambridge University Press: Cambridge, UK, 1997.
- (4) Vogt, R.; Sander, R.; von Glasow, R.; Crutzen, P. J. *J. Atmos. Chem.* **1999**, *32*, 375.
- (5) Cicerone, R. J. *Rev. Geophys. Space Phys.* **1981**, *19*, 123.
- (6) Randles, J. E. B. *Discuss. Faraday Soc.* **1957**, 194.
- (7) Jarvis, N. L. *J. Geophys. Res.* **1972**, *77*, 5177.
- (8) Jarvis, N. L.; Scheiman, M. A. *J. Phys. Chem.* **1968**, *72*, 74.

- (9) Macintyre, F. J. *Phys. Chem.* **1968**, 72, 589.
- (10) Macintyre, F. *Tellus* **1970**, 22, 451.
- (11) Kunz, W. *Pure Appl. Chem.* **2006**, 78, 1611.
- (12) Kunz, W.; Lo Nostro, P.; Ninham, B. W. *Curr. Opin. Colloid Interface Sci.* **2004**, 9, 1.
- (13) Enami, S.; Vecitis, C. D.; Cheng, J.; Hoffmann, M. R.; Colussi, A. J. *J. Phys. Chem. A* **2007**, 111, 8749.
- (14) Finlayson-Pitts, B. J. *Chem. Rev.* **2003**, 103, 4801.
- (15) Jungwirth, P.; Tobias, D. J. *Chem. Rev.* **2006**, 106, 1259.
- (16) Hunt, S. W.; Roeselova, M.; Wang, W.; Wingen, L. M.; Knipping, E. M.; Tobias, D. J.; Dabdub, D.; Finlayson-Pitts, B. J. *J. Phys. Chem. A* **2004**, 108, 11559.
- (17) Knipping, E. M.; Lakin, M. J.; Foster, K. L.; Jungwirth, P.; Tobias, D. J.; Gerber, R. B.; Dabdub, D.; Finlayson-Pitts, B. J. *Science* **2000**, 288, 301.
- (18) Tobias, D. J.; Hemminger, J. C. *Science* **2008**, 319, 1197.
- (19) Ninham, B. W.; Bostrom, M. *Cell. Mol. Bio.* **2005**, 51, 803.
- (20) Karlstrom, G.; Hagberg, D. *J. Phys. Chem. B* **2002**, 106, 11585.
- (21) Collins, K. D.; Neilson, G. W.; Enderby, J. E. *Biophys. Chem.* **2007**, 128, 95.
- (22) Ninham, B. W.; Yaminsky, V. *Langmuir* **1997**, 13, 2097.
- (23) Gavryushov, S.; Linse, P. *J. Phys. Chem. B* **2003**, 107, 7135.
- (24) van Oss, C. J.; Absolom, D. R.; Neumann, A. W. *Coll. Surf.* **1980**, 1, 45.
- (25) Parsegian, V. A. *Van der Waals Forces*; Cambridge University Press: New York, 2006.
- (26) Dzyaloshinskii, I.E.; Lifshitz, E. M.; Pitaevskii, L. P. *Adv. Phys.* **1961**, 10, 165.

- (27) Frediani, L.; Mennucci, B.; Cammi, R. *J. Phys. Chem. B* **2004**, *108*, 13796.
- (28) Garrett, B. C. *Science* **2004**, *303*, 1146.
- (29) Stone, A. J. *Science* **2007**, *315*, 1228.
- (30) Pegram, L. M.; Record, M. T., Jr. *Proc. Natl. Acad. Sci. USA* **2006**, *103*, 14278.
- (31) Pegram, L. M.; Record, M. T., Jr. *J. Phys. Chem. B* **2007**, *111*, 5411.
- (32) Petersen, P. B.; Johnson, J. C.; Knutsen, K. P.; Saykally, R. J. *Chem. Phys. Lett.* **2004**, *397*, 46.
- (33) Petersen, P. B.; Saykally, R. J. *Chem. Phys. Lett.* **2004**, *397*, 51.
- (34) Petersen, P. B.; Saykally, R. J. *Annu. Rev. Phys. Chem.* **2006**, *57*, 333.
- (35) Petersen, P. B.; Saykally, R. J. *J. Am. Chem. Soc.* **2006**, *127*, 15446.
- (36) Smith, J. D.; Saykally, R. J.; Geissler, P. L. *J. Am. Chem. Soc.* **2007**, *129*, 13847.
- (37) Wilson, K. R.; Rude, B. S.; Smith, J.; Cappa, C.; Co, D. T.; Schaller, R. D.; Larsson, M.; Catalano, T.; Saykally, R. J. *Rev. Sci. Instrum.* **2004**, *75*, 725.
- (38) Davidovits, P.; Kolb, C. E.; Williams, L. R.; Jayne, J. T.; Worsnop, D. R. *Chem. Rev.* **2006**, *106*, 1323.
- (39) Cheng, J.; Vecitis, C. D.; Hoffmann, M. R.; Colussi, A. J. *J. Phys. Chem. B* **2006**, *110*, 25598.
- (40) Prtay, L. B.; Jedlovszky, P. I.; Vincze, A.; Horvai, G. *J. Phys. Chem. B* **2008**.
- (41) Chen, H.; Gan, W.; Lu, R.; Guo, Y.; Wang, H. F. *J. Phys. Chem. B* **2005**, *109*, 8064.
- (42) Liu, W. T.; Zhang, L. N.; Shen, Y. R. *J. Chem. Phys.* **2006**, *125*, 6.
- (43) Liu, Q.; Schurter, L. M.; Muller, C. E.; Aloisio, S.; Francisco, J. S.; Margerum, D. W. *Inorg. Chem.* **2001**, *40*, 4436.
- (44) Donaldson, D. J.; Vaida, V. *Chem. Rev.* **2006**, *106*, 1445.

- (45) Krisch, M. J.; D'Auria, R.; Brown, M. A.; Tobias, D. J.; Hemminger, J. C.; Ammann, M.; Starr, D. E.; Bluhm, H. *J. Phys. Chem. C* **2007**, *111*, 13497.
- (46) Smoydzin, L.; von Glasow, R. *Atmo. Chem. Phys.* **2007**, *7*, 5555.
- (47) Cwiklik, L.; Andersson, G.; Dang, L. X.; Jungwirth, P. *Chemphyschem* **2007**, *8*, 1457.
- (48) Kebarle, P. *J. Mass Spectrom.* **2000**, *35*, 804.
- (49) Kebarle, P.; Peschke, M. *Anal. Chim. Acta* **2000**, *406*, 11.
- (50) Kebarle, P.; Tang, L. *Anal. Chem.* **1993**, *65*, A972.
- (51) Mucha, M.; Frigato, T.; Levering, L. M.; Allen, H. C.; Tobias, D. J.; Dang, L. X.; Jungwirth, P. *J. Phys. Chem. B* **2005**, *109*, 7617.
- (52) Tuma, L.; Jenicek, D.; Jungwirth, P. *Chem. Phys. Lett.* **2005**, *411*, 70.
- (53) Eggimann, B. L.; Siepmann, J. I. *J. Phys. Chem. C* **2008**, *112*, 210.
- (54) Ashbaugh, H. S. *J. Phys. Chem. B* **2000**, *104*, 7235.
- (55) Marcus, Y. *Ion Properties*; Marcel Dekker: New York, 1997.
- (56) Chang, T. M.; Dang, L. X. *J. Phys. Chem. B* **2005**, *109*, 5759.
- (57) Wolfrum, K.; Graener, H.; Laubereau, A. *Chem. Phys. Lett.* **1993**, *213*, 41.
- (58) Israelachvili, J. N. *Quart. Rev. Biophys.* **1974**, *6*, 341.
- (59) Israelachvili, J. *Intermolecular & Surface Forces*, 2nd ed.; Academic Press: London, 1992.
- (60) Israelachvili, J.; Wennerstrom, H. *Nature* **1996**, *379*, 219.
- (61) Enami, S.; Hoffmann, M. R.; Colussi, A. J. *Proc. Natl. Acad. Sci. U.S.A.*, **2008**, *105*, 7365.
- (62) Bin, A. K. *Ozone-Science & Engineering* **2006**, *28*, 67.

- (63) van Oss, C. J.; Chaudhury, M. K. *Chem. Rev.* **1988**, 88, 927.
- (64) Omta, A. W.; Kropman, M. F.; Woutersen, S.; Bakker, H. J. *Science* **2003**, 301, 347.
- (65) Bakker, H. J. *Chem. Rev.* **2008**, 108, 1456.
- (66) Hildebrandt, A.; Blossey, R.; Rjasanow, S.; Kohlbacher, O.; Lenhof, H. P. *Phys. Rev. Lett.* **2004**, 93, 108104.
- (67) Bakker, H. J.; Kropman, M. F.; Omta, A. W. *J. Phys. Condens. Matter* **2005**, 17, S3215.
- (68) Grossfield, A. *J. Chem. Phys* **2005**, 122, 024506.
- (69) Akerlof, G. *J. Am. Chem. Soc.* **1932**, 54, 4125.
- (70) Baumgartner, E.; Busch, M.; Fernandez, R. *J. Phys. Chem.* **1970**, 74, 1821.

Table 3.1. Interfacial affinities and molecular properties of anions <sup>55</sup>

Anion X <sup>-</sup>	Affinities $f_{X^-}$ <sup>a</sup>	Radii $a_{X^-}$ (10 <sup>-12</sup> m)	Dehydration Energies (kJ mol <sup>-1</sup> )	Polarizability (10 <sup>-30</sup> m <sup>3</sup> )	Ion Volume (cm <sup>3</sup> mol <sup>-1</sup> )
IO <sub>3</sub> <sup>-</sup>	0.0103	181	408	7.41	30.8
NO <sub>3</sub> <sup>-</sup>	0.0149	206 <sup>b</sup>	306	4.20	34.5
BF <sub>4</sub> <sup>-</sup>	0.0661	230	200	2.78	50.6
ClO <sub>4</sub> <sup>-</sup>	0.0814	240	214	4.99	49.6
PF <sub>6</sub> <sup>-</sup>	0.8273	295 <sup>70</sup>	-	4.36 <sup>[c]</sup>	58.0

a. See text for definition

b. Equatorial radius

c. Value for SiF<sub>6</sub><sup>2-</sup>

Figure 3.1. ES-MS of a 10  $\mu\text{M}$  equimolar aqueous solution of the sodium salts of the following anions:  $\text{NO}_3^-$ ,  $\text{BF}_4^-$ ,  $\text{ClO}_4^-$ ,  $\text{PF}_6^-$ , and  $\text{IO}_3^-$  at  $\text{pH} = 6.5$ . Ion signal intensities are normalized to total ion intensity.

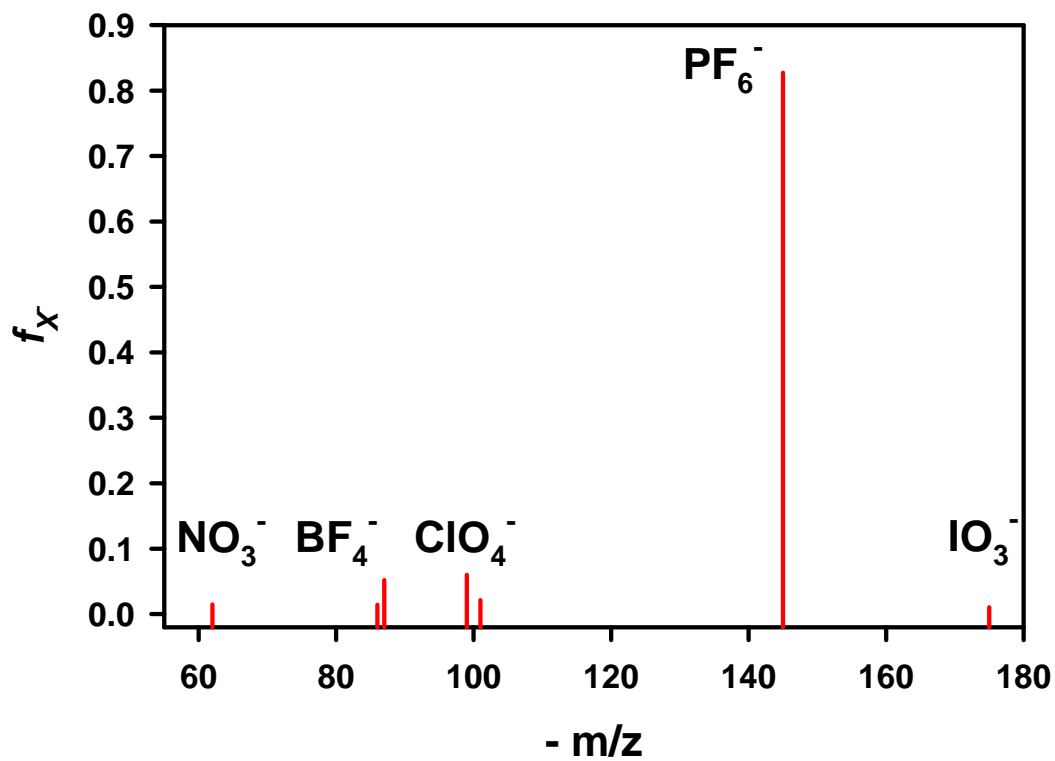


Figure 3.2. Symbols: Normalized anion affinities,  $f_X^-$  versus crystalline ion radii,  $a_{X^-}$ .  
Solid line: linear regression of  $\ln f_X^-$  vs.  $a_{X^-}$ .

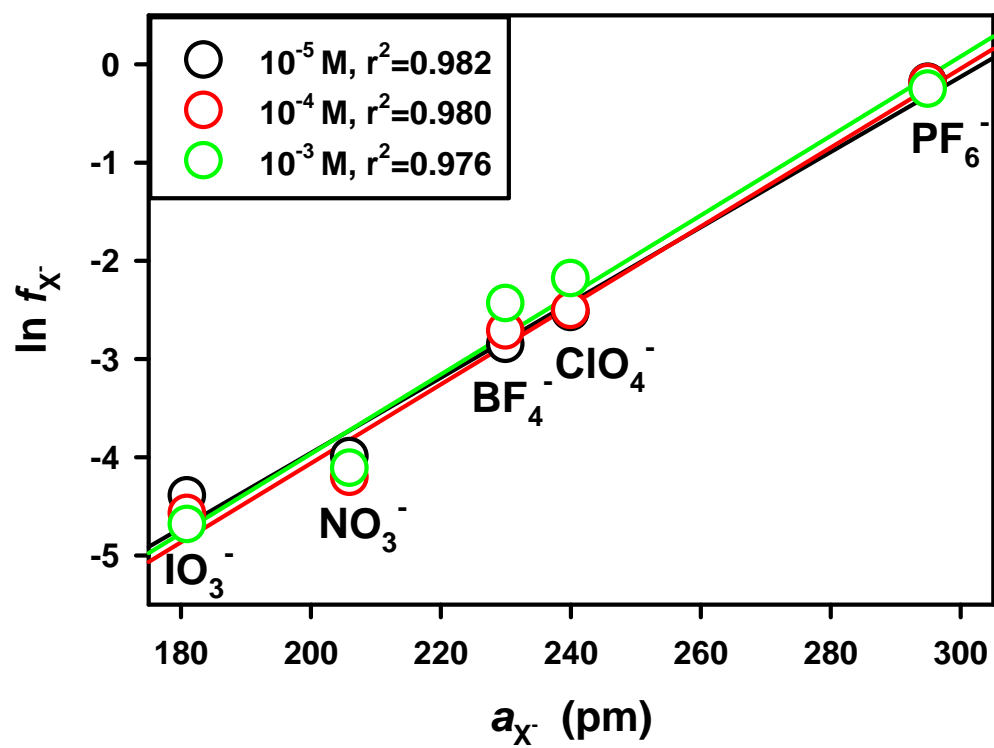


Figure 3.3. (a)  $f_X$  measured in 10  $\mu\text{M}$  solutions of the sodium salts of the corresponding anions; (b) the fractional coverage of  $-\text{CH}_3$  groups at the surface,  $\theta$ , and in the layer beneath,  $\sigma$ ; <sup>41</sup> (c) the dielectric permittivity of the solvent, <sup>69</sup> as functions of methanol molar fraction in water:methanol mixtures.

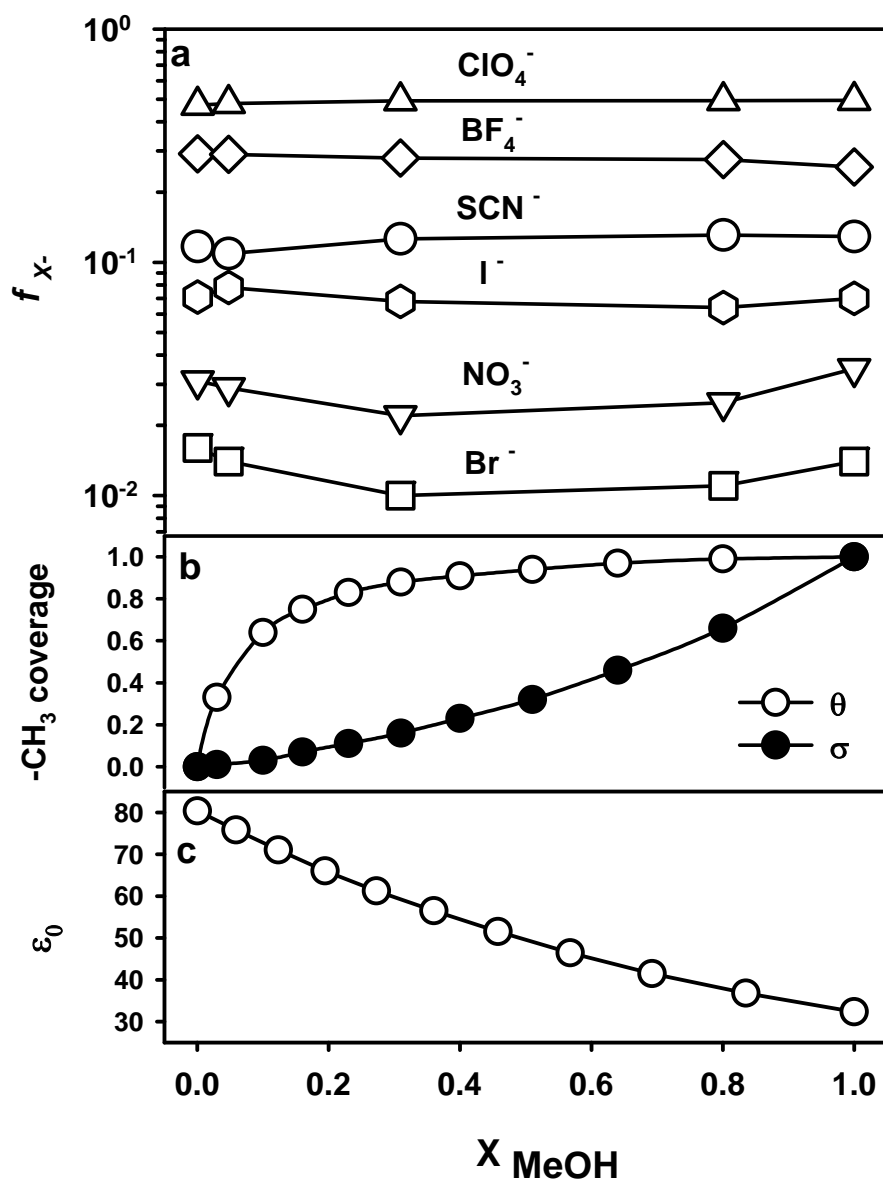


Figure 3.4. Symbols: normalized interfacial iodide concentration  $[I^-]/[I^-]_0$  versus  $[O_3(g)]$  in (a)  $H_2O$  and (b)  $MeOH$ ;  $[I^-]_0 = 10 \mu M$ . The data are fitted with exponential decay curves ( $r^2 > 0.99$ ).

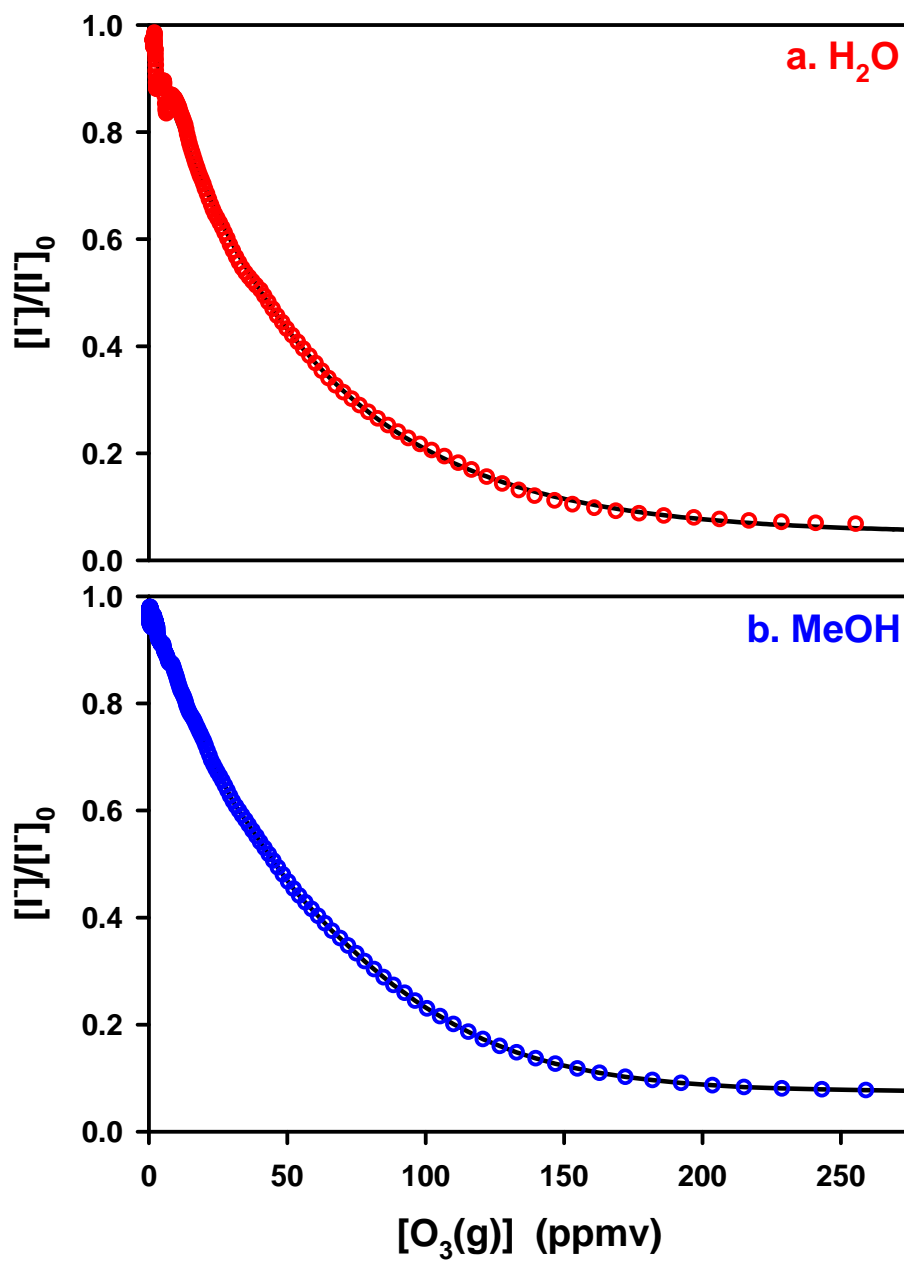
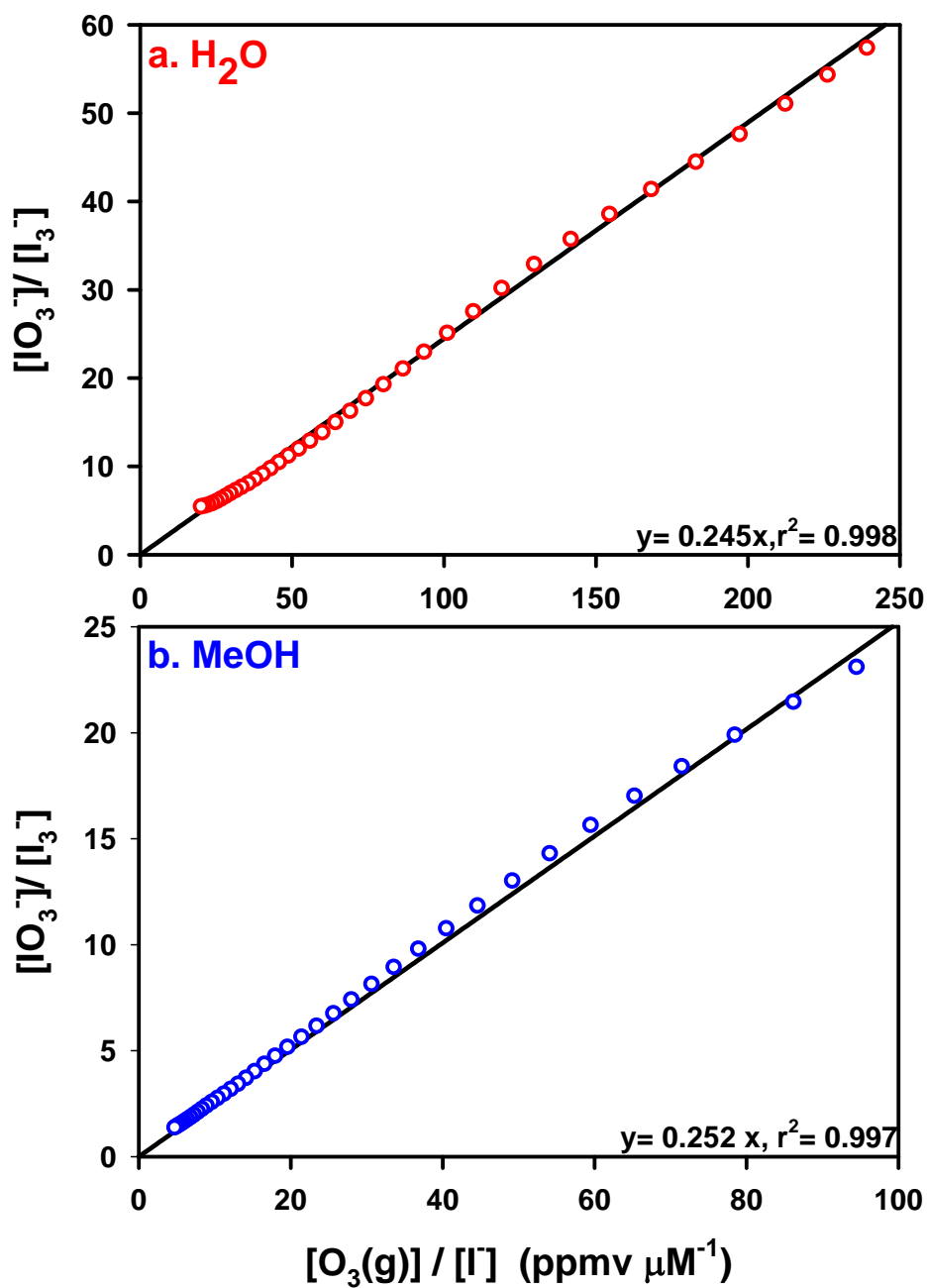
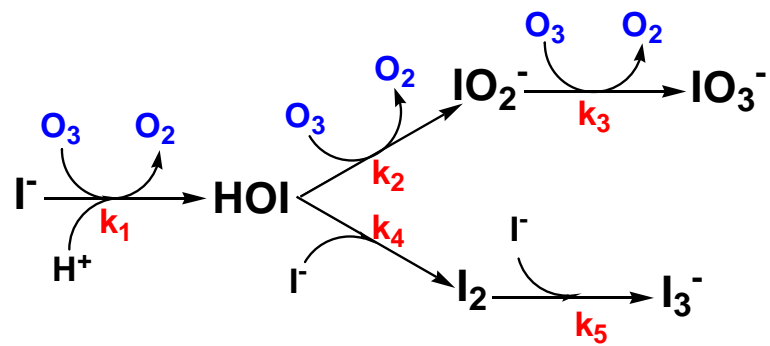


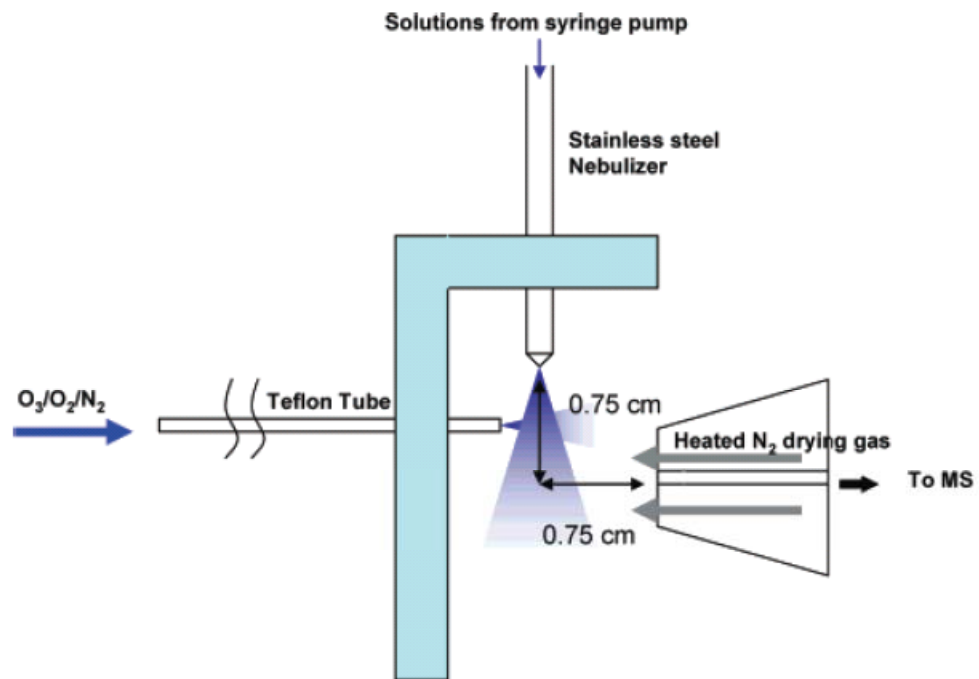
Figure 3.5. The product branching ratio  $[\text{IO}_3^-]/[\text{I}_3^-]$  as a function of  $[\text{O}_3(\text{g})]/[\text{I}^-]$  in (a)  $\text{H}_2\text{O}$  and (b)  $\text{MeOH}$ ;  $[\text{I}^-]_0 = 100 \mu\text{M}$ .



Scheme 3.1. Iodide oxidation by ozone in water.



Scheme 3.2. Schematic diagram of the spraying chamber,  $O_3$  (g) injection, and mass spectrometer sampling inlet.



## Chapter 4

### Enrichment Factors of Perfluoroalkyl Oxoanions at the Air/Water interface\*

---

\* This chapter is reproduced with permission from E. Psillakis, J. Cheng, M. R. Hoffmann, and A. J. Colussi, *Journal of Physical Chemistry A*, **2009**, 113, 8826. Copyright © 2009, American Chemical Society

#### 4. 1 Abstract

The refractory, water-bound perfluoro-*n*-alkyl carboxylate  $F(CF_2)_nCO_2^-$  and sulfonate  $F(CF_2)_nSO_3^-$  surfactant anions reach remote locations by mechanisms that are not well understood. Here we report experiments in which the relative concentrations of these anions on the surface of microdroplets produced by nebulizing their aqueous solutions are measured via electrospray ionization mass spectrometry. Enrichment factors  $f$  (relative to  $Br^-$ :  $f(Br^-) \equiv 1$ ) increase with  $n$ , asymptotically reaching  $f[F(CF_2)_nSO_3^-] \sim 2 f[F(CF_2)_nCO_2^-] \sim 200 f(Br^-)$  values above  $n \sim 8$ . The larger  $f$  values for  $F(CF_2)_nSO_3^-$  over their  $F(CF_2)_nCO_2^-$  congeners are consistent with a closer approach of the bulkier, less-hydrated  $-SO_3^-$  headgroup to the air/water interface. A hyperbolic, rather than the predicted linear  $\log f[F(CF_2)_nCO_2^-]$  vs.  $n$  dependence suggests the onset of conformational restrictions to interfacial enrichment above  $n \sim 4$ . Marine aerosols produced from contaminated ocean surface waters are therefore expected to be highly enriched in  $F(CF_2)_nCO_2^-/F(CF_2)_nSO_3^-$  species.

## 4.2 Introduction

The exceptionally persistent perfluoroalkyl (*F*-alkyl) sulfonates,  $F(CF_2)_nSO_3^-$ , and *F*-alkyl carboxylates,  $F(CF_2)_nCO_2^-$ , surfactants have spread and bioaccumulated globally since their inception ~50 years ago.<sup>1-4</sup> Because their strong conjugated *F*-alkyl acids ( $pK_a < 1$ )<sup>5</sup> are fully dissociated in water (particularly in seawater pH ~ 8.1) oceans are expected to be the main reservoir, and ocean currents the ultimate conduits for these water-bound anions.<sup>6-10</sup> *F*-alkyl anions, however, reach water bodies and continental sites far removed from both sources and oceans.<sup>9</sup> The short (within oceanic transport time frames) bioaccumulation times and decay half-life of  $F(CF_2)_8SO_3^-$  in Canadian Arctic seals after its phase-out<sup>11-12</sup> suggest an atmospheric mechanism of dispersal.<sup>8,10,13</sup>

*F*-alkyl anions can be indirectly transported by gaseous alcohol (PFOH) and sulfonamide (PFSN) precursors.<sup>14</sup> However, *F*-alkyl surfactant anions can also be aerosolized.<sup>8,10,15-16</sup> There is conclusive evidence that aerosols produced from the ocean's uppermost microlayer are highly enriched in ionic and non-ionic amphiphiles, carrying them far afield over continental masses.<sup>16-29</sup> Fine aerosol particles may be transported over  $10^2$ – $10^3$  km without settling.<sup>30</sup> The recently reported spatial and depth concentration profiles of several *F*-alkyl anions in the world's oceans, particularly in the Labrador Sea and the Middle Atlantic Ocean,<sup>7</sup> together with regional atmospheric and oceanic circulation patterns,<sup>31-39</sup> could provide key data to test whether the aerosolization of marine *F*-alkyl anions is a key stage in their global dispersal.<sup>8,13,40-41</sup>

Partition coefficients of *F*-alkyl acids between *n*-octanol and water have been estimated empirically and theoretically without experimental validation.<sup>42</sup> Until very recently,<sup>43</sup> no information was available on the partitioning of their hydrophobic

anions between water and organic solvents, although it had been reported that perfluorooctyl oxoanions could be extracted from biological matrices into methyl *tert*-butyl ether as tetrabutylammonium salts for subsequent mass spectrometric detection.<sup>44-45</sup> Selective partition of the perfluorooctyl species versus chloride from water into lipophilic polymer membranes or fluoruous solvents had been previously demonstrated by potentiometry.<sup>46</sup>

We have recently investigated the fractionation of globular anions at the air/water interface using a novel approach in which relative interfacial anion concentrations in microdroplets produced by pneumatic nebulization of multicomponent solutions are simultaneously measured by online thermospray ionization mass spectrometry.<sup>17,47-48</sup> Here we report the dynamic enrichment factors of various *F*-alkyl anions at the air/water interface, and analyze their physicochemical and environmental implications.

### 4. 3 Experimental Section

Sodium acetate (EM Science 99%), CF<sub>3</sub>COOH (Aldrich 99%), CH<sub>3</sub>SO<sub>3</sub>Na and CF<sub>3</sub>SO<sub>3</sub>Na (Aldrich 98%), NaCl, NaBr, NaI, NaNO<sub>3</sub>, NaClO<sub>4</sub> and NaSCN (> 98%, Aldrich), sodium dodecylsulfate (SDS, Baker), 1-octanol (Aldrich), potassium *F*-butane-1-sulfonate (4-PFSK 98%, Aldrich), potassium *F*-hexane-1-sulfonate (6-PFSO<sub>3</sub>K 98%, Fluka), potassium *F*-octane-1-sulfonate (8-PFSO<sub>3</sub>K 98%, Fluka), *F*-butyric acid (3-PFCO<sub>2</sub>H, 98%, Aldrich), *F*-pentanoic acid (4-PFCO<sub>2</sub>H, 97%, Aldrich), *F*-hexanoic acid (5-PFCO<sub>2</sub>H, 97%, Fluka), *F*-heptanoic acid (6-PFCO<sub>2</sub>H, 99%, Aldrich), *F*-octanoic acid (7-PFCO<sub>2</sub>H, 97%, Aldrich), and *F*-nonanoic acid (8-PFCO<sub>2</sub>H, 97%, Aldrich), were used as received. Individual stock solutions (1 mM) were prepared with Milli-Q water (resistivity 18.2 MΩ cm) in borosilicate bottles.

Negative ion mass spectra of multicomponent aqueous solutions (1 μM in each surfactant unless otherwise indicated) were obtained via direct infusion into a

commercial thermospray ionization mass spectrometer (ESI-MS, HP-1100 MSD) operated under the following conditions: drying gas flow, 10 L min<sup>-1</sup>; drying gas temperature, 340 °C; nebulizer pressure, 28 psi; collector capillary voltage, 3.5 kV; fragmentor voltage, 80 V. Solutions were pumped (50 μL/min) into the spraying chamber of the mass spectrometer through a *grounded* stainless steel needle inserted in a coaxial sheath issuing nebulizer N<sub>2</sub> gas. The high velocity nebulizer gas breaks up the liquid jet into a conical mist of microdroplets carrying net charges of either sign.<sup>49-53</sup> Pneumatic nebulization generates weakly negatively charged microdroplets.<sup>49</sup> Fast solvent evaporation leads to droplet shrinkage and concomitant surface charge crowding.<sup>54</sup> Droplets become mechanically unstable when electrostatic repulsion among charges overcomes liquid cohesion, and spontaneously shed their interfacial films into even smaller droplets. A series of these events ultimately leads to nanodroplets from which unsolvated ions are electrostatically ejected into the gas phase.<sup>55-59</sup> Gas-phase ions are then deflected into the mass spectrometer by applying a suitable electric bias to its inlet port orthogonal to the injector. It has been shown that surfactant species tend to accumulate in the periphery of the conical mist,<sup>60</sup> i.e., precisely in the finer microdroplets sampled by the orthogonal port.<sup>47</sup> This technique therefore probes the composition of nanodroplets created from the interfacial layers of the microdroplets produced by pneumatic nebulization of test solutions.

Mass spectra were acquired in single ion mode preset at  $m/z = [149 + (n - 1) 50]$  for  $F(CF_2)_nSO_3^-$ , at  $[69 + (n - 1) 50]$  and  $[113 + (n - 1) 50]$  for  $F(CF_2)_nCO_2^-$ , 58 and 60 (<sup>32,34</sup>SCN<sup>-</sup>), 62 (NO<sub>3</sub><sup>-</sup>), 79 and 81 (<sup>79,81</sup>Br<sup>-</sup>), 99 and 101 (<sup>35,37</sup>ClO<sub>4</sub><sup>-</sup>), 127 (I<sup>-</sup>), and 265 (SDS). MS signal intensities for the various *F*-alkyl anions were found to increase linearly with the concentration of their solutions in the range 0.1 to 5 μM, relative to the  $m/z = 265$  signal of 0.2 μM SDS used as a reference (Figure 4.1). Repeatability

and reproducibility of the derived enrichment factors  $f$  (see below), expressed as % RSD, were better than 2.5% and 4%, respectively. Reported data are the average of at least duplicate runs.

#### 4.4 Results and Discussion

Under present instrumental settings,  $F(CF_2)_nSO_3^-$  are detected as molecular monoanions (M) at  $[149 + (n - 1) 50]$  Da, whereas  $F(CF_2)_nCO_2^-$  decarboxylate significantly and appear both at  $[113 + (n - 1) 50]$  Da (M) and  $[69 + (n - 1) 50]$  Da (M -  $CO_2$ ). The relative enrichment factor of anion  $i$ ,  $f(i)$ , is defined herein as the sum of the mass spectral signal intensities of the  $j$  ions originating from this species:  $\sum S_{i,j}$ , divided by those for  $^{79,81}Br^-$ , the least-enriched anion of the set, measured (or extrapolated) at the same bulk molar concentration:

$$f(i) = \frac{\sum_j S_{i,j}}{S_{79} + S_{81}} \quad (4.1)$$

The  $f[F(CF_2)_nSO_3^-]$ s and  $f[F(CF_2)_nCO_2^-]$ s calculated using equation (4.1) and the data from Figure 4.2 and Table 4.1 are shown in Figure 4.3.  $f(i) > f_{Br^-} \equiv 1$  signifies that the  $i$ -anion is enriched relative to  $Br^-$  at the air/water interfacial layers monitored in these experiments. It should be emphasized that  $f$ s are lower bounds to absolute enrichment factors because  $Br^-$  itself is slightly enriched relative to  $Cl^-$ , which has been shown to be nearly neutral toward interfacial enrichment.<sup>61-62</sup> Since  $f(i)$  were determined at, or scaled to 1  $\mu$ M in all cases, they are proportional to the partition coefficient between bulk water ( $B$ ) and its aerial interface ( $S$ ):<sup>63</sup>

$$f(i) \propto K_i = \frac{x_i^S}{x_i^B} \quad (4.2)$$

$$\log f(i) \propto -\frac{\Delta G_{B \rightarrow S}^o(i)}{4.6kT} \quad (4.3)$$

where  $x_i^P$  represents the molar fraction of  $i$  in phase  $P$ , and  $\Delta G^\circ_{B \rightarrow S}$  the molar free energy released upon transferring  $i$  from the bulk to the air/water interface.

Figure 4.3 shows that  $f_s$  for carboxylates are most sensitive to alkyl chain length between  $n = 1$  and 3 and appear to plateau beyond  $n = 9$ . It is apparent that both  $F(CF_2)_nSO_3^-$  and  $F(CF_2)_nCO_2^-$  are highly enriched at the interface, with  $f[F(CF_2)_nSO_3^-] \sim 2.3 f[F(CF_2)_nCO_2^-] \sim 190 f(Br^-)$  as  $n \rightarrow \infty$  (Figure 4.3). Figure 4.4 shows that the addition of 100  $\mu M$  electrolyte tends to depress  $f_s$  for the shorter, least-enriched homologues and enhance those for higher members of both carboxylate and sulfonate classes. A similar trend is observed upon saturation with 1-octanol. These phenomena are consistent with the competition of various solutes for the air/water interface. Simple anions at 100  $\mu M$  will crowd the interface in competition with surfactant anions at 1  $\mu M$ . Short  $F$ -alkyl chain surfactant anions will be rejected, whereas the longer homologues will be expelled from the interface by electrostatic forces.

We have previously shown that  $f_s$  for globular anions at air/liquid interfaces increase exponentially with ionic radius  $R$ .<sup>48</sup> Hydrated ions have a smaller dielectric constant than water and will be expelled to the interface by many-body electrodynamic dispersive interactions that scale with  $R$ .<sup>48,64-65</sup> Since the sulfonate headgroup is larger than the carboxylate,  $f[F(CF_2)_nSO_3^-]$ s are predictably larger than  $f[F(CF_2)_nCO_2^-]$ s (Figure 4.3, Table 4.1). This result is consistent with previous observations that the alkyl sulfonates with a larger ionic radius is more lipophilic than the corresponding carboxylate at water/1,2-dichloroethane or nitrobenzene interfaces.<sup>46</sup> Perfluorination enhances anion partitioning to the aerial interface, viz.:  $f(CF_3SO_3^-)/f(CH_3SO_3^-) = 2.7$ ,  $f(CF_3COO^-)/f(CH_3COO^-) = 3.0$  (see Table 4.1).<sup>66</sup>

From equations (4.2)-(4.4), enrichment factors of  $F$ -alkyl surfactants  $f$  should increase exponentially with  $n$ .<sup>63</sup>

$$\Delta G_{B \rightarrow S}^o[\text{F}(\text{CF}_2)_n \text{CO}_2^-] = \Delta G_P^o + n \Delta G_{B \rightarrow S}^o(\text{CF}_2) \quad (4.4)$$

if the  $\Delta G_{B \rightarrow S}^o(\text{CF}_2) = \Delta G_{B \rightarrow \text{AIR}}^o(\text{CF}_2) + \Delta G_{\text{AIR} \rightarrow S}^o(\text{CF}_2) = -2.74 - 2.32 = -5.06 \text{ kJ mol}^{-1}$ <sup>67-68</sup> group contribution to the molar free energy of  $B \rightarrow S$  transfer were independent of  $n$ .  $\Delta G_P^o$  is the contribution of the headgroup plus the difference between the  $\text{CF}_3$ - and  $\text{CF}_2$ -group contributions. Note that both  $\Delta G_{B \rightarrow S}^o(\text{CF}_2)$  and  $\Delta G_{\text{AIR} \rightarrow S}^o(\text{CF}_2)$  are negative, meaning that the location of lowest free energy for  $\text{CF}_2$  groups is the interface. Since linear  $\log f$  vs.  $n$  dependences have been verified for most surfactant classes,<sup>63</sup> enrichment factors for  $F$ -alkyl surfactant homologues were expected to increase as  $f[\text{F}(\text{CF}_2)_n \text{CO}_2^-]/f[\text{F}(\text{CF}_2)_{n-1} \text{CO}_2^-] = \exp[-\Delta G_{B \rightarrow S}^o(\text{CF}_2)/2kT] = 2.7$  at 300 K. Figures 4.2 and 4.3, and Table 4.1 show that this is not the case. Neither  $\log f$  increases linearly with  $n$ , nor  $f[\text{F}(\text{CF}_2)_8 \text{CO}_2^-]/f[\text{F}(\text{CF}_3) \text{CO}_2^-]$  exceeds  $\sim 28$  (vs.  $2.7^7 \sim 1244$ ). Instead, we find that  $\log f[\text{F}(\text{CF}_2)_n \text{CO}_2^-]$  increases as predicted up to  $n \sim 3$ , and considerably less so afterward (Figure 4.3). The experimental  $f[\text{F}(\text{CF}_2)_n \text{CO}_2^-]/f[\text{F}(\text{CF}_2)_{n-1} \text{CO}_2^-] \sim 1.16$  (vs. 2.7) in the range  $3 \leq n \leq 8$  effectively corresponds to  $\Delta G_{B \rightarrow S}^o(\text{CF}_2) = -0.74 \text{ kJ mol}^{-1}$  (vs.  $-5.06 \text{ kJ mol}^{-1}$ ). Since  $f(\text{PF}_6^-)$ , which has a similar value to  $f[\text{F}(\text{CF}_2)_8 \text{SO}_3^-]$ , adhered to the linear  $\log f$  vs.  $R$  correlation followed by smaller anions,<sup>47-48</sup> we infer that non-linearity is not due to dynamic range limitations and less-than-linear instrumental response but likely reflects molecular properties of the  $F$ -alkyl chain. It is also possible, given the dynamic nature of our experiments, that the microdroplets surfaces we probe here might not be fully equilibrated with these highly surface-active species. However, since a similar limitation is expected to apply to  $F$ -alkyl oxoanion surfactant partitioning during bubble bursting events,<sup>34,35</sup> we believe that our results are particularly relevant to surfactant enrichment in aerosols of marine origin.

In this context, the rather sharp inflection in the  $\log f[\text{F}(\text{CF}_2)_n\text{CO}_2^-]$  vs.  $n$  plot (Figure 4.3) amounts to a  $4.32 \text{ kJ mol}^{-1}$  increase of the net  $\Delta G_{B \rightarrow S}^0(\text{CF}_2)$  contribution beyond  $n \sim 3$ . Since  $\Delta G_{AIR \rightarrow S}^0(\text{CF}_2) = -2.32 \text{ kJ mol}^{-1}$ <sup>67</sup> thermodynamics dictates that *F*-alkyl chains should tend to lie flat on the water surface.<sup>69</sup> Scheme 4.1 shows that the (most stable in an isotropic and homogeneous medium) *anti*  $\text{F}(\text{CF}_2)_3\text{CO}_2^-$  rotamer at the air/water interface is unable to maximize the attractive dispersive interactions of *F*-alkyl chains with the water surface, a restriction that is relaxed by a  $\pm 90^\circ$  torsion about the  $\text{C}_2\text{-C}_3$  bond. It is apparent that only the *syn* rotamer can keep the headgroup immersed and the *F*-alkyl chain bent over the water surface.

A recent report suggests that the higher lipophilicity of *F*-alkyl oxoanions relative to their alkyl counterparts is actually due to the electron-withdrawing effect of the *F*-alkyl chain on the headgroup,<sup>43</sup> because the insertion of a  $(\text{CH}_2)_2$  spacer between a perfluorohexyl chain and the  $-\text{CO}_2\text{H}$  group increases the  $\text{pK}_a$  of the latter by 2.32 units, and reduces about 400 times the lipophilicity of the corresponding nonanoate. We wish to point out that both outcomes could not be physically correlated were interfacial partitioning actually involved. Distance effects on electron withdrawal from oxoanion headgroups by  $\text{CF}_2$  moieties would be probably responsible for changes in acidity, whereas the large concomitant reduction of lipophilicity could be due to the loss of the dominant  $\text{C}(2)\text{F}_2$  and  $\text{C}(3)\text{F}_2$  hydrophobic contributions to interfacial partitioning.

Positive fractionation to the air/water interface underlies surfactant enrichment in the microdroplets probed in our experiments, as well as in the aerosol droplets produced via bubble bursting over the oceans.<sup>24</sup> Because microdroplets are electrically charged, in our experiments as well as in the atmospheric aerosol,<sup>17,70</sup> solvent evaporation may induce further fragmentation into progeny droplets. A

cascade of these events is equivalent to a distillation process in which solute enrichment is multiplicatively amplified at each stage, i.e., the net fractionation after  $m$  stages will be given by  $f_m = (f_1)^m$ . The implication is that the most enriched marine aerosol droplets will be the finest, i.e., those whose settling velocity is lowest,<sup>71</sup> have the longest atmospheric lifetimes and can, therefore, be transported farther and at higher altitudes.<sup>23,72</sup> The bioaccumulation rates of  $F$ -alkyl oxoanions in water- or air-breathing animals, including humans, depends on their partitioning from lipids to water or air interfaces, respectively.<sup>73</sup> Our results, in conjunction with Jing et. al., data,<sup>43</sup> show that aqueous perfluorosurfactant oxoanions may have similar affinities for 1-octanol and air interfaces. Further work is underway.

#### 4.5 Acknowledgments

This project was financially supported by the National Science Foundation (ATM-0534990). E. P. is grateful to the Fullbright Foundation for financial support.

#### 4.6 References

- (1) Houde, M.; Martin, J. W.; Letcher, R. J.; Solomon, K. R.; Muir, D. C. G. *Environ. Sci. Technol.* **2006**, *40*, 3463.
- (2) Shoeib, M.; Harner, T.; Vlahos, P. *Environ. Sci. Technol.* **2006**, *40*, 7577.
- (3) Giesy, J. P.; Kannan, K. *Environ. Sci. Technol.* **2001**, *35*, 1339.
- (4) Giesy, J. P.; Kannan, K. *Environ. Sci. Technol.* **2001**, *35*, 1339.
- (5) Goss, K. U. *Environ. Sci. Technol.* **2008**, *42*, 456.
- (6) Wania, F. *Environ. Sci. Technol.* **2007**, *41*, 4529.
- (7) Yamashita, N.; Taniyasu, S.; Petrick, G.; Wei, S.; Gamo, T.; Lam, P. K. S.; Kannan, K. *Chemosphere* **2008**, *70*, 1247.

- (8) Young, C. J.; Furdui, V. I.; Franklin, J.; Koerner, R. M.; Muir, D. C. G.; Mabury, S. A. *Environ. Sci. Technol.* **2007**, *41*, 3455.
- (9) Simcik, M. F. *J. Environ. Monit.* **2005**, *7*, 759.
- (10) Armitage, J.; Cousins, I. T.; Buck, R. C.; Prevedouros, K.; Russell, M. H.; MacLeod, M.; Korzeniowski, S. H. *Environ. Sci. Technol.* **2006**, *40*, 6969.
- (11) Olsen, G. W.; Mair, D. C.; Church, T. R.; Ellefson, M. E.; Reagen, W. K.; Boyd, T. M.; Herron, R. M.; Medhdizadehkashi, Z.; Nobilett, J. B.; Rios, J. A.; Butenhoff, J. L.; Zobel, L. R. *Environ. Sci. Technol.* **2008**, *42*, 4989.
- (12) Renner, R. *Environ. Sci. Technol.* **2008**, *42*, 4618.
- (13) Powley, C. R.; George, S. W.; Russell, M. H.; Hoke, R. A.; Buck, R. C. *Chemosphere* **2008**, *70*, 664.
- (14) Schenker, U.; Scheringer, M.; Macleod, M.; Martin, J. W.; Cousins, I. T.; Hungerbuhlert, K. *Environ. Sci. Technol.* **2008**, *42*, 3710.
- (15) Prevedouros, K.; Cousins, I. T.; Buck, R. C.; Korzeniowski, S. H. *Environ. Sci. Technol.* **2006**, *40*, 32.
- (16) McMurdo, C. J.; Ellis, D. A.; Webster, E.; Butler, J.; Christensen, R. D.; Reid, L. K. *Environ. Sci. Technol.* **2008**, *42*, 3969.
- (17) Enami, S.; Vecitis, C. D.; Cheng, J.; Hoffmann, M. R.; Colussi, A. J. *J. Phys. Chem. A* **2007**, *111*, 8749.
- (18) Liss, P. S.; Duce, R. A. *The Sea Surface and Global Change*; Cambridge University Press: Cambridge, UK, 1997.
- (19) Duce, R. A.; Hoffman, E. J. *Ann. Rev. Earth Planet. Sci.* **1976**, *4*, 187.
- (20) Rontu, N.; Vaida, V. *J. Phys. Chem. C* **2007**, *111*, 11612.
- (21) Calace, N.; Petronio, B. M.; Cini, R.; Stortini, A. M.; Pampaloni, B.; Udisti, R. *Internat. J. Environ. Anal. Chem.* **2001**, *79*, 331.

- (22) Desideri, P. G.; Lepri, L.; Udisti, R.; Checchini, L.; Del Bubba, M.; Cini, R.; Stortini, A. M. *Int. J. Environ. Anal. Chem.* **1998**, *71*, 331.
- (23) Oppo, C.; Bellandi, S.; Degli Innocenti, N.; Stortini, A. M.; Loglio, G.; Schiavuta, E.; Cini, R. *Mar. Chem.* **1999**, *63*, 235.
- (24) Blanchard, D. C. *Science* **1964**, *146*, 396.
- (25) Macintyre, F. *J. Phys. Chem.* **1968**, *72*, 589.
- (26) Macintyre, F. *Tellus* **1970**, *22*, 451.
- (27) Donaldson, D. J.; Vaida, V. *Chem. Rev.* **2006**, *106*, 1445.
- (28) Cavalli, F.; Facchini, M. C.; Decesari, S.; Mircea, M.; Emblico, L.; Fuzzi, S.; Ceburnis, D.; Yoon, Y. J.; O'Dowd, C. D.; Putaud, J. P.; Dell'Acqua, A. J. *Geophys. Res. –Atmospheres* **2004**, *109*, D24215.
- (29) Latif, M. T.; Brimblecombe, P. *Environ. Sci. Technol.* **2004**, *38*, 6501.
- (30) Seinfeld, J. H.; Pandis, S. N. *Atmospheric chemistry and physics : from air pollution to climate change*, 2nd ed.; Wiley: Hoboken, N.J. , 2006.
- (31) Hutterli, M. A.; Crueger, T.; Fischer, H.; Andersen, K. K.; Raible, C. C.; Stocker, T. F.; Siggaard-Andersen, M. L.; McConnell, J. R.; Bales, R. C.; Burkhart, J. F. *Clim. Dyn.* **2007**, *28*, 635.
- (32) Eckhardt, S.; Stohl, A.; Beirle, S.; Spichtinger, N.; James, P.; Forster, C.; Junker, C.; Wagner, T.; Platt, U.; Jennings, S. G. *Atmos. Chem. Phys.* **2003**, *3*, 1769.
- (33) Hameed, S.; Piontkovski, S. *Geophys. Res. Lett.* **2004**, *31*, L09303.
- (34) Francis, J. A.; Hunter, E.; Zou, C. Z. *J. Climate* **2005**, *18*, 2270.
- (35) Barreiro, M.; Fedorov, A.; Pacanowski, R.; Philander, S. G. *Annu. Rev. Earth Planet. Sci.* **2008**, *36*, 33.

- (36) Kieke, D.; Rhein, M.; Stramma, L.; Smethie, W. M.; Bullister, J. L.; LeBel, D. A. *Geophys. Res. Lett.* **2007**, *34*, L06605.
- (37) Dickson, B.; Yashayaev, I.; Meincke, J.; Turrell, B.; Dye, S.; Holfort, J. *Nature* **2002**, *416*, 832.
- (38) Curry, R.; Mauritzen, C. *Science* **2005**, *308*, 1772.
- (39) Peterson, B. J.; McClelland, J.; Curry, R.; Holmes, R. M.; Walsh, J. E.; Aagaard, K. *Science* **2006**, *313*, 1061.
- (40) Dietz, R.; Bossi, R.; Riget, F. F.; Sonne, C.; Born, E. W. *Environ. Sci. Technol.* **2008**, *42*, 2701.
- (41) Smithwick, M.; Norstrom, R. J.; Mabury, S. A.; Solomon, K.; Evans, T. J.; Stirling, I.; Taylor, M. K.; Muir, D. C. G. *Environ. Sci. Technol.* **2006**, *40*, 1139.
- (42) Arp, H. P. H.; Niederer, C.; Goss, K. U. *Environ. Sci. Technol.* **2006**, *40*, 7298.
- (43) Jing, P.; Rodgers, P. J.; Amemiya, S. *J. Am. Chem. Soc.* **2009**, *131*, 2290.
- (44) Hansen, K. J.; Clemen, L. A.; Ellefson, M. E.; Johnson, H. O. *Environ. Sci. Technol.* **2001**, *35*, 766.
- (45) Kannan, K.; Koistinen, J.; Beckmen, K.; Evans, T.; Gorzelany, J. F.; Hansen, K. J.; Jones, P. D.; Helle, E.; Nyman, M.; Giesy, J. P. *Environ. Sci. Technol.* **2001**, *35*, 1593.
- (46) Kihara, S.; Suzuki, M.; Sugiyama, M.; Matsui, M. *J. Electroanal. Chem.* **1988**, *249*, 109.
- (47) Cheng, J.; Vecitis, C.; Hoffmann, M. R.; Colussi, A. J. *J. Phys. Chem. B* **2006**, *110*, 25598.
- (48) Cheng, J.; Hoffmann, M. R.; Colussi, A. J. *J. Phys. Chem. B* **2008**, *112*.

- (49) Zilch, L. W.; Maze, J. T.; Smith, J. W.; Ewing, G. E.; Jarrold, M. F. *J. Phys. Chem. A* **2008**, *112*, 13352.
- (50) Dodd, E. E. *J. Appl. Phys.* **1953**, *24*, 73.
- (51) Manisali, I.; Chen, D. D. Y.; Schneider, B. B. *Trends Anal. Chem.* **2006**, *25*, 243.
- (52) Hirabayashi, A.; Sakairi, M.; Koizumi, H. *Anal. Chem* **1994**, *66*, 4557.
- (53) Van Berkel, G. J.; Pasilis, S. P.; Ovchinnikova, O. *J. Mass Spectrom.* **2008**, *43*, 1161.
- (54) Kebarle, P.; Peschke, M. *Anal. Chim. Acta* **2000**, *406*, 11.
- (55) Iribarne, J. V.; Dziedzic, P. J.; Thomson, B. A. *Int. J. Mass Spectrom. Ion Process.* **1983**, *50*, 331.
- (56) Hirabayashi, A.; Sakairi, M.; Koizumi, H. *Anal. Chem* **1995**, *67*, 2878.
- (57) Pol, J.; Kauppila, T. J.; Haapala, M.; Saarela, V.; Franssila, S.; Ketola, R. A.; Kotiaho, T.; Kostiainen, R. *Anal. Chem.* **2007**, *79*, 3519.
- (58) Nguyen, S.; Fenn, J. B. *Proc. Natl. Acad. Sci. U.S.A.* **2007**, *104*, 1111.
- (59) Yamashita, M.; Fenn, J. B. *J. Phys. Chem.* **1984**, *88*, 4671.
- (60) Tang, K.; Smith, R. D. *J. Am. Soc. Mass Spectrom.* **2001**, *12*, 343.
- (61) Pegram, L. M.; Record, M. T., Jr. *Proc. Natl. Acad. Sci. U.S.A.* **2006**, *103*, 14278.
- (62) Pegram, L. M.; Record, M. T., Jr. *J. Phys. Chem. B* **2007**, *111*, 5411.
- (63) Fainerman, V. B.; Miller, R.; Mohwald, H. *J. Phys. Chem. B* **2002**, *106*, 809.
- (64) Israelachvili, J. *Intermolecular & Surface Forces*, 2nd ed.; Academic Press: London, 1992.
- (65) Parsegian, V. A. *Van der Waals Forces*; Cambridge University Press: New York, 2006.

- (66) Shinoda, K.; Hato, M.; Hayashi, T. *J. Phys. Chem.* **1972**, *76*, 909.
- (67) Goss, K. U.; Bronner, G. *J. Phys. Chem. A* **2006**, *110*, 9518.
- (68) Goss, K. U.; Bronner, G. *J. Phys. Chem. A* **2006**, *110*, 14054.
- (69) Tyrode, E.; Johnson, C. M.; Rutland, M. W.; Day, J. P. R.; Bain, C. D. *J. Phys. Chem. C* **2007**, *111*, 316.
- (70) Reiter, R. *J. Geophys. Res.* **1994**, *99*, 10807.
- (71) Finlayson-Pitts, B. J.; Pitts, J. N. *Chemistry of the Upper and Lower Atmosphere*; Academic Press: San Diego, CA, 2000.
- (72) Cincinelli, A.; Stortini, A. M.; Checchini, L.; Martellini, T.; Del Bubba, M.; Lepri, L. *J. Environ. Monit.* **2005**, *7*, 1305.
- (73) Kelly, B. C.; Ikonomou, M. G.; Blair, J. D.; Morin, A. E.; Gobas, F. *Science* **2007**, *317*, 236.

Table 4.1. Relative anion enrichment factors  $f$  at the air/water interface

Anion	$f$
CH <sub>3</sub> COO <sup>-</sup>	0.95
<sup>79,81</sup> Br <sup>-</sup>	1.00
<sup>32,34</sup> SCN <sup>-</sup>	2.08
I <sup>-</sup>	2.61
NO <sub>3</sub> <sup>-</sup>	2.65
CF <sub>3</sub> COO <sup>-</sup>	2.86
CH <sub>3</sub> SO <sub>3</sub> <sup>-</sup>	6.65
<sup>35,37</sup> ClO <sub>4</sub> <sup>-</sup>	13.4
F(CF <sub>2</sub> ) <sub>2</sub> COO <sup>-</sup>	22.4
F(CF <sub>2</sub> ) <sub>4</sub> COO <sup>-</sup>	36.1
CF <sub>3</sub> SO <sub>3</sub> <sup>-</sup>	37.9
H(CH <sub>2</sub> ) <sub>12</sub> OSO <sub>3</sub> <sup>-</sup>	42.8
F(CF <sub>2</sub> ) <sub>5</sub> COO <sup>-</sup>	45.0
F(CF <sub>2</sub> ) <sub>3</sub> COO <sup>-</sup>	46.3
F(CF <sub>2</sub> ) <sub>6</sub> COO <sup>-</sup>	55.9
F(CF <sub>2</sub> ) <sub>7</sub> COO <sup>-</sup>	77.9
F(CF <sub>2</sub> ) <sub>8</sub> COO <sup>-</sup>	79.6
F(CF <sub>2</sub> ) <sub>4</sub> SO <sub>3</sub> <sup>-</sup>	133.8
F(CF <sub>2</sub> ) <sub>6</sub> SO <sub>3</sub> <sup>-</sup>	175.2
F(CF <sub>2</sub> ) <sub>8</sub> SO <sub>3</sub> <sup>-</sup>	182.7

Figure 4.1. Ratio of  $F(CF_2)_nSO_3^-/DS^-$  signal intensities in mass spectra of aqueous  $[F(CF_2)_nSO_3^- + 0.2 \mu\text{M dodecyl sulfate}]$  solutions at pH 6.0 as functions of  $F$ -surfactant concentration. Lines are linear regressions to the experimental data ( $R^2 > 0.99$ ). Linear plots were also obtained for  $F(CF_2)_nCO_2^-$ . Error bars contained within symbol size.

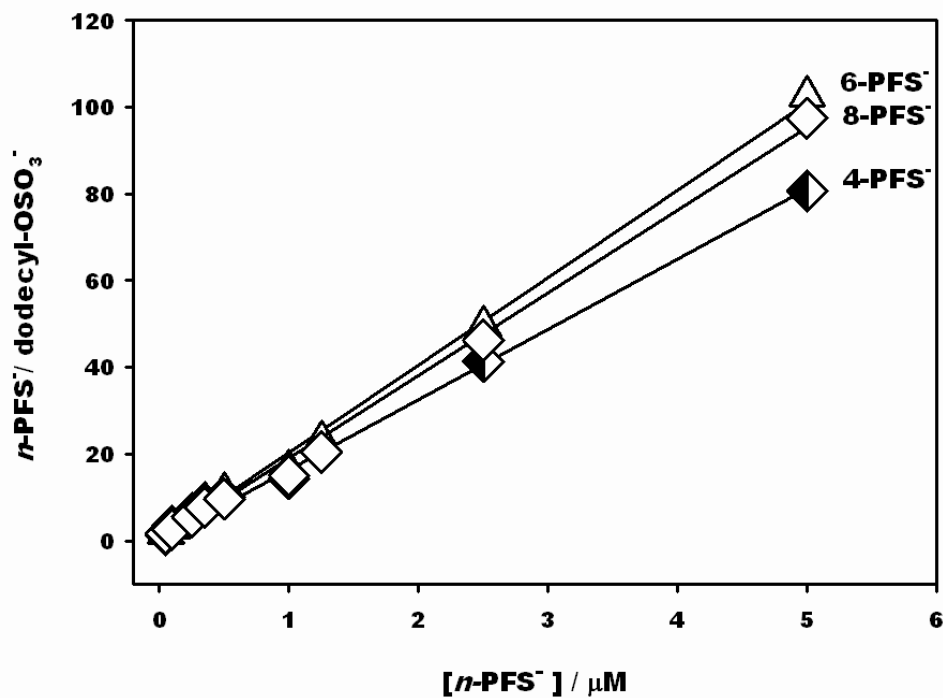


Figure 4.2 Electrospray ionization mass spectrum of a 1  $\mu\text{M}$  equimolar multianion aqueous solution at pH 7. Signal intensities  $S$  normalized to  $(S_{79} + S_{81}) \equiv 1$  (see text for details). The inset is a semilogarithmic plot. Blue and red drop lines and legends correspond to  $\text{F}(\text{CF}_2)_n\text{CO}_2^-$  and  $\text{F}(\text{CF}_2)_n\text{SO}_3^-$  surfactants, respectively. DS is dodecyl sulfate.

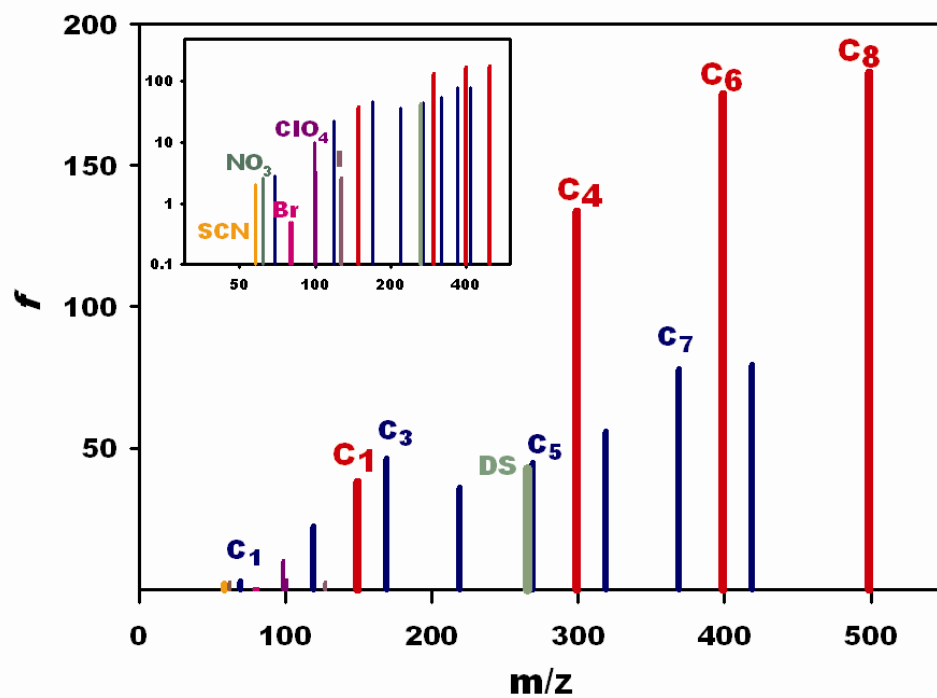


Figure 4.3. Enrichment factors  $f$  versus  $n$ -alkyl chain length. Gray-red symbols:  $f[\text{F}(\text{CF}_2)_n\text{SO}_3^-]$ . Gray-blue symbols (connected by straight lines; diamonds/circles stand for odd/even  $n$ -homologues):  $f[\text{F}(\text{CF}_2)_n\text{CO}_2^-]$ . All data obtained in  $1\ \mu\text{M}$  solutions.  $S_{\text{th}}$  designates the theoretical  $\log f$  vs.  $n$  slope predicted by equation (4.2) – (4.4) and data from References 67 and 68. Error bars contained within symbol size.

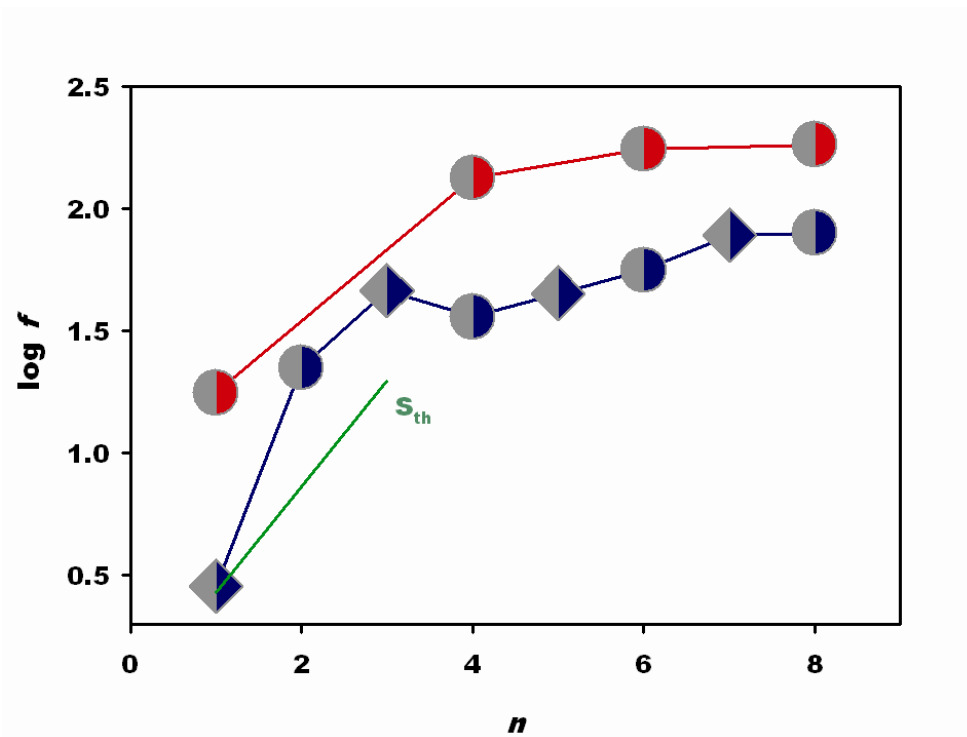
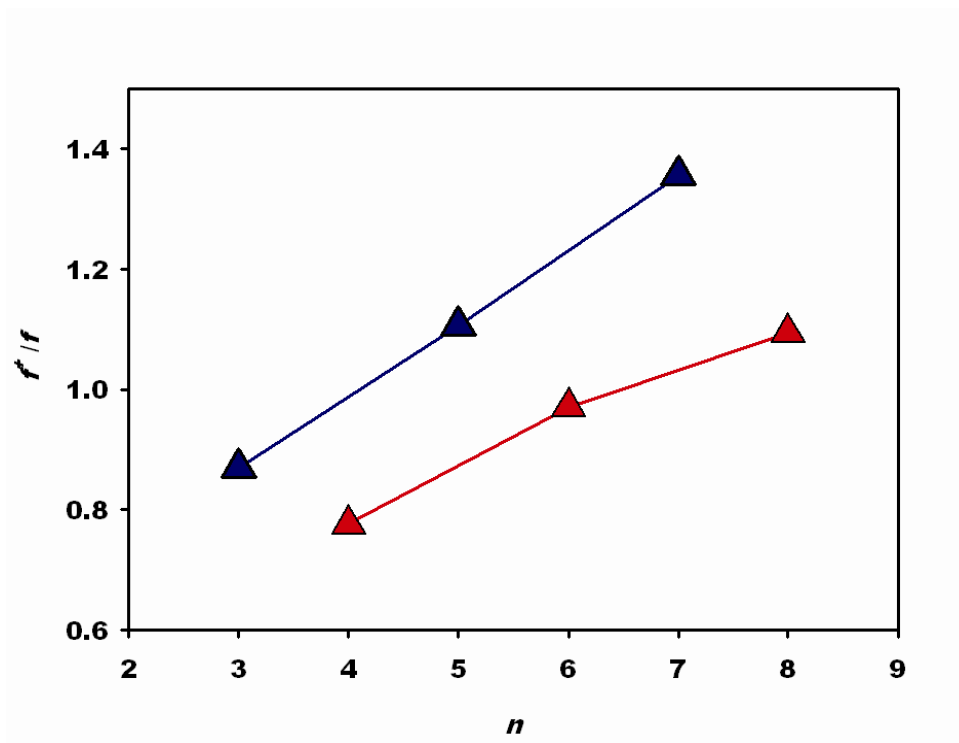
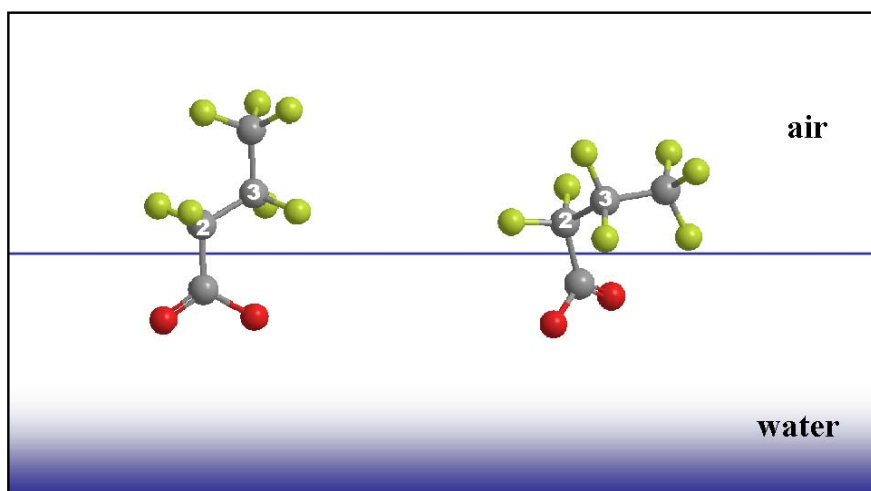


Figure 4.4. Enrichment factors ratios  $f^+/f$  for  $F(\text{CF}_2)_n\text{SO}_3^-$  (red) and  $F(\text{CF}_2)_n\text{CO}_2^-$  (blue) surfactants.  $f$ : in 1  $\mu\text{M}$  aqueous  $F$ -surfactant solutions,  $f^+$ : plus 100  $\mu\text{M}$  NaCl and 1-octanol saturation. Error bars contained within symbol size.



Scheme 4.1. *Anti*-perfluorobutanoate (left) and *gauche*-perfluorobutanoate (right) at the air/water interface. A closer approach of fluorine atoms to the water surface minimizes the free energy of the system.<sup>48,64,67</sup>



## Chapter 5

### Acid Dissociation versus Molecular Association of Perfluoroalkyl Oxoacids: Environmental Implications\*

---

\* This chapter is reproduced with permission from J. Cheng, E. Psillakis, M. R. Hoffmann, and A. J. Colussi, *Journal of Physical Chemistry A*, **2009**, 113, 8152. Copyright © 2009, American Chemical Society

## 5.1 Abstract

Perfluorooctanoate (PFO) and perfluorooctanesulfonate (PFOS) surfactant anions, once released, may rapidly reach remote regions. This phenomenon is puzzling because the water-bound anions of strong *F*-alkyl acids should be largely transported by slow oceanic currents. Herein we investigate whether these hydrophobic *F*-alkyl oxoanions would behave anomalously under environmental conditions, as suggested elsewhere. Negative electrospray ionization mass spectra of micromolar aqueous PFO or PFOS solutions from pH 1.0 to 6.0 show: (1)  $m/z = 499$  (PFOS) signals that are independent of pH, (2)  $m/z = 413$  (PFO) and  $369$  (PFO – CO<sub>2</sub>) signals plus  $m/z = 213$  (C<sub>3</sub>F<sub>7</sub>CO<sub>2</sub><sup>-</sup>) and  $169$  (C<sub>3</sub>F<sub>7</sub><sup>-</sup>) signals at higher collision energies and, below pH ~ 4,  $m/z = 827$  signals from a remarkably stable (PFO)<sub>2</sub>H<sup>-</sup> cluster that increase with decreasing pH. Since the sum of  $m/z = 369$ ,  $413$ , and  $827$  signal intensities is independent of pH, i.e., effectively encompasses all major species, we infer that  $pK_a(\text{PFOSA}) < 1.0$  and  $pK_a(\text{PFOA}) < 1.0$ . We also derive  $K_2 \leq 4 \times 10^7 \text{ M}^{-2}$  for the clustering equilibrium:  $2 \text{ PFO} + \text{H}^+ \rightleftharpoons (\text{PFO})_2\text{H}$ . Thus, although (PFO)<sub>2</sub>H is held together by an exceptionally strong homonuclear covalent hydrogen bond, neither PFOS nor PFO will associate or protonate significantly at environmentally relevant sub-nanomolar concentrations above pH ~ 1.

## 5. 2 Introduction

Perfluoroalkyl (*F*-alkyl) chemicals (PFCs) began to be produced and commercialized about 50 years ago.<sup>1-3</sup> Exceptional chemical inertness confers on these materials valuable properties but also ensures unwanted environmental persistence.<sup>4,5</sup> As a result, they have spread and bioaccumulated globally with unforeseeable consequences.<sup>5-13</sup> The most conspicuous congeners perfluorooctanoate (PFO) and perfluorooctanesulfonate (PFOS) have been detected in surface waters and precipitation,<sup>14-16</sup> sediments,<sup>17</sup> and biota worldwide.<sup>18-22</sup> *F*-alkyl oxoanions apparently perturb peptide chains and DNA strands conformations via non-covalent, entropy-driven interactions.<sup>9,11,23,24</sup>

The rapid decline of PFOS levels in Canadian Arctic seals following its phaseout in 2000 strongly suggests an atmospheric transport mechanism,<sup>25</sup> and defies the notions that oceans are the ultimate sink, and that slow ocean currents the long-range conduits for these weakly basic *F*-alkyl oxoanions.<sup>26-28</sup> The issue of whether marine aerosols enriched in these anionic surfactants<sup>29,30</sup> or their gas-phase conjugated acids mediate atmospheric transport<sup>31</sup> clearly hinges on the extent of *F*-alkyl oxoacids dissociation under environmental conditions.<sup>32</sup> Their long-range transport can also be indirectly effected, in part, by degradable gas-phase precursors. Although the powerful electron-withdrawing *F*-alkyl chains demonstrably stabilize these anions, viz.,  $\text{pK}_a(\text{CF}_3\text{COOH}) = 0.3$  vs.  $\text{pK}_a(\text{CH}_3\text{COOH}) = 4.8$ ,<sup>33</sup> and more than  $\sim 8$   $\text{CH}_2$ -links are required to insulate functional groups from *F*-alkyl segments,<sup>34</sup> the acidity of PFOA remains elusive. Titrations in water/alcohol solvents yielded  $\text{pK}_a(\text{PFOA}) = 2.8$  and  $3.8$ ,<sup>35,36</sup> whereas SPARC/COSMO models<sup>37</sup> and semiempirical PM6 computations<sup>38</sup> predict  $\text{pK}_a(\text{PFOA}) \leq 0.7$ . The significantly larger than predicted experimental  $\text{pK}_a(\text{PFOA})$  values have been tentatively

ascribed to the aggregation of hydrophobic PFOA (note that PFO aggregation should have the opposite effect) in aqueous solvents at amenable laboratory mM concentrations.<sup>39-41</sup> Herein we address these basic issues<sup>36,42-46</sup> and report experiments on the speciation of the PFOA (perfluorooctanoic acid) and PFOSA (perfluorooctanesulfonic acid, not to be confused with perfluorooctane sulfonamide) in micromolar aqueous solutions as a function of pH via pneumatically assisted electrospray ionization mass spectrometry (ESI-MS).

### 5.3 Experimental Section

PFONH<sub>4</sub> and PFOSK (3M), NaClO<sub>4</sub> (EM Science, >99%), Na-hexanoate and Na-octanoate (Sigma Aldrich, >99%), 3M NaOH and 6M HCl solutions (VWR, Reagent grade) were used as received. Aqueous solutions were prepared with purified water from a Millipore Milli-Q system (18.2 MΩ cm resistivity). Aqueous 1 to 10 μM PFO or PFOS solutions also contained ClO<sub>4</sub><sup>-</sup> [pK<sub>a</sub>(HClO<sub>4</sub>) <-7] at fivefold larger concentrations as internal standard. HCl or NaOH were used to adjust the pH in the range of 1.0 to 6.0 at constant ionic strength, unless otherwise specified. Solutions were directly infused into a HP 1100 MSD ESI-MS operated in the negative ion mode.<sup>47-49</sup> The initial search for anion signals in the 50 ≤ m/z ≤ 2000 range was performed in the scan mode. Signal intensities of m/z = 499 (PFOS), 413 and 369 (PFO, PFO – CO<sub>2</sub>), 99 and 101 (<sup>35</sup>ClO<sub>4</sub><sup>-</sup>, <sup>37</sup>ClO<sub>4</sub><sup>-</sup>), and 827 [(PFO)<sub>2</sub>H] peaks were quantified from mass spectra acquired in the SIM mode under the following conditions: drying gas flow rate = 10 L min<sup>-1</sup>, drying gas temperature = 250 °C, capillary voltage = 3500 V, fragmentor (cone) voltage FV varied from 30 to 150 V.

## 5.4 Results and Discussion

Given the ongoing debate about whether proton activity at the air/water interface, from which the ions detected by ESI-MS arise, is larger or smaller than in bulk solution,<sup>50-54</sup> we deemed it essential to validate our procedures by reproducing the titration curves of *n*-hexanoic and *n*-octanoic acids in this setup (Figure 5.1). Non-linear regressions ( $R^2 = 0.995$ ) through the experimental data based on the universal titration function, equation (5.1):

$$\frac{[A^-]}{[A]_T} = \frac{1}{1 + 10^{pK_a - pH}} \quad (5.1)$$

led to  $pK_a$  (*n*-hexanoic acid) =  $4.81 \pm 0.05$ ,  $pK_a$  (*n*-octanoic acid) =  $4.81 \pm 0.06$  values in excellent agreement with their  $pK_a$  values in bulk solution.<sup>55</sup> This agreement cannot be regarded fortuitous or accidental, and has important implications. Since equation (5.1) can be construed as a function of the difference ( $pK_a - pH$ ) rather than of pH alone, the same data would have been obtained had  $pK_a$  and pH shifted equally at the interface relative to their bulk values.<sup>56</sup> Such coincidental shifts, however, are deemed unlikely because we cannot envision a physical reason that it should be so. More importantly, the observed agreement further implies that the output signal sets generated by our ESI mass spectrometer are linear transfer functions of the ionic composition of the interfacial layers of infused solutions. This is not a trivial observation because the detected ions are field-ejected from nanodroplets produced after extensive solvent evaporation from nascent microdroplets.<sup>57,58</sup> Thus, nascent microdroplets emanating from the aerial interface faithfully reflect its composition, which, as Figure 5.1 shows, is evidently preserved during successive solvent evaporation, microdroplet fragmentation, and ion ejection events. Since charge imbalances must persist in non-interacting microdroplets carrying

anions in excess over cations, anion neutralization is prevented even in concentrated nanodroplets. Elsewhere, we have provided conclusive evidence that: (1) anion composition of the air/water interface may be quite different from that of the bulk,<sup>47,48</sup> and (2) surfactant anion signals are linearly proportional to bulk anion submillimolar concentrations.<sup>29</sup> We infer that the pH of the interfacial layers sampled by our instrument is, on average, identical to that in bulk solution.

Figure 5.2a–c shows ESI-MS ( $50 \leq m/z \leq 1000$ ) of 10  $\mu\text{M}$  PFOS solutions in water at pH 6.5, in 10 mM HCl at pH 2.0 and in 10 mM NaCl at pH 7.0 obtained at  $FV = 70$  V. PFOS only produces the molecular anion at  $m/z = 499$  (PFOS) without evidence of a  $(\text{PFOS})_2\text{H}$  cluster at  $m/z = 999$ . The small signal at  $m/z = 399$  is a perfluorohexanoate impurity. In contrast, ESI-MS of PFO solutions reveal the presence of a major  $(\text{PFO})_2\text{H}$  cluster anion at  $m/z = 827$ , in addition to the anticipated signals at  $m/z = 413$  (PFO), and 369 (PFO –  $\text{CO}_2$ ) (Figure 5.3a–c).<sup>59</sup> The relative intensity of the  $m/z = 828$  [ $^{13}\text{C}_1$ – $(\text{PFO})_2\text{H}$ ] satellite peak confirms that  $m/z = 827$  corresponds to a singly charged  $\text{C}_{16}$  species (Table 5.1). The more extensive collisionally induced secondary dissociation of PFO at  $FV = 150$  V (Figure 5.3d) leads to new signals at  $m/z = 213$  ( $\text{C}_3\text{F}_7\text{CO}_2^-$ ) and 169 ( $\text{C}_3\text{F}_7^-$ ). Note that the  $\text{C}_3\text{F}_7^-$  carbanion is a secondary species produced from  $\text{C}_7\text{F}_{15}^-$  (PFO –  $\text{CO}_2$ ) via a neutral  $\text{C}_4\text{F}_8$  loss,<sup>59</sup> whereas  $\text{C}_3\text{F}_7\text{CO}_2^-$  is a primary species ensuing from PFO by splitting  $\text{C}_4\text{F}_8$ , presumably through a higher energy fragmentation channel. Remarkably, since we can still detect  $m/z = 827$  ion signals under 150 V acceleration potentials, the  $(\text{PFO})_2\text{H}$  cluster is apparently held together by a very strong  $[\text{O}^-\cdots\text{H}-\text{O}^- \leftrightarrow \text{O}^-\cdots\text{H}-\text{O}]$  homonuclear, three-center four-electron covalent hydrogen bond whose resonant forms are rigorously equivalent (Scheme 5.1).<sup>60,61</sup> This bond is a much stronger

version of those observed among most carboxylate-carboxylic acid dimers.<sup>62,63</sup> The detection of (PFO)<sub>2</sub>H signals in HCl, but not in NaCl solutions of identical ionic strength, and the absence of a (PFOS)<sub>2</sub>H cluster in PFOS solutions of similar concentrations suggest that clustering is not an analytical artifact under present experimental conditions.<sup>64-66</sup> There is no evidence for the formation of PFOS or PFOA trimeric/tetrameric aggregates under present conditions.

Figure 5.4 shows that normalized PFOS (*m/z* = 499) signal intensities are independent of pH down to pH 1.0, confirming that PFOSA is a strong acid, i.e., p*K*<sub>a</sub>(PFOSA) < 1. The sum of the signal intensities of the anions derived from PFO (at FV = 70 V), (2 I<sub>827</sub> + I<sub>413</sub> + I<sub>369</sub>) ∝ [PFO]<sub>T</sub>, is also independent of pH, implying negligible concentrations of other species such as the undissociated PFOA acid at pH ≥ 1. Therefore, p*K*<sub>a</sub>(PFOA) < 1. Figure 5.5 shows how the molar fraction (2 [(PFO)<sub>2</sub>H]/[PFO]<sub>T</sub>) varies with pH. This dependence is consistent with the clustering equilibrium, equation (5.2):



$$K_2 = \frac{[\text{PFO}]_T - [\text{PFO}]}{2[\text{H}^+][\text{PFO}]^2} \quad (5.3)$$

$$\frac{[(\text{PFO})_2\text{H}]}{[\text{PFO}]_T} = \frac{1}{2} - \frac{1}{2} \left[ \frac{-K_2^{-1} + \sqrt{K_2^{-2} + 8K_2^{-1}[\text{PFO}]_T 10^{-\text{pH}}}}{4[\text{PFO}]_T 10^{-\text{pH}}} \right]$$

Non-linear regressions to the experimental data of Figure 5.5 based on equation (5.3) and bulk concentration values yield  $K_2 \sim (3.9 \pm 0.3) \times 10^7 \text{ M}^{-2}$ . Although many studies have shown that the noncovalent complexes observed by electrospray mass spectrometry are not artifactual because their abundances respond to subtle molecular effects,<sup>64-66</sup> interfacial PFO concentrations are demonstrably larger than in the bulk,<sup>31</sup> and the derived  $K_2$  value should be strictly considered an upper limit. Thus, the calculated  $2[(\text{PFO})_2\text{H}]/$

[PFO]<sub>T</sub> values (blue triangles in Figure 5.5) using  $K_2 \sim (3.9 \pm 0.3) \times 10^7 \text{ M}^{-2}$  for [PFO]<sub>T</sub> = 2 nM (a hard upper bound to PFOA concentrations in environmental aqueous media)<sup>14,67,68</sup> show that neither PFOS nor PFO will appreciably self-associate or protonate under realistic environmental conditions. [PFOSA]/[PFOS] and [PFOA]/[PFO] ratios should remain well below  $10^{-7}$  in ocean waters at pH  $\sim 8.1$ , but may significantly increase in marine aerosols that become acidified over polluted regions. Further work is underway.

### 5.5 Acknowledgments

This project was financially supported by the National Science Foundation (ATM-0714329). E. P. is grateful to the Fullbright Foundation for financial support.

### 5.6 References

- (1) Persistent Organic Pollutants: A Global Issue, A Global Response; U. S. Environmental Protection Agency, <http://epa.gov/oia/toxics/pop.htm>, 2009.
- (2) Draft Risk Profiles on Perfluoroalkyl Surfactants. In <http://chm.pops.int/Convention/POPsReviewCommittee/Submissions20062007/CommentsondraftsofRMEYear2006/PFOSInformationsubmitted/tabid/473/language/en-US/Default.aspx>; Stockholm Convention on Persistent Organic Pollutants, 2008.
- (3) Kissa, E. *Fluorinated Surfactants and Repellents*, 2nd ed.; Marcel Dekker: New York, 2001.
- (4) Wang, T.; Wang, Y.; Liao, C. Y.; Cai, Y.; Jiang, G. B. *Environ. Sci. Technol.* **2009**, *43*, doi: 10.1021/es900464a.
- (5) Conder, J. M.; Hoke, R. A.; De Wolf, W.; Russell, M. H.; Buck, R. C. *Environ. Sci. Technol.* **2008**, *42*, 995.

- (6) Lau, C.; Butenhoff, J. L.; Rogers, J. M. *Toxicol. Appl. Pharmacol.* **2004**, *198*, 231.
- (7) Hekster, F. M.; Laane, R.; de Voogt, P. Environmental and toxicity effects of perfluoroalkylated substances. In *Reviews of Environmental Contamination and Toxicology*; Springer-Verlag: New York, 2003; vol. 179; pp 99.
- (8) Houde, M.; Martin, J. W.; Letcher, R. J.; Solomon, K. R.; Muir, D. C. G. *Environ. Sci. Technol.* **2006**, *40*, 3463.
- (9) Cui, L.; Zhou, Q. F.; Liao, C. Y.; Fu, J. J.; Jiang, G. B. *Arch. Environ. Contam. Toxicol.* **2009**, *56*, 338.
- (10) Slotkin, T. A.; MacKillop, E. A.; Melnick, R. L.; Thayer, K. A.; Seidler, F. J. *Environ. Health Perspect.* **2008**, *116*, 716.
- (11) Zhang, X.; Chen, L.; Fei, X. C.; Ma, Y. S.; Gao, H. W. *BMC Mol. Biol.* **2009**, *10*.16
- (12) Mollenhauer, M. A. M.; Carter, B. J.; Peden-Adams, M. M.; Bossart, G. D.; Fair, P. A. *Aquat. Toxicol.* **2009**, *91*, 10.
- (13) Kelly, B. C.; Ikonomou, M. G.; Blair, J. D.; Surridge, B.; Hoover, D.; Grace, R.; Gobas, F. *Environ. Sci. Technol.* **2009**, *43*, 4037.
- (14) Yamashita, N.; Taniyasu, S.; Petrick, G.; Wei, S.; Gamo, T.; Lam, P. K. S.; Kannan, K. *Chemosphere* **2008**, *70*, 1247.
- (15) Young, C. J.; Furdui, V. I.; Franklin, J.; Koerner, R. M.; Muir, D. C. G.; Mabury, S. A. *Environ. Sci. Technol.* **2007**, *41*, 3455.
- (16) Scott, B. F.; Spencer, C.; Mabury, S. A.; Muir, D. C. G. *Environ. Sci. Technol.* **2006**, *40*, 7167.

- (17) Higgins, C. P.; Field, J. A.; Criddle, C. S.; Luthy, R. G. *Environ. Sci. Technol.* **2005**, *39*, 3946.
- (18) Sinclair, E.; Mayack, D. T.; Roblee, K.; Yamashita, N.; Kannan, K. *Arch. Environ. Contam. Toxicol.* **2006**, *50*, 398.
- (19) Dietz, R.; Bossi, R.; Riget, F. F.; Sonne, C.; Born, E. W. *Environ. Sci. Technol.* **2008**, *42*, 2701.
- (20) Butt, C. M.; Mabury, S. A.; Muir, D. C. G.; Braune, B. M. *Environ. Sci. Technol.* **2007**, *41*, 3521.
- (21) Powley, C. R.; George, S. W.; Russell, M. H.; Hoke, R. A.; Buck, R. C. *Chemosphere* **2008**, *70*, 664.
- (22) Giesy, J. P.; Kannan, K. *Environ. Sci. Technol.* **2001**, *35*, 1339.
- (23) Bjork, J. A.; Lau, C.; Chang, S. C.; Butenhoff, J. L.; Wallace, K. B. *Toxicology* **2008**, *251*, 8.
- (24) Grasty, R. C.; Bjork, J. A.; Wallace, K. B.; Lau, C. S.; Rogers, J. M. *Birth Defects Res. Part B–Dev. Reprod. Toxicol.* **2005**, *74*, 405.
- (25) Butt, C. M.; Muir, D. C. G.; Stirling, I.; Kwan, M.; Mabury, S. A. *Environ. Sci. Technol.* **2007**, *41*, 42.
- (26) Prevedouros, K.; Cousins, I. T.; Buck, R. C.; Korzeniowski, S. H. *Environ. Sci. Technol.* **2006**, *40*, 32.
- (27) Wania, F. *Environ. Sci. Technol.* **2007**, *41*, 4529.
- (28) Czub, G.; Wania, F.; McLachlan, M. S. *Environ. Sci. Technol.* **2008**, *42*, 3704.
- (29) Psillakis, E.; Cheng, J.; Hoffmann, M. R.; Colussi, A. J. *J. Phys. Chem. A* **2009**, *113*.

- (30) Bennett, M. K.; Zisman, W. A. *Advances in Chemistry Series* **1975**, 199.
- (31) McMurdo, C. J.; Ellis, D. A.; Webster, E.; Butler, J.; Christensen, R. D.; Reid, L. K. *Environ. Sci. Technol.* **2008**, *42*, 3969.
- (32) Armitage, J. M.; MacLeod, M.; Cousins, I. T. *Environ. Sci. Technol.* **2009**, *43*, 1134.
- (33) Goss, K. U. *Environ. Sci. Technol.* **2008**, *42*, 5032.
- (34) Jiao, H. J.; Le Stang, S.; Soos, T.; Meier, R.; Kowski, K.; Rademacher, P.; Jafarpour, L.; Hamard, J. B.; Nolan, S. P.; Gladysz, J. A. *J. Am. Chem. Soc.* **2002**, *124*, 1516.
- (35) Brace, N. O. *J. Org. Chem.* **1962**, *27*, 4491.
- (36) Burns, D. C.; Ellis, D. A.; Li, H.; McMurdo, C. J.; Webster, E. *Environ. Sci. Technol.* **2008**, *42*, 9283.
- (37) Goss, K. U. *Environ. Sci. Technol.* **2008**, *42*, 456.
- (38) Rayne, S.; Forest, K.; Friesen, K. J. *J. Environ. Sci. Health Part A–Toxic/Hazard. Subst. Environ. Eng.* **2009**, *44*, 317.
- (39) Lopez-Fontan, J. L.; Gonzalez-Perez, A.; Costa, J.; Ruso, J. M.; Prieto, G.; Schulz, P. C.; Sarmiento, M. J. *Colloid Interface Sci.* **2006**, *294*, 458.
- (40) Lopez-Fontan, J. L.; Sarmiento, F.; Schulz, P. C. *Colloid Polym. Sci.* **2005**, 283, 862.
- (41) Moroi, Y.; Yano, H.; Shibata, O.; Yonemitsu, T. *Bull. Chem. Soc. Jpn.* **2001**, *74*, 667.
- (42) Burns, D. C.; Ellis, D. A.; Webster, E.; McMurdo, C. J. *Environ. Sci. Technol.* **2009**, *43*.

- (43) Goss, K. U.; Arp, H. P. H. *Environ. Sci. Technol.* **2009**, *43*.
- (44) Barton, C. A.; Kaiser, M. A.; Russell, M. H. *J. Environ. Monit.* **2007**, *9*, 839.
- (45) Ellis, D. A.; Webster, E. *Environ. Sci. Technol.* **2009**, *43*, 1234.
- (46) Mader, B. T. *Environ. Sci. Technol.* **2009**, *43*, 1232.
- (47) Cheng, J.; Hoffmann, M. R.; Colussi, A. J. *J. Phys. Chem. B* **2008**, *112*.
- (48) Cheng, J.; Vecitis, C.; Hoffmann, M. R.; Colussi, A. J. *J. Phys. Chem. B* **2006**, *110*, 25598.
- (49) Enami, S.; Vecitis, C. D.; Cheng, J.; Hoffmann, M. R.; Colussi, A. J. *J. Phys. Chem. A* **2007**, *111*, 8749.
- (50) Beattie, J. K. *Phys. Chem. Chem. Phys.* **2008**, *10*, 330.
- (51) Buch, V.; Milet, A.; Vacha, R.; Jungwirth, P.; Devlin, J. P. *Proc. Natl. Acad. Sci. U. S. A.* **2007**, *104*, 7342.
- (52) Iuchi, S.; Chen, H. N.; Paesani, F.; Voth, G. A. *J. Phys. Chem. B* **2009**, *113*, 4017.
- (53) Vacha, R.; Buch, V.; Milet, A.; Devlin, J. P.; Jungwirth, P. *Phys. Chem. Chem. Phys.* **2008**, *10*, 332.
- (54) Beattie, J. K. *Faraday Discuss.* **2009**, *141*, 31.
- (55) Perrin, D. D. *Pure Appl. Chem.* **1969**, *20*, 132.
- (56) Ariga, K.; Nakanishi, T.; Hill, J. P.; Shirai, M.; Okuno, M.; Abe, T.; Kikuchi, J. *J. Am. Chem. Soc.* **2005**, *127*, 12074.
- (57) Kebarle, P.; Peschke, M. *Analytica Chimica Acta* **2000**, *406*, 11.
- (58) Nguyen, S.; Fenn, J. B. *Proc. Natl. Acad. Sci. U. S. A.* **2007**, *104*, 1111.
- (59) Arsenault, G.; McAlees, A.; McCrindle, R.; Riddell, N. *Rapid Commun. Mass Spectrom.* **2007**, *21*, 3803.

- (60) Gilli, P.; Bertolasi, V.; Ferretti, V.; Gilli, G. *J. Am. Chem. Soc.* **1994**, *116*, 909.
- (61) Gilli, P.; Pretto, L.; Bertolasi, V.; Gilli, G. *Accounts Chem. Res.* **2009**, *42*, 33.
- (62) Steiner, T. *Angew. Chem. –Int. Ed.* **2002**, *41*, 48.
- (63) Hibbert, F.; Emsley, J. *Adv. Phys. Org. Chem* **1990**, *26*, 255.
- (64) Ganem, B.; Li, Y. T.; Henion, J. D. *J. Am. Chem. Soc.* **1991**, *113*, 7818.
- (65) Ganem, B.; Li, Y. T.; Henion, J. D. *J. Am. Chem. Soc.* **1991**, *113*, 6294.
- (66) McCullough, B. J.; Gaskell, S. J. *Comb. Chem. High Throughput Screen* **2009**, *12*, 203.
- (67) Ju, X. D.; Jin, Y. H.; Sasaki, K.; Saito, N. *Environ. Sci. Technol.* **2008**, *42*, 3538.
- (68) Yamashita, N.; Kannan, K.; Taniyasu, S.; Horii, Y.; Petrick, G.; Gamo, T. *Mar. Pollut. Bull.* **2005**, *51*, 658.

Table 5.1. Isotope ratios of PFO species observed by ES-MS.<sup>a</sup>

	m/z	I <sub>m/z</sub> (a.u.)	I <sub>m/z+1</sub> (a.u.)	I <sub>(m+1)/z</sub> /I <sub>m/z</sub> measured (%)	I <sub>(m+1)/z</sub> /I <sub>m/z</sub> calculated(%)
PFO <sup>-</sup>	413	7027	165	8.8	9.0
PFO-CO <sub>2</sub> <sup>-</sup>	369	2212	619	7.5	7.9
(PFO) <sub>2</sub> H <sup>-</sup>	827	1564	283	18.1	18.0

- a. ES-MS signal intensities were recorded at m/z= 369, 370, 413, 414, 827, 828 for 5 mM PFOA solution at pH 1.5 under the SIM mode. Values in the last column are calculated as  $I_{(m+1)/z}/I_{m/z} = n \times 0.0111/0.9889$  for C<sub>n</sub>-species.

Figure 5.1. Titration curves of *n*-hexanoic and *n*-octanoic acids. ESI-MS signal intensities of *n*-hexanoate ( $m/z = 115$ , blue circles) and *n*-octanoate ( $m/z = 143$ , red circles) relative to  $\text{ClO}_4^-$  ( $m/z = 99, 101$ ) as functions of solution pH. Solutions are  $100 \mu\text{M}$  in  $\text{NaClO}_4$  and *n*-hexanoic or *n*-octanoic acids. HCl or NaOH solutions were used to adjust pH while keeping the total chloride concentration at  $1.0 \text{ mM}$  by NaCl addition.

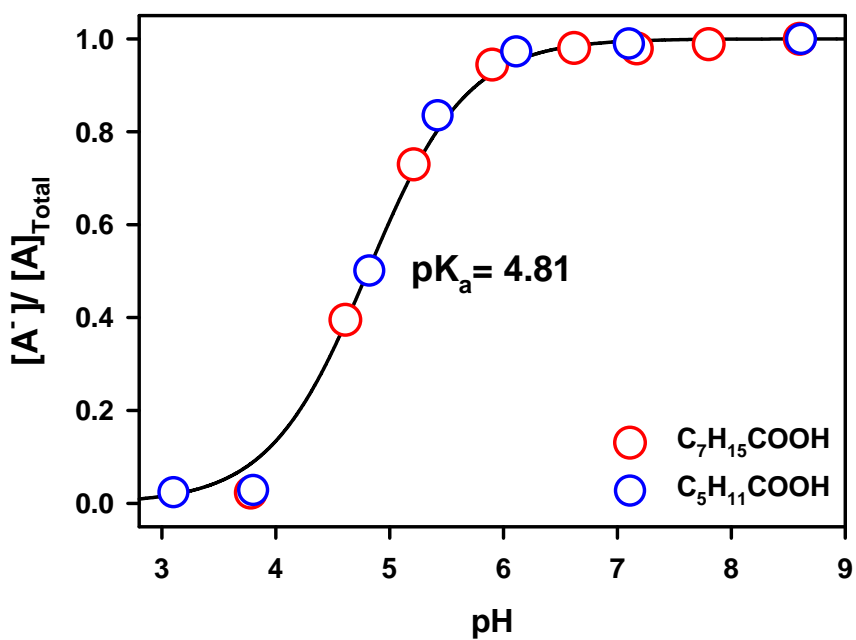


Figure 5.2. ESI-MS spectra of 10  $\mu\text{M}$  PFOS in: (a) MilliQ water at pH 6.5, (b) 10 mM HCl at pH 2.0, (c) 10 mM NaCl at pH 7.0. Spectra were acquired in the scan mode at a fragmentor voltage of 70 V. Maximum signal intensities  $\equiv$  100.

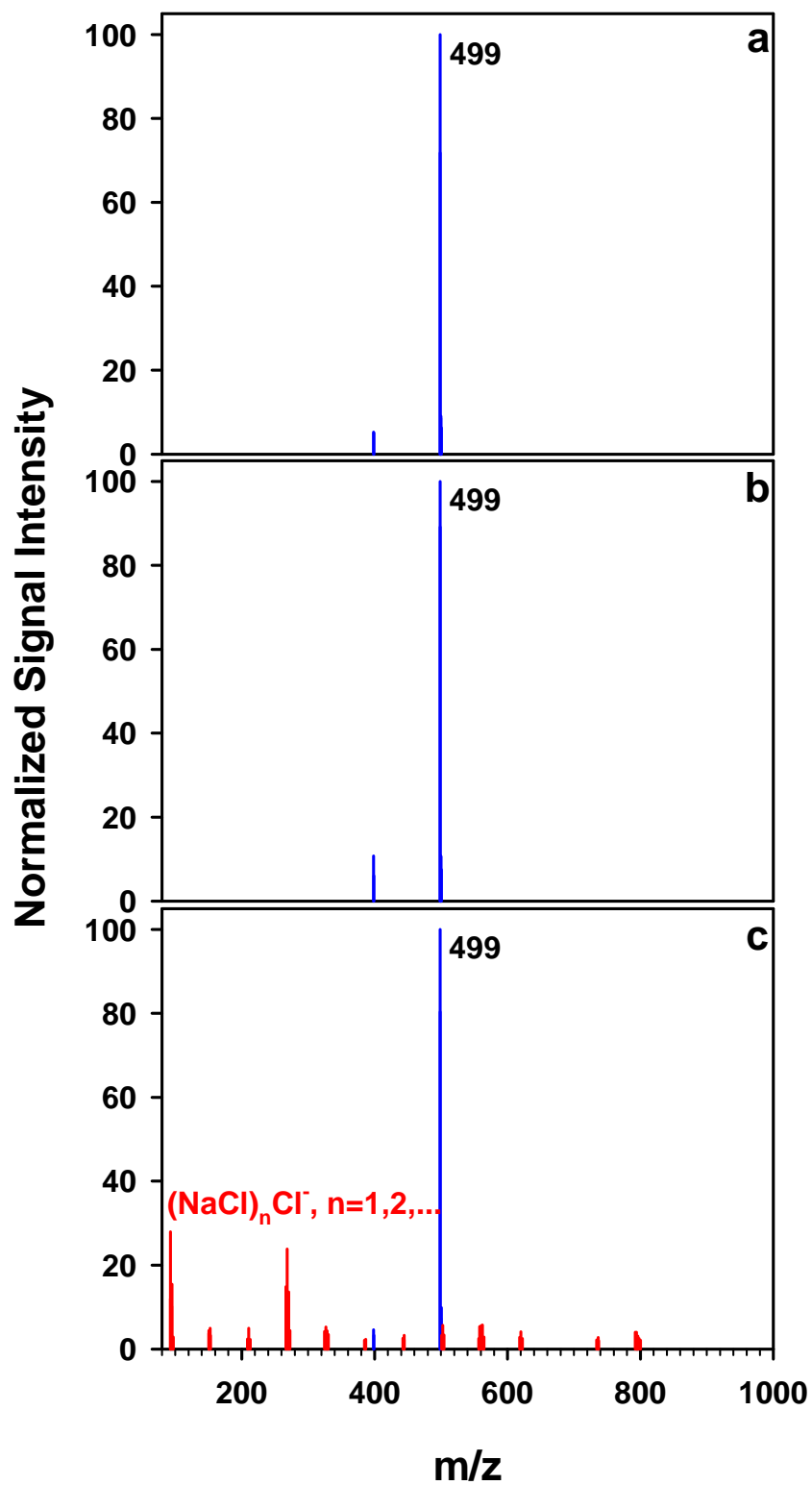


Figure 5.3. ESI-MS spectra of 10  $\mu\text{M}$  PFO in: (a) MilliQ water at pH 6.0, (b) 10 mM HCl at pH 2.0, (c) 10 mM NaCl at pH 7.0, (d) 10 mM HCl at pH 2.0. Spectra were acquired in the scan mode at a fragmentor voltage set at 70 V for (a)-(c) and at 150 V for (d). Maximum signal intensities = 100.

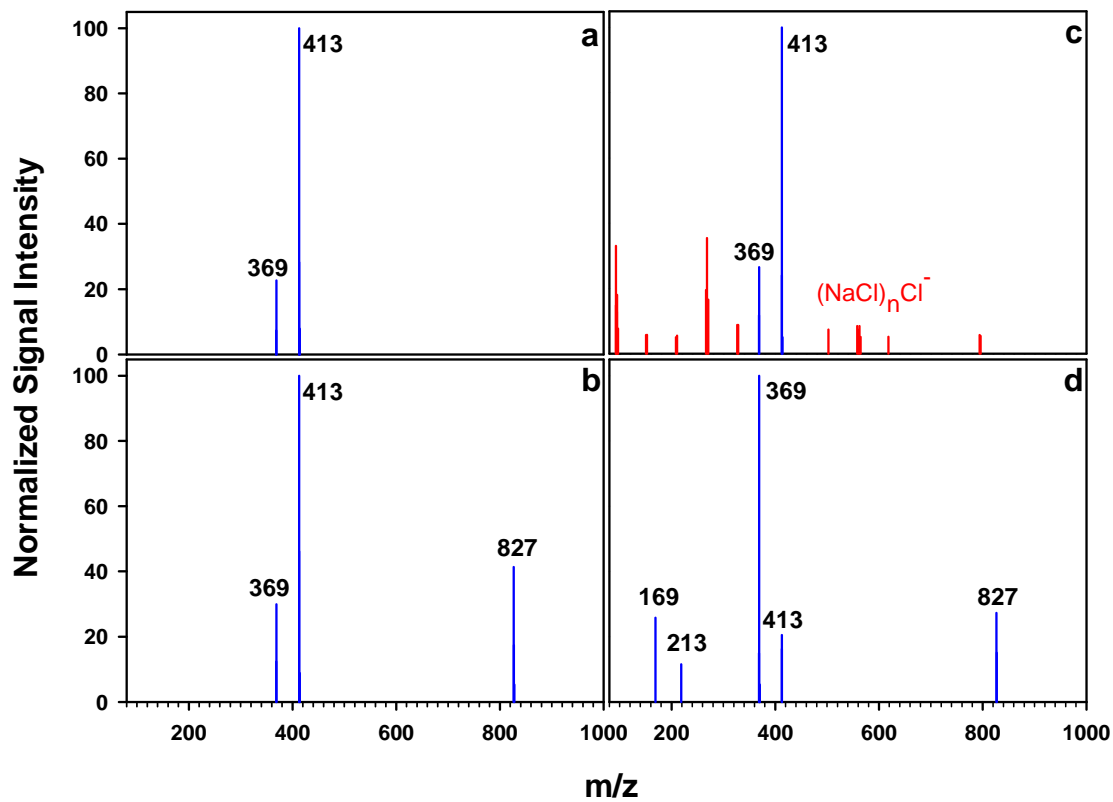


Figure 5.4. ESI-MS titration curves for PFOSA and PFOA. ESI-MS signal intensities from PFOS ( $m/z = 499$ , black circles) and PFOA ( $I_{369} + I_{413} + I_{827}$ , red circles) relative to  $\text{ClO}_4^-$  ( $m/z = 99, 101$ ) as functions of solution pH. Solutions are  $10 \mu\text{M}$  in  $\text{NaClO}_4$  and PFOSA or PFOA.  $10 \text{ mM}$   $\text{HCl}$  and varying concentrations of  $\text{NaOH}$  were added to adjust pH while keeping the total chloride concentration constant at  $10 \text{ mM}$ , with the exception of the solution at pH 1.

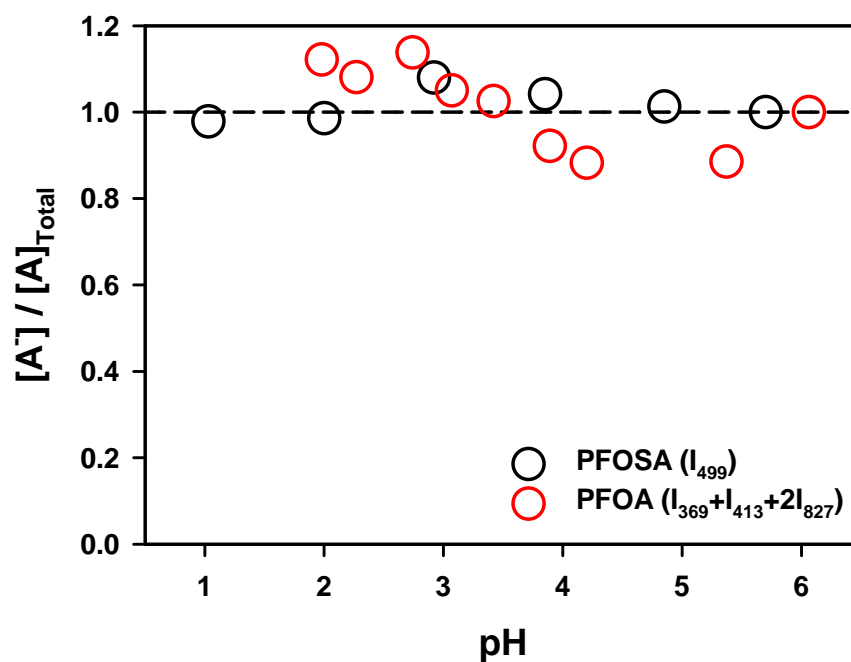
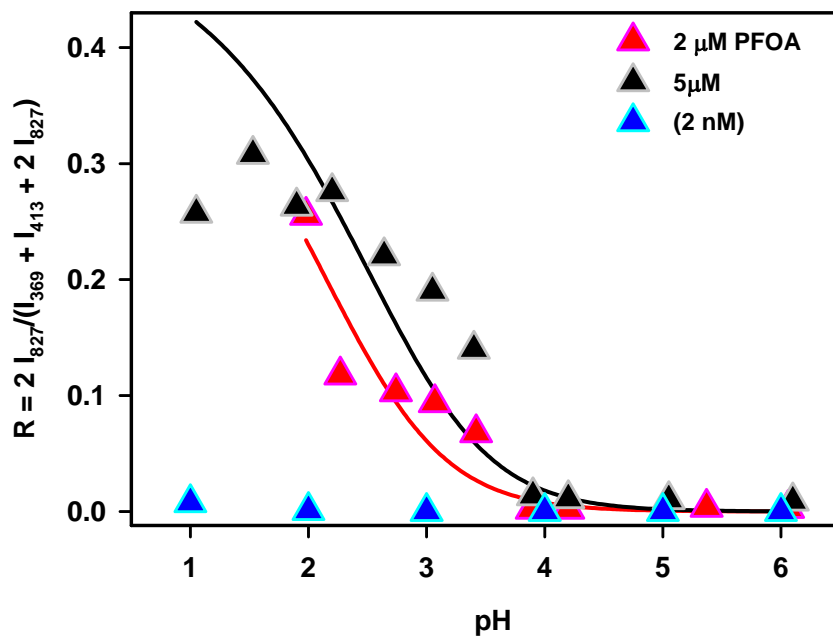
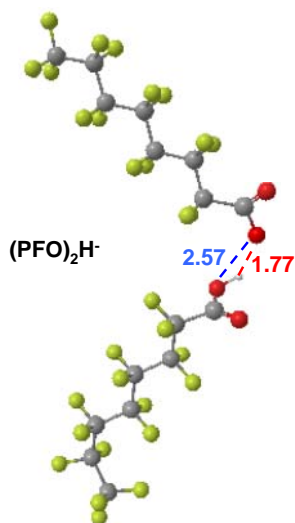


Figure 5.5. The ratio of the ESI-MS intensities of  $(\text{PFOA})_2\text{H}^-$  ( $m/z = 827$ ) to the sum of the intensities of all PFOA species:  $R = 2 I_{827}/[I_{369} + I_{413} + 2 I_{827}]$ , as a function of pH for 2  $\mu\text{M}$  (red triangles) and 5  $\mu\text{M}$  (black triangles) PFOA solutions.



Scheme 5.1. Schematic drawing of The MM2 structure of the  $(\text{PFO})_2\text{H}^-$  cluster.

## **Chapter 6**

### **Sonochemical Degradation of Perfluorooctane Sulfonate (PFOS) and Perfluorooctanoate (PFOA) in Landfill Groundwater: Environmental Matrix Effect\***

---

\*This chapter is reproduced with permission from J. Cheng, C. D. Vecitis, H. Park, B. T. Mader, and M.R. Hoffmann, *Environmental Science and Technology*, **2008**, 42, 8057. Copyright © 2008, American Chemical Society

## 6.1 Abstract

Perfluorinated chemicals such as perfluorooctane sulfonate (PFOS) and perfluorooctanoic acid (PFOA) are environmentally persistent and recalcitrant to most conventional chemical and microbial treatment technologies. In this chapter, we show that sonolysis is able to decompose PFOS and PFOA present in groundwater beneath a landfill. However, the pseudo-first-order rate constant for the sonochemical degradation in the landfill groundwater is reduced by 61% and 56% relative to Milli-Q water for PFOS and PFOA, respectively, primarily due to the presence of other organic constituents. In this study, we evaluate the effect of various organic compounds on the sonochemical decomposition rates of PFOS and PFOA. Organic components in environmental matrices may reduce the sonochemical degradation rates of PFOS and PFOA by competitive adsorption onto the bubble-water interface or by lowering the average interfacial temperatures during transient bubble collapse events. The effect of individual organic compounds depends on the Langmuir adsorption constant, the Henry's law constant, the specific heat capacity, and the overall endothermic heat of dissociation. Volatile organic compounds (VOCs) are identified as the primary cause of the sonochemical rate reduction for PFOS and PFOA in landfill groundwater, whereas the effect of dissolved natural organic matter (DOM) is not significant. Finally, a combined process of ozonation and sonolysis is shown to substantially recover the rate loss for PFOS and PFOA in landfill groundwater.

## 6.2 Introduction

Perfluorooctane sulfonate (PFOS) and perfluorooctanoate (PFOA) have been found to be widespread in the environment due to their persistence and the long-range atmospheric and oceanic transport of their precursors such as perfluoroalkyl sulfonamides (PFASs) and fluorotelomer alcohols (FTOHs).<sup>1-3</sup> PFOS and PFOA have been measured in most natural waters from non-detectable to  $\text{ng L}^{-1}$  levels,<sup>4-6</sup> whereas higher concentrations (up to 2300 and 6570  $\mu\text{g L}^{-1}$  for PFOS and PFOA, respectively) have been measured in groundwater collected from military bases where aqueous film-forming foams (AFFF) are used for fire-training activities.<sup>7</sup> Recently, PFOS and PFOA, together with other perfluorinated chemicals, have been detected in groundwater emanating from disposal sites in the Minneapolis/St. Paul area.<sup>8</sup> In addition, PFOS and PFOA have been detected in wildlife<sup>9-11</sup> as well as in human blood serum,<sup>12</sup> seminal plasma,<sup>13</sup> and breast milk.<sup>14</sup>

The presence of PFOS and PFOA has initiated efforts to develop effective water treatment technologies. Both compounds are recalcitrant to most conventional chemical and microbial treatment schemes.<sup>15,16</sup> It was found in a wastewater treatment process that in some cases the mass flows of PFOS and PFOA could increase as a result of precursor degradation.<sup>16,17</sup> Advanced oxidation processes (AOPs) are also ineffective for treating PFOS and PFOA due to their relatively slow reaction rates with OH radicals.<sup>18</sup> Wastewater containing perfluorochemicals can potentially be treated by activated carbon adsorption, reverse osmosis (RO), or nanofiltration (NF).<sup>19,20</sup> Nevertheless, the removal efficiency may be significantly impaired by other components in the wastewater matrix.<sup>19,20</sup> On the other hand, treating PFOS and PFOA at lower concentrations present in natural waters presents certain challenges. Various treatment techniques have been

evaluated, such as UV photolysis,<sup>21,22</sup> reduction by elemental iron,<sup>23</sup> and acoustic cavitation,<sup>24</sup> but to our knowledge, none have been tested on environmental samples.

Sonochemical degradation is effective in treating PFOS and PFOA present in aqueous solution over a wide range of concentrations.<sup>25</sup> Acoustic cavitation induced by high-frequency ultrasonic irradiation of aqueous solutions produces transient high temperatures in the bubble vapor phase and at the bubble-water interface. Because of their high surface activity, PFOS and PFOA preferentially partition to the bubble-water interface, where temperatures are on the order of 1000 K during a transient bubble collapse,<sup>26</sup> and are thus decomposed via *in situ* pyrolysis. Following the initial rate-limiting pyrolysis step, PFOS and PFOA are rapidly converted to CO, CO<sub>2</sub>, fluoride (F<sup>-</sup>), and sulfate (SO<sub>4</sub><sup>2-</sup>). A sonochemical degradation half-life under 30 minutes has been reported for both PFOS and PFOA.<sup>25</sup> In addition, the sonochemical degradation rates are observed to increase linearly with increasing acoustic power density, and scaling-up the reactor size has minimal effect on reaction rates,<sup>27</sup> thus making sonochemical degradation a promising treatment method for PFOS and PFOA.

Previous studies on the sonochemical decomposition of PFOS and PFOA have focused on pure aqueous solutions. It is of practical interest to examine this process in environmentally relevant matrices, as the various matrix components may significantly affect the sonochemical kinetics and therefore the overall treatment efficiency. In this chapter, we determined the sonochemical kinetics of PFOS and PFOA present in the groundwater beneath a landfill. In addition, landfill groundwater components including volatile organic compounds (VOCs) and dissolved natural organic matter (DOM) were evaluated individually with respect to their effect on sonochemical degradation rates.

Finally, the sonozone process, i.e., sonolysis combined with ozonation, was applied in an attempt to enhance the degradation rates of PFOS and PFOA in the landfill groundwater. Results from this study can be used to estimate the matrix effect on the sonochemical degradation rates of PFOS and PFOA in various environmental media and to design remediation strategies accordingly.

### 6.3 Experimental Methods

**Materials.** Ammonium perfluorooctanoate (APFO) and potassium perfluorooctane sulfonate (PFOS-K<sup>+</sup>) standards were provided by 3M. Methanol, acetone, isopropyl alcohol, methyl-t-butyl-ether (MTBE), ethyl acetate, toluene, p-xylene, m-xylene, ethyl benzene, methyl isobutyl ketone (MIBK), and ammonium acetate were obtained from EMD chemicals. Suwannee River humic and fulvic acid standards were purchased from International Humic Substances Society. Sep-Pak Vac tC18 (6 cc, 1 g) solid phase extraction (SPE) cartridges were purchased from Waters. Purified water (18.2 M $\Omega$  cm<sup>-1</sup> resistivity) was prepared using the Millipore Milli-Q Gradient water purification system.

**Sonolysis.** Sonications were performed in a 600 mL jacketed glass reactor at a frequency of 354 or 612 kHz using an Allied Signal–ELAC Nautik ultrasonic transducer. The applied power density was 250 W L<sup>-1</sup> with an average energy-transfer efficiency of 72% as measured by calorimetry. The solutions were maintained at 10 °C by water cooling and sparged with argon 30 minutes prior to and during the course of the reaction. In sonozone experiments, an ozone/oxygen gaseous mixture (2.5% v/v ozone) produced by an Orec V10-0 corona ozone generator was sparged into the reaction solution at 0.5 L min<sup>-1</sup>. In all experiments the initial concentrations of both PFOS and PFOA were approximately 100  $\mu$ g L<sup>-1</sup>.

**Solid phase extraction.** Landfill groundwater samples taken during the sonochemical reactions were purified by SPE using Sep-Pak Vac tC18 cartridges (6 cc, 1 g) to remove matrix components that may interfere with the LC/MS analysis. The SPE cartridges were conditioned by passing 10 mL methanol and 50 mL water through the cartridges at a flow rate of 2 mL min<sup>-1</sup>. The analytical samples were subsequently loaded onto the wet cartridges at 1 mL min<sup>-1</sup>. The columns were dried with nitrogen gas for 5 minutes, rinsed with 10 mL 20% methanol in water at 2 mL min<sup>-1</sup>, and dried with nitrogen gas for another 30 minutes. The analytes were eluted with methanol at 1 mL min<sup>-1</sup>, and 4.0 mL samples were collected into 14 mL polypropylene tubes (Falcon). Sample aliquots (700 µL) were transferred to HPLC vials (Agilent) for the LC/MS analysis. All steps except sample loading were performed on a Caliper AutoTrace SPE Work Station.

**LC/MS analyses.** The concentrations of PFOS and PFOA were quantified by LC/MS. Sample aliquots (700 µL) were withdrawn from the reactor using disposable plastic syringes, transferred into 750 µL polypropylene autosampler vials, and sealed with PTFE septum crimp caps (Agilent). 20 µL of samples were injected into an Agilent 1100 HPLC for separation on a Thermo-Electron Betasil C18 column (100 mm × 2.1 mm, 5 µm). An identical guard column was placed in front of the analytical column. The flow rate was maintained at 0.3 mL min<sup>-1</sup> with a mobile phase of 2 mM ammonium acetate in water (A) and methanol (B). The eluent gradient started with 5% B over the first minute, was ramped to 90% B over 10 minutes and held for 2.5 minutes, then ramped back to 5% B over 0.5 minutes and held for 3 minutes, and finished with a 3 minute post time. Chromatographically separated samples were analyzed by an Agilent Ion Trap in negative mode monitoring for the perfluorooctanesulfonate molecular ion ( $m/z = 499$ )

and the decarboxylated perfluorooctanoate ( $m/z = 369$ ). Instrumental parameters were set at the following levels: nebulizer pressure 40 PSI, drying gas flow rate  $9 \text{ L min}^{-1}$ , drying gas temperature  $325 \text{ }^\circ\text{C}$ , capillary voltage  $+3500 \text{ V}$ , and skimmer voltage  $-15 \text{ V}$ . Quantification was based on a 8-point calibration curve spanning the  $1$  to  $200 \text{ } \mu\text{g L}^{-1}$  range fitted to a quadratic with  $X^{-1}$  weighting. Analytical standards, quality control, and reagent blank samples were included in each analytical batch along with the unknown samples. Further analytical details were described in Table 6.3 and Figure 6.10, and in a previous paper (25).

*Surface tension measurements.* The surface tension of sample solutions was determined by a du Nouy interfacial tensiometer using the standard ring method (ASTM D1331-89).

## 6.4 Experimental Results

*Groundwater characterization.* The groundwater used in this study was sampled from beneath a landfill located within the city of Oakdale, MN, and therefore contains organic chemicals that are also present in the landfill. As summarized in Table 6.1, the landfill groundwater has a total organic carbon (TOC) concentration of  $20 \text{ mg L}^{-1}$ , primarily volatile organic compounds (VOCs) such as acetone, diisopropyl ether, and 2-butanone at  $\text{mg L}^{-1}$  levels. It also contains a moderately high level of bicarbonate and iron. The concentrations of PFOS and PFOA in the landfill groundwater are  $30$  and  $65 \text{ } \mu\text{g L}^{-1}$ , respectively.

*Sonolysis of PFOS and PFOA- Matrix Effects.* The sonochemical degradation kinetics of PFOS and PFOA ( $[\text{PFOS}]_i = [\text{PFOA}]_i = 100 \text{ } \mu\text{g L}^{-1}$ ) in landfill groundwater and Milli-Q water are shown in Figure 6.1. Sonolysis was performed under the following

conditions: ultrasonic frequency set at 354 or 612 kHz, applied power density set at a constant  $250 \text{ W L}^{-1}$ , and temperature maintained at  $10 \text{ }^{\circ}\text{C}$  under an argon atmosphere. PFOS and PFOA were spiked into the groundwater to increase the concentration to  $100 \text{ } \mu\text{g L}^{-1}$  each. The sonochemical degradation of groundwater PFOS and PFOA follows pseudo first-order kinetics as is observed in Milli-Q, which agrees with the hypothesis that the initial decomposition mechanism remains the same. However, at 354 kHz, the first-order rate constant for the sonolysis of groundwater PFOS,  $k_{\text{GW}}^{-\text{PFOS}} = 0.0094 \text{ min}^{-1}$ , is 39% of the Milli-Q rate constant,  $k_{\text{MQ}}^{-\text{PFOS}} = 0.024 \text{ min}^{-1}$ . Similar results are observed for PFOA, where the rate constant for groundwater PFOA,  $k_{\text{GW}}^{-\text{PFOA}} = 0.021 \text{ min}^{-1}$ , is 44% of the Milli-Q rate constant,  $k_{\text{MQ}}^{-\text{PFOA}} = 0.047 \text{ min}^{-1}$ . At a sonolytic frequency of 612 kHz, a similar reduction in rate constant is observed when comparing sonolysis in Milli-Q versus in groundwater (Figure 6.7).

In order to probe the organic chemical species present in the landfill groundwater that are the most responsible for the reduction in sonochemical degradation rates, representative organic compounds were individually added to the aqueous solution of PFOS and PFOA, and their effect on the sonochemical degradation rates of PFOS and PFOA evaluated under the same sonolytic conditions as used in the previous experiments. Figure 6.2 shows the effect of methanol, acetone, isopropyl alcohol, ethyl acetate, and MTBE on the sonochemical degradation rates of PFOS and PFOA. In all cases, two regimes are observed with respect to the decrease in the sonochemical degradation rates as a function of increasing organic concentrations. The sonochemical degradation rate constant gradually decreases at relatively low organic concentrations, but above an

organic-specific threshold concentration, the decrease in rate constant shifts to a much steeper slope.

The effect of larger organic compounds such as toluene, ethyl benzene, p-xylene, m-xylene, and MIBK was also evaluated. At  $10^{-4}$  mol L<sup>-1</sup>, no significant effect on the sonochemical degradation rates is observed (Figure 6.3), but at  $10^{-3}$  mol L<sup>-1</sup>, MIBK reduces the sonochemical degradation rates of PFOA and PFOS by 46% and 66%, respectively. The effect of MIBK is greater than any of the five organic compounds in Figure 6.2. For the other four larger compounds, no higher concentrations were tested due to their low water solubilities.

In addition to VOCs, the effect of DOM on the sonochemical kinetics of PFOS and PFOA was also examined. DOM is composed of heterogeneous organic compounds including humic and fulvic acids. As is shown in Figure 6.4, no significant difference is found between the sonochemical degradation kinetics of PFOS and PFOA in Milli-Q water, a 15 mg L<sup>-1</sup> humic acid solution, and a 15 mg L<sup>-1</sup> fulvic acid solution. 15 mg L<sup>-1</sup> represents the highest concentration of DOM found in most natural waters.

***Sonozone treatment of PFOS and PFOA.*** We evaluated the performance of sonozone, a process that combines ozonation and sonolysis, on the degradation of PFOS and PFOA in landfill groundwater. As Figure 6.5 shows, by continuously sparging an oxygen/ozone mix gas (2.5% v/v O<sub>3</sub>) during the course of sonolysis, the degradation rates are increased to 0.019 min<sup>-1</sup> for PFOS and 0.033 min<sup>-1</sup> for PFOA. This is equal to 79% and 70% of the Milli-Q rate constant for PFOS and PFOA, respectively. In comparison, replacing argon with either oxygen or an oxygen/ozone mix gas has no significant effect on the sonochemical kinetics of PFOS and PFOA in Milli-Q water (Figure 6.8).

## 6.5 Discussion

Based on the observation of two distinct regimes as shown in Figure 6.2, we propose that two different mechanisms are active in reducing the sonochemical degradation rates of PFOS and PFOA. The first mechanism is competitive adsorption onto the bubble-water interface by organic compounds other than PFOS and PFOA, which reduces the number of active surface sites available for PFOS and PFOA pyrolysis. The second mechanism is evaporation of the volatile organic compounds into the bubble vapor phase, which reduces the bubble vapor and interfacial temperatures during transient bubble collapse events by increasing the specific heat capacity of the bubble vapor and subsequent endothermic dissociation of these organic vapors.<sup>28</sup>

The two mechanisms are further elucidated by examining the mathematical expression for the sonochemical degradation rates of PFOS and PFOA. Assuming that competitive adsorption is active at the bubble-water interface, and that interfacial pyrolysis is the only viable degradation pathway for PFOS and PFOA, the sonochemical degradation rate of PFOX (PFOX denotes PFOS or PFOA) can be expressed as<sup>29</sup>

$$\frac{d[PFOX]}{dt} = -k_{app}^{-PFOX} [PFOX] = -k_{\Delta}^{-PFOX} \theta^{PFOX} \quad (6.1)$$

where  $k_{app}^{-PFOX}$  is the apparent pseudo first-order rate constant,  $k_{\Delta}^{-PFOX}$  the maximum absolute rate attained when all of the transiently cavitating bubble surface sites are occupied by PFOX molecules, and  $\theta^{PFOX}$  the fraction of PFOX molecules at the bubble-water interface in the presence of other organic compounds.  $k_{\Delta}^{-PFOX}$  is given by

$$k_{\Delta}^{-PFOX} = [S]A^{PFOX} \exp\left(-E_A^{PFOX} / R\langle T_{int}^{bub} \rangle\right) \quad (6.2)$$

where  $[S]$  is the molarity of bubble adsorption sites,  $A^{PFOX}$  and  $E_A^{PFOX}$  are the pre-exponential constant and activation energy for the initial PFOX pyrolysis, respectively, and  $\langle T_{int}^{bub} \rangle$  is the average interfacial temperature during the high-temperature period of a transient bubble collapse.  $\theta^{PFOX}$ , in the presence of other organic compounds competing for bubble interfacial sites, is given by

$$\theta^{PFOX} = \frac{K_L^{PFOX} [PFOX]}{1 + K_L^{PFOX} [PFOX] + \sum_i K_L^{org,i} [Org, i]} \quad (6.3)$$

where  $K_L^X$  is the Langmuir adsorption constant for compound X in  $L \text{ mol}^{-1}$ . The  $K_L$  values for the five organic compounds in Figure 6.2 can be obtained from the surface tension curves shown in Figure 6.6. Least square fitting of the surface tension curves  $\gamma(c)$ 's to the Szyszkowski equation (Eq. (6.4)), the surface equation of state for the Langmuir isotherm (Eq. (6.5)), yields  $K_L$  as well as  $\Gamma_{max}$ , the maximum surface concentration, for these five compounds (Table 6.2).

$$\Pi = \gamma_0 - \gamma(c) = nRT\Gamma_{max} \ln(1 + K_L c) \quad (6.4)$$

$$\Gamma = \Gamma_{max} \frac{K_L c}{1 + K_L c} \quad (6.5)$$

In Eq. (6.4),  $\Pi$  is the surface pressure in  $N \text{ m}^{-1}$ ,  $\gamma_0 = 0.072 \text{ N m}^{-1}$  is the surface tension of pure water and  $\gamma(c)$  is the surface tension of the aqueous solution of an organic compound at a given concentration  $c$ . As is shown in Table 6.2,  $\Gamma_{max}$  varies little among the five organic compounds, ranging from  $4.7 \times 10^{-6}$  to  $8.2 \times 10^{-6} \text{ mol m}^{-2}$ . In contrast,  $K_L$  spans a much wider range from  $3.9 \times 10^{-4} \text{ m}^3 \text{ mol}^{-1}$  for methanol to around  $1.9 \times 10^{-2} \text{ m}^3 \text{ mol}^{-1}$  for ethyl acetate, which is about 50 times higher. Thus  $K_L$  is the key determining

factor for surface activity. According to Eq. (6.3), organic compounds with greater  $K_L$  values are more effective in reducing the sonochemical degradation rates of PFOS and PFOA by competitive adsorption onto the bubble-water interface. This trend is consistent with the experimental results shown in Figure 6.2.

As Eq. (6.2) suggests, another key driver for the sonochemical degradation rate of PFOS and PFOA is the average interfacial temperature during the high-temperature period of a transient bubble collapse. For example, considering that the activation energy for PFOA pyrolysis is  $E_A^{PFOA} = 172 \text{ kJ mol}^{-1}$ ,<sup>30</sup> lowering  $\langle T_{\text{int}}^{\text{bub}} \rangle$  from 1000 K to 900 K will reduce the reaction rate by 10 times. Volatile solutes such as alcohols are known to be able to significantly reduce the vapor and interfacial temperatures during bubble collapse.<sup>28, 31, 32</sup> The magnitude of the effect that an organic compound has on the bubble and interfacial temperatures is positively correlated with its Henry's law constant, its specific heat capacity, and its overall endothermic heat of dissociation. First, the Henry's law constant will determine the relative amount of solute that partitions to the bubble vapor phase during bubble expansion. Second, the presence of VOCs in the bubble vapor phase which have larger specific heat capacities than argon ( $C_{p,\text{Ar}} = 20.8 \text{ J mol}^{-1} \text{ K}^{-1}$  at 298 K) will reduce the maximum bubble and interfacial temperatures achieved during bubble collapse. In addition, the organic compounds will be thermally decomposed under high temperatures inside the bubble, producing  $\text{H}_2$ ,  $\text{CO}$ , and smaller organic compounds.<sup>33-35</sup> The endothermic dissociation of these compounds will further reduce bubble vapor and interfacial temperatures. Table 6.2 lists the Henry's law constants and the specific heat capacities at 298 K of the five organic compounds in Figure 6.2, and the values at a wider range of temperatures can be found in Figure 6.9. Although a complete

calculation of the overall heat of dissociation values taking into account all thermal reaction pathways is beyond the scope of this chapter, a positive correlation can be assumed between the overall heat of dissociation and the molecular size. The argument that VOCs affect the sonochemical kinetics by lowering the interfacial temperature is supported by the trend among the five organic compounds shown in Figure 6.2. The interfacial temperature reduction is also consistent with the observation that the groundwater matrix has a greater effect on the sonochemical degradation rate of PFOS than that of PFOA, since PFOS has a higher thermal activation energy.<sup>36</sup>

At concentrations up to 15 mg L<sup>-1</sup>, neither humic nor fulvic acid has a significant effect on the sonochemical degradation rates of PFOS and PFOA. This suggests that neither of the aforementioned mechanisms is significant under these conditions. First, humic and fulvic acids are non-volatile and thus are expected to have little effect on the interfacial temperatures during bubble collapse. Second, though DOM is considered to be moderately surface active,<sup>37</sup> the effect of competitive adsorption onto the bubble-water interface is expected to be negligible at 15 mg L<sup>-1</sup>. Given that the average molecular weight of DOM is at least 1 kDa<sup>38</sup> and that the average  $K_L$  value of DOM is arguably much smaller than  $K_L^{PFOS} = 1.97 \text{ m}^3 \text{ mol}^{-1}$  and  $K_L^{PFOA} = 0.36 \text{ m}^3 \text{ mol}^{-1}$ ,<sup>29</sup> the term  $\sum_i K_L^{Org,i} [Org,i]$  in Eq. 6.3 is  $\ll 1$ , and thus negligible, at a DOM concentration of 15 mg L<sup>-1</sup>.

Given the relatively low concentrations and surface activities of groundwater organic components evaluated in this study, competitive adsorption onto the bubble-water interface is expected to be of minor importance. However, this effect may be important in environmental matrices with higher concentrations of surface active components such as

aqueous film-forming foams (AFFF). The landfill groundwater in this study contains approximately  $0.3 \sim 0.5 \text{ mmol L}^{-1}$  VOCs, including larger and more volatile compounds such as diisopropyl ether and MIBK that are more effective than smaller VOCs (Figure 6.2) in reducing interfacial temperatures during bubble collapse. Therefore, temperature reduction by VOCs should be considered as the primary cause of the sonochemical rate reduction for PFOS and PFOA in the landfill groundwater. Inorganic components such as bicarbonate and sulfate ions may also contribute to the sonochemical rate reduction. In addition, adsorption of PFOS and PFOA onto organic matter and iron oxides in the landfill groundwater may reduce their concentrations at the bubble-water interface and therefore the degradation rates. However, the effect is not expected to be significant due to the relatively low partitioning coefficients of PFOS and PFOA.<sup>39, 40</sup>

The sonozone process is shown to significantly enhance the degradation rates of PFOS and PFOA in landfill groundwater, though it has no significant effect in Milli-Q water. The sonozone process has been shown to enhance the OH production rate.<sup>35, 41, 42</sup> Though reactions of OH radical with PFOS and PFOA are kinetically limited, OH radicals will react with VOCs present in the bubble vapor phase at a much faster rate than the thermal dissociation of these molecules and will increase their mineralization rates. The rapid destruction of VOCs will reduce their negative impact on interfacial temperatures during bubble collapse. The sonozone process shows potential for improving the degradation rates of PFOS and PFOA in landfill groundwater and other environmental media with high levels of VOCs.

## 6.6 Acknowledgements

The authors would like to thank 3M for the financial support and the Caltech Environmental Analysis Center (Dr. Nathan Dalleska) for technical assistance in sample analysis.

## 6.7 References

- (1) Prevedouros, K.; Cousins, I. T.; Buck, R. C.; Korzeniowski, S. H., *Environ. Sci. Technol.* **2006**, *40*, 32-44.
- (2) Ellis, D. A.; Martin, J. W.; De Silva, A. O.; Mabury, S. A.; Hurley, M. D.; Andersen, M. P. S.; Wallington, T. J., *Environ. Sci. Technol.* **2004**, *38*, 3316-3321.
- (3) Shoeib, M.; Harner, T.; Vlahos, P., *Environ. Sci. Technol.* **2006**, *40*, 7577-7583.
- (4) Yamashita, N.; Kannan, K.; Taniyasu, S.; Horii, Y.; Okazawa, T.; Petrick, G.; Gamo, T., *Environ. Sci. Technol.* **2004**, *38*, 5522-5528.
- (5) So, M. K.; Taniyasu, S.; Yamashita, N.; Giesy, J. P.; Zheng, J.; Fang, Z.; Im, S. H.; Lam, P. K. S., *Environ. Sci. Technol.* **2004**, *38*, 4056-4063.
- (6) Yamashita, N.; Kannan, K.; Taniyasu, S.; Horii, Y.; Petrick, G.; Gamo, T., *Mar. Pollut. Bull.* **2005**, *51*, 658-668.
- (7) Schultz, M. M.; Barofsky, D. F.; Field, J. A., *Environ. Sci. Technol.* **2004**, *38*, 1828-1835.
- (8) Minnesota Pollution Control Agency. *Investigation of Perfluorochemical (PFC) Contamination in Minnesota – Phase One*; Minnesota Pollution Control Agency, St. Paul, MN, 2006.
- (9) Smithwick, M.; Mabury, S. A.; Solomon, K. R.; Sonne, C.; Martin, J. W.; Born, E. W.; Dietz, R.; Derocher, A. E.; Letcher, R. J.; Evans, T. J.; Gabrielsen, G. W.;

- Nagy, J.; Stirling, I.; Taylor, M. K.; Muir, D. C. G., *Environ. Sci. Technol.* **2005**, *39*, 5517-5523.
- (10) Sinclair, E.; Mayack, D. T.; Roblee, K.; Yamashita, N.; Kannan, K., *Arch. Environ. Contam. Toxicol.* **2006**, *50*, 398-410.
- (11) Gulkowska, A.; Jiang, Q. T.; So, M. K.; Taniyasu, S.; Lam, P. K. S.; Yamashita, N., *Environ. Sci. Technol.* **2006**, *40*, 3736-3741.
- (12) Yeung, L. W. Y.; So, M. K.; Jiang, G. B.; Taniyasu, S.; Yamashita, N.; Song, M. Y.; Wu, Y. N.; Li, J. G.; Giesy, J. P.; Guruge, K. S.; Lam, P. K. S., *Environ. Sci. Technol.* **2006**, *40*, 715-720.
- (13) Guruge, K. S.; Taniyasu, S.; Yamashita, N.; Wijeratna, S.; Mohotti, K. M.; Seneviratne, H. R.; Kannan, K.; Yamanaka, N.; Miyazaki, S., *J. Environ. Monit.* **2005**, *7*, 371-377.
- (14) So, M. K.; Yamashita, N.; Taniyasu, S.; Jiang, Q. T.; Giesy, J. P.; Chen, K.; Lam, P. K. S., *Environ. Sci. Technol.* **2006**, *40*, 2924-2929.
- (15) Key, B. D.; Howell, R. D.; Criddle, C. S., *Environ. Sci. Technol.* **1998**, *32*, 2283-2287.
- (16) Schultz, M. M.; Higgins, C. P.; Huset, C. A.; Luthy, R. G.; Barofsky, D. F.; Field, J. A., *Environ. Sci. Technol.* **2006**, *40*, 7350-7357.
- (17) Sinclair, E.; Kannan, K., *Environ. Sci. Technol.* **2006**, *40*, 1408-1414.
- (18) Schroder, H. F.; Meesters, R. J. W., *J. Chromatogr. A* **2005**, *1082*, 110-119.
- (19) Tang, C. Y. Y.; Fu, Q. S.; Robertson, A. P.; Criddle, C. S.; Leckie, J. O., *Environ. Sci. Technol.* **2006**, *40*, 7343-7349.

- (20) Tang, C. Y.; Fu, Q. S.; Criddle, C. S.; Leckie, J. O., *Environ. Sci. Technol.* **2007**, *41*, (6), 2008-2014.
- (21) Hori, H.; Yamamoto, A.; Hayakawa, E.; Taniyasu, S.; Yamashita, N.; Kutsuna, S., *Environ. Sci. Technol.* **2005**, *39*, 2383-2388.
- (22) Yamamoto, T.; Noma, Y.; Sakai, S. I.; Shibata, Y., *Environ. Sci. Technol.* **2007**, *41*, 5660-5665.
- (23) Hori, H.; Nagaoka, Y.; Yamamoto, A.; Sano, T.; Yamashita, N.; Taniyasu, S.; Kutsuna, S.; Osaka, I.; Arakawa, R., *Environ. Sci. Technol.* **2006**, *40*, 1049-1054.
- (24) Moriwaki, H.; Takagi, Y.; Tanaka, M.; Tsuruho, K.; Okitsu, K.; Maeda, Y., *Environ. Sci. Technol.* **2005**, *39*, 3388-3392.
- (25) Vecitis, C. D., Park, H., Cheng, J., Mader, B. T., Hoffmann, M. R., *J. Phys. Chem. A* **2008**, *112*, 4261-4270
- (26) Kotronarou, A.; Mills, G.; Hoffmann, M. R., *J. Phys. Chem.* **1991**, *95*, 3630-3638.
- (27) Destailats, H.; Lesko, T. M.; Knowlton, M.; Wallace, H.; Hoffmann, M. R., *Ind. Eng. Chem. Res.* **2001**, *40*, (18), 3855-3860.
- (28) Yasui, K., *J. Chem. Phys.* **2002**, *116*, 2945-2954.
- (29) Vecitis, C. D.; Park, H.; Cheng, J.; Mader, B. T.; Hoffmann, M. R., *J. Phys. Chem. A*, **2008**, *112*, 16850-16857
- (30) Krusic, P. J.; Roe, D. C., *Anal. Chem.* **2004**, *76*, 3800-3803.
- (31) Ciawi, E.; Rae, J.; Ashokkumar, M.; Grieser, F., *J. Phys. Chem. B* **2006**, *110*, 13656-13660.
- (32) Rae, J.; Ashokkumar, M.; Eulaerts, O.; von Sonntag, C.; Reisse, J.; Grieser, F., *Ultrason. Sonochem.* **2005**, *12*, 325-329.

- (33) Anbar, M.; Pecht, I., *J. Phys. Chem.* **1964**, *68*, 1462-1465.
- (34) Buttner, J.; Gutierrez, M.; Henglein, A., *J. Phys. Chem.* **1991**, *95*, 1528-1530.
- (35) Kang, J. W.; Hoffmann, M. R., *Environ. Sci. Technol.* **1998**, *32*, 3194-3199.
- (36) Glockner, V.; Lunkwitz, K.; Prescher, D., *Z. Tenside Surf. Det.* **1989**, *26*, 376-380.
- (37) Ma, J.; Jiang, J.; Pang, S.; Guo, J., *Environ. Sci. Technol.* **2007**, *41*, 4959-4964.
- (38) Perminova, I. V.; Frimmel, F. H.; Kudryavtsev, A. V.; Kulikova, N. A.; Abbt-Braun, G.; Hesse, S.; Petrosyan, V. S., *Environ. Sci. Technol.* **2003**, *37*, 2477-2485.
- (39) Johnson, R. L.; Anschutz, A. J.; Smolen, J. M.; Simcik, M. F.; Penn, R. L., *J. Chem. Eng. Data.* **2007**, *52*, 1165-1170.
- (40) Higgins, C. P.; Luty, R. G., *Environ. Sci. Technol.* **2007**, *41*, 3254-3261
- (41) Weavers, L. K.; Ling, F. H.; Hoffmann, M. R., *Environ. Sci. Technol.* **1998**, *32*, 2727-2733.
- (42) Lesko, T.; Colussi, A. J.; Hoffmann, M. R., *Environ. Sci. Technol.* **2006**, *40*, 6818-6823.
- (43) Staudinger, J.; Roberts, P. V., *Chemosphere* **2001**, *44*, 561-576.
- (44) Yaws, C. L. *Chemical Properties Handbook*; McGraw-Hill: New York, 1999.

Table 6.1. Primary components of the landfill groundwater <sup>a</sup>

pH	6.9-7.9	Dissolved Oxygen	2 mg L <sup>-1</sup>
Temperature	10 – 15 °C	TIC	40 mg L <sup>-1</sup> C
TOC	20 mg L <sup>-1</sup> C	Fe <sub>(s)</sub>	30 mg L <sup>-1</sup>
Acetone	7.15 mg L <sup>-1</sup>	Fe <sub>(aq)</sub>	5-8 mg L <sup>-1</sup>
Diisopropyl Ether	3.54 mg L <sup>-1</sup>	Mn <sub>(s)</sub>	2 mg L <sup>-1</sup>
MEK	3.37 mg L <sup>-1</sup>	Mn <sub>(aq)</sub>	0.5-1.6 mg L <sup>-1</sup>
2-Propanol	2.47 mg L <sup>-1</sup>	NH <sub>4</sub> <sup>+</sup>	0.2-0.6 mg L <sup>-1</sup>
2-Butyl Alcohol	0.92 mg L <sup>-1</sup>	SO <sub>4</sub> <sup>2-</sup>	4-30 mg L <sup>-1</sup>
MIBK	0.55 mg L <sup>-1</sup>	HS <sup>-</sup>	0.2-0.5 mg L <sup>-1</sup>

a. Measurements completed by Pace Analytical.

Table 6.2. Physical and thermodynamic properties of the five organic compounds in Figure 6.2

	$\Gamma_{\max} \times 10^6$ <sup>a</sup> (mol m <sup>-2</sup> )	$K_L$ <sup>b</sup> (m <sup>3</sup> mol <sup>-1</sup> )	$K_{iaw}$ <sup>c</sup>	$C_{p,g}$ <sup>d</sup> (J mol <sup>-1</sup> K <sup>-1</sup> )
Methanol	8.2	$3.9 \times 10^{-4}$	$1.8 \times 10^{-4}$	45.2
Acetone	5.1	$3.2 \times 10^{-3}$	$1.4 \times 10^{-3}$	75.3
Isopropanol	4.8	$7.8 \times 10^{-3}$	$3.2 \times 10^{-4}$	90.0
Ethyl Acetate	4.7	$1.9 \times 10^{-2}$	$6.9 \times 10^{-3}$	117.5
MTBE	6.1	$1.8 \times 10^{-2}$	$2.6 \times 10^{-2}$	131.8
PFOS <sup>e</sup>	5.1	1.97	-	-
PFOA <sup>e</sup>	4.5	0.36	-	-

a.  $\Gamma_{\max}$ , maximum surface concentration in Langmuir isotherm

b.  $K_L$ , Langmuir adsorption constant

c.  $K_{iaw}$ , Henry's law constant at 298 K, Reference 43

d.  $C_{p,g}$ , specific heat capacity at 298 K, Reference 44

e.  $\Gamma_{\max}$  and  $K_L$  values for PFOS and PFOA listed for comparison, Reference 29

Table 6.3. Representative analytical results of quality-control samples

Standard concentration (ppb)	Average measurement (ppb) (n ≥ 4)	Standard deviation (%) (n ≥ 4)
PFOS		
10	9.5	3.3
25	24.1	5.8
50	53.3	2.3
100	104.3	4.6
PFOA		
10	9.6	6.9
25	26.5	3.7
50	51.4	3.7
100	106.1	3.4

Figure 6.1.  $\ln([\text{PFOS}]_t / [\text{PFOS}]_i)$  (a) and  $\ln([\text{PFOA}]_t / [\text{PFOA}]_i)$  (b) vs. time in minutes during sonochemical degradation in Milli-Q water ( $\circ$ ) and landfill groundwater ( $\square$ ) under 354 kHz, 250 W L<sup>-1</sup>, Ar, 10 °C for  $[\text{PFOS}]_i = [\text{PFOA}]_i = 100 \mu\text{g L}^{-1}$ . Each error bar represents one standard deviation from the mean of at least three experiments.

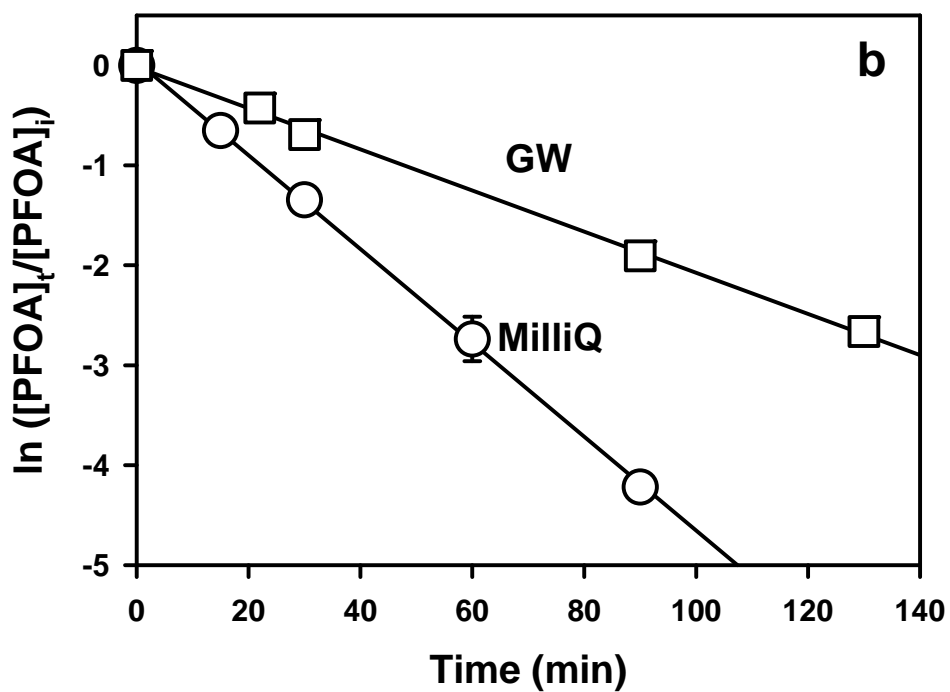
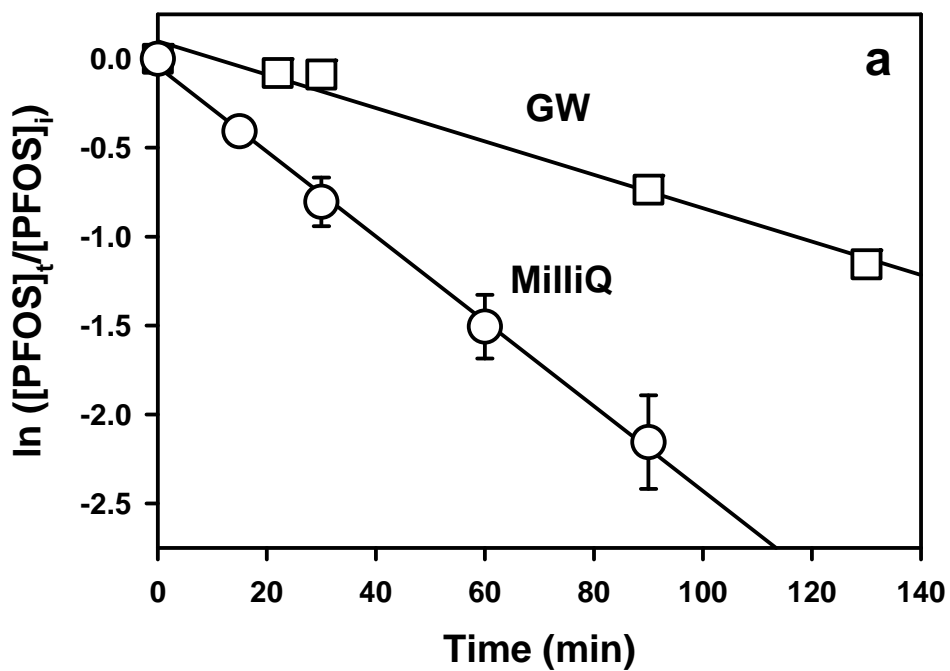


Figure 6.2. The observed pseudo first-order rate constant normalized to the Milli-Q rate constant,  $k^{-\text{PFOS}}/k_0^{-\text{PFOS}}$  (a) and  $k^{-\text{PFOA}}/k_0^{-\text{PFOA}}$  (b), vs. molar concentration of methanol (MeOH, ○), acetone (AC, ▽), isopropyl alcohol (IPA, □), ethyl acetate (EA, ◇), and MTBE (△) in aqueous solutions. The reaction conditions are: 354 kHz, 250 W L<sup>-1</sup>, Ar, 10 °C, and [PFOS]<sub>i</sub> = [PFOA]<sub>i</sub> = 100 μg L<sup>-1</sup>. Note that since the rate constant at 0.2 mol L<sup>-1</sup> MTBE virtually drops to 0, the corresponding data point is not shown in the figure.

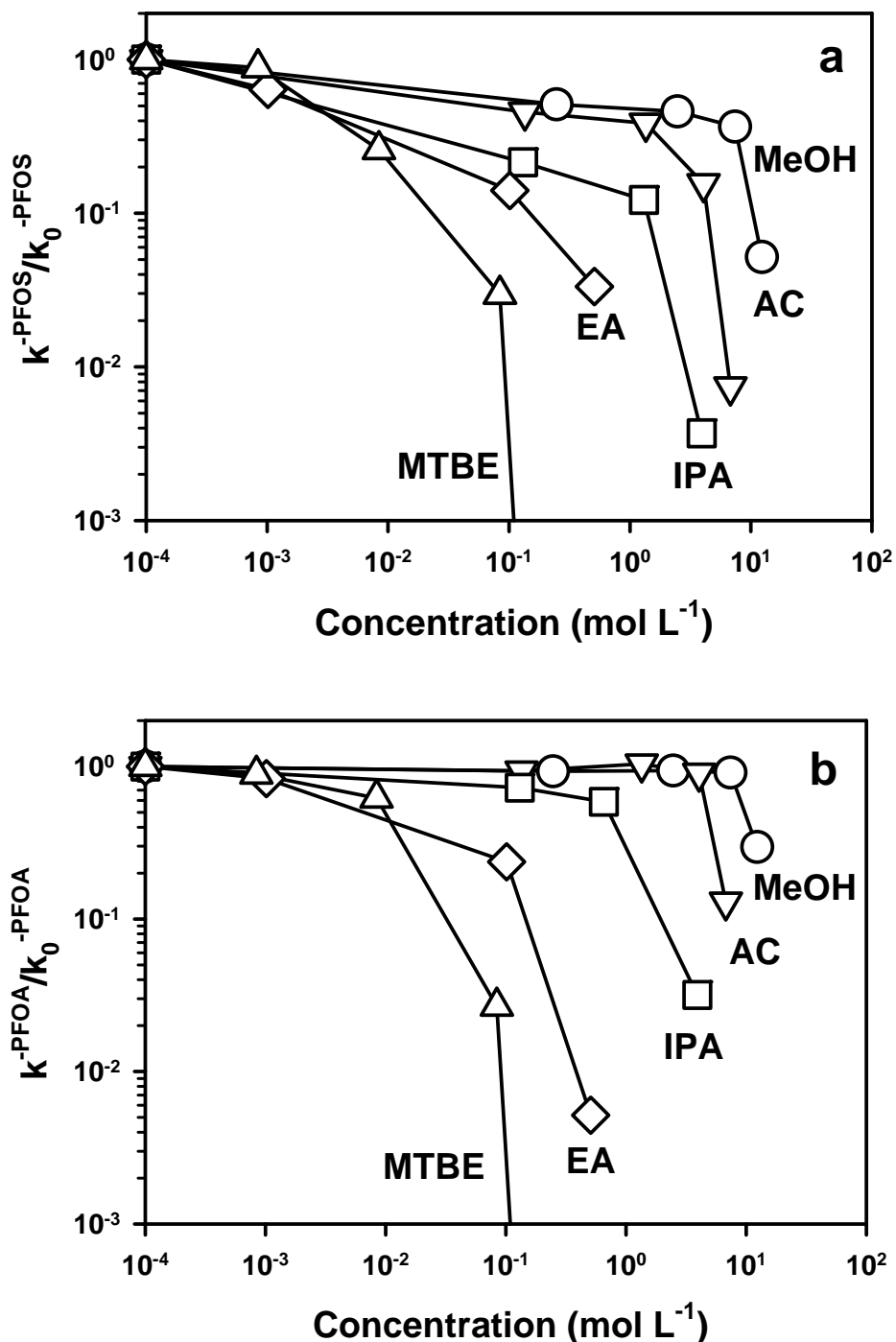


Figure 6.3. The pseudo-first-order rate constant for sonolysis of PFOA (clear bars) and PFOS (filled bars) in Milli-Q, 0.1 mM ethyl benzene (EB), 0.1 mM toluene (TL), 0.1 mM m-xylene (m-XL), 0.1 mM p-xylene (p-XL), 0.1 mM MIBK (MIBK), and 1 mM MIBK (MIBK\*). The reaction conditions are 354 kHz, 250 W L<sup>-1</sup>, Ar, 10 °C, [PFOS]<sub>i</sub> = [PFOA]<sub>i</sub> = 100 µg L<sup>-1</sup>.

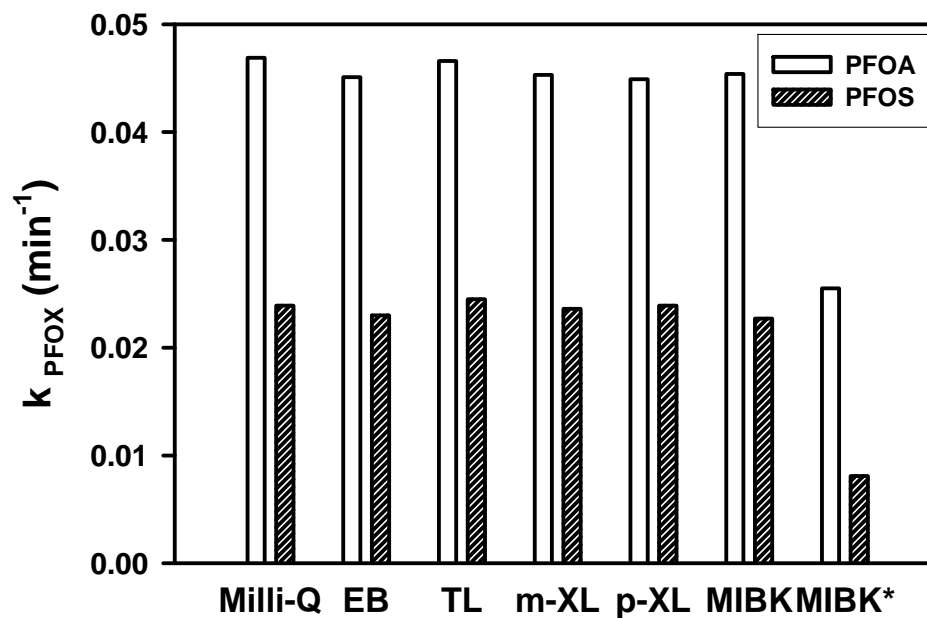


Figure 6.4  $\ln([PFOS]_t / [PFOS]_i)$  (a) and  $\ln([PFOA]_t / [PFOA]_i)$  (b) vs. time in minutes during sonochemical degradation in Milli-Q water ( $\circ$ ), 15 mg L<sup>-1</sup> humic acid solution ( $\nabla$ ), and 15 mg L<sup>-1</sup> fulvic acid solution ( $\square$ ) under 612 kHz, 250 W L<sup>-1</sup>, Ar, 10 °C, for  $[PFOS]_i = [PFOA]_i = 100 \mu\text{g L}^{-1}$ .

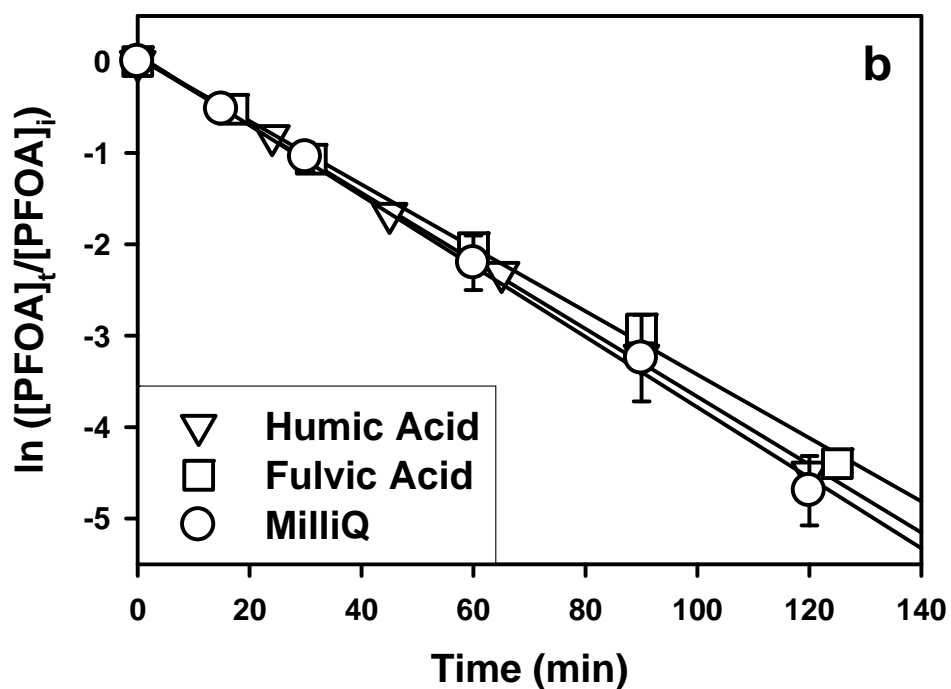
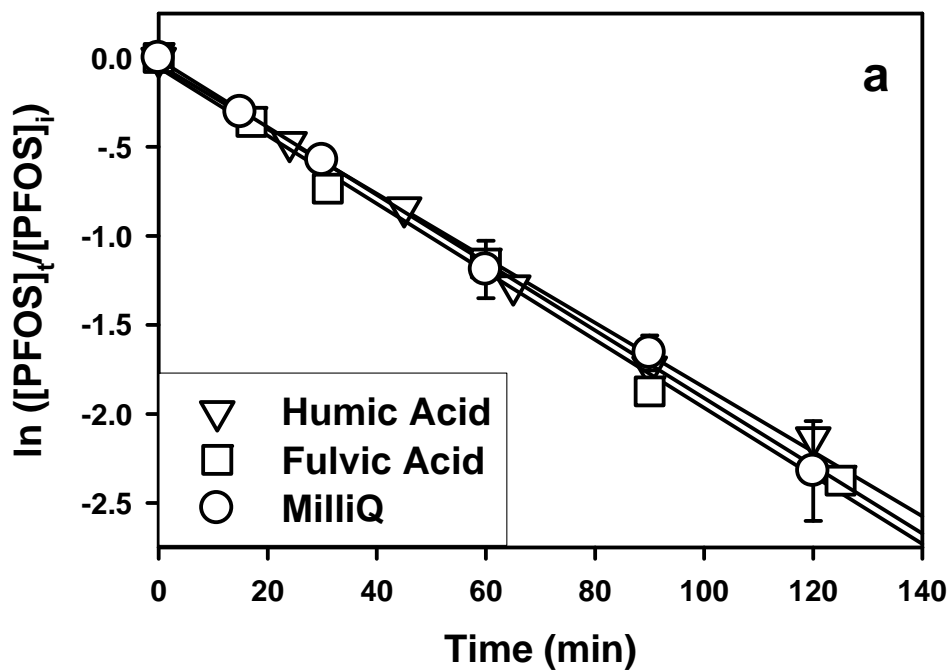


Figure 6.5. (a)  $\ln([PFOS]_t / [PFOS]_i)$  and  $\ln([PFOA]_t / [PFOA]_i)$  (b) vs. time in minutes during the sonolysis ( $\circ$ ) and sonozone ( $\nabla$ ) process of PFOS and PFOA in landfill groundwater. Sonochemical degradation kinetics in Milli-Q ( $\square$ ) are also included for comparison. Other reaction parameters are: 354 kHz, 250 W L<sup>-1</sup>, Ar, 10 °C, and  $[PFOS]_i = [PFOA]_i = 100 \mu\text{g L}^{-1}$ .

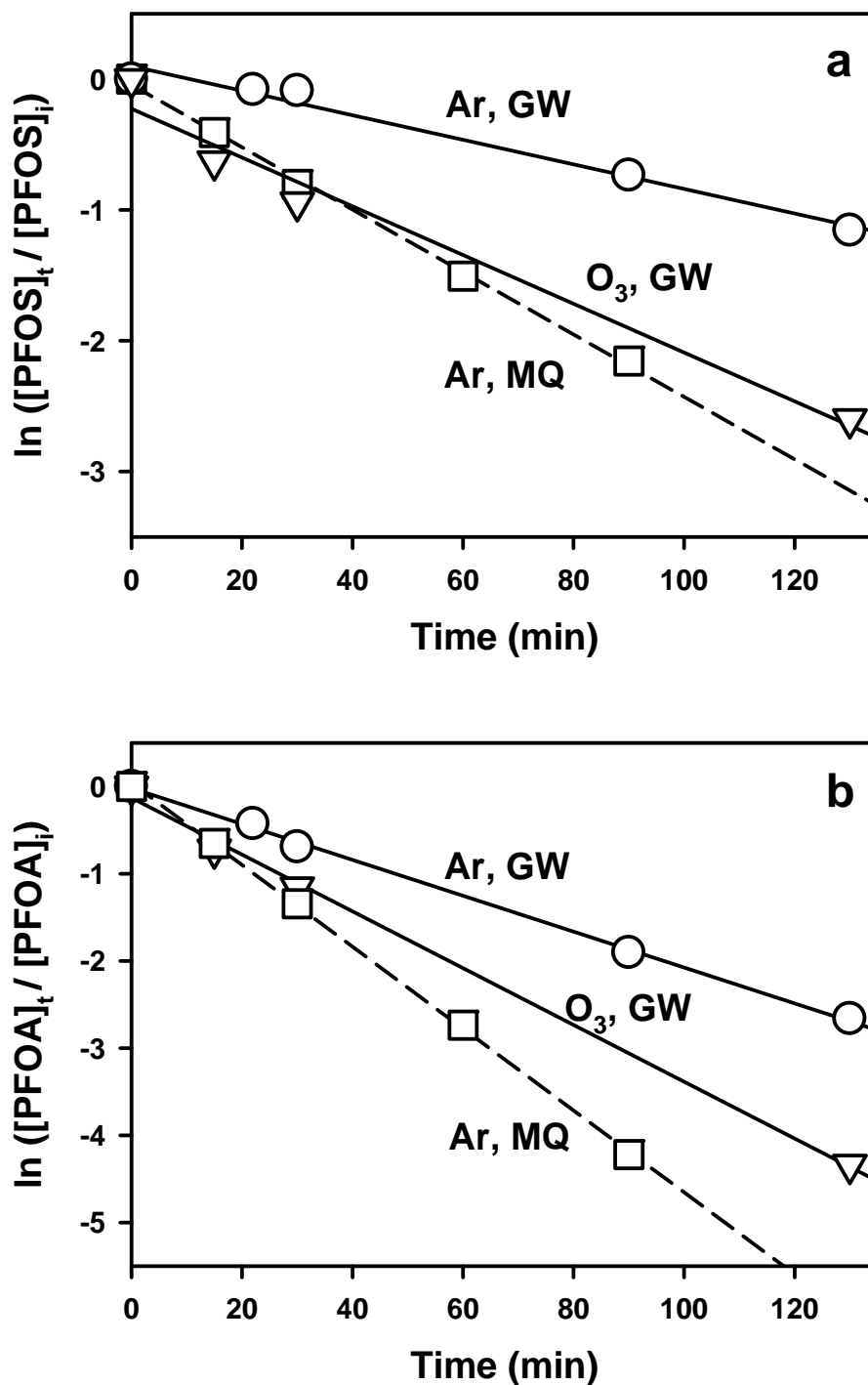


Figure 6.6. Surface tension vs. molar concentration of methanol (○), acetone (▽), isopropyl alcohol (□), ethyl acetate (◇), and MTBE (△) in aqueous solutions, measured at 298 K.

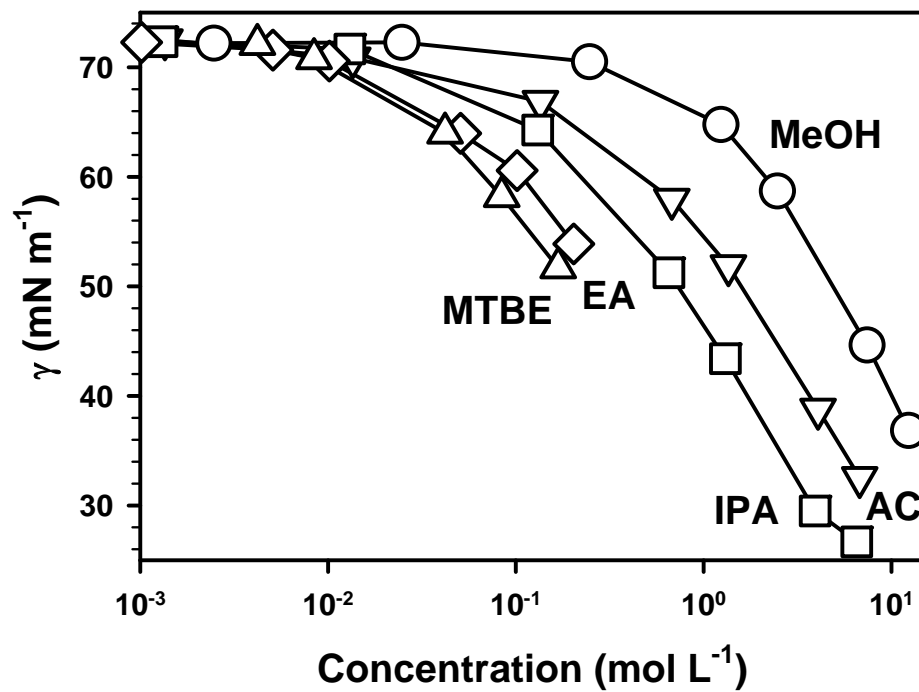


Figure 6.7.  $\ln([PFOS]_t / [PFOS]_i)$  (a) and  $\ln([PFOA]_t / [PFOA]_i)$  (b) vs. time in minutes during sonochemical degradation in Milli-Q water ( $\circ$ ) and landfill groundwater ( $\nabla$ ) under 612 kHz, 250 W L<sup>-1</sup>, Ar, 10 °C for  $[PFOS]_i = [PFOA]_i = 100 \mu\text{g L}^{-1}$ .

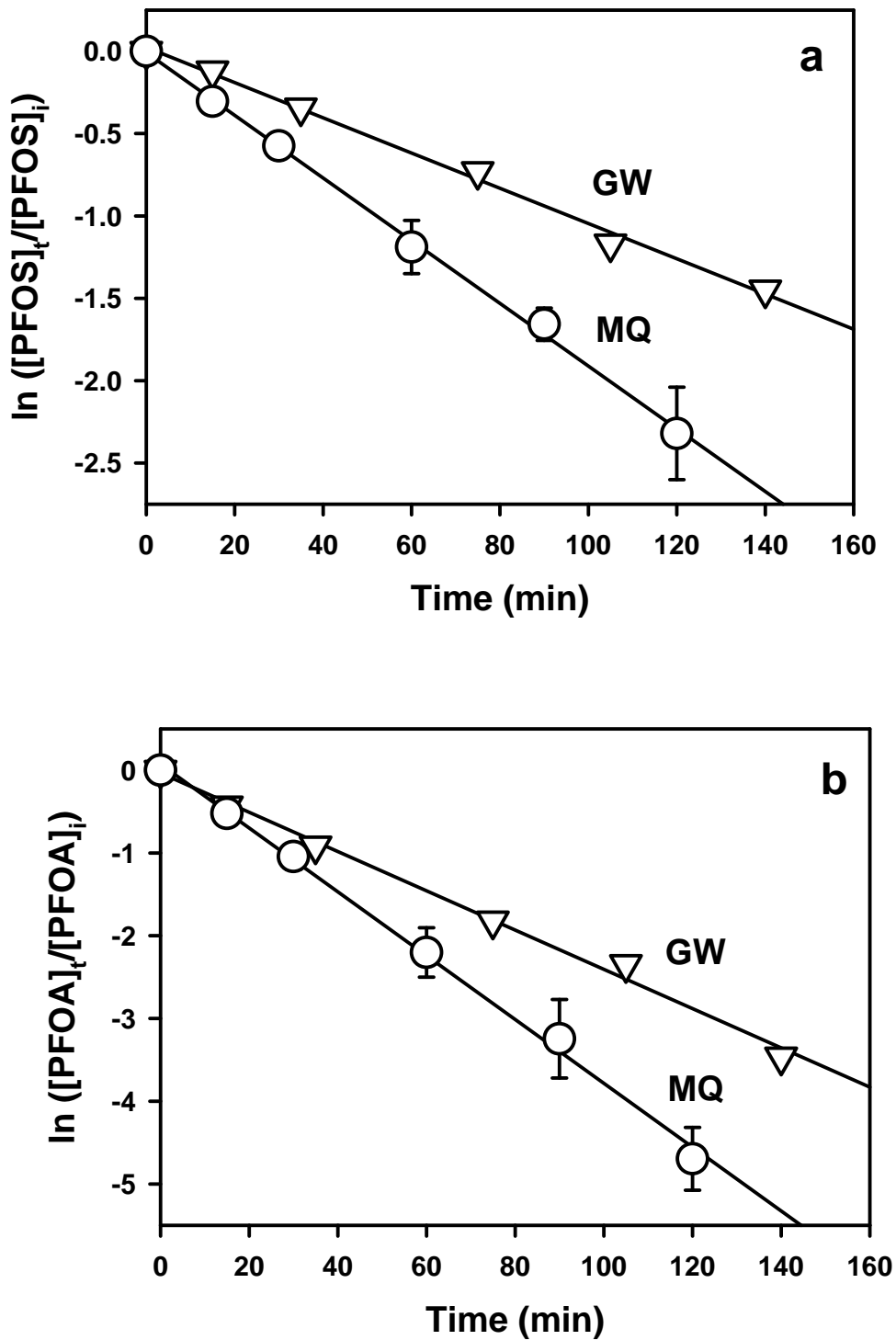


Figure 6.8.  $\ln([PFOS]_t / [PFOS]_i)$  (a) and  $\ln([PFOA]_t / [PFOA]_i)$  (b) vs. time in minutes during sonochemical degradation in Milli-Q water under Ar ( $\circ$ ),  $O_2$  ( $\nabla$ ) and 2.5%  $O_3$  in  $O_2$  ( $\square$ ). Other reaction parameters are: 354 kHz, 250 W L<sup>-1</sup>, 10 °C, and  $[PFOS]_i = [PFOA]_i = 100 \mu\text{g L}^{-1}$ .

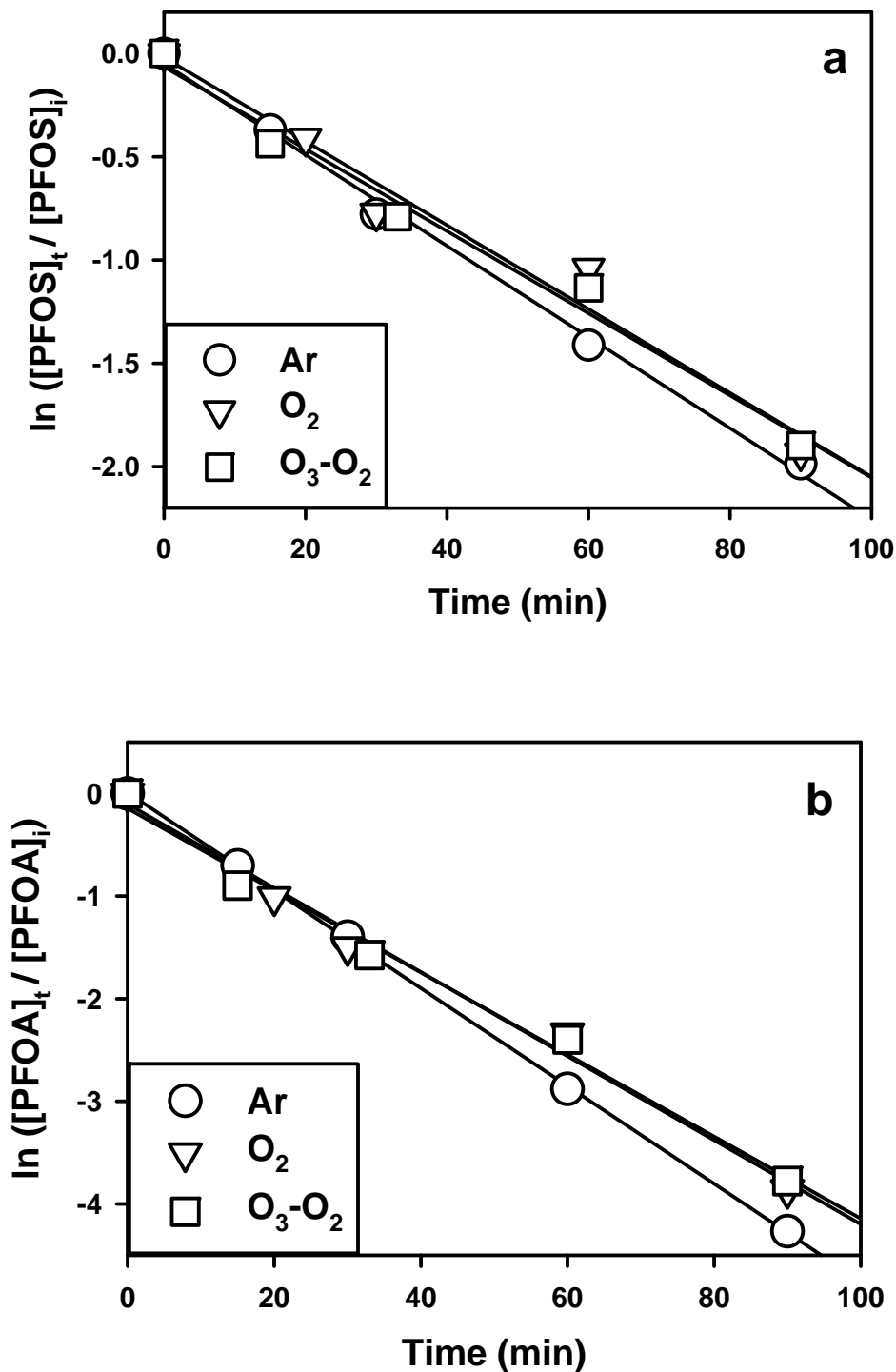


Figure 6.9. The gas phase specific heat capacity  $C_{p,g}$  from  $T = 200$  K to  $T = 1500$  K (a), and the Henry's law constant  $k_{iaw}$  from  $T = 273$  K to  $T = 373$  K (b), for methanol (MeOH,  $\circ$ ), acetone (AC,  $\nabla$ ), isopropyl alcohol (IPA,  $\square$ ), ethyl acetate (EA,  $\diamond$ ), and MTBE ( $\triangle$ ).

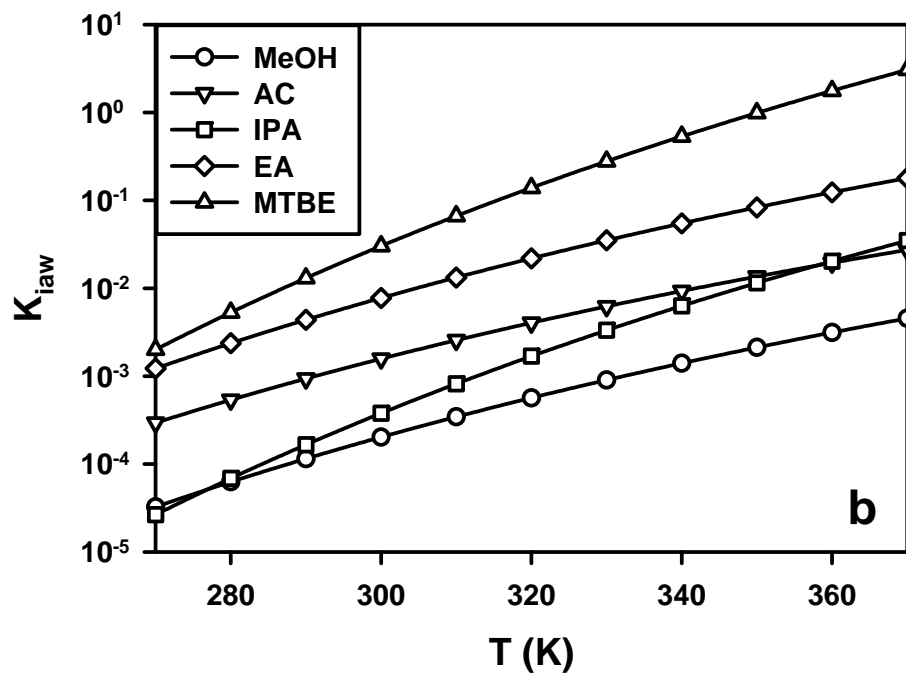
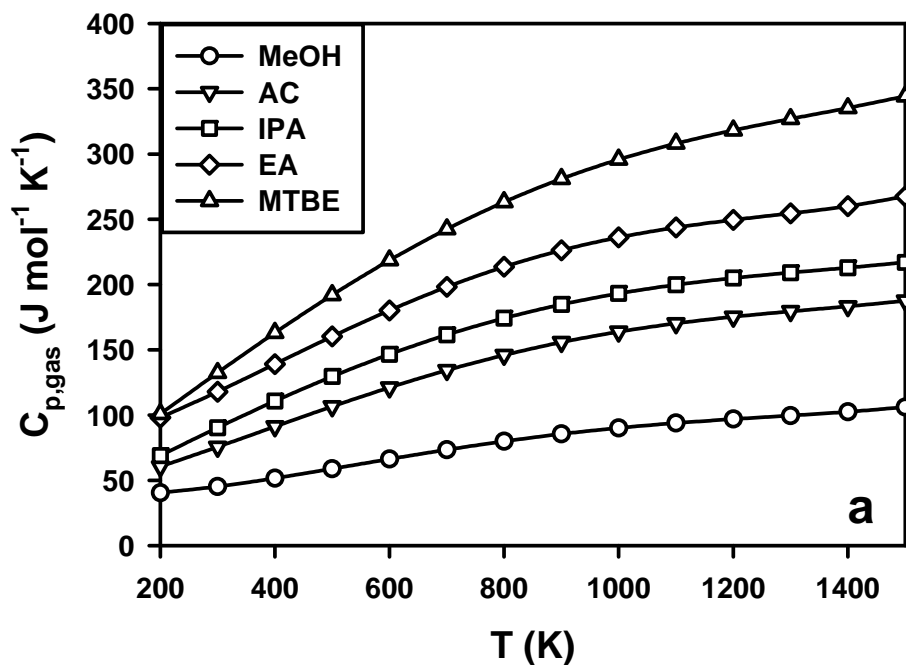
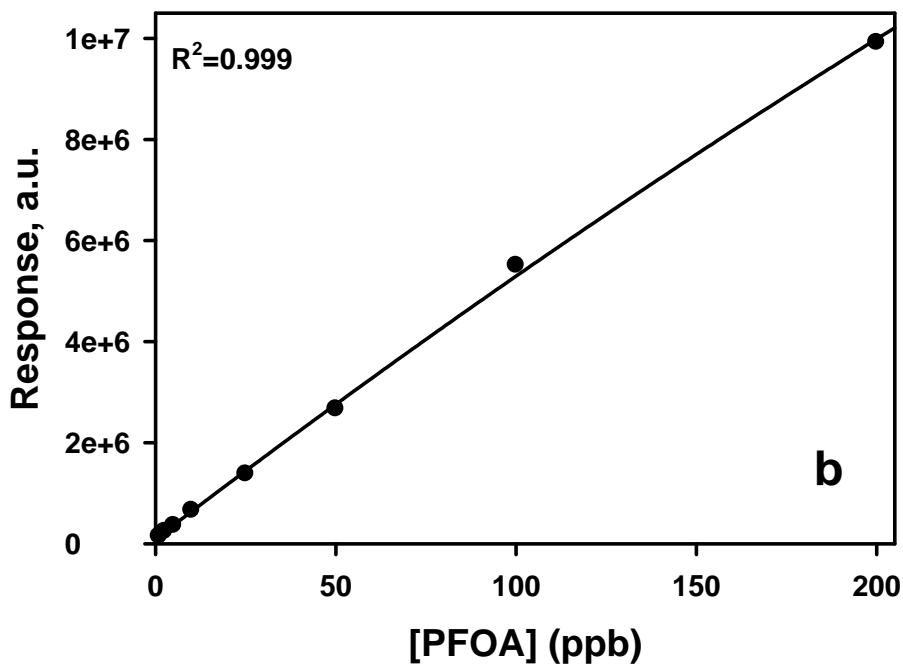
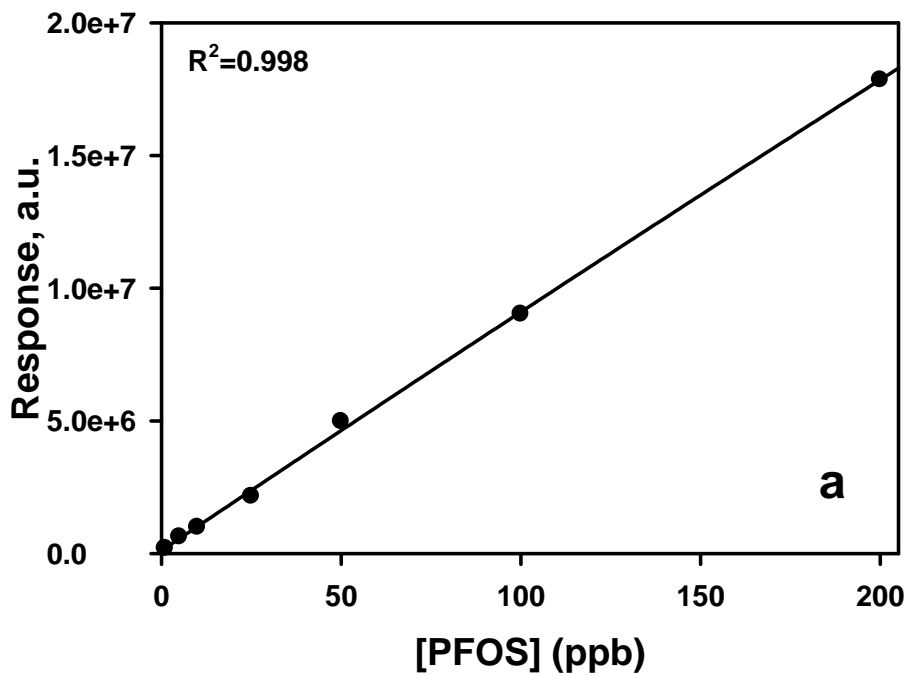


Figure 6.10. The LC/MS calibration curves for PFOS (a) and PFOA (b) from 1 to 200 ppb.



## **Chapter 7**

### **Sonochemical Degradation of Perfluorooctane Sulfonate (PFOS) and Perfluorooctanoate (PFOA) in Groundwater: Kinetic Effects of Matrix Inorganics\***

---

\* The chapter is reproduced with permission from J. Cheng, C. D. Vecitis, H. Park, B. T. Mader, and M. R. Hoffmann, *Environmental Science and Technology*, Article ASAP, December 1, 2009. Copyright © 2009, American Chemical Society

## 7.1 Abstract

Ultrasonic irradiation has been shown to effectively degrade perfluorinated chemicals (PFCs) such as perfluorooctane sulfonate (PFOS) and perfluorooctanoate (PFOA) in aqueous solution. Reduced PFC sonochemical degradation rates in organic-rich groundwater taken from beneath a landfill, however, testify to the negative kinetic effects of the organic groundwater constituents. In this study, the PFOX (X = S or A) sonochemical degradation rates in a groundwater sample with organic concentrations 10 times lower than those in the groundwater taken from beneath a landfill are found to be 29.7% and 20.5% lower, respectively, than the rates in MilliQ water, suggesting that inorganic groundwater constituents also negatively affect PFC sonochemical kinetics. To determine the source of the groundwater matrix effects, we evaluate the effects of various inorganic species on PFOX sonochemical kinetics. Anions over the range of 1-10 mM show Hofmeister effects on the sonochemical degradation rates of PFOX,  $k_{\text{ClO}_4^-}^{-\text{PFOX}} > k_{\text{NO}_3^-}^{-\text{PFOX}} \sim k_{\text{Cl}^-}^{-\text{PFOX}} \geq k_{\text{MQ}}^{-\text{PFOX}} > k_{\text{HCO}_3^-}^{-\text{PFOX}} \sim k_{\text{SO}_4^{2-}}^{-\text{PFOX}}$ . In contrast, common cations at 5 mM have negligible effects. Initial solution pH enhances the degradation rates of PFOX at 3, but has negligible effects over the range of 4 to 11. The observed inorganic effects on sonochemical kinetics are hypothesized to be due to ions' partitioning to and interaction with the bubble-water interface. Finally, it is shown that the rate reduction in the groundwater in this study is primarily due to the presence of bicarbonate and thus can be fully rectified by pH adjustment prior to sonolysis.

## 7.2 Introduction

Perfluorinated chemicals (PFCs) such as perfluorooctane sulfonate (PFOS) and perfluorooctanoate (PFOA) have been manufactured for use in a variety of industrial and consumer applications.<sup>1-2</sup> Due to their environmental persistence, PFOX (X= S or A) have been detected in surface waters at a number of locations at concentrations ranging from  $\text{pg L}^{-1}$  to low  $\text{ng L}^{-1}$ .<sup>3-6</sup> Elevated concentrations (on the order of  $\text{mg L}^{-1}$ ) of PFOX have been measured in surface and ground waters near specific point sources.<sup>7-11</sup>

PFOX are chemically inert due to the strength of the C-F bonds, and there is no direct evidence to date of their biodegradation.<sup>12-13</sup> PFOX cannot be removed by conventional water and wastewater treatment processes that do not utilize activated carbon adsorption or reverse osmosis.<sup>13-15</sup> Various treatment techniques have been proposed to abiotically decompose aqueous PFOX, including direct UV photolysis,<sup>16</sup> thermal- or UV-activated persulfate oxidation,<sup>17-18</sup> reductive defluorination using elemental iron at subcritical water conditions,<sup>19</sup> UV-iodide reduction,<sup>20</sup> B<sub>12</sub>-mediated reduction,<sup>21</sup> and ultrasonic irradiation.<sup>22</sup> It is shown that ultrasonic irradiation can effectively degrade perfluoroalkylsulfonates such as PFOS and perfluoroalkylcarboxylates such as PFOA via pyrolysis under transient high temperatures at the bubble-water interface.<sup>23</sup> Advantages of the sonochemical degradation of PFOX include fast and complete mineralization of PFOX and a wide effective concentration range.<sup>24</sup>

It is important to understand the various environmental matrix effects on PFCs sonochemical degradation in order to better evaluate the prospect of its environmental applications. Our previous study on the sonochemical decomposition of PFOX in organic-rich groundwater taken from beneath a landfill has suggested that volatile

organic constituents decrease the sonochemical degradation rates of PFOX by reducing the average cavitation temperature at the bubble-water interface. Surface-active organic compounds may also compromise the sonochemical degradation efficiency via competitive adsorption onto the bubble-water interface. The rate reductions can be rectified by simultaneous application of ozonation and ultrasonic irradiation.<sup>25</sup>

Herein, we now report on the sonochemical degradation kinetics of PFOX in a distinctively different groundwater sample with a 10-fold lower total organic concentration (TOC) and a much higher electrolyte concentration. We extend the discussion of environmental matrix effects on PFC sonochemical degradation kinetics to include the inorganic ions most commonly found in surface and ground waters. A more comprehensive scheme of matrix effects will enable engineering improvements on the sonochemical degradation efficiency of PFOX in a variety of environmental waters.

### 7.3 Experimental Methods

**Materials.** Ammonium perfluorooctanoate (APFO) and potassium perfluorooctane sulfonate (PFOS-K<sup>+</sup>) standards were provided by 3M. The sodium salts of chloride, nitrate, perchlorate, sulfate, and bicarbonate, ammonium chloride, magnesium chloride, and calcium chloride (Sigma Aldrich, 99% or higher purity) were used as received. Sep-Pak Vac tC18 (6 cc, 1 g) solid phase extraction (SPE) cartridges were purchased from Waters. Purified water (18.2 M $\Omega$  cm<sup>-1</sup> resistivity) was prepared from a Millipore MilliQ Gradient water purification system.

**Sonolysis.** The sonochemical degradation kinetics of PFOX was measured in MilliQ, aqueous electrolyte solutions, and groundwater. Ultrasonication was performed in a 600

mL jacketed glass reactor at a frequency of 612 or 354 kHz using an Allied Signal - ELAC Nautik ultrasonic transducer. The applied power density was  $250 \text{ W L}^{-1}$  with an average energy transfer efficiency of  $72 \pm 5\%$  as determined by calorimetry. The PFOX solutions were maintained at  $10 \pm 2 \text{ }^\circ\text{C}$  by water cooling and sparged with argon 30 minutes prior to and during the course of the reaction. In all experiments the initial concentrations of PFOS and PFOA were spiked to approximately  $100 \text{ } \mu\text{g L}^{-1}$ , or 200 nM and 240 nM, respectively.

***Solid Phase Extraction for Groundwater Samples.*** Groundwater samples taken during the sonochemical reactions were purified by SPE using Sep-Pak Vac tC18 cartridges (6 cc, 1 g) to remove matrix components that may interfere with the LC/MS analysis. The SPE cartridges were conditioned by passing 10 mL methanol, and then 50 mL water through the cartridges at a flow rate of  $2 \text{ mL min}^{-1}$ . The analytical samples were subsequently loaded onto the wet cartridges at  $1 \text{ mL min}^{-1}$ . The columns were dried with nitrogen gas for 5 minutes, rinsed with 10 mL 20% methanol in water at  $2 \text{ mL min}^{-1}$ , and dried with nitrogen gas for another 30 minutes. The analytes were eluted with methanol at  $1 \text{ mL min}^{-1}$ , and 4.0 mL samples were collected into 14 mL polypropylene tubes (Falcon). The recovery rates of PFOX were above 90%, consistent with literature values.<sup>26</sup> All steps except sample loading were performed on a Caliper AutoTrace SPE Work Station.

***LC/MS Analyses.*** The PFOX concentrations were quantified by LC/MS. For MilliQ and electrolyte solutions, sample aliquots ( $700 \text{ } \mu\text{L}$ ) were withdrawn from the reactor using disposable plastic syringes, transferred into  $750 \text{ } \mu\text{L}$  polypropylene autosampler vials, and sealed with PTFE septum crimp caps (Agilent). Groundwater samples were

purified by SPE before they were transferred to the autosampler vials. 20  $\mu\text{L}$  of samples were injected into an Agilent 1100 HPLC for separation on a Thermo-Electron Betasil C18 column (100 mm  $\times$  2.1 mm, 5  $\mu\text{m}$ ). The flow rate was maintained at 0.3  $\text{mL min}^{-1}$  with a mobile phase of 2 mM ammonium acetate in water (A) and methanol (B). The eluent gradient started with 5% B over the first minute, was ramped to 90% B over 10 minutes and held for 2.5 minutes, then ramped back to 5% B over 0.5 minute and held for 3 minutes, and finished with a 3 minute post-time. Chromatographically separated samples were analyzed by an Agilent Ion Trap in negative mode monitoring for the perfluorooctanesulfonate molecular ion ( $m/z = 499$ ) and the decarboxylated perfluorooctanoate ( $m/z = 369$ ). Instrumental parameters were set at the following levels: nebulizer pressure 40 PSI, drying gas flow rate 9  $\text{L min}^{-1}$ , drying gas temperature 325  $^{\circ}\text{C}$ , capillary voltage +3500 V, and skimmer voltage  $-15$  V. Quantification was based on a 8-point calibration curve spanning the 1 to 200  $\mu\text{g L}^{-1}$  range fitted to a quadratic with  $X^{-1}$  weighting. Analytical standards, quality control, and reagent blank samples were included in each analytical batch along with the unknown samples. Further analytical details were described in a previous paper.<sup>23</sup>

#### 7.4 Results

**Groundwater Characterization.** The groundwater used in the study was sampled from a well in the city of Oakdale, MN. The groundwater sample was stored in darkness at 4 $^{\circ}\text{C}$  in a sealed container with minimal headspace. As summarized in Table 7.1, the TOC concentration of the groundwater sample is 1.5  $\text{mg L}^{-1}$ , about an order of magnitude lower than that of groundwater taken from beneath a landfill that was used in our previous study,<sup>25</sup> whereas the concentrations of common groundwater ions such as

bicarbonate, sulfate, chloride, calcium, and magnesium are much higher than in the previous study. PFOX were spiked into the groundwater to increase the concentration to approximately  $100 \mu\text{g L}^{-1}$ , or 200 and 240 nM for PFOS and PFOA, respectively.

***Sonolysis of Groundwater PFOS and PFOA.*** The sonochemical degradation kinetics of PFOX in groundwater and MilliQ water are shown in Figure 7.1a and b, respectively ( $f = 612 \text{ kHz}$ ,  $PD = 250 \text{ W L}^{-1}$ ,  $T = 10 \text{ }^\circ\text{C}$ , argon). The sonochemical degradation of groundwater PFOX follows pseudo-first-order kinetics as is observed in MilliQ. However, the pseudo-first-order rate constant for groundwater PFOS at 612 kHz,  $k_{\text{GW}}^{\text{-PFOS}} = 0.0135 \text{ min}^{-1}$ , is 70.3% of the MilliQ rate constant,  $k_{\text{MQ}}^{\text{-PFOS}} = 0.0192 \text{ min}^{-1}$ . Similar results are observed for PFOA, where the rate constant for groundwater PFOA,  $k_{\text{GW}}^{\text{-PFOA}} = 0.0291 \text{ min}^{-1}$ , is 79.5% of the MilliQ rate constant,  $k_{\text{MQ}}^{\text{-PFOA}} = 0.0366 \text{ min}^{-1}$ . At a frequency of 354 kHz, a similar reduction in rate constant is observed when comparing sonolysis in MilliQ versus in groundwater (Figure 7.6).

***Sonolysis of PFOS and PFOA in Aqueous Electrolyte Solutions.*** In order to evaluate the electrolytes most responsible for the rate reduction in the groundwater sample, the sonochemical degradation kinetics of PFOX in selected aqueous electrolyte solutions were evaluated under the same sonolysis conditions as in previous experiments. Figure 7.2a and b shows the concentration-dependent effect of 1-10 mM  $\text{Na}_2\text{SO}_4$ ,  $\text{NaHCO}_3$ ,  $\text{NaCl}$ ,  $\text{NaNO}_3$ , or  $\text{NaClO}_4$  on the sonochemical degradation rates of PFOX. The sonochemical rate constants for PFOX increase steadily as the concentration of  $\text{NaClO}_4$  increases from 0 to 10 mM, with the rate enhancement at 10 mM being 47% for PFOS and 11% for PFOA. In aqueous solutions of  $\text{NaNO}_3$  and  $\text{NaCl}$ , the sonochemical

degradation rates for PFOS are moderately enhanced, whereas those for PFOA are identical within experimental error to the MilliQ rate. NaHCO<sub>3</sub> and Na<sub>2</sub>SO<sub>4</sub> are found to reduce the sonochemical rate constants for PFOX. Thus, with Na<sup>+</sup> being the common cation, the overall effect of anions on the differential sonochemical degradation rate constants relative to those in MilliQ for PFOX,  $\Delta k_i^{-\text{PFOX}} = k_i^{-\text{PFOX}} - k_{\text{MQ}}^{-\text{PFOX}}$ , follows the order:  $\Delta k_{\text{ClO}_4^-}^{-\text{PFOX}} > \Delta k_{\text{NO}_3^-}^{-\text{PFOX}} \sim \Delta k_{\text{Cl}^-}^{-\text{PFOX}} \geq 0 > \Delta k_{\text{HCO}_3^-}^{-\text{PFOX}} > \Delta k_{\text{SO}_4^{2-}}^{-\text{PFOX}}$ . The negative effects of SO<sub>4</sub><sup>2-</sup> and HCO<sub>3</sub><sup>-</sup> on PFOA degradation rates are of similar magnitude. This order is consistent with the Hofmeister series, which was initially observed for specific ion effects on protein solubility and now has been extended to a number of other systems including ion partitioning between bulk water and the air-water interface.<sup>27-28</sup> It is also of note that the specific anion effects on the sonochemical degradation rates, though similar in order, are greater for PFOS than for PFOA.

In contrast, the effect of cations on the sonochemical degradation rates of PFOX is much less pronounced than that of anions over the same concentration range. As shown in Figure 7.3, no significant difference in sonochemical rate constant is observed in aqueous solutions of NaCl and NH<sub>4</sub>Cl at 5 mM and of CaCl<sub>2</sub> and MgCl<sub>2</sub> at 2.5 mM.

The effect of solution pH, as adjusted by addition of NaOH or HCl, on the sonochemical degradation rates of PFOX in MilliQ water was also examined. As is shown in Figure 7.4, the sonochemical rate constants remain unchanged within experimental error as a function of pH over the range of 4 to 11. At pH 3, the rate constants increase by 23.4% and 13.7% for PFOS and PFOA, respectively, relative to those in MilliQ water at pH 7. For comparison, the rate enhancement in the 1 mM HCl solution is significantly greater than that in the 1 mM NaCl solution, indicating the role of

increased proton concentration. Also, acidification increases the degradation rate of PFOS to a greater extent, consistent with the effect of anions reported in this text as well as that of organics reported in our previous study.<sup>25</sup> Together, these suggest that PFOS sonochemical kinetics is more susceptible to matrix effects.

***Sonolysis of PFOS and PFOA in Groundwater after pH Adjustment.*** Given that bicarbonate ( $pK_1 = 6.3$ ,  $pK_2 = 10.3$ ), at approximately 2.2 mM, is the primary anionic component of the groundwater sample, we evaluated the effect of bicarbonate removal by pH adjustment, both acidification and alkalization, on the sonochemical degradation rates of PFOX, as shown in Figure 7.5a and b. Sonolysis conditions were the same as in previous experiments. For the alkalization experiments, the groundwater pH was adjusted from its initial value of 8.0 to 11.0 by NaOH and the white  $\text{CaCO}_3$  precipitate thus formed was removed by filtration. The PFOS and PFOA sonochemical rate constants in the alkaline groundwater supernatant are rectified to 101.0% and 94.0%, respectively, of the MilliQ rates. For the acidification experiments, the groundwater was acidified to pH 3.9 by HCl to convert bicarbonate to carbon dioxide (titration curve shown in Figure 7.7), which was then removed from solution by bubbling with argon. The acidification may also have removed volatile organic acids from the groundwater through a similar mechanism. The sonochemical degradation rates are enhanced to 133.9% for PFOS and 104.4% for PFOA relative to the MilliQ rates. Both experiments suggest that bicarbonate is primarily responsible for the reduction in PFOX sonochemical kinetics in the groundwater in this study.

## **7.5 Discussion**

A sonochemical kinetic model is defined and utilized to better understand the specific ion effects observed in Figures 7.2 to 7.4. Assuming that interfacial pyrolysis is the only viable sonochemical degradation pathway for PFOX, and that adsorption to the bubble-water interface is required for interfacial pyrolysis to occur,<sup>23</sup> the sonochemical degradation rate of PFOX can be expressed as eq. (7.1).

$$\frac{d[\text{PFOX}]}{dt} = -k_{app}^{-\text{PFOX}}[\text{PFOX}] = -k_{\Delta}^{-\text{PFOX}}\theta^{\text{PFOX}} \quad (7.1)$$

$k_{app}^{-\text{PFOX}}$  is the apparent pseudo first-order rate constant,  $k_{\Delta}^{-\text{PFOX}}$  the maximum absolute rate, i.e., the pyrolytic unimolecular decomposition rate attained when all of the transiently cavitating bubble surface sites are occupied by PFOX molecules, and  $\theta^{\text{PFOX}}$  the fraction of bubble-water interface sites occupied by PFOX molecules.  $k_{\Delta}^{-\text{PFOX}}$  is defined by eq. (7.2).

$$k_{\Delta}^{-\text{PFOX}} = [S]A^{\text{PFOX}} \exp\left(-E_A^{\text{PFOX}} / R\langle T_{\text{int}}^{\text{bub}} \rangle\right) \quad (7.2)$$

where [S] is the molarity of transiently cavitating bubble-water interfacial sites,  $A^{\text{PFOX}}$  the preexponential constant in  $\text{s}^{-1}$ ,  $E_A^{\text{PFOX}}$  the activation energy for the pyrolytic cleavage of the ionic head group of PFOX in  $\text{kJ mol}^{-1}$ ,<sup>29-30</sup> and  $\langle T_{\text{int}}^{\text{bub}} \rangle$  the average interfacial temperature during the high-temperature period of a transient bubble collapse.<sup>31-32</sup> In the presence of other matrix components that may compete for bubble-water interfacial sites,  $\theta^{\text{PFOX}}$  is represented by eq. (7.3).

$$\theta^{\text{PFOX}} = \frac{K^{\text{PFOX}}[\text{PFOX}]}{1 + K^{\text{PFOX}}[\text{PFOX}] + \sum_i K^i[i]} \quad (7.3)$$

$K^i$  is the bulk water to air-water interface partitioning coefficient for species  $i$ . It has been observed that sonochemical partitioning coefficients,  $K_{\text{sono}}^{\text{PFOX}}$ , are enhanced over equilibrium partitioning coefficients,  $K_{\text{eq}}^{\text{PFOX}}$ , due to high-velocity radial bubble oscillations.<sup>24</sup>

Our previous study on the effect of groundwater taken from beneath a landfill on PFOX sonochemical kinetics suggests that matrix organics may reduce PFOX degradation kinetics through reduction both in  $\langle T_{\text{int}}^{\text{bub}} \rangle$  due to energy consumption by volatile organics in the bubble vapor phase, and in  $\theta^{\text{PFOX}}$  due to competition for bubble-water interfacial sites by surface-active organics.<sup>25</sup> As for aqueous electrolyte solutions, since ions cannot partition to the bubble vapor phase, temperature effects, if present, should be caused by other mechanisms. Given that the more surface active  $\text{ClO}_4^-$  actually increases the PFOX degradation rates whereas the less surface active  $\text{SO}_4^{2-}$  and  $\text{HCO}_3^-$  reduce the PFOX degradation rates, the surface competition effect is minimal, i.e.,  $\sum_i K^i [i] \ll 1$  in eq. (7.3).

Addition of electrolytes such as NaCl has been reported to enhance both the sonoluminescence intensity<sup>33-34</sup> and the sonochemical degradation rates of compounds such as phenol and 2,4-dinitrophenol.<sup>35-36</sup> The enhancement has been explained by the effect of electrolytes on gas solubility in aqueous solution and by the “salting out” effect that increases the concentration of organics at the bubble-water interface, respectively. However, both effects were observed at significantly higher electrolyte concentrations than those used in this study.

Observations that anions have both positive and negative effects on PFOX sonochemical kinetics indicate specific ion effects. Relative anionic effects on PFOX sonochemical kinetics (Figure 7.2) follow the Hofmeister series. We hypothesize that these effects are correlated to the ion partitioning between the bulk water and the bubble-water interface, which will affect bubble-water interfacial properties such as surface potential and interfacial water structure. For example,  $\text{ClO}_4^-$  is highly enriched at the air-water interface relative to the bulk solution,<sup>28</sup> and therefore yields a more negatively charged bubble-water interface. The increase in negative surface potential at the bubble-water interface enhances electrostatic repulsion between cavitating bubbles, thus reducing their propensity to coalesce.<sup>37</sup> This further results in a population of smaller bubbles with greater surface area to volume ratio and thus a greater number of surface sites available for PFOX pyrolysis, i.e., greater  $[S]$  in eq. (7.2). Well hydrated and thus less surface active anions such as  $\text{SO}_4^{2-}$  will reduce the negative potential at the bubble-water interface. The results in Figure 7.2 are qualitatively consistent with measured surface potentials of various aqueous electrolyte solutions.<sup>38</sup>

A quantitative explanation based on the surface potential measurements is difficult to establish, not only because the exact relationship between  $[S]$  and bubble-water interfacial potential is unclear, but also because surface potential measurements yield equilibrium air-water interface partitioning values, whereas ion partitioning to the ultrasonically cavitating bubble interface is kinetically constrained. Cavitating bubble lifetimes (100  $\mu\text{s}$ ) are much shorter than ion partitioning half-lives ( $>1$  ms), and high-velocity bubble radial oscillations will dominate over chemical diffusion. Thus, relative

differences in equilibrium surface potential can only be used as a rough guideline for adsorption processes at acoustically cavitating bubble interfaces.

In addition, the observed anionic effects on PFOX sonochemical kinetics may also be due to the effect of anions on the interfacial water structure. The propensity of anions to orient interfacial water has been observed to follow the Hofmeister series:  $\text{NaClO}_4 > \text{NaNO}_3 > \text{NaCl} > \text{pure water} > \text{Na}_2\text{SO}_4$ .<sup>39</sup> Altering the interfacial water structure may affect the amount of water vapor transported into the bubble, and thus  $\langle T_{\text{int}}^{\text{bub}} \rangle$ . Alterations in water structure and composition at the bubble-water interface may also affect heat transfer from the bubble vapor to the bulk liquid. The resulting changes in average bubble-water interfacial temperatures during transient cavitation will subsequently affect the observed sonochemical rates of PFOX degradation.

The negligible effect of cations on PFOX sonochemical kinetics, as shown in Figure 7.3, is likely due to their much greater degree of hydration that limits their interactions with the sonochemically active bubble-water interface. This is consistent with observations in other systems that the Hofmeister effects of small cations, if present, are much smaller in magnitude than those of anion.<sup>39-41</sup>

The enhanced PFOX sonochemical kinetics at pH below 4 may also result from the interactions of proton with the bubble-water interface. The interface is believed to become increasingly positively charged as the pH drops below 4, despite the uncertainty over the extent of proton and hydroxide enhancement at the bubble-water interface.<sup>42-43</sup> The increasingly positive surface charge may not only reduce bubble coalescence, thus increasing  $[S]$  in eq. (7.2), but also attract more of the oppositely charged PFOX to the surface, thus increasing  $\theta^{\text{PFOX}}$  in eq. (7.3). It is also of note that at pH 3, PFOA may form

a  $(\text{PFO})_2\text{H}^-$  cluster, which may affect the overall sonochemical degradation rate of PFOA.<sup>44</sup>

Bicarbonate, whose concentration in the groundwater sample is nearly 2 orders of magnitude greater than TOC, is likely to be the primary matrix component affecting PFOX sonochemical kinetics as shown in Figure 7.1. Indeed, the rate reduction in a 2 mM  $\text{HCO}_3^-$  aqueous solution as shown in Figure 7.2,  $k_{\text{HCO}_3^-}^{-\text{PFOS}} / k_{\text{MQ}}^{-\text{PFOS}} = 0.82$  and  $k_{\text{HCO}_3^-}^{-\text{PFOA}} / k_{\text{MQ}}^{-\text{PFOA}} = 0.86$ , does account for a major part of the rate reduction observed in the groundwater,  $k_{\text{GS}}^{-\text{PFOS}} / k_{\text{MQ}}^{-\text{PFOS}} = 0.70$  and  $k_{\text{GS}}^{-\text{PFOA}} / k_{\text{MQ}}^{-\text{PFOA}} = 0.80$ . Since the primary sonochemical degradation mechanism for PFOX is interfacial pyrolysis, the effect of bicarbonate on PFOX sonochemical kinetics is likely due to its impact on the interfacial pyrolysis conditions. The effect of bicarbonate as OH radical scavenger, while having been shown in general to reduce sonochemical degradation rates,<sup>45</sup> is inconsequential in this case, because the reaction of PFOX with OH radical is slow.<sup>23</sup> Other groundwater matrix components such as sulfate and organic compounds may have minor impacts on the sonochemical degradation rates of PFOX.

The sonochemical degradation rates post-acidification are even higher than the MilliQ rates, presumably due to a combination of factors including the effect of pH and  $\text{Cl}^-$ . First, at pH 3.9 the sonochemical degradation rates may be slightly enhanced. Second, the addition of 2.5 mM  $\text{Cl}^-$  to adjust pH may also increase the degradation rates, but as shown in Figure 7.2, the rate enhancement in MilliQ upon addition of 2 mM  $\text{Cl}^-$  is smaller than 5%. Since both factors combined cannot fully account for the observed rate enhancement, synergistic effects from the groundwater matrix are likely to be present.

The observed reduction in PFOX sonochemical degradation rates in groundwater relative to MilliQ rates in the range of 20%–30% is moderate considering the relative concentrations of PFOX ( $100 \mu\text{g L}^{-1}$ ) to the various groundwater components: on a mass basis,  $\text{TOC} / [\text{PFOX}] = 15$ ,  $[\text{SO}_4^{2-}] / [\text{PFOX}] = 180$ , and  $[\text{HCO}_3^-] / [\text{PFOX}] = 1400$ . It is found in our previous study that even in a groundwater with  $\text{TOC} / [\text{PFOX}] > 100$ , the sonochemical PFOX degradation rates are decreased by no more than 60%. Some other oxidative or reductive degradation methods<sup>46</sup> may be more significantly affected by matrix compounds at these concentrations, since reactions rates with these compounds greatly exceed reaction rates with PFOX. In the example of UV-persulfate oxidation where PFOX is effectively degraded by reaction with sulfate anion radical, the matrix effect of  $\text{HCO}_3^-$  is expected to be much more significant because sulfate anion radical reacts with PFOX with a second-order rate constant of  $10^4 \text{ M}^{-1} \text{ s}^{-1}$  and with  $\text{HCO}_3^-$  with a second-order rate constant of  $9 \times 10^6 \text{ M}^{-1} \text{ s}^{-1}$ .<sup>47-48</sup> Finally, the decrease in PFOX sonochemical degradation rates due to bicarbonate can be effectively rectified by a simple pH adjustment. Both alkalization and acidification have been observed to rectify rates to at least those observed in MilliQ, with acidification even amplifying rates over those expectations.

## 7.6 Acknowledgements

The authors would like to thank 3M for the financial support and Dr. Nathan Dalleska and the Caltech Environmental Analysis Center for technical assistance in sample analysis.

## 7.7 References

- (1) Houde, M.; Martin, J. W.; Letcher, R. J.; Solomon, K. R.; Muir, D. C. G., *Environ. Sci. Technol.* **2006**, *40*, 3463-3473.
- (2) Prevedouros, K.; Cousins, I. T.; Buck, R. C.; Korzeniowski, S. H., *Environ. Sci. Technol.* **2006**, *40*, 32-44.
- (3) So, M. K.; Taniyasu, S.; Yamashita, N.; Giesy, J. P.; Zheng, J.; Fang, Z.; Im, S. H.; Lam, P. K. S., *Environ. Sci. Technol.* **2004**, *38*, 4056-4063.
- (4) Murakami, M.; Imamura, E.; Shinohara, H.; Kiri, K.; Muramatsu, Y.; Harada, A.; Takada, H., *Environ. Sci. Technol.* **2008**, *42*, 6566-6572.
- (5) Furdui, V. I.; Helm, P. A.; Crozier, P. W.; Lucaciu, C.; Reiner, E. J.; Marvin, C. H.; Whittle, D. M.; Mabury, S. A.; Tomy, G. T., *Environ. Sci. Technol.* **2008**, *42*, 4739-4744.
- (6) Yamashita, N.; Kannan, K.; Taniyasu, S.; Horii, Y.; Petrick, G.; Gamo, T. In *A Global Survey of Perfluorinated Acids in Oceans*, 2005; Pergamon-Elsevier Science Ltd: 2005; pp 658-668.
- (7) Konwick, B. J.; Tomy, G. T.; Ismail, N.; Peterson, J. T.; Fauver, R. J.; Higginbotham, D.; Fisk, A. T., *Environ. Toxicol. Chem.* **2008**, *27*, 2011-2018.

- (8) Clara, M.; Scheffknecht, C.; Scharf, S.; Weiss, S.; Gans, O., *Water Sci. Technol.* **2008**, *58*, 59-66.
- (9) Oliaei, F. O.; Kriens, D.; Kessler, K. *Investigation of Perfluorochemical (PFC) Contamination in Minnesota Phase One*; Minnesota Pollution Control Agency: 2006.
- (10) Schultz, M. M.; Barofsky, D. F.; Field, J. A., *Environ. Sci. Technol.* **2004**, *38*, 1828-1835.
- (11) Moody, C. A.; Hebert, G. N.; Strauss, S. H.; Field, J. A., *J. Environ. Monit.* **2003**, *5*, 341-345.
- (12) Key, B. D.; Howell, R. D.; Criddle, C. S., *Environ. Sci. Technol.* **1998**, *32*, 2283-2287.
- (13) Schultz, M. M.; Higgins, C. P.; Huset, C. A.; Luthy, R. G.; Barofsky, D. F.; Field, J. A., *Environ. Sci. Technol.* **2006**, *40*, 7350-7357.
- (14) Sinclair, E.; Kannan, K., *Environ. Sci. Technol.* **2006**, *40*, 1408-1414.
- (15) Takagi, S.; Adachi, F.; Miyano, K.; Koizumi, Y.; Tanaka, H.; Mimura, M.; Watanabe, I.; Tanabe, S.; Kannan, K., *Chemosphere* **2008**, *72*, 1409-1412.
- (16) Yamamoto, T.; Noma, Y.; Sakai, S. I.; Shibata, Y., *Environ. Sci. Technol.* **2007**, *41*, 5660-5665.
- (17) Hori, H.; Nagaoka, Y.; Murayama, M.; Kutsuna, S., *Environ. Sci. Technol.* **2008**, *42*, 7438-7443.
- (18) Hori, H.; Yamamoto, A.; Kutsuna, S., *Environ. Sci. Technol.* **2005**, *39*, 7692-7697.

- (19) Hori, H.; Nagaoka, Y.; Yamamoto, A.; Sano, T.; Yamashita, N.; Taniyasu, S.; Kutsuna, S.; Osaka, I.; Arakawa, R., *Environ. Sci. Technol.* **2006**, *40*, 1049-1054.
- (20) Park, H.; Vecitis, C. D.; Cheng, J.; Choi, W.; Mader, B. T.; Hoffmann, M. R., *J. Phys. Chem. A* **2009**, *113*, 690-696.
- (21) Ochoa-Herrera, V.; Sierra-Alvarez, R.; Somogyi, A.; Jacobsen, N. E.; Wysocki, V. H.; Field, J., *Environ. Sci. Technol.* **2008**, *42*, 3260-3264.
- (22) Moriwaki, H.; Takagi, Y.; Tanaka, M.; Tsuruho, K.; Okitsu, K.; Maeda, Y., *Environ. Sci. Technol.* **2005**, *39*, 3388-3392.
- (23) Vecitis, C. D.; Park, H.; Cheng, J.; Mader, B. T.; Hoffmann, M. R., *J. Phys. Chem. A* **2008**, *112*, 4261-4270.
- (24) Vecitis, C. D.; Park, H.; Cheng, J.; Mader, B. T.; Hoffmann, M. R., *J. Phys. Chem. C* **2008**, *112*, 16850-16857.
- (25) Cheng, J.; Vecitis, C. D.; Park, H.; Mader, B. T.; Hoffmann, M. R., *Environ. Sci. Technol.* **2008**, *42*, 8057-8063.
- (26) Hansen, K. J.; Johnson, H. O.; Eldridge, J. S.; Butenhoff, J. L.; Dick, L. A., *Environ. Sci. Technol.* **2002**, *36*, 1681-1685.
- (27) Cacace, M. G.; Landau, E. M.; Ramsden, J. J., *Q. Rev. Biophys.* **1997**, *30*, 241-277.
- (28) Cheng, J.; Vecitis, C. D.; Hoffmann, M. R.; Colussi, A. J., *J. Phys. Chem. B* **2006**, *110*, 25598-25602.
- (29) Krusic, P. J.; Marchione, A. A.; Roe, D. C., *J. Fluor. Chem.* **2005**, *126*, 1510-1516.
- (30) Krusic, P. J.; Roe, D. C., *Anal. Chem.* **2004**, *76*, 3800-3803.

- (31) Kotronarou, A.; Mills, G.; Hoffmann, M. R., *J. Phys. Chem.* **1991**, *95*, 3630-3638.
- (32) Suslick, K. S.; Hammerton, D. A.; Cline, R. E., *J. Am. Chem. Soc.* **1986**, *108*, 5641-5642.
- (33) Wall, M.; Ashokkumar, M.; Tronson, R.; Grieser, F., *Ultrason. Sonochem.* **1999**, *6*, 7-14.
- (34) Tronson, R.; Ashokkumar, M.; Grieser, F., *J. Phys. Chem. B* **2002**, *106*, 11064-11068.
- (35) Mahamuni, N. N.; Pandit, A. B., *Ultrason. Sonochem.* **2006**, *13*, 165-174.
- (36) Guo, Z. B.; Feng, R.; Li, J. H.; Zheng, Z.; Zheng, Y. F., *J. Hazard. Mater.* **2008**, *158*, 164-169.
- (37) Sunartio, D.; Ashokkumar, M.; Grieser, F., *J. Am. Chem. Soc.* **2007**, *129*, 6031-6036.
- (38) Jarvis, N. L.; Scheiman, M. A., *J. Phys. Chem.* **1968**, *72*, 74-&.
- (39) Chen, X.; Yang, T.; Kataoka, S.; Cremer, P. S., *J. Am. Chem. Soc.* **2007**, *129*, 12272-12279.
- (40) Piazza, R.; Pierno, M. In *Protein Interactions near Crystallization: A Microscopic Approach to the Hofmeister Series*, 2000; Iop Publishing: 2000; pp A443-A449.
- (41) Fesinmeyer, R. M.; Hogan, S.; Saluja, A.; Brych, S. R.; Kras, E.; Narhi, L. O.; Brems, D. N.; Gokarn, Y. R., *Pharm. Res.* **2009**, *26*, 903-913.
- (42) Beattie, J. K.; Djerdjev, A. N.; Warr, G. G., **2009**, *141*, 31-39.
- (43) Winter, B.; Faubel, M.; Vacha, R.; Jungwirth, P., *Chem. Phys. Lett.* **2009**, *474*, 241-247.

- (44) Cheng, J.; Psillakis, E.; Hoffmann, M. R.; Colussi, A. J., *J. Phys. Chem. A* **2009**, *113*, 8152-8156.
- (45) Hung, H. M.; Kang, J. W.; Hoffmann, M. R., *Water Environ. Res.* **2002**, *74*, 545-556.
- (46) Vecitis, C. D.; Park, H.; Cheng, J.; Mader, B. T.; Hoffmann, M. R., *Front. Environ. Sci. Eng. China* **2009**, *3*, 129-151.
- (47) Kutsuna, S.; Hori, H., *Int. J. Chem. Kinet.* **2007**, *39*, 276-288.
- (48) Neta, P.; Huie, R. E.; Ross, A. B., *J. Phys. Chem. Ref. Data* **1988**, *17*, 1027-1284.

Table 7.1, Primary components of the groundwater sample <sup>a</sup>

pH	7.9	Chloride, mg L <sup>-1</sup> as Cl	14
Temperature, °C	11.7	Nitrate-nitrite, mg L <sup>-1</sup> as N	1.9
Dissolved oxygen, mg L <sup>-1</sup>	6.3	Calcium, mg L <sup>-1</sup> as Ca	64
TOC, mg L <sup>-1</sup>	1.5	Magnesium, mg L <sup>-1</sup> as Mg	20
Total suspended solids, mg L <sup>-1</sup>	3.0	Sodium, mg L <sup>-1</sup> as Na	7.3
Total alkalinity, mg L <sup>-1</sup> as CaCO <sub>3</sub>	220	Potassium, mg L <sup>-1</sup> as K	1.0
Bicarbonate alkalinity, mg L <sup>-1</sup> as CaCO <sub>3</sub>	220	Iron, mg L <sup>-1</sup> as Fe	<0.05
Sulfate, mg L <sup>-1</sup> as SO <sub>4</sub>	18	Manganese, mg L <sup>-1</sup> as Mn	<0.01

a. Measurements completed by PACE Analytical

Figure 7.1.  $\ln([\text{PFOS}]_t / [\text{PFOS}]_i)$  (a) and  $\ln([\text{PFOA}]_t / [\text{PFOA}]_i)$  (b) vs. time in minutes during sonochemical degradation in MilliQ water ( $\circ$ ) and groundwater ( $\square$ ). Reaction conditions are 612 kHz, 250 W L<sup>-1</sup>, Ar, 10 °C, and  $[\text{PFOS}]_i = [\text{PFOA}]_i = 100 \mu\text{g L}^{-1}$ . Each error bar represents one standard deviation from the mean of at least three experiments.  $k_{\text{MQ}}^{-\text{PFOS}} = 0.0192 \text{ min}^{-1}$ ,  $k_{\text{GW}}^{-\text{PFOS}} = 0.0135 \text{ min}^{-1}$ ,  $k_{\text{MQ}}^{-\text{PFOA}} = 0.0366 \text{ min}^{-1}$ , and  $k_{\text{GW}}^{-\text{PFOA}} = 0.0291 \text{ min}^{-1}$ .

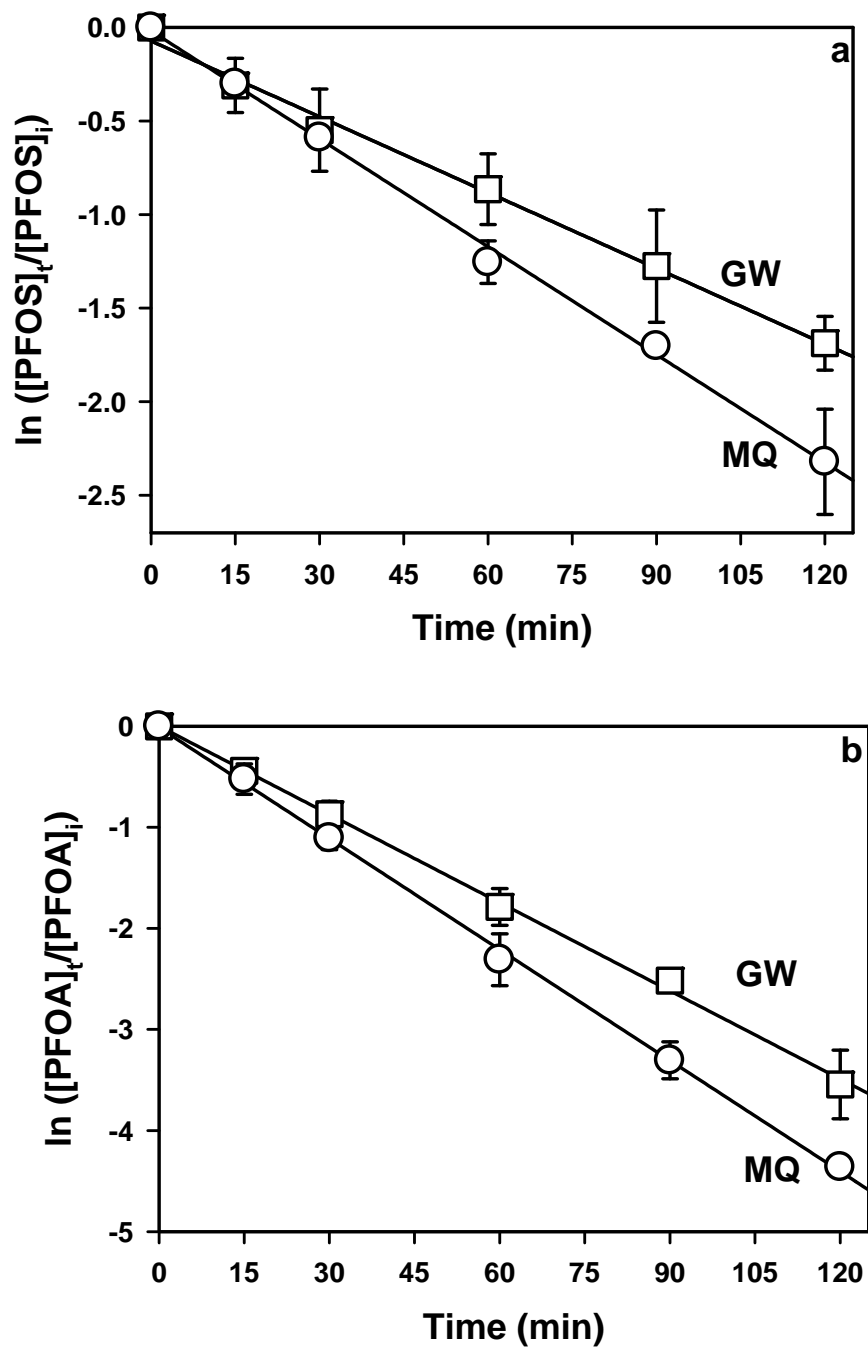


Figure 7.2. The observed pseudo-first-order rate constant normalized to the MilliQ rate constant,  $k^{-\text{PFOS}} / k_{\text{MQ}}^{-\text{PFOS}}$  (a) and  $k^{-\text{PFOA}} / k_{\text{MQ}}^{-\text{PFOA}}$  (b), vs. concentration of  $\text{NaClO}_4$  ( $\circ$ ),  $\text{NaNO}_3$  ( $\square$ ),  $\text{NaCl}$  ( $\triangle$ ),  $\text{Na}_2\text{SO}_4$  ( $\nabla$ ), and  $\text{NaHCO}_3$  ( $\diamond$ ) in mM. Reaction conditions are 612 kHz,  $250 \text{ W L}^{-1}$ , Ar,  $10 \text{ }^\circ\text{C}$ , and  $[\text{PFOS}]_i = [\text{PFOA}]_i = 100 \text{ } \mu\text{g L}^{-1}$ .

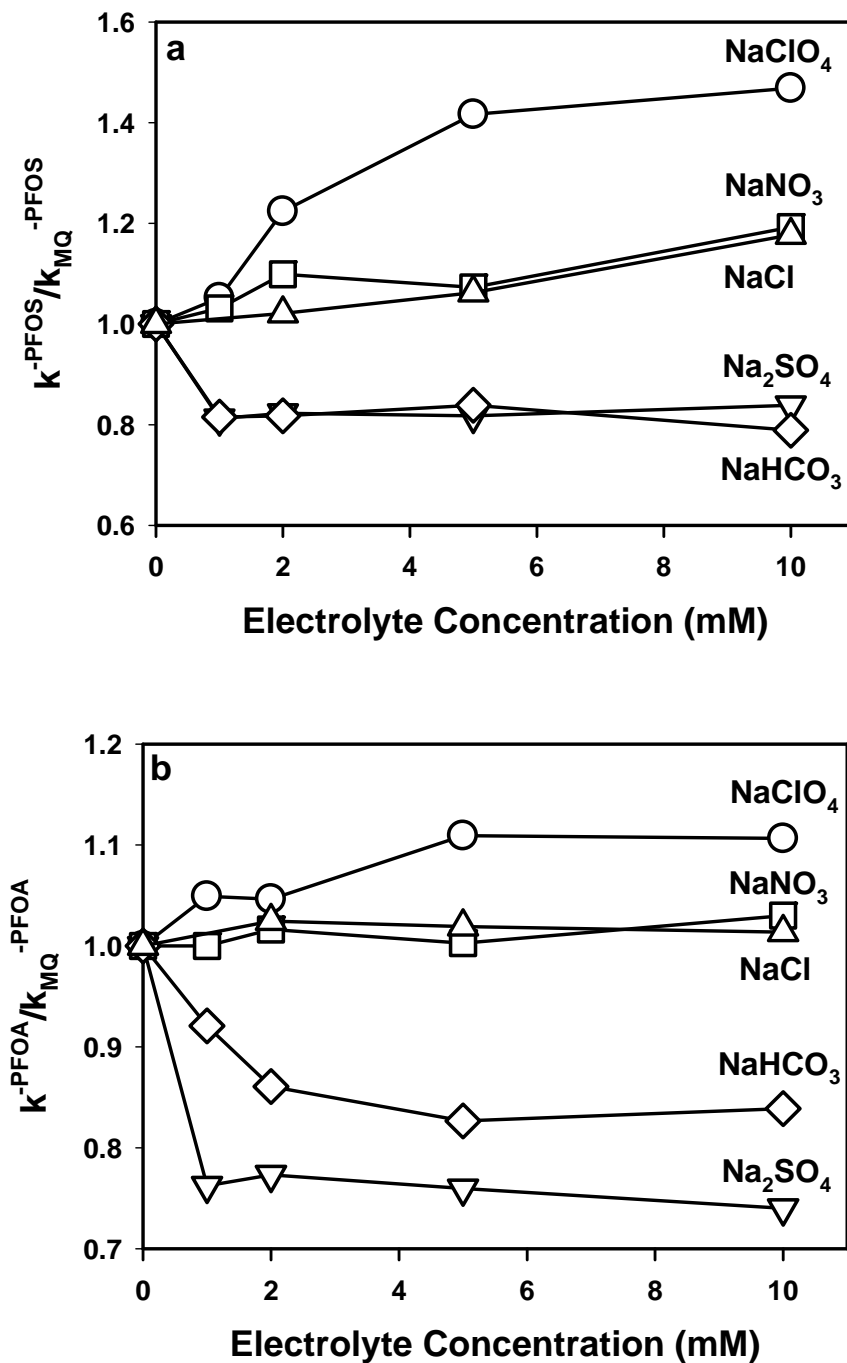


Figure 7.3. The observed pseudo-first-order rate constant for sonolysis of PFOA (clear bars) and PFOS (filled bars) in MilliQ water, aqueous solutions of 5mM NaCl, 5mM NH<sub>4</sub>Cl, 2.5mM CaCl<sub>2</sub>, and 2.5 mM MgCl<sub>2</sub>. Reaction conditions are 612 kHz, 250 W L<sup>-1</sup>, Ar, 10 °C, and [PFOS]<sub>i</sub> = [PFOA]<sub>i</sub> = 100 μg L<sup>-1</sup>.

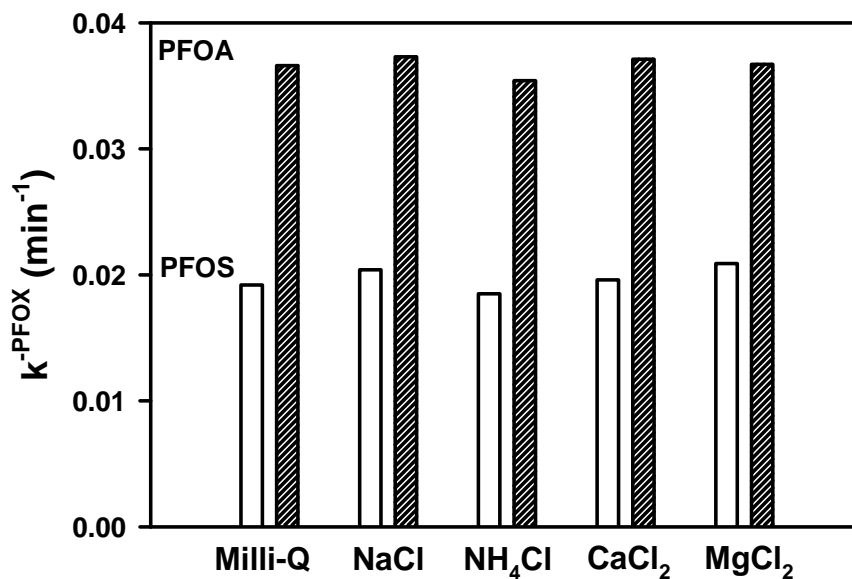


Figure 7.4.  $k^{\text{PFOX}}$ , the pseudo-first-order rate constant for sonolysis of PFOS ( $\circ$ ) and PFOA ( $\nabla$ ), vs. pH of the aqueous solution. Dashed lines represent values of plus and minus one standard deviation from the mean rate constant obtained under pH 7,  $k^{\text{PFOS}} = 0.0192 \pm 0.0016 \text{ min}^{-1}$ , and  $k^{\text{PFOA}} = 0.0366 \pm 0.0003 \text{ min}^{-1}$ .

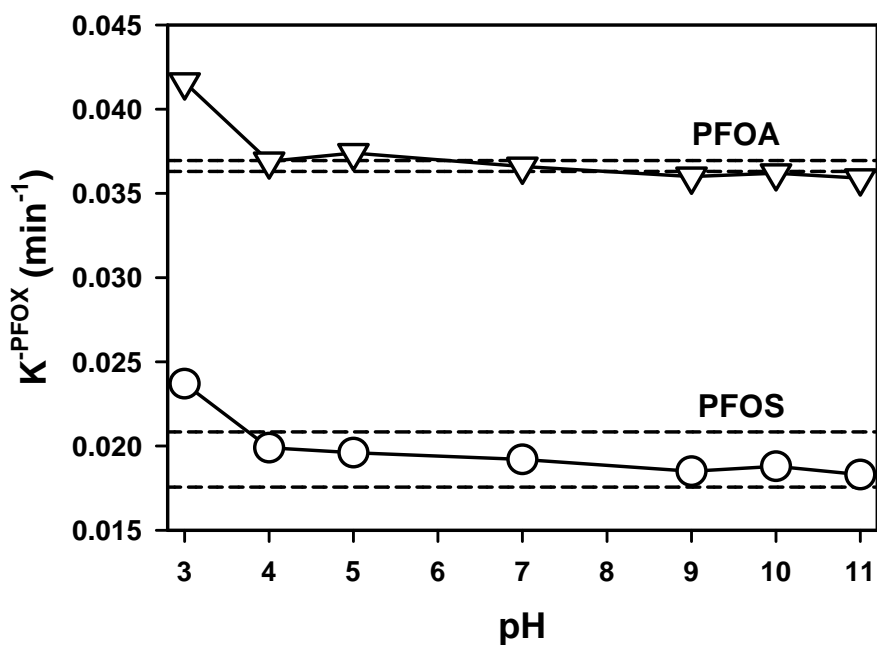


Figure 7.5. (a)  $\ln([PFOS]_t / [PFOS]_i)$  and  $\ln([PFOA]_t / [PFOA]_i)$  (b) vs. time in minutes during the sonolysis of PFOS and PFOA in groundwater under its original pH 8.0 (○), pH 11.0 (□), and pH 3.9 (▽). Other reaction parameters are: 612 kHz, 250 W L<sup>-1</sup>, Ar, 10 °C, and  $[PFOS]_i = [PFOA]_i = 100 \mu\text{g L}^{-1}$ .

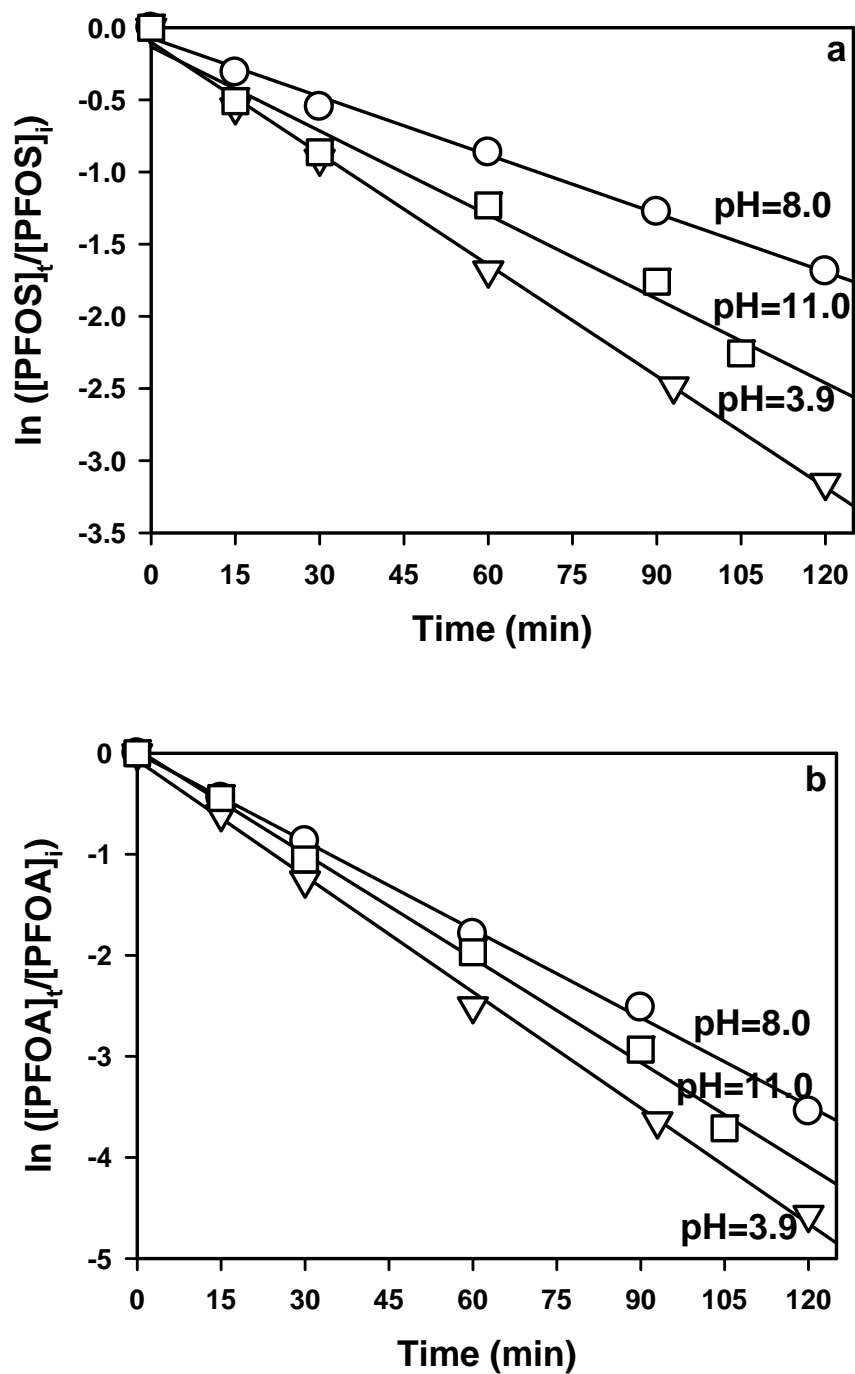


Figure 7.6.  $\ln([\text{PFOS}]_t / [\text{PFOS}]_i)$  (a) and  $\ln([\text{PFOA}]_t / [\text{PFOA}]_i)$  (b) vs. time in minutes during sonochemical degradation in Milli-Q water ( $\circ$ ) and groundwater ( $\square$ ) under 354 kHz,  $250 \text{ W L}^{-1}$ , Ar,  $10 \text{ }^\circ\text{C}$  for  $[\text{PFOS}]_i = [\text{PFOA}]_i = 100 \text{ } \mu\text{g L}^{-1}$ . Each error bar represents one standard deviation from the mean of at least three experiments.  $k_{\text{MQ}}^{-\text{PFOS}} = 0.0239 \text{ min}^{-1}$ ,  $k_{\text{GW}}^{-\text{PFOS}} = 0.0170 \text{ min}^{-1}$ ,  $k_{\text{MQ}}^{-\text{PFOA}} = 0.0469 \text{ min}^{-1}$ , and  $k_{\text{GW}}^{-\text{PFOA}} = 0.0356 \text{ min}^{-1}$ .

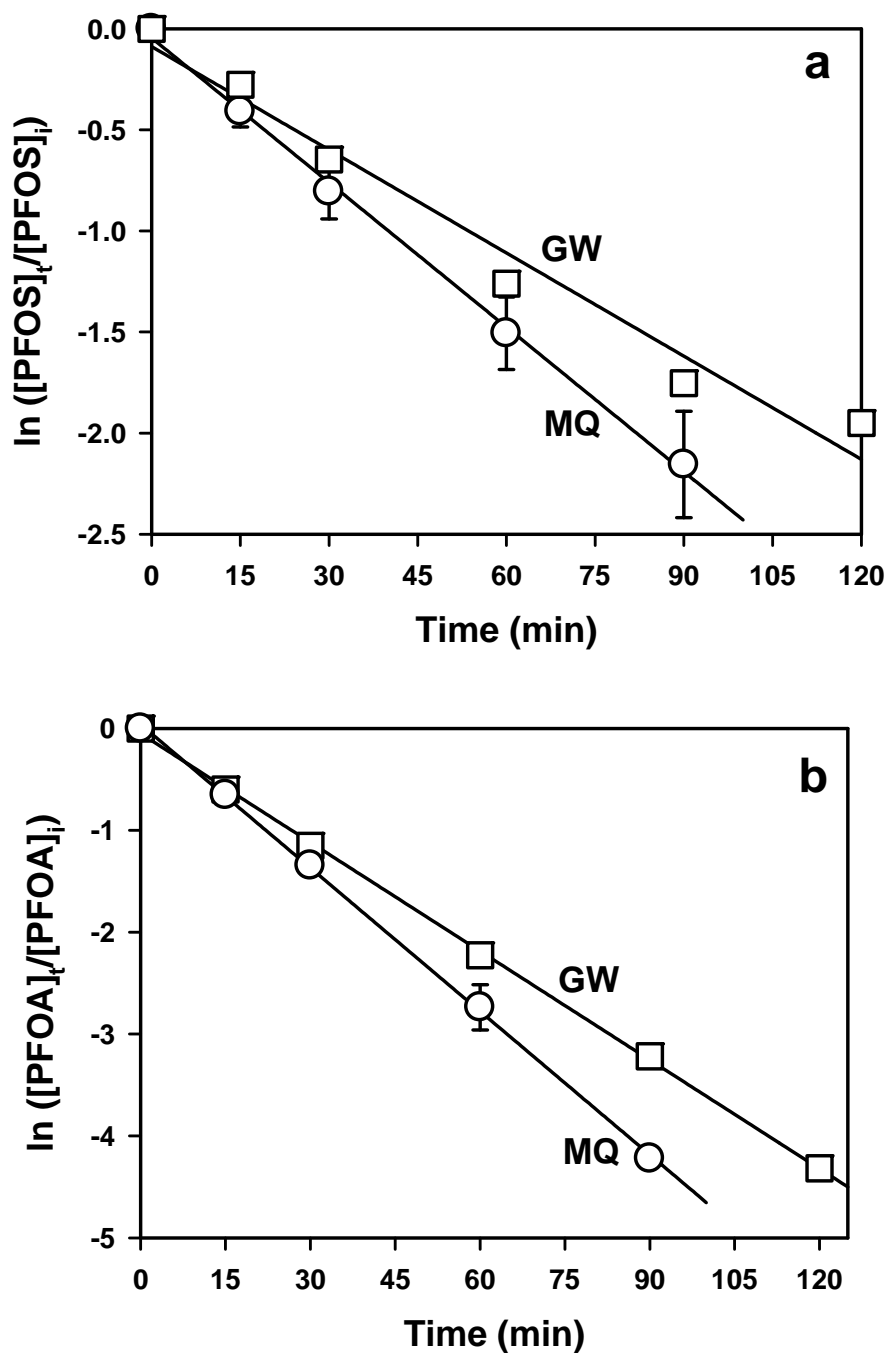
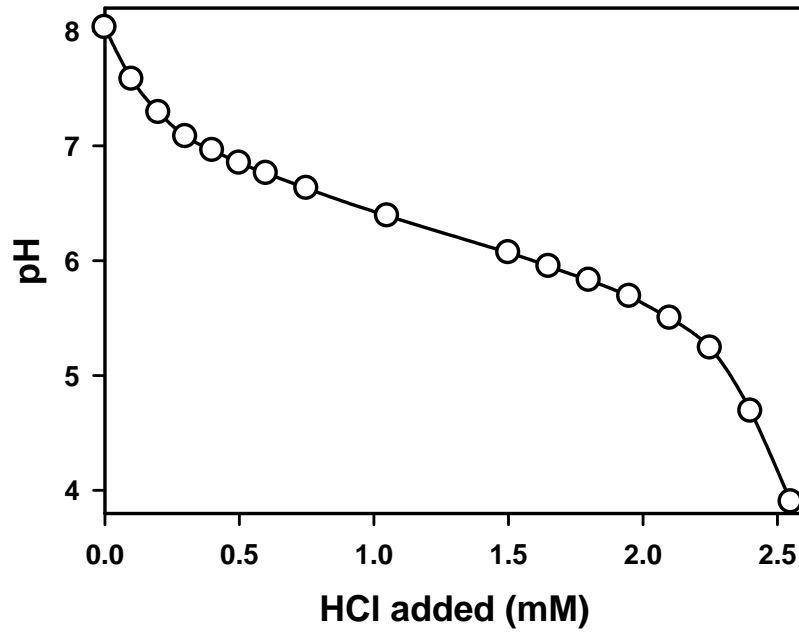


Figure 7.7. The titration curve of the groundwater sample: pH of the groundwater sample vs. the concentration of HCl added in mM.



## **Chapter 8**

### **Confocal Fluorescence Microscopy of Interstitial Fluids in Freezing Electrolyte Solutions\***

---

\* This chapter is reproduced, with moderate changes, with permission from J. Cheng, C. Soetjpto, M. R. Hoffmann, and A. J. Colussi, *Journal of Physical Chemistry Letters*, **2010**, 1, 374-378. Copyright © 2010, American Chemical Society

## 8.1 Abstract

The information content of ice core records and the strength of ice-atmosphere interactions depend on the morphology and composition of the fluid films threading polycrystalline ice. Flat ice surfaces separated by pure water always attract by dispersive forces. Thus, these films owe their existence to the presence of impurities and to curvature effects. Electrolyte impurities induce colligative effects, but also adsorb on charged ice surfaces and screen their resulting electrostatic repulsion. Film thickness  $\delta$  is not therefore a monotonically increasing function of electrolyte concentration as it may be surmised. This possibility is herein demonstrated via time-resolved confocal fluorescence microscopy imaging of the freezing and thawing process of electrolyte solutions doped with a dual-emission pH probe. During freezing of water, the pH probe accumulates into  $12 \pm 2 \mu\text{m}$  thick veins embedded in a pristine ice matrix. The ice front advancing into a 1.0 mM NaCl electrolyte solution, in contrast, engulfs the pH probe into small pockets ( $< 1 \times 1 \mu\text{m}^2$ ) distributed over the sample. Together, these observations are consistent with a non-monotonic dependence of  $\delta$  on ion concentration. The local pH value increases by less than 0.4 units in the interstitial liquid films during freezing of a 0.1 mM NaCl solution, and by over 1.0 units upon subsequent thawing, revealing that the excess negative charge generated by the preferential incorporation of  $\text{Cl}^-$  over  $\text{Na}^+$  into the ice phase is relieved by the seepage of  $\text{OH}^-$  slowly produced via  $\text{H}_2\text{O} \rightarrow \text{H}^+ + \text{OH}^-$ . In contrast, preferential incorporation of the  $\text{NH}_4^+$  over the  $\text{Ac}^-$  into ice leads to the acidification of the interstitial liquid films in ice frozen from dilute  $\text{NH}_4\text{Ac}$  solutions.

## 8.2 Introduction

Most solids exist as polycrystalline aggregates. Their properties, ranging from the rheology and paleogeography of glacial ice to the reduction of critical current density in high-temperature superconductors<sup>1-3</sup> are determined by the composition and geometry of grain boundaries. Gaps among grains arise because advancing planar solid fronts are unstable and bifurcate under the thermal and concentration gradients generated by freezing itself.<sup>4-6</sup> They persist within thermally equilibrated (but dynamically arrested)<sup>7-10</sup> frozen materials because the fractionation of melt components at grain boundaries usually minimizes interfacial free energy. Chemical<sup>11-13</sup> and biological activity<sup>14-16</sup> in snow, ice cores and permafrost actually takes place in microfluids wetting polycrystalline ice grains that contain the solutes and nutrients rejected by the ice matrix.

Ice is notoriously intolerant to impurities, but interstitial fluids are not concentrates of the starting solutions,<sup>17-21</sup> because molecular isomorphism imposes strong selectivity rules. For example, ammonium ( $\text{NH}_4^+$ ) and fluoride ( $\text{F}^-$ ), being isoelectronic with  $\text{H}_2\text{O}$  and  $\text{OH}^-$ , respectively, are selectively but marginally ( $\sim 1$  out of  $10^4$ ) incorporated into the ice matrix over their counterions. This phenomenon generates transient charge imbalances between the solid and the liquid phases during freezing that eventually relax via migration of the intrinsic  $\text{H}^+/\text{HO}^-$  ice carriers.<sup>22-26</sup> Preferential incorporation of cations over anions into the ice lattice therefore leads to acidification of the liquid, and vice versa. The local acidity of interstitial fluids determines, for example, whether weak, volatile acids or bases can be exchanged between ice and the gas phase, and whether reactions between dopants are inhibited or catalyzed in frozen media.<sup>27-34</sup>

The equilibrium fluid films that persist at the air/ice interface below the normal melting point have been characterized theoretically and experimentally.<sup>17,35-39</sup> Only the dihedral angle of water channels along ice grain boundaries is, however, known with any certainty.<sup>18,21,40-44</sup> Optically transparent polycrystalline ice seems ideally suited to test current views on grain boundary melting<sup>18</sup>. Herein we address these issues, and report preliminary results of a time-resolved confocal fluorescence microscopy study of freezing aqueous electrolyte solutions, and their subsequent thawing.

### 8.3 Experimental Section

C-SNARF-1 (Invitrogen, C1270, see Scheme 8.1) was used as the dual-emission fluorescence pH indicator. A 50  $\mu\text{M}$  stock C-SNARF-1 solution in MilliQ water was prepared and stored frozen at  $-20\text{ }^{\circ}\text{C}$  until use. Sodium chloride ( $> 99.9\%$  purity; EMD), ammonium acetate ( $>99.999\%$  purity; Aldrich), and ammonium sulfate ( $> 99.5\%$  purity; EMD) were used as received. 1 M sodium hydroxide solution (VWR), 30% ammonium hydroxide solution (J.T. Baker), 1 M hydrochloric acid (VWR), 1 M sulfuric acid (VWR),  $\text{KH}_2\text{PO}_4 \cdot 3\text{H}_2\text{O}$  (AR; Mallinckrodt), and  $\text{KH}_2\text{PO}_4$  ( $>99.7\%$  purity; Mallinckrodt) were used to adjust the pH of the sample solutions as indicated. All solutions were prepared with deionized water (resistivity 18.2  $\text{M}\Omega\text{ cm}$ ) purified with a Milli-Q ultrapure water system (Millipore).

Temporally and spectrally resolved fluorescence imaging of test solutions was performed with a Zeiss LSM 510 META NLO confocal laser scanning microscope (CLSM) equipped with a programmable PE-120 Peltier cryostage (Linkam). 1.0  $\mu\text{M}$  C-SNARF-1 test solutions were prepared by dilution of the stock solution in water, or in a

binary electrolyte of known concentration, as indicated. Their pH was adjusted prior to freezing by means of acid (basic) solutions containing the same anion (cation) as the selected electrolyte. Fluorescence was acquired from 30  $\mu\text{l}$  samples of the test solutions contained in a cylindrical well (6.0 mm in diameter, 1.0 mm deep) bored into a clear quartz plate, which was tightly clamped to the cryostage lying on the (x, y)-movable plate of the CLSM. A typical freeze-and-thaw cycle involved a temperature program consisting of three consecutive steps: (1) cooling at  $-10 \text{ K min}^{-1}$  from 298 K to 268 K, (2) holding at 268 K for 5 minutes after completion of sample freezing, and (3) warming at  $10 \text{ K min}^{-1}$  back to 298 K. The actual sample temperature was simultaneously measured with a calibrated type-K thin wire thermocouple immersed in the test solution (Figure 8.1).

The fluorescence emitted by the sample was continuously scanned during the freeze-thaw cycle, which allowed tracking the advancing ice front by adjusting the position of the stage. LD C-Apochromat 40 $\times$ /1.1 W Corr M27 or EC Plan-Neofluar 10 $\times$ /0.3 objective lenses were used to collect images from x-y planes with (512  $\times$  512) pixels resolution, which corresponds to (225  $\mu\text{m} \times 225 \mu\text{m}$ ) and (900  $\mu\text{m} \times 900 \mu\text{m}$ ) frames, respectively. The following instrumental parameters were used unless otherwise specified:  $\lambda_{\text{exc}} = 488$  or 514 nm at 50% argon laser output power, 15% transmission; scan speed: 1.0 frame  $\text{s}^{-1}$ ; pinhole set at 750, corresponding to a z-slice of  $< 9.3 \mu\text{m}$  for the 40 $\times$ /1.1 objective; detector gain: 720. The META detector and the Lambda acquisition mode were used to obtain fluorescence emission spectra from 565.1 nm to 650.7 nm with a step size of 10.7 nm. The images were analyzed using Zeiss LSM Image Examiner software.

The pH dependence of C-SNARF-1 fluorescence emissions was independently calibrated with a Perkin Elmer LS 50B luminescence spectrometer. 3.0 mL of 0.2  $\mu\text{M}$  C-SNARF-1 solutions in 0.05 M  $\text{KH}_2\text{PO}_4/\text{K}_2\text{HPO}_4$  buffers contained in square prismatic silica cuvettes were excited at  $\lambda_{\text{exc}} = 514$  nm, and emission spectra recorded between 550 and 750 nm. The excitation slit and scan speed were set at 10 and 200  $\text{nm min}^{-1}$ , respectively.

#### 8.4 Results and Discussion

The fluorescence emission of C-SNARF-1 as a function of pH was calibrated with the CLSM using 1.0  $\mu\text{M}$  C-SNARF-1 solutions in 0.05 M  $\text{KH}_2\text{PO}_4/\text{K}_2\text{HPO}_4$  buffer at different pH values ranging from 5.6 to 9.2, under different conditions of temperature, C-SNARF-1 concentration, laser intensity, scan speed, and detector gain. The fluorescence emission spectra of C-SNARF-1 show two distinctive emission maxima at  $\lambda_1 = 581$  nm and  $\lambda_2 = 635$  nm.  $R = I(\lambda_1)/I(\lambda_2)$ , is the ratio of their corresponding fluorescence intensities. Figure 8.2 shows  $R$  vs. pH calibration curves obtained by fitting equation (8.1):

$$\text{pH} = \text{p}K_a + \beta \log \frac{R - R_{\min}}{R_{\max} - R} + \log \frac{I^a}{I^b} \quad (8.1)$$

to CLSM or fluorometer  $R$  measurements.  $\text{p}K_a$  (C-SNARF-1) = 7.5,  $R_{\max}$  and  $R_{\min}$  are the maximum and minimum  $R$ -values, respectively, and  $I(\lambda_1)^a/I(\lambda_2)^b$  is the ratio of  $I(\lambda_1)$  in acid to that in base. Ratiometric measurements minimize uneven probe distribution, differences in sample thickness, photobleaching and self-quenching effects.<sup>45-46</sup> As long as fluorescence is not oversaturated, calibration curves are also insensitive to sample

concentration and instrumental parameters such as excitation laser intensity, scan speed, and detector gain (See Figure 8.7). Temperature has a minor effect on  $R$  vs. pH calibration curves ( $\sim 0.01$  pH K<sup>-1</sup> between 268 and 298 K, see Table 8.1 and Figure 8.6). Other factors, such as ionic strength variations are negligible under present conditions.<sup>47</sup>

Figure 8.1 shows that under a preset cooling ramp of  $-10.0$  K min<sup>-1</sup>, the sample temperature  $T_s$  fell at about  $-7.9$  K min<sup>-1</sup> down to  $T_s \sim 268$  K during step (1), when the electrolyte solution began to freeze, releasing latent heat.  $T_s$  remained at  $\sim 273$  K during freezing, before cooling to 265 K for the rest of step (2). We found that cooling ramp settings affect the velocity of the ice front rather than  $T_s$  during step (2). As the ice front moves radially inward at  $\sim 5$   $\mu\text{m s}^{-1}$  toward the axis of the cylindrical sample, the fluorescent probe C-SNARF-1 is rejected by the ice and trapped in the liquid channels, whose morphology depends markedly on the presence of electrolytes (Figure 8.3). C-SNARF-1 in MilliQ water or very dilute electrolyte solutions accumulates into liquid channels arranged in a hexagonal network with well-developed veins,  $\delta = (12 \pm 2)$   $\mu\text{m}$ , and nodes occluded in very pure ice (Figure 8.3a). In contrast, C-SNARF is randomly distributed in pockets and dendritic channels, except in the last stages, upon freezing NaCl and (NH<sub>4</sub>)<sub>2</sub>SO<sub>4</sub> solutions at concentrations above 1 mM (Figure 8.3b and c). Topological considerations suggest that the average number of sides of the disordered polygonal cells arising spontaneously in systems far from equilibrium via symmetry breaking is six (Figure 8.3a).<sup>48</sup> We infer that dynamic instabilities, rather than thermodynamics, determine the morphologies observed in our experiments.<sup>6</sup>

Figure 8.4 shows in detail the fluorescence intensity and pH ( $x, y$ )-distributions during the freezing of a solution containing 10  $\mu\text{M}$  C-SNARF-1 and 0.1 mM NaCl. Figure 8.4a

shows that the probe was evenly distributed in the sample solution at pH 6.4 across the entire imaging area prior to freezing. As freezing started, C-SNARF-1 was observed to accumulate at the ice front, forming a band of approximately 20  $\mu\text{m}$  in width (Figure 8.4 b), showing that C-SNARF-1 diffusion is slow relative to the forward velocity of the ice front. As shown in Figures 8.4b and c, the pH of the liquid phase increased moderately to  $\sim 7.2$  in the interfacial region and to  $\sim 7.0$  in the bulk liquid away from the interface. pH rose to  $\sim 8.4$ , however, upon thawing the sample after being frozen for 5 minutes (Figure 8.4(d)). The timescales involved are quite consistent with the seepage of  $\text{OH}^-$  produced at rates:  $k_f(\text{H}_2\text{O} \rightarrow \text{H}^+ + \text{OH}^-) = K_w k_b < 10^{-14} \text{ M} \times 10^{10} \text{ M}^{-1} \text{ s}^{-1} = 10^{-4} \text{ s}^{-1}$ ,<sup>49</sup> into the pockets, as suggested by Bronshteyn and Chernov.<sup>29,34,47,50-51</sup> pH returned to the initial value after the sample has completely melted. We verified that the areas under the fluorescence intensity curves (black traces) in Figures 8.4 (c) and (d), along the path  $\rho = (x = y)$ :  $A = \int I(\rho) d\rho$ , are identical within experimental error, proving the reversibility of freeze-and-thaw cycles, and indirectly, the absence of self-quenching and other possible artifacts.

Figure 8.5 shows the pH changes during freezing a 0.05 mM  $\text{CH}_3\text{COONH}_4$  solution. The pH of the liquid phase was expected to drop during freezing due to preferential incorporation of  $\text{NH}_4^+$  into the ice lattice. However, as shown in Figure 8.5 (a) and 8.5 (b), during freezing the pH of the liquid phase slightly increased from approximately 7.9 to 8.2, presumably due to freeze-concentration of an initially basic solution and to the temperature effect. When the sample was thawed after being frozen for 5 minutes, the pH did decrease to 6.8 in the liquids surrounding the air bubbles (Figure 8.5(c)).

## 8.5 Acknowledgements

This project was financially supported by the National Science Foundation (ATM-0534990).

## 8.6 Reference

- (1) Duval, P.; Arnaud, L.; Brissaud, O.; Montagnat, M.; de la Chapelle, S. *Ann. Glaciol.* **2000**, *30*, 83.
- (2) Cuffey, K.; Conway, H.; Gades, A.; Hallet, B.; Raymond, C.; Whitlow, S. J. *Geophys. Res.* **2000**, *105*, 27895.
- (3) Cullen, D.; Baker, I. J. *Glaciol.* **2000**, *46*, 703.
- (4) Coriell, S. R.; McFadden, G. B.; Sekerka, R. F. *Annu. Rev. Mater. Sci.* **1985**, *15*, 119.
- (5) Nagashima, K.; Furukawa, Y. *J. Phys. Chem. B* **1997**, *101*, 6174.
- (6) Wettlaufer, J. S. *Europhys. Lett.* **1992**, *19*, 337.
- (7) Brader, J. M.; Voigtmann, T.; Fuchs, M.; Larson, R. G.; Cates, M. E. *Proc. Natl. Acad. Sci. U. S. A.* **2009**, *106*, 15186.
- (8) Cates, M. E.; Wittmer, J. P.; Bouchaud, J. P.; Claudin, P. *Phys. Rev. Lett.* **1998**, *81*, 1841.
- (9) Lu, K.; Brodsky, E. E.; Kavehpour, H. P. *Nat. Phys.* **2008**, *4*, 404.
- (10) Smart, A.; Ottino, J. M. *Soft Matter* **2008**, *4*, 2125.
- (11) Grannas, A. M.; Jones, A. E.; Dibb, J.; Ammann, M.; Anastasio, C.; Beine, H. J.; Bergin, M.; Bottenheim, J.; Boxe, C. S.; Carver, G.; Chen, G.; Crawford, J. H.; Domine, F.; Frey, M. M.; Guzman, M. I.; Heard, D. E.; Helmig, D.; Hoffmann, M.

- R.; Honrath, R. E.; Huey, L. G.; Hutterli, M.; Jacobi, H. W.; Klan, P.; Lefer, B.; McConnell, J.; Plane, J.; Sander, R.; Savarino, J.; Shepson, P. B.; Simpson, W. R.; Sodeau, J. R.; von Glasow, R.; Weller, R.; Wolff, E. W.; Zhu, T. *Atmos. Chem. Phys.* **2007**, *7*, 4329.
- (12) Domine, F.; Albert, M.; Huthwelker, T.; Jacobi, H. W.; Kokhanovsky, A. A.; Lehning, M.; Picard, G.; Simpson, W. R. *Atmos. Chem. Phys.* **2008**, *8*, 171.
- (13) Huthwelker, T.; Ammann, M.; Peter, T. *Chem. Rev.* **2006**, *106*, 1375.
- (14) Price, P. B. *FEMS Microbiol. Ecol.* **2007**, *59*, 217.
- (15) Price, P. B.; Rohde, R. A.; Bay, R. C. *Biogeosciences* **2009**, *6*, 479.
- (16) Rohde, R. A.; Price, P. B.; Bay, R. C.; Bramall, N. E. *Proc. Natl. Acad. Sci. U. S. A.* **2008**, *105*, 8667.
- (17) Dash, J. G.; Rempel, A. W.; Wettlaufer, J. S. *Rev. Mod. Phys.* **2006**, *78*, 695.
- (18) Benatov, L.; Wettlaufer, J. S. *Phys. Rev. E* **2004**, *70*.
- (19) Mader, H. M. *J. Glaciol.* **1992**, *38*, 333.
- (20) Mader, H. M. *J. Glaciol.* **1992**, *38*, 359.
- (21) Nye, J. F. *J. Glaciol.* **1989**, *35*, 17.
- (22) Workman, E. J.; Reynolds, S. E. *Phys. Rev.* **1950**, *78*, 254.
- (23) Cobb, A. W.; Gross, G. W. *J. Electrochem. Soc.* **1969**, *116*, 796.
- (24) Gross, G. W. *Adv. Chem. Ser.* **1968**, *27*.
- (25) Grimm, R. E.; Stillman, D. E.; Dec, S. F.; Bullock, M. A. *J. Phys. Chem. B* **2008**, *112*, 15382.
- (26) Gross, G. W.; Wong, P. M.; Humes, K. J. *Chem. Phys.* **1977**, *67*, 5264.

- (27) O'Driscoll, P.; Minogue, N.; Takenaka, N.; Sodeau, J. *J. Phys. Chem. A* **2008**, *112*, 1677.
- (28) Takenaka, N.; Ueda, A.; Maeda, Y. *Nature* **1992**, *358*, 736.
- (29) Takenaka, N.; Tanaka, M.; Okitsu, K.; Bandow, H. *J. Phys. Chem. A* **2006**, *110*, 10628.
- (30) Takenaka, N.; Bandow, H. *J. Phys. Chem. A* **2007**, *111*, 8780.
- (31) Sato, K.; Furuya, S.; Takenaka, N.; Bandow, H.; Maeda, Y.; Furukawa, Y. *Bull. Chem. Soc. Jpn.* **2003**, *76*, 1139.
- (32) Sato, K.; Takenaka, N.; Bandow, H.; Maeda, Y. *J. Phys. Chem. A* **2008**, *112*, 7600.
- (33) Takenaka, N.; Furuya, S.; Sato, K.; Bandow, H.; Maeda, Y.; Furukawa, Y. *Int. J. Chem. Kinet.* **2003**, *35*, 198.
- (34) Takenaka, N.; Ueda, A.; Daimon, T.; Bandow, H.; Dohmaru, T.; Maeda, Y. *J. Phys. Chem.* **1996**, *100*, 13874.
- (35) Wettlaufer, J. S.; Worster, M. G. *Ann. Rev. Fluid Mech.* **2006**, *38*, 427.
- (36) Sadtchenko, V.; Ewing, G. E. *J. Chem. Phys.* **2002**, *116*, 4686.
- (37) Wei, X.; PB, M.; C, Z.; Shen, Y. R. *Phys. Rev. B* **2002**, *66*, art. no.
- (38) Wei, X.; Miranda, P. B.; Shen, Y. R. *Phys. Rev. Lett.* **2001**, *86*, 1554.
- (39) Doppenschmidt, A.; Butt, H.-J. *Langmuir* **2000**, *16*, 6709.
- (40) Barnes, P. R. F.; Wolff, E. W. *J. Glaciol.* **2004**, *50*, 311.
- (41) Barnes, P. R. F.; Wolff, E. W.; Mallard, D. C.; Mader, H. M. *Microsc. Res. Tech.* **2003**, *62*, 62.

- (42) Baker, I.; Iliescu, D.; Obbard, R.; Chang, H.; Bostick, B.; Daghljan, C. P. Microstructural characterization of ice cores. In *Ann. Glaciol.*; Dowdeswell, J., Willis, I. C., eds., 2005; vol. 42; pp 441.
- (43) Rempel, A. W.; Waddington, E. D.; Wettlaufer, J. S.; Worster, M. G. *Nature* **2001**, *411*, 568.
- (44) Hobbs, P. V. *Ice Physics*; Clarendon Press: Oxford, 1974.
- (45) Pawley, J. B. *Handbook of Biological Confocal Microscopy*, 2nd ed.; Plenum Press: New York, 1995.
- (46) Mason, W. T. *Fluorescent and Luminescent Probes for Biological Activity*, 2nd ed.; Academic Press: London, U.K., 1999.
- (47) Robinson, C.; Boxe, C. S.; Guzman, M. I.; Colussi, A. J.; Hoffmann, M. R. *J. Phys. Chem. B* **2006**, *110*, 7613.
- (48) Schliecker, G. *Adv. Phys.* **2002**, *51*, 1319.
- (49) Geissler, P. L.; Dellago, C.; Chandler, D.; Hutter, J.; Parrinello, M. *Science* **2001**, *291*, 2121.
- (50) Bronshteyn, V. L.; Chernov, A. A. *J. Cryst. Growth* **1991**, *112*, 129.
- (51) Sola, M. I.; Corti, H. R. *An. Asoc. Quim. Argent.* **1993**, *81*, 483.

Table 8.1. Fitting parameters of equation (8.2) obtained under various temperature and instrument conditions.

Instrument	T (k)	$\lambda_1(\text{nm})$	$\lambda_2(\text{nm})$	$c$	$R_{\min}$	$R_{\max}$	$\log \frac{I^a}{I^b}$
FL	298	587	634	-1.089	0.078	2.184	-0.425
CLSM	298	581	635	-1.119	0.095	2.413	-0.321
CLSM	288	581	635	-1.144	0.095	2.409	-0.229
CLSM	278	581	635	-1.145	0.099	2.379	-0.114
CLSM	268	581	635	-1.148	0.100	2.360	0.005

Figure 8.1. A typical temperature profile during the freeze-thaw cycle of electrolyte solution sample. Red line: cryostage programmed temperature. Black line: actual sample temperature.

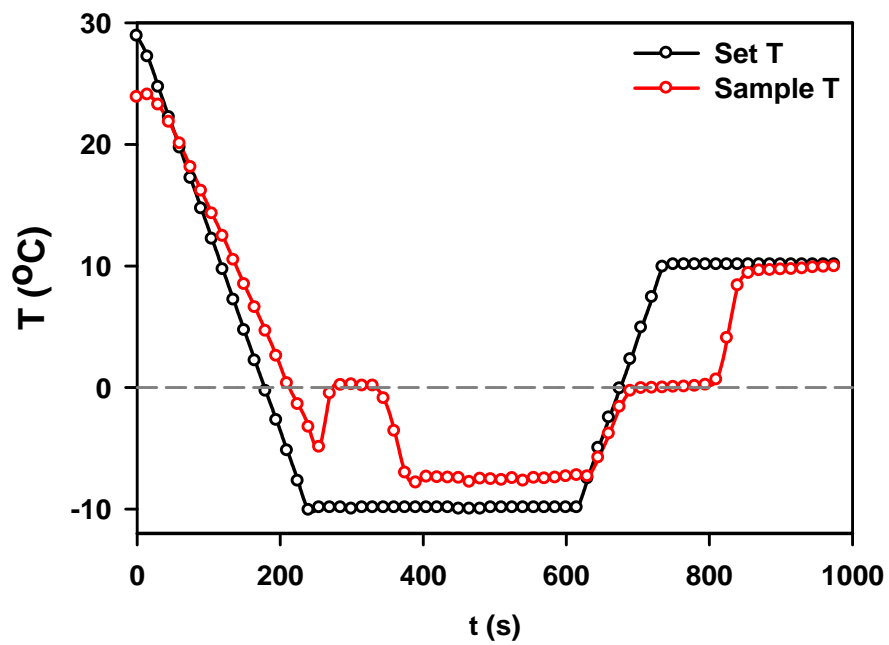


Figure 8.2. Fluorescence emission ratio vs. pH measured by fluorometer (FL, blue line;  $\lambda_1 = 587$  nm,  $\lambda_2 = 634$  nm) and by CLSM (red line;  $\lambda_1 = 581$  nm,  $\lambda_2 = 635$  nm). The solutions measured by fluorometer experiments contain 0.2  $\mu$ M C-SNARF-1 and 0.05 M  $\text{KH}_2\text{PO}_4/\text{K}_2\text{HPO}_4$  buffer, and those measured by CLSM contain 1.0  $\mu$ M C-SNARF-1 and 0.05 M phosphate buffer.

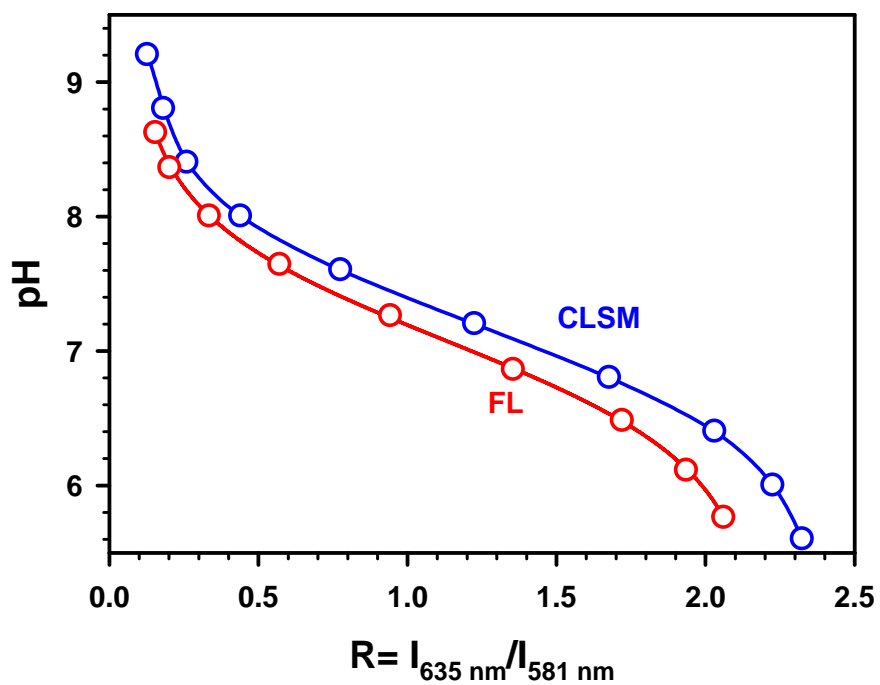
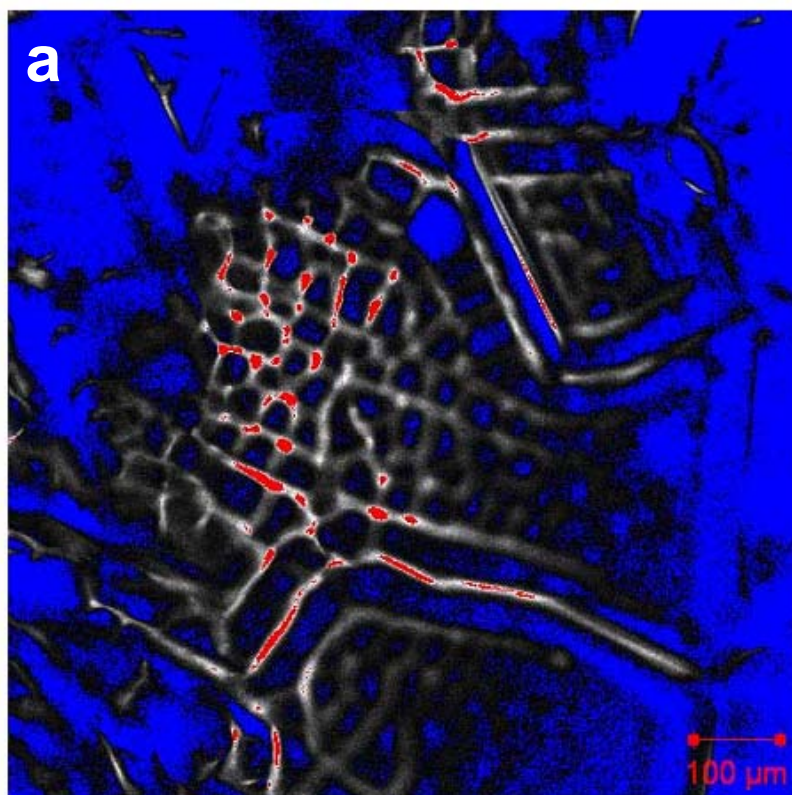


Figure 8.3. 10  $\mu\text{M}$  C-SNARF-1 in (a) MilliQ, (b) 1mM NaCl solution, (c) 1mM  $(\text{NH}_4)_2\text{SO}_4$  solution during freezing. Fluorescence intensity is indicated by a color scale (blue: zero-low intensity, red: high intensity-saturation). Frame sizes are  $900\ \mu\text{m} \times 900\ \mu\text{m}$  for (a) and  $225\ \mu\text{m} \times 225\ \mu\text{m}$  for (b) (c).



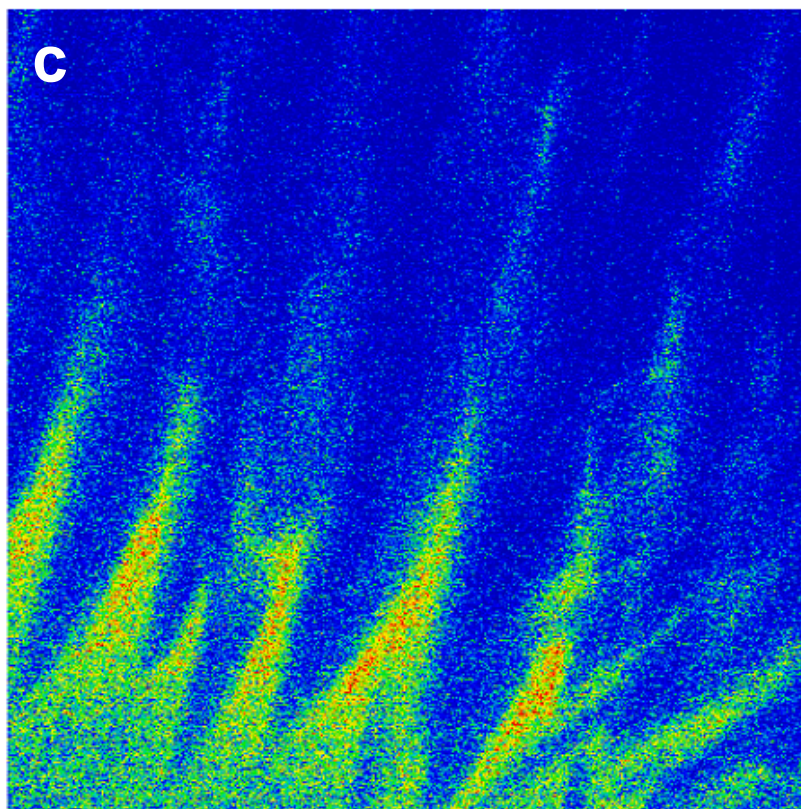
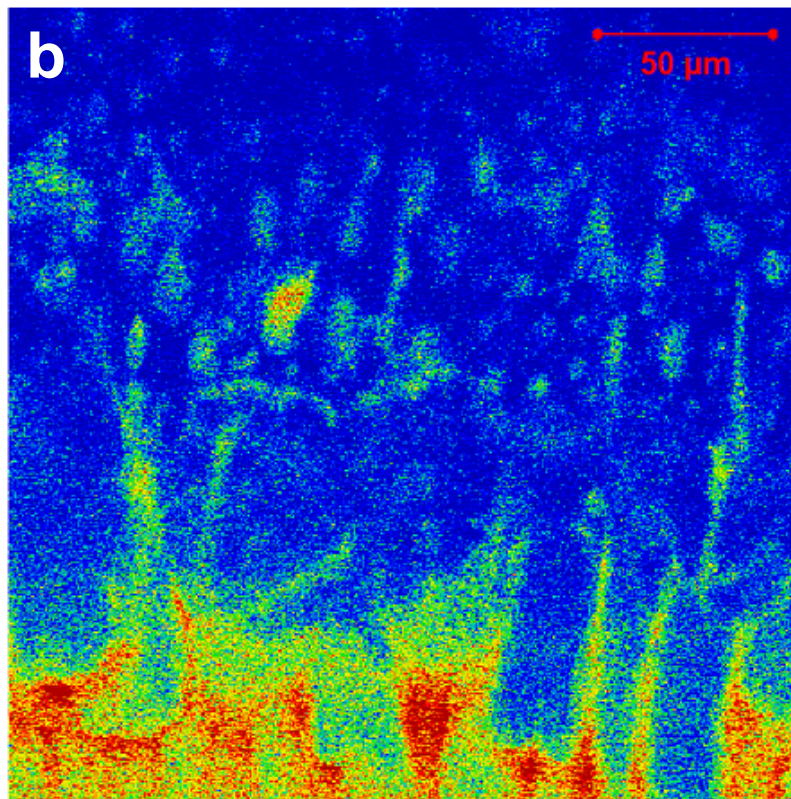
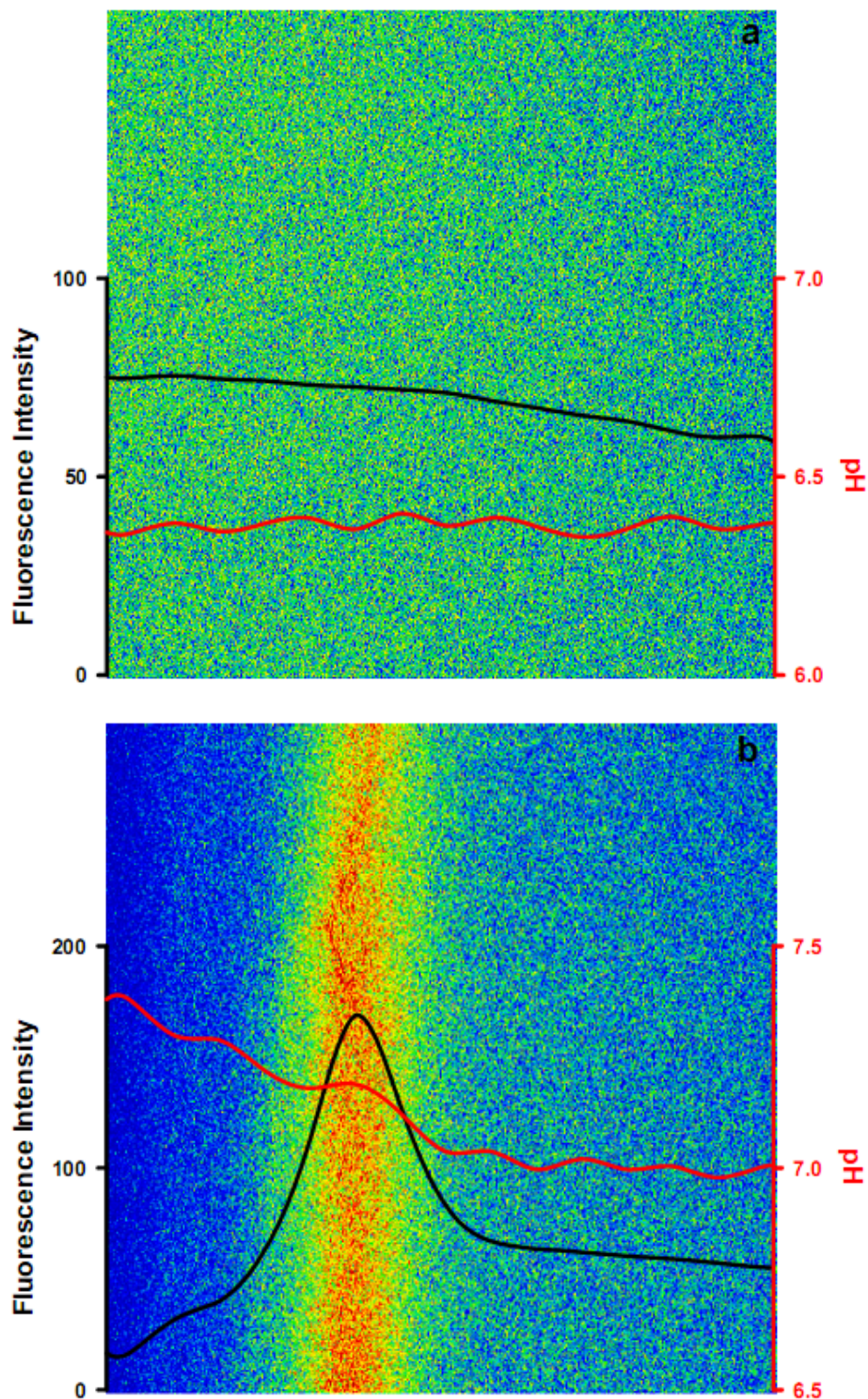


Figure 8.4 Fluorescence emission spectra of an aqueous solution containing 10  $\mu\text{M}$  C-SNARF-1 and 0.1 mM NaCl (a) before freezing, (b) 9.8s after freezing began, (c) 52.4 s after freezing began, and (d) 20 s after thawing began. The pH values shown are based on the emission ratio averaged over the area of interest. The frame size is  $225 \mu\text{m} \times 225 \mu\text{m}$ .



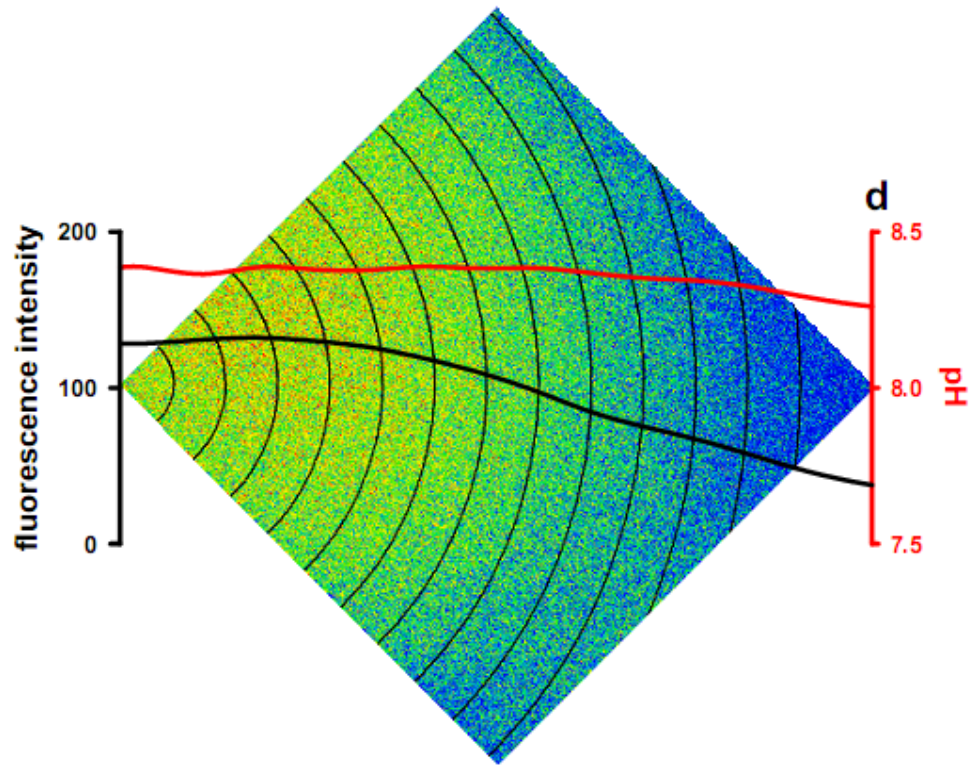
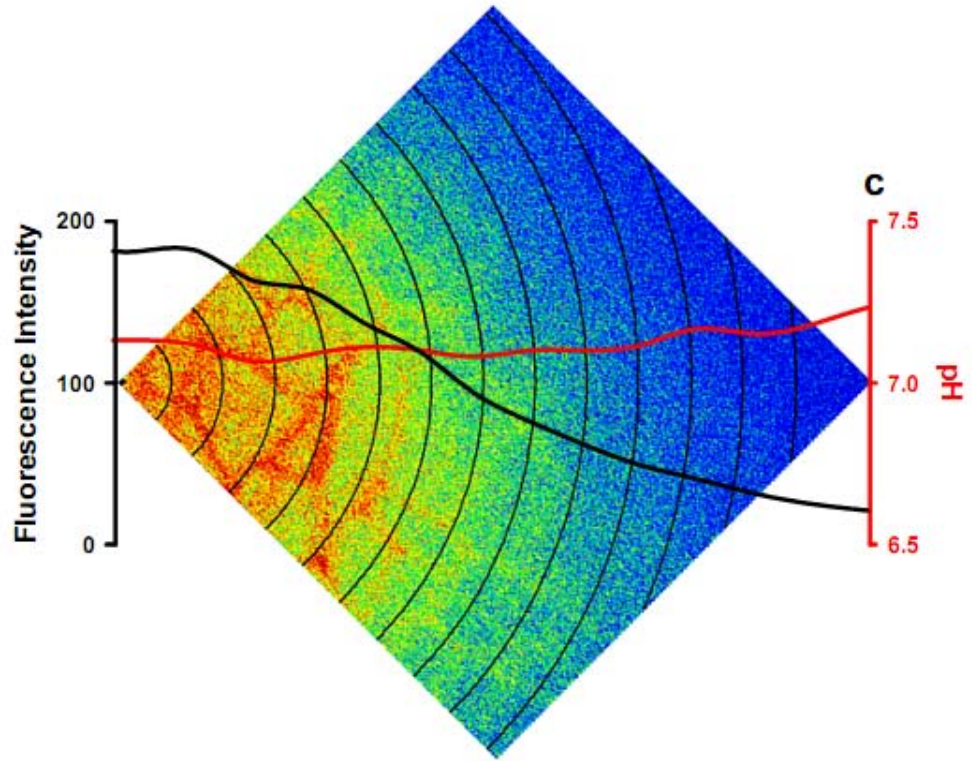
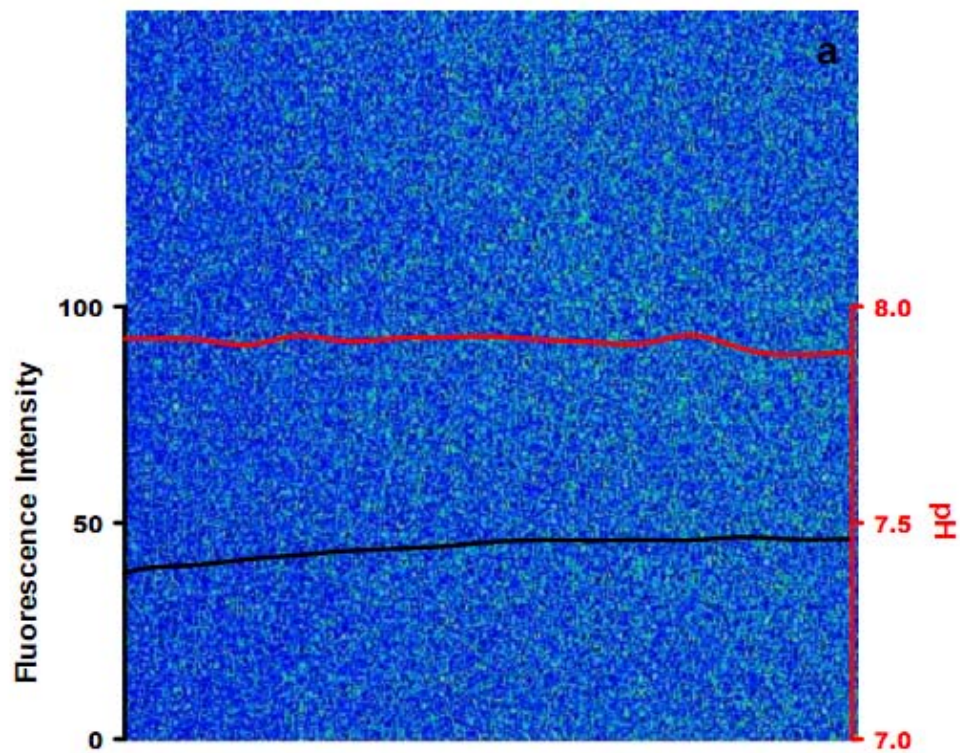


Figure 8.5. Fluorescence emission spectra of an aqueous solution containing 5  $\mu\text{M}$  C-SNARF-1 and 0.05 mM  $\text{CH}_3\text{COONH}_4$  (a) before freezing at 298 K, (b) during freezing, and (c) during thawing. The pH values shown are based on the emission ratio averaged over the area of interest. The frame size is 225  $\mu\text{m} \times 225 \mu\text{m}$ .



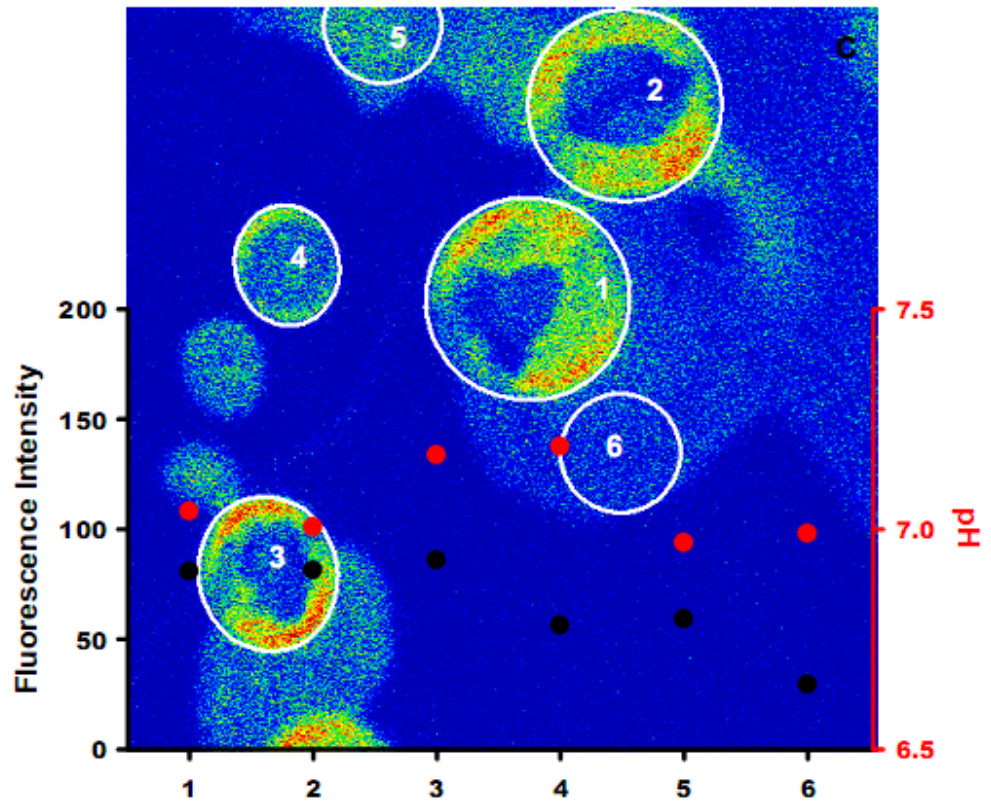
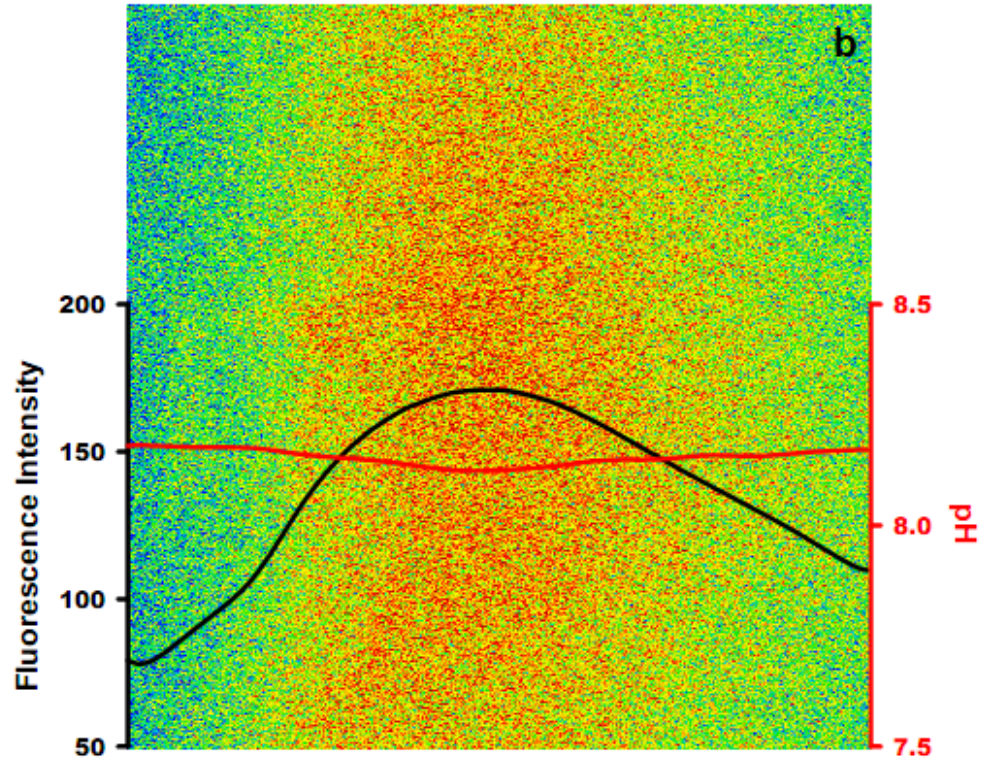


Figure 8.6. fluorescence emission ratio vs. pH measured by CLSM at different temperatures. The solutions contain 1.0  $\mu\text{M}$  C-SNARF-1 and 0.05 M phosphate buffer.

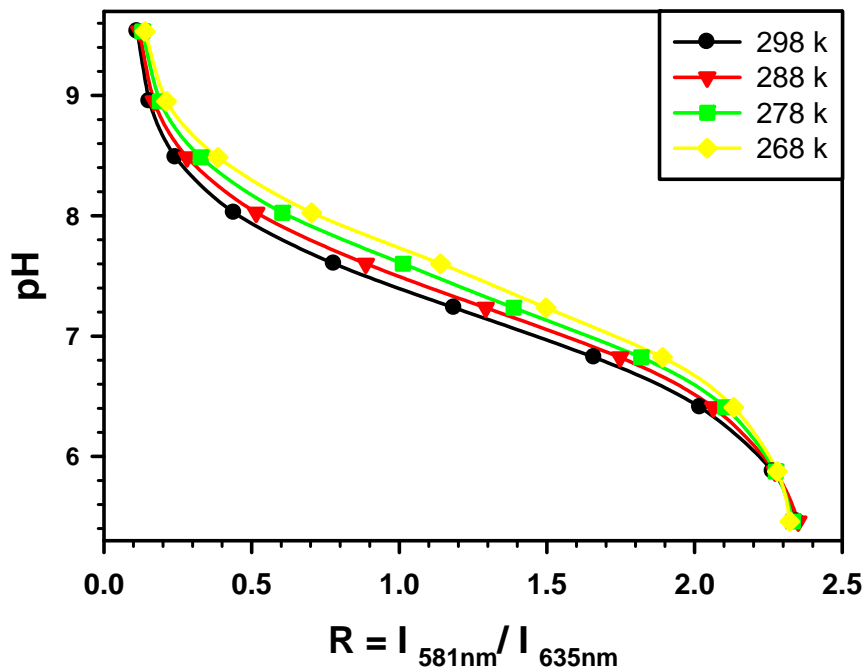


Figure 8.7. fluorescence emission ratio measured by CLSM as a function of (a) laser intensity and (b) C-SNARF-1 concentration.

